RESONANT TWO-PHOTON IONIZATION SPECTROSCOPY

OF JET COOLED OsN, IrSi AND CuCCH

by

Maria A. Garcia

A dissertation submitted to the faculty of
The University of Utah
in partial fulfillment of the requirements for the degree of

Doctor of Philosophy

Department of Chemistry

The University of Utah

August 2013

The University of Utah Graduate School

STATEMENT OF DISSERTATION APPROVAL

The dissertation of **Maria A. Garcia**

has been approved by the following supervisory committee members:

Michael D. Morse	, Chair	**5/09/2013** Date Approved
Peter B. Armentrout	, Member	**5/21/2013** Date Approved
Thomas G. Richmond	, Member	**5/09/2013** Date Approved
Michael H. Bartl	, Member	**5/09/2013** Date Approved
Christoph Boehme	, Member	**5/09/2013** Date Approved

and by **Henry S. White**, Chair of the Department of **Chemistry**

and by Donna M. White, Interim Dean of The Graduate School.

ABSTRACT

The optical transitions of supersonically cooled OsN have been investigated in the range from 19 200 to 23 900 cm^{-1} using resonant two-photon ionization spectroscopy. More than 20 vibronic bands were observed, 17 of which were rotationally resolved and analyzed. The ground state is confirmed to be $^2\Delta_{5/2}$, deriving from the $1\sigma^2\ 2\sigma^2\ 1\pi^4\ 1\delta^3\ 3\sigma^2$ electronic configuration. The X $^2\Delta_{5/2}$ ground state rotational constant for $^{192}Os^{14}N$ was found to be $B_0 = 0.491\ 921(34)\ cm^{-1}$, giving $r_0 = 1.620\ 42(6)$ Å (1σ error limits). The observed bands were grouped into three band systems with $\Omega' = 7/2$ and four with $\Omega' = 3/2$, corresponding to the three $^2\Phi_{7/2}$ and four $^2\Pi_{3/2}$ states expected from the $1\sigma^2\ 2\sigma^2\ 1\pi^4\ 1\delta^3\ 3\sigma^1\ 2\pi^1$ and $1\sigma^2\ 2\sigma^2\ 1\pi^4\ 1\delta^2\ 3\sigma^2\ 2\pi^1$ electronic configurations.

The optical spectrum of diatomic IrSi has been investigated for the first time, with transitions observed in the range from 17 200 to 23 850 cm^{-1} (581 – 419 nm). A rich spectrum has been recorded, consisting of 14 electronic band systems and a number of unclassified bands. Thirty-one bands have been investigated with rotational resolution, allowing the ground state to be identified as $X^2\Delta_{5/2}$ arising from the $1\sigma^2\ 1\pi^4\ 2\sigma^2\ 1\delta^3\ 3\sigma^2$ configuration. The ground $X^2\Delta_{5/2}$ state is characterized by $\Delta G_{1/2} = 533\ cm^{-1}$ and $r_0 = 2.0899(1)$ Å for the more abundant isotopic form, $^{193}Ir^{28}Si$ (57.8%). The measured excited electronic states have equilibrium bond lengths ranging from 2.17 to 2.25 Å and vibrational frequencies ranging from 365 to 452 cm^{-1}.

The optical spectrum of the linear CuCCH molecule has been investigated for the first time, using resonant two-photon ionization spectroscopy employing ArF (193 nm) or F_2 (157 nm) excimer radiation for photoionization. Scans over the range 19 400-25 200 cm^{-1} were conducted, leading to the observation of three electronic band systems. These are identified as the [20.2] $\widetilde{a}1 \leftarrow \widetilde{X}\,^1\Sigma^+$, the $\widetilde{A}\,^1\Sigma^+ \leftarrow \widetilde{X}\,^1\Sigma^+$, and the [24.7] $\widetilde{B}\,^1\Pi \leftarrow \widetilde{X}\,^1\Sigma^+$ systems, although only the first two have been rotationally resolved. The $\widetilde{a}1$ state is tentatively assigned as having $^3\Pi_1$ symmetry, becoming optically accessible through spin-orbit interaction with the $\widetilde{B}\,^1\Pi$ state.

For my mother
Andrea T. Garcia

Nature and nature's laws lay hid in night;
God said "Let Newton be" and all was light.

Alexander Pope

TABLE OF CONTENTS

LIST OF TABLES

Table

LIST OF FIGURES

Figure

ACKNOWLEDGMENTS

Graduate school has been a transformative experience; after many years of working with one singular focus, you eventually emerge as a scientist but also as a changed person. I would not be here today, about to embark on a second career much different from the one I had originally chosen several decades ago if it had not been for the following individuals.

First I must express my sincere gratitude to my advisor Michael Morse for all of his help and support during my tenure at the University of Utah. He is the finest small molecule spectroscopist in his field as well as an excellent professor. His enthusiasm is contagious and his obvious love of science is apparent. I will also never forget his rendition of the James Brown classic song "*I feel good*" when a new molecules rotationally resolved spectrum was initially revealed.

I am also extremely thankful for both past and present Morse group members all of whom I can call my friends; Alonzo Martinez, Ramya Nagarajan, Olha Krechkivska, Ned Lindholm, Dan Matthew, Eric Johnson and Sergie Aksyonov. I must offer a special thanks to Alonzo Martinez; without his friendship and support I may not have survived the many trials and tribulations I encountered working in the lab. In addition, I owe a debt of gratitude Ramya Nagarajan, who initially instructed me on how to run experiments in the R2PI and LIF labs. She did not merely show me how to turn

equipment on, but how to successfully collect data. I would also like to thank Olha Krechkivska for her friendship and support, not to mention the many laughs and sometimes tears we shared together over the years.

I don't want to neglect to thank Dennis Romney in the machine shop, Dale Heisler and Ron Jones in the electronic shop. Without their help experiments would have been near impossible to complete.

Lastly, I would like to thank my friends and family for their love, encouragement and support, especially to my partner Isabel Velez.

CHAPTER 1

INTRODUCTION

1.1 Historical Perspective

In Isaac Newton's 1675 letter to Robert Hooke, he wrote "If I have seen farther, it is by standing upon the shoulders of giants."[1] Although it was backhanded jab at his contemporary rival, Newton understood that his predecessors had laid the foundation for his scientific discoveries. With a simple glass prism, Newton demonstrated that sunlight was not as it seemed. The light could be broken down into its individual color components that we familiarly call the visible portion of the electromagnetic spectrum. Although the electromagnetic spectrum contains far more than just the visible colors dispersed through a prism, Newton laid a foundation for those who followed to add the parts of the spectrum which could not be seen by the human eye.

Johann Jakob Balmer had little understanding of physics, but was very interested in numbers. His expertise was in mathematics and yet he is remembered for discovering the Balmer series in atomic physics, completely altering the way physicists would think about spectral lines. His fascination with four numbers began after Anders Jonas Ångström measured the four visible spectral lines of atomic hydrogen: 6562.10, 4860.74, 4341.1 and 4101.2 Å. Balmer wondered if there was a pattern in this series of numbers, so through trial and error in 1885 he discovered the now famous formula,[2]

$$\lambda = b\frac{m^2}{m^2 - n^2} \quad , \tag{1.1}$$

where the wavelength λ is given in Ångströms (Å), b is what Balmer called the fundamental hydrogen number, which has a numerical value of 3645.6 Å, n is the integer *2,* and m is another integer with a starting value of *3*. The spectral lines of hydrogen correspond to specific jumps that an electron makes between energy levels when it is said to be excited. The electron does not remain in the excited state indefinitely; it will quickly relax down to the n=2 level in the hydrogen atom, emitting a photon to conserve energy. The physical meaning of the Balmer series was not understood by Balmer himself, but he knew that his formula could predict the wavelengths of the spectral lines of atomic hydrogen. He went further to suggest that there might be additional lines of atomic hydrogen, calculating the m=7 level as 3969.65 Å, unaware that Ångström had already measured this wavelength to be 3968.10 Å, in very good agreement with the calculated value.

Balmer also predicted that giving n other small integer values would result in additional emission lines in the atomic hydrogen spectrum. This prediction was correct as well; in 1906 the Lyman series was found for the n=1 level, followed in 1908 by the Paschen series for n=3, then the Brackett series in 1922 for n=4 and the Pfund series in 1924 for n=5. The series that were found after the discovery of the Balmer series reflect the nonvisible portion of the electromagnetic spectrum. Figure 1.1 is an illustration of the various series discovered early in the 20th century.

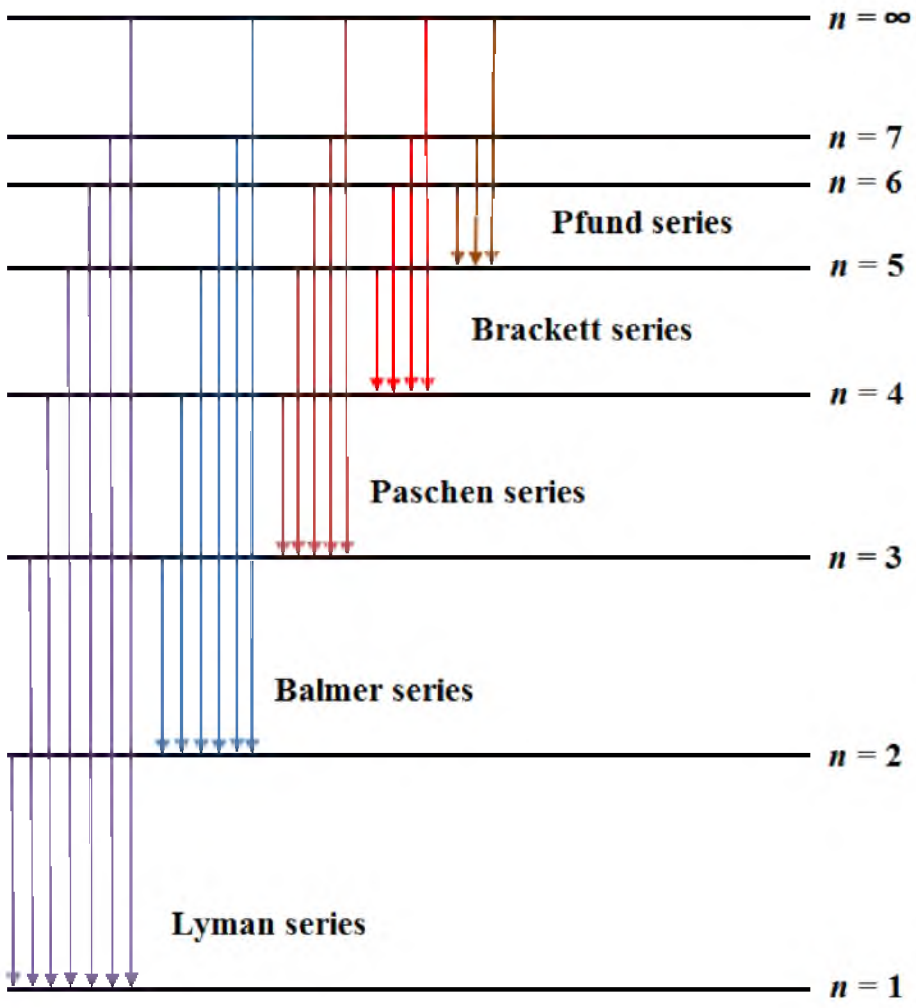

Figure 1.1 Illustration of the various series of atomic hydrogen. (not to scale)

1.2 The Model of the Atom

At the end of the 19th century many scientists were working on understanding the building blocks of matter, the once-thought indivisible atom. In 1897 J.J. Thomson was the first to suggest that the atom was made up of subatomic particles.[3, 4] He made this claim based on his experiments with cathode rays. Cathode rays were a stream of electrons traveling through a vacuum tube that struck a thermal junction, where the heat generated was measured and compared to the magnetic deflection angle. Thomson used this information to estimate the mass of the particle in the cathode ray and found it to be 1000 times lighter than the mass of the hydrogen atom. In addition, he found that no matter what element was used as the source of the rays, the mass of the cathode ray remained the same. Thomson concluded that the particles were very light and negatively charged. He named them "corpuscles" and they later became known as electrons. Concluding that the atom was divisible and comprised of corpuscles, he rationalized the nature of the neutral atom as having a sea of positive charges in which the negatively charged corpuscles were immersed, thereby balancing the charge. This model became known as the Plum Pudding Model (Figure 1.2).

The Plum Pudding Model would quickly be replaced by the Rutherford Model (Figure 1.3). In 1909 Earnest Rutherford conducted an experiment where alpha particles emitted from a radioactive source were used to bombard a gold foil.[5] While many of the alpha particles penetrated the gold foil, some were deflected at large angles or reflected back toward the source. This result was astonishing because it meant that the alpha particle was either colliding with the positive charge or passing close enough to it that it was deflected by the charge. Further, conservation of momentum required that the

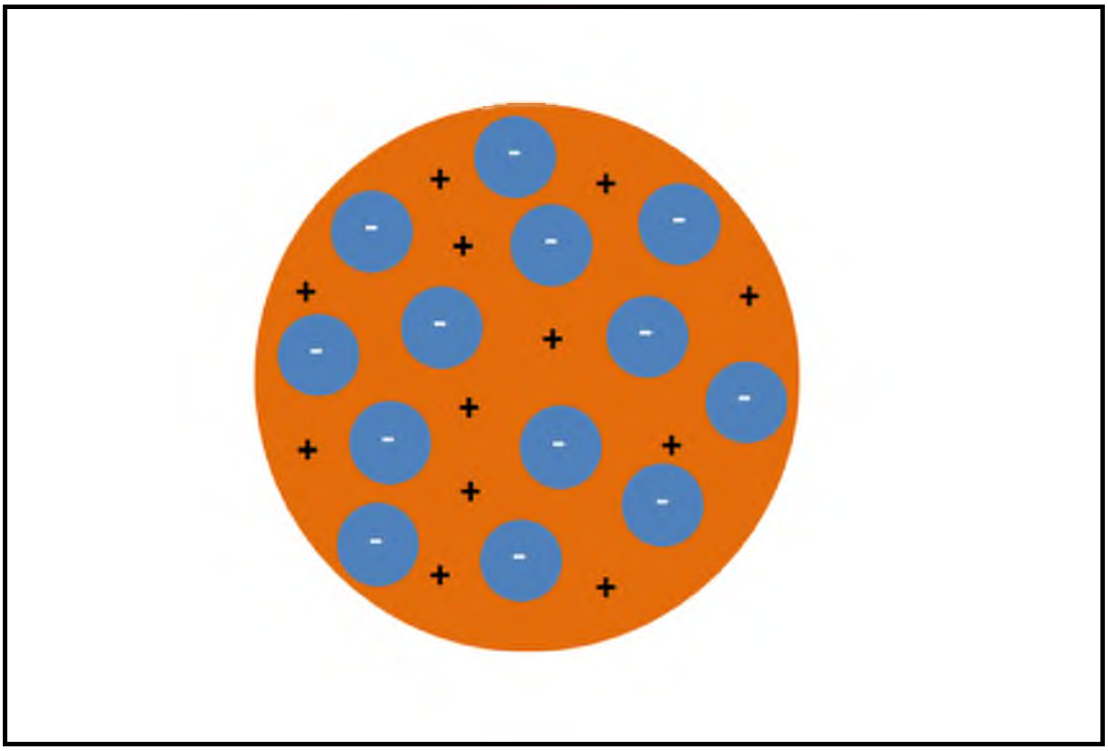

Figure 1.2 The Plum Pudding Model

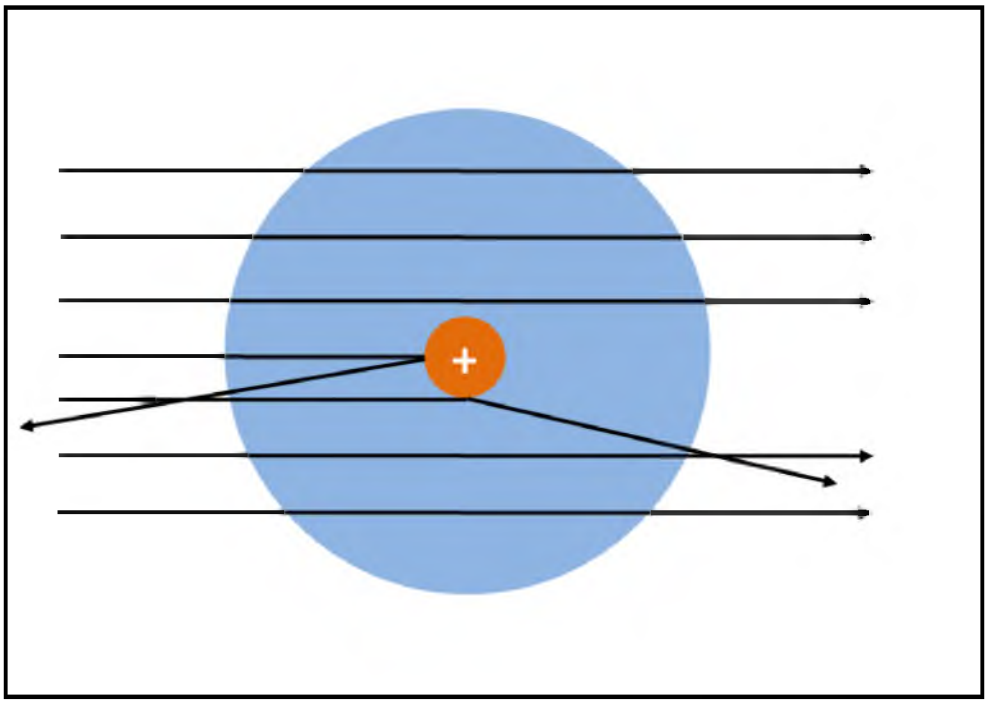

Figure 1.3 The Rutherford Model

alpha particle was colliding with a massive, positively charged object, but only on rare occasions. This experiment demonstrated that the Plum Pudding Model was incorrect because the positive charge was not distributed throughout the volume of the atom. Rutherford concluded that the large angle scattering was the result of a single collision between an alpha particle and a massive charge that was confined to a volume much smaller than the entire atom. He proposed that the atom was made up of mostly empty space with a large concentration of positive charge at the center.

Although the Rutherford Model greatly improved upon the Plum Pudding Model, it had problems explaining the actual behavior of the electron. Rutherford compared an atom with a massive, positively charged nucleus and an orbiting negative charge to the sun with its much lighter orbiting planets in our solar system. However this was not exactly accurate. The planets and the sun do not carry a charge and it was well known at the time that an oscillating electric charge experiencing acceleration emits electromagnetic radiation, resulting in a loss of energy. This meant that the electron would necessarily spiral into the nucleus, resulting in the collapse of the atom. Life and the universe as we know it could not exist. At this point the theory was in conflict with reality.

The contradiction between electromagnetic theory and the Rutherford gold foil experiment was confronted by a young Niels Bohr during his postdoctoral work at Victoria University of Manchester in 1912. Adopting Planck's relation that

$$E = h\upsilon \tag{1.2}$$

where h is equal to Planck's constant and υ is the frequency of the electromagnetic

radiation, he reasoned that if electromagnetic energy was quantized, so too was mechanical energy. Taking that line of thinking further, he proposed that electrons had fixed energy levels at a defined distance from the nucleus.[6] When an electron absorbed energy it jumped to a higher energy level, farther from the nucleus. Conversely, when the electron dropped to a lower energy level closer to the nucleus, it emitted radiation equal to the difference between the two energy levels. Although this model proved to be oversimplified, it was used by others to develop a more rigorous theory of quantum mechanics. In addition, it was not until Bohr presented his model of atomic hydrogen that an explanation could be provided as to why the Balmer formula worked.

It would take 12 years and a new generation of scientists to rigorously develop the theory of quantum mechanics. Between 1925 and 1927 three independent papers were published[7] by Werner Heisenberg, Edwin Schrödinger and Paul Dirac that began with three different assumptions but resulted in equivalent results, ultimately describing the energy levels of hydrogen and verifying the Balmer emission lines. This discovery would result in the exact solution to the energy levels of the hydrogen atom. Unfortunately, however, an exact solution for multielectron atoms or molecules would not be possible. Theoretical treatment of systems beyond one electron can only be done by approximation, so in order for scientist to evaluate these approximations, accurate experimental data are needed for comparison.

Over the course of many decades, spectroscopy has been used to interrogate atoms and molecules, allowing for repeated verification of the quantum mechanical theory that was developed early in the 20th century. This has led to its wide acceptance. Mapping the energy levels or eigenstates of atoms and molecules is a primary focus of

spectroscopy, although it can be used for analytical purposes as well. The analysis of the measured energy levels also allows other properties to be determined, including rotational constants, bond lengths, and vibrational frequencies for the ground and excited states of the molecules of interest. Armed with this detailed information, the quantum chemist can improve the approximations that are used to calculate molecular electronic structure, leading to a useful symbiosis: Quantum theory provides the underlying framework for interpreting spectroscopic data, while accurate spectroscopic data provide the benchmarks that are needed to verify that the approximations made in quantum chemical calculations are sufficiently accurate to provide useful results.

1.3 Thesis Outline

This thesis is divided into five chapters and two appendices. Following the introduction to the subject matter in Chapter 1, there is a detailed description of the equipment and experimental techniques in Chapter 2. When I was a new student of spectroscopy, I found that reading previous dissertations from the group was an invaluable tool in learning the two-photon ionization technique prior to actually starting my own experiments. It is the hope of this experimenter that I can provide the same guidance to future novice spectroscopy students.

Next, in Chapter 3 is the investigation of the OsN molecule which has been published in the Journal of Chemical Physics.[8] Transition metal molecules are of great interest and importance as catalysts in organic and organometallic chemistry.[9] This species is particularly interesting because of the ability of the osmium atom to form strong π-bonds due to the increased size and accessibility of the 5*d* orbitals, as compared to the 3*d* and *4d* elements. This study confirmed that the ground state of OsN is $^2\Delta_{5/2}$,

arising from the $1\sigma^2\ 2\sigma^2\ 1\pi^4\ 1\delta^3\ 3\sigma^2$ electronic configuration. Contained in Chapter 4 is an extensive investigation of the IrSi molecule which has also been published in the Journal of Chemical Physics. [10] Transition metal silicides have been of interest in the electronics industry for a number of years, owing to their hardness, resistance to oxidation, useful electronic properties, and compatibility with silicon-based microelectronics. In particular, several transition metal silicides have potential uses as Schottky-barrier infrared detection devices, including NiSi[11] and PtSi.[12] Iridium silicide has also been studied for purposes of infrared detection in Schottky barrier devices.[13] The ground state of diatomic IrSi is well-described as a single configuration $1\sigma^2\ 1\pi^4\ 2\sigma^2\ 1\delta^3\ 3\sigma^2$, $^2\Delta_{5/2}$ state. This ground term is consistent with the found for the isovalent IrC[14-17] and OsN[8, 18] molecules, but differs from the $^2\Sigma^+$ ground term of the isovalent 4*d* molecules RhC,[14, 16], RhSi,[19] and RuN.[20]

Chapter 5 describes the spectroscopic investigation of the polyatomic species, CuCCH which was published in the Journal of Physical Chemistry A.[21] Organometallics and, more specifically, organocopper reagents[22, 23] are extremely useful in synthetic organic chemistry. Commonly, these reagents make use of the weak sigma bond that exists between the metal atom and an organic radical to activate the organic species for subsequent reactions. One of the earliest known organometallic reactions, the Grignard reaction, employs an alkyl- or aryl-magnesium halide to form carbon-carbon bonds, and has been used in organic synthesis since the early 1900s.[24] The Gilman reagent, a lithium diorganylcuprate (I) salt, $Li^+[R\text{-}Cu\text{-}R]^-$, reacts with organic halides, R′X, to form new carbon-carbon bonds as well, producing R-R′ compounds.[25] The Ullman reaction is another copper catalyzed reaction that has been used to homocouple two aryl iodides to

form a biaryl compound.[26] The CuCCH molecule is of particular interest because copper acetylides are key catalytic intermediates in the Sonogashira coupling reaction.[27-30] In my studies of the spectrum of CuCCH, three excited electronic states have been found. These are identified as the [20.2] $\widetilde{a}1$, [23.1] $\widetilde{A}\,^1\Sigma^+$, and the [24.7] $\widetilde{B}\,^1\Pi$ states. The [20.2] $\widetilde{a}1$ state is thought to be of $^3\Pi_1$ symmetry, becoming optically allowed in transitions from the ground $\widetilde{X}\,^1\Sigma^+$ state via spin-orbit mixing with the [24.7] $\widetilde{B}\,^1\Pi$ state. A close correspondence with the electronic structure of the copper halides is noted, leading to the conclusion that CuCCH can be described as primarily an ionic molecule, in both the ground and the lowest group of excited states.

The final sections of this dissertation contain Appendices A and B, which provide detailed spectroscopic data, compiled into tables and figures, for the osmium nitride and iridium silicide molecules.

1.4 References

[1] I. Newton, Phil. Trans.Roy. Soc. **80,** 3075-87 (1672).

[2] J. J. Balmer, Ann. der Phys. **261,** 80–7 (1885).

[3] J. J. Thomson, The Electrician **39,** 104 (1897).

[4] J. J. Thomson, Phil. Mag. **44,** 293 (1897).

[5] E. Rutherford, Phil. Mag. **21,** 669-88 (1911).

[6] N. Bohr, Phil. Mag. **26,** 1-25 (1913).

[7] G. Gamow, *Thirty Years That Shook Physics: The Story of Quantum Theory* (Dover, New York, 1985).

[8] M. A. Garcia and M. D. Morse, J. Chem. Phys. **135,** 114304/1-12 (2011).

[9] *The Chemical Physics of Solid Surfaces and Heterogeneous Catalyst, Vol 4*, Vol., edited by M. Grunze (Elsevier, New York, 1982).

[10] M. A. Garcia, C. Vietz, F. Ruipérez, M. D. Morse, and I. Infante, J. Chem. Phys. **138,** 154306/1-9 (2013).

[11] J. Kurianski, J. Van Damme, J. Vermeiren, K. Maex, and C. Claeys, Proc. SPIE-Int. Soc. Opt. Eng. **1308,** 27-35 (1990).

[12] J. L. Gates, W. G. Connelly, T. D. Franklin, R. E. Mills, F. W. Price, and T. Y. Wittwer, Proceedings of SPIE - International Society of Optical Engineering **1540,** 262-73 (1991).

[13] X. Ma, Thin Solid Films **484,** 257-60 (2005).

[14] K. Jansson and R. Scullman, J. Mol. Spectrosc. **36,** 248 - 67 (1970).

[15] H. Tan, M. Liao, and K. Balasubramanian, Chem. Phys. Lett. **280,** 219-26 (1997).

[16] T. Ma, J. W. H. Leung, and A. S. C. Cheung, Chem. Phys. Lett. **385,** 259-62 (2004).

[17] H. F. Pang and A. S. C. Cheung, Chem. Phys. Lett. **471,** 194-7 (2009).

[18] R. S. Ram, J. Liévin, and P. F. Bernath, J. Chem. Phys. **111,** 3449-56 (1999).

[19] A. G. Adam, A. D. Granger, W. J. Balfour, and R. Li, J. Mol. Spectrosc. **258,** 35-41 (2009).

[20] R. S. Ram, J. Liévin, and P. F. Bernath, J. Chem. Phys. **109,** 6329-37 (1998).

[21] M. A. Garcia and M. D. Morse, J. Phys. Chem. A**,** Ahead of Print.

[22] R. D. Rieke and M. V. Hanson, Tetrahedron **53,** 1925-56 (1997).

[23] R. D. Rieke, Science (Washington, D. C., 1883-) **246,** 1260-4 (1989).

[24] M. S. Kharasch and P. O. Tawney, J.Am. Chem. Soc. **63,** 2308-15 (1941).

[25] H. Gilman, R. G. Jones, and L. A. Woods, J. Org. Chem. **17,** 1630-4 (1952).

[26] J. Hassan, M. Sevignon, C. Gozzi, E. Schulz, and M. Lemaire, Chem. Rev. (Washington, D. C.) **102,** 1359-469 (2002).

[27] K. Sonogashira, Y. Tohda, and N. Hagihara, Tetrahedron Lett.**,** 4467-70 (1975).

[28] K. Sonogashira, J. Organomet. Chem. **653,** 46-9 (2002).

[29] R. Chinchilla and C. Najera, Chem. Soc. Rev. **40,** 5084-121 (2011).

[30] R. Chinchilla and C. Najera, Chem. Rev. (Washington, DC, U. S.) **107,** 874-922 (2007).

CHAPTER 2

THE EXPERIMENTAL METHOD

2.1 Introduction

Spectroscopy is defined as the interaction between light and matter. Spectroscopy can be used as an analytical tool, but for the molecules that are studied in this dissertation, the purpose is to map the energy levels or eigenstates of the species of interest. Analysis of the measured energy levels allows other properties to be determined as well, including rotational constants, bond lengths, and vibrational frequencies for the ground and excited states of the molecules of interest. The technique employed is resonant two-photon ionization (R2PI) spectroscopy, an absorption technique that became widely used with the development of the tunable dye laser and supersonic expansion techniques.[1, 2] Interrogating the molecules of interest with a tunable dye laser probes their electronic structure by recording their electronic spectra. In addition, the use of a supersonic expansion cools the molecules to low vibrational and rotational temperatures, greatly reducing the spectral congestion that is inevitably present in studies conducted at higher temperatures. Supersonic expansion also permits studies of larger molecules that generally suffer from spectral congestion at higher temperatures, due to the greater number of vibrational levels that can be populated at these temperatures.

In addition to these advantages, the process by which the ions are detected also brings many benefits. First, ions are more efficiently collected than photons because

their motion can be controlled by electrostatic fields. Second, the background signal is often very low because scattered laser light does not contribute, as it does in fluorescence-based methods. Finally, by detecting the ions with a mass spectrometer, a mass-specific signal is obtained, allowing direct confirmation of the carrier of the spectrum. It is even possible to record isotopically-specific spectra without having to purchase isotopically enriched samples.

The molecules studied in the Morse group are generally transition metal molecules with two to four atoms, but larger species can be studied as well. The transition metal can be bonded to the same metal to form a dimer such as Pt_2,[3] to a different metal such as VMo,[4] or it can be bonded to a nonmetallic ligand such as carbon, nitrogen, fluorine, or silicon to form species such as OsC[5], OsN[6], ZrF,[7] and PdSi.[8] This chapter details the experimental set up required for the R2PI technique.

2.2 The Vacuum Chamber

In order to study the electronic structure of molecules one must collect their rotationally resolved spectra so that it can be fitted to extract the spectroscopic constants and further analyzed to identify the electronic states involved in the spectroscopic transition. To apply the R2PI technique, the molecules must be interrogated in the ionization region of a mass spectrometer, necessitating their formation and study under vacuum.

2.2.1 The Source Chamber

The apparatus used to conduct the resonant two-photon ionization experiment is illustrated in the schematic diagram shown in Figure 2.1. The source chamber is located

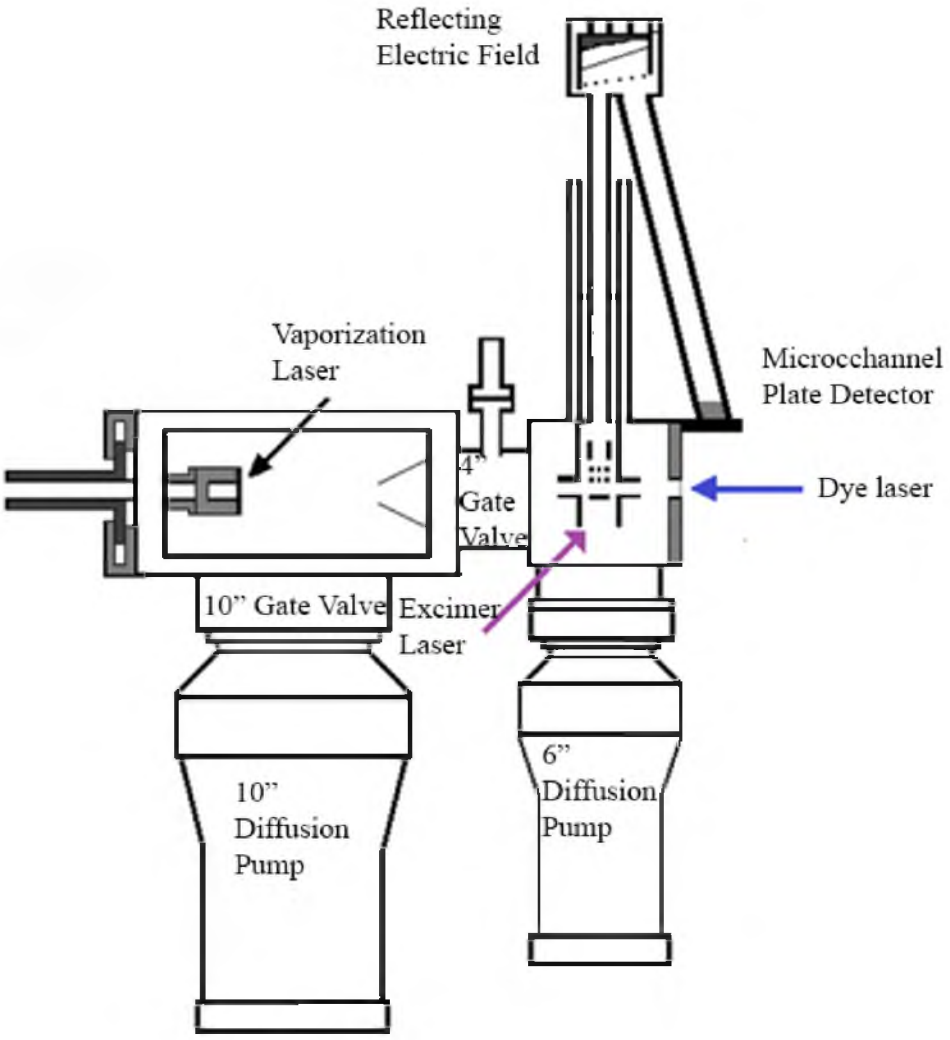

Figure 2.1 The resonant two-photon ionization instrument

on the left side of the figure and is pumped by a two-stage vacuum system. The chamber is approximately 71 cm wide by 41 cm high and 46 cm deep, enclosing a volume of approximately 108 L. The source chamber is evacuated to 3 torr or less using an Edwards E2M80 two-stage mechanical pump (53 cfm pumping speed), at which time an EH500 Mechanical Booster pump (236 cfm pumping speed) backed by the Edwards E2M80 is turned on, rapidly reducing the pressure in the source chamber to about 20 mtorr. Finally, a 10 inch Varian VHS-10 diffusion pump is turned on, reducing the final operating pressure to about 5×10^{-7} torr when the pulsed nozzle is turned off. The interface between the chamber and the diffusion pump is an electropneumatic 10-inch gate valve that when opened allows the chamber to be evacuated at a rate of 5300 liters per second for air. The diffusion pump is backed by the Edwards EH500/E2M80 mechanical and booster pump combination.

2.2.2 The A-Chamber

The A-chamber, which is also referred to as the spectroscopy chamber, is to the right of the source chamber in the schematic in Figure 2.1 and is isolated from the source chamber by a 4-inch electropneumatic Temescal gate valve. This is where the molecules are interrogated by the dye laser and ionization laser radiation. On the remaining three sides of the square chamber there are three circular flanges with a 2-inch optical window in the center of each flange. The A-chamber is composed of two pieces: the bottom portion, which is approximately 27 cm on each side, enclosing a volume of about 14 liters; and the top portion, which is composed of a 5 cm diameter tube that extends upwards about 61 cm, terminating at a cylinder that is approximately 20 cm in diameter

and 25 cm in height. This cylinder houses the reflectron that is part of the time-of-flight mass spectrometer. Extending down from this cylinder at an angle of about 18 degrees is another 7.6 cm diameter tube with a length of about 62 cm, which terminates at the housing for the microchannel plate detector. The tube that extends upward from the spectroscopy chamber is surrounded by a vacuum insulated Dewar formed from 2 concentric cylinders that extends about 44 cm in height above the top of the A-chamber. This Dewar can be filled with about 4.5 liters of liquid nitrogen for the purpose of cooling a copper box containing the extraction electrode assembly to liquid nitrogen temperature (about -196° C). In some experiments, this is needed to condense diffusion pump oil vapors and thereby reduce the background signal at specific masses of interest.

The A-chamber is first evacuated to approximately 40 mtorr by an Edwards RV12 rotary vane mechanical pump, which is capable of pumping 8.4 cfm of air. It is then further evacuated to a pressure of about 2×10^{-7} torr by a 6 inch Edwards Diffstak 160 Series diffusion pump capable of pumping 700 liters per second of air. The interface between the A-chamber and the diffusion pump is a butterfly valve that is operated using an electropneumatic Edwards BRV25 (backing-roughing valve). The BRV25 combines the function of separate backing/roughing valves into a one port unit. When the mechanical pump is completing the initial evacuation, the BRV is in the roughing position. Once the chamber has been evacuated to about 40 mtorr, the valve is actuated electropneumatically to switch into backing mode, and the butterfly valve on the top of the diffusion pump is also electropneumatically activated to open the chamber to the diffusion pump. The chamber pressure is ultimately reduced to about 2×10^{-7} torr. Unlike the source chamber, the A-chamber is held constantly under vacuum to protect the

microchannel plate detector from water vapor, which can damage the detector when high voltage is applied.

2.3 Molecular Source

The molecules that are studied in the Morse group are rarely purchased from chemical companies but instead are created and studied *in situ*. These molecules are stable as isolated species, but are highly reactive in collisions with species such as O_2, H_2O, or other molecules of the same kind. Clustering processes are usually exothermic, and the only thing preventing formation of larger clusters is the finite time during which collisions occur in the supersonic expansion. To produce the molecule of interest in good yield often requires a great deal of trial and error. When the molecule to be studied is not merely a metal cluster that is formed by collisions between the gaseous atoms produced by laser ablation of a metal sample, it involves a chemical reaction with some sort of reaction gas, as was the case for all of the molecules investigated in this dissertation. Typical reaction gases that are seeded into the helium (rarely argon) carrier gas are methane, acetylene, ammonia, sulfur hexafluoride, and silane. The two key components of the R2PI instrument that are involved in the process of forming the molecule of interest are the pulsed laser ablation and the supersonic expansion, both of which occur in the source chamber of this instrument.

Typically the metal sample that is used to make molecules in the Morse group is either a pure metal or alloy disk with diameter between 1.5 and 3 cm or a metal rod with a diameter of about 6.35 mm. To produce a large quantity of the molecule of interest in a stable manner, it is best that the sample have a smooth, homogeneous surface. Any irregularities in the surface cause fluctuations in the molecular signal, making the

interrogation of the molecule much more difficult. After the molecules pass through the skimmer (1 cm diameter) into the spectroscopy chamber, they are irradiated with dye laser light followed by the ionization laser radiation about 20 to 40 nanoseconds later. If the species of interest is not present in sufficient quantity, a low signal-to-noise ratio will result. With this in mind, care must be taken prior to beginning a spectral scan to ensure that an adequate concentration of the molecule of interest is stably produced.

The metal sample disk is mounted to a sample holder that is attached to an assembly that has a series of gears, pulleys and cams, driven by an external electric motor. The sample is pressed up against the vaporization block so that the surface can be vaporized without having an opportunity for the carrier gas to leak out between the sample and the block. A schematic of the molecular source is displayed in Figure 2.2. The sample is rotated and translated to maintain uniform vaporization of the metal sample, resulting in a nearly constant concentration of the desired molecule in the beam and avoiding drilling a hole into the sample. The stainless steel vaporization block measures 5 cm × 5 cm × 2.5 cm and consist of two perpendicular channels that have been drilled completely through the block. The channel that provides a path for the vaporization laser radiation to strike the metal target has an approximate diameter of 2 mm and a length of 2.5 cm. The second channel directs the carrier gas flow over the sample as it is being vaporized and then expands into vacuum via a circular orifice. Several vaporization blocks have been used that differ in the diameter of the expansion orifice, with the other dimensions being identical. The work completed for this dissertation employed the blocks with a 1 mm and a 5 mm diameter expansion orifice. The portion of the channel with the expansion orifice, where the molecular collisions

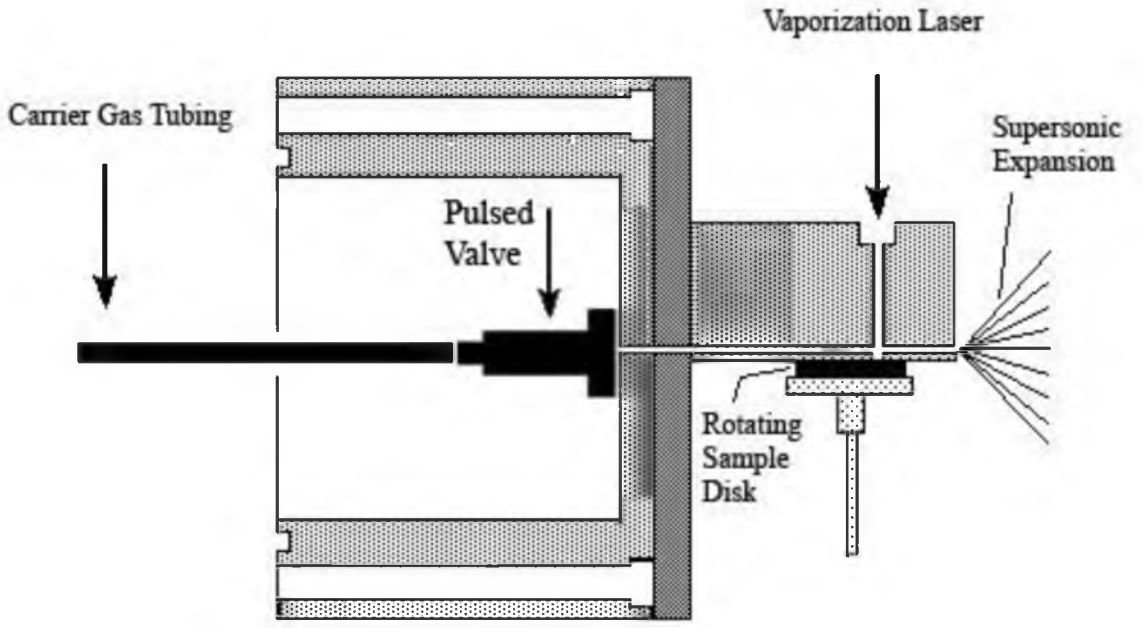

Figure 2.2 The molecular source

occur, is measured from the point where the vaporization laser beam strikes the metal target to the expansion orifice, giving a path length of about 12.7 mm. The diameter of the final expansion orifice greatly affects the amount of cooling that result from the supersonic expansion. Figure 2.3 displays two short sections of rotationally resolved spectra of the CuCCH molecule, as recorded with either a 5 mm or a 1 mm final expansion orifice. In the 5 mm orifice scan, Figure 2.3 (a), the individual lines are barely perceptible. There are so many rotational levels populated that the total intensity of the band is spread out over many lines, making each line barely distinguishable from the noise. When the 5 mm expansion orifice block is replaced with a 1 mm expansion orifice (Figure 2.3 (b)) the difference is remarkable. Fewer levels are populated and the intensity of each line is significantly increased, making it much easier to identify branches and assign the individual lines.

The molecules described in this dissertation were produced using a Quantel Brilliant pulsed Nd:YAG laser (3^{rd} harmonic radiation, 355 nm) to ablate the metal sample at a rate of 10 Hz. The beam profile measures approximately 5 mm in diameter at the laser aperture, but was focused onto the sample using a 50 cm focal length lens, leading to a beam diameter of about 0.5 mm at the sample. An important procedure to be performed when initially optimizing the production of the molecule of interest is to vary the timing between pulsing the gas valve and firing the vaporization laser, in order to insure that sample ablation occurs during the most intense part of the gas pulse.

The short duration of the laser pulse, about 4 nanoseconds, combined with the small focal diameter, causes the incident laser power density to reach values in the range of 0.7-2.5 GW/cm^2. This high rate of energy input heats the sample surface so rapidly

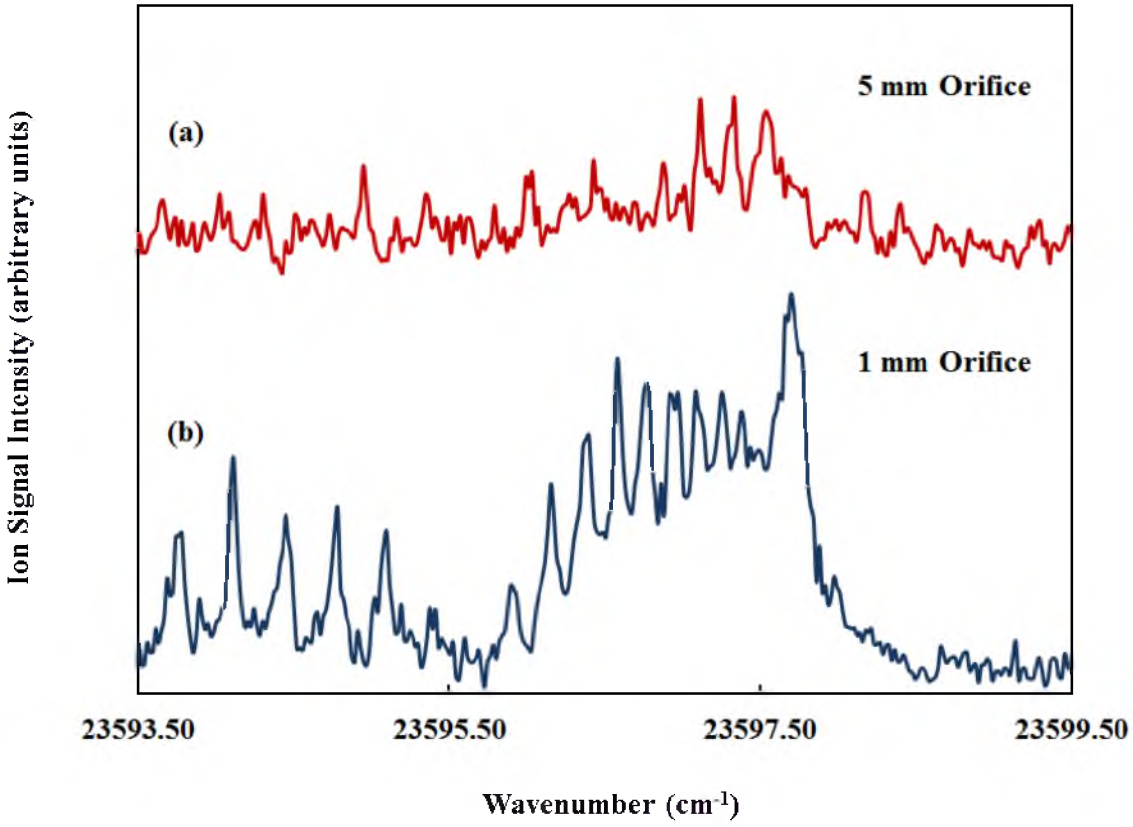

Figure 2.3 The effects of cooling

that atoms are ejected into the gas phase and are quickly ionized to form a plasma consisting of atomic ions, neutral atoms, and electrons.[9] A Series 9 General pulsed valve (Parker Hannifin) is attached to a flange directly behind the vaporization block, and is timed to fire prior to the ablation laser so that high pressure gas is present above the metal surface when the laser is fired. The gas pulse emitted by the pulsed valve is directed through a channel, flowing over the point of ablation about 3.7 cm downstream from the pulsed valve orifice. Downstream from the point of ablation, the metal plasma products are entrained in the carrier gas and collisions with reactive molecules seeded into the gas occur to form a variety of species, including neutral and ionic species as well as larger clusters. The chemistry involved in this process is not at all selective, and conditions must be optimized to form the desired species, generally by trial and error. The experimenter must modify conditions in order to make the molecule of interest and detect it in the mass spectrum, while obtaining a large enough density of the desired species and at the same time minimizing or eliminating competing species. This is not a trivial step in the overall experiment and can be critical in determining the eventual success of the spectroscopic investigation. The experimental conditions that can be varied are: (1) the concentration of reactant gas that is mixed with the carrier gas, (2) the backing pressure, (3) the duration of the gas pulse, (4) the vaporization laser energy, and (5) the length of the channel in the vaporization block through which the gas pulse is directed, which can be modified by the use of an extender.

2.4 Supersonic Expansion

The key to the successful collection of a rotationally resolved spectrum is to cool the molecule significantly in all of its degrees of freedom. If the molecule is not cooled

sufficiently, spectral congestion can make it exceptionally difficult to record and analyze the spectrum. The multitudes of states that can be populated in a beam that is insufficiently cooled reduce the population in each individual level, resulting in a poor signal-to-noise ratio.

Much of the cooling from the high temperatures associated with the nascent plasma is accomplished in the 12.5 mm long channel prior to supersonic expansion. In this region, ion-electron recombination takes place, mediated by collisions with helium. The initially formed species undergo many collisions with the helium carrier gas in this region and it is thought that this results in the thermalization of the reaction products to temperatures near room temperature. Additional cooling to extremely low temperatures then occurs when the high pressure gas expands into vacuum through the supersonic expansion process.

To achieve a supersonic expansion, a monatomic gas is expanded from a high-pressure (1 atm to 13.6 atm) reservoir at a temperature T (300K in these experiments), through a pulsed gas valve into a channel, which directs the gas flow over the sample. Two-body collisions between the carrier gas and the species produced in the laser-ablated plasma cause redistribution of energy, leading to thermalization of the entrained species. It is thought that this equilibrates the temperature of the entrained species to the approximate temperature of the carrier gas in the reservoir. Three-body collisions between two metal atoms and the carrier gas can result in stabilization of the diatomic metal molecule, which is the first step in the production of larger metal clusters. Similarly, reactive collisions between the ablated metal atoms and reaction gas molecules can produce metal-ligand complexes that can go on to further reactions. In general, the

large number of possible reactions in the channel downstream of the point of ablation makes the process quite difficult to model. This is why a trial and error method is often the best for optimizing the production of a given species.

The supersonic expansion occurs through a small circular orifice into the vacuum of the source chamber. The diameter of the expansion orifice used in most of the experiments conducted in this dissertation is 1 mm, which means that the mean free path (λ_0) between He-He collisions is much smaller than the diameter (D) of the expansion orifice. The mean free path of He is approximately 193.6 nm at 300 K and 1 atm, as calculated using

$$\lambda_0 = \frac{k_B T}{\sqrt{2}\pi d^2 P} \tag{2.1}$$

where k_B is the Boltzmann constant in J/K, T is the temperature (in kelvins), d is the molecular diameter and P is the pressure in pascals. The requirement that $\lambda_0 << D$ is the defining requirement for a supersonic expansion, since this condition enables the expanding gas to maintain thermal equilibrium in the course of the expansion. If the heat flow between the expanding gas and the expansion nozzle is negligible, the expansion is adiabatic. Further, if thermal equilibrium is maintained at all stages of the expansion, the expansion is in principle reversible. A process that is adiabatic (q=0) and reversible is also isentropic. Thus, the expansion of a high pressure gas into a low pressure region through an orifice that is much larger than the mean free path within the gas is an adiabatic, isentropic expansion. Such expansions are generally also called supersonic expansions, for reasons that are explained below.

In an adiabatic, isentropic process, the enthalpy of the gas is reduced but is converted into directed mass flow, which means that the directed kinetic energy is increased while obeying the overall conservation of energy. This is described by

$$H(x)+\frac{1}{2}mu(x)^2=\text{constant} \tag{2.2}$$

where H is the molar enthalpy, m is the molar mass, u is the flow velocity and x is the distance downstream from the expansion orifice.[1]

The supersonic expansion cools the translational degrees of freedom directly, while collisions between the translationally cold carrier gas atoms and the molecules seeded into the carrier gas cool the molecular degrees of freedom by bathing them in a cold translational bath.[10] The degrees of freedom that have more closely spaced energy levels (rotational energy levels) are cooled more effectively and continue to cool farther downstream into the low density portion of the molecular beam. Those with more widely spaced energy levels are cooled less effectively, and cooling of these degrees of freedom does not continue so far downstream. The electronic and vibrational degrees of freedom are cooled more effectively in the channel prior to expansion or in the high density region of the expansion, where they suffer relatively higher energy collisions. The rotational temperature in the beam is closer to the translational temperature, while the vibrational and electronic degrees of freedom are less effectively cooled.

The velocity of the beam is dictated by the mass of the carrier gas and the temperature of the reservoir. The pressure only becomes significant if it is too low to achieve a full supersonic expansion. The ultimate flow velocity occurs when all of the enthalpy of the carrier gas is converted into directed mass flow and is given by

$$u_{\max} = \sqrt{\frac{2C_p T_0}{m}} \quad , \tag{2.3}$$

where C_p is the constant pressure molar heat capacity, m is the molar mass and T_0 is the temperature of the reservoir of the monatomic ideal gas.[1] Helium is typically used in the vast majority of the experiments conducted in the Morse Group. For helium or any monatomic gas, C_p equals 5/2 R. For an approximate reservoir temperature of 300 K, equation (2.3) then provides a terminal velocity for helium of 1.77×10^5 cm/s. Occasionally argon has been used as the carrier gas and it is immediately evident how much longer it takes for the molecules to travel through the chamber and finally arrive in the ionization region. For argon, equation (2.3) provides a terminal velocity of 5.59×10^4 cm/s.

When the ratio of the flow velocity, *u(x)*, to the local speed of sound, *a(x)*, exceeds unity, it is said that the beam has become supersonic. This ratio is also referred to as the Mach number, defined as

$$M(x) = \frac{u(x)}{a(x)} \tag{2.4}$$

The speed of sound in an ideal gas is given by

$$a(x) = \sqrt{\frac{\gamma RT(x)}{m}} \tag{2.5}$$

with γ being the ratio of C_p/C_v.[1] The supersonic expansion is easily achievable by converting the random motion in the gas reservoir to directed mass flow, thereby draining

random kinetic energy out of the gas and reducing its temperature. This reduces the local speed of sound while simultaneously increasing the average velocity of the molecular beam, causing M(x) to exceed unity. Indeed, it is not difficult to achieve Mach numbers of 30 or more.

As the jet-cooled molecular beam expands into vacuum, the central portion passes through a 1 cm diameter conical skimmer, collimating the beam so that the central portion of the molecular beam enters into the A-chamber for spectroscopic interrogation. The skimmer also serves to minimize the gas load on the A-chamber, thereby helping to maintain a low pressure in the A-chamber. The skimmer is also equipped with a pair of electrodes that prevent ions that are created in the supersonic expansion from entering the A-chamber and reducing the signal-to-noise ratio. The electrodes do not prevent all of the ions from entering the interrogation region but do substantially reduce background noise in the mass spectrum that is associated with these stray ions. The transit of the molecular beam between the source chamber and the A-chamber is allowed by opening the 4-inch gate valve.

2.5 Resonant Two-Photon Ionization Process

Once the molecule of interest has been detected in the mass spectrum, the focus of the experiment shifts to probing the molecule with the tunable dye laser in order to record its spectrum. The incident photon can be absorbed only if its energy matches the separation between two molecular eigenstates. However absorption of a dye laser photon generally is insufficient to ionize the molecule, and in itself does not lead to a detectable ion signal. The key to the R2PI spectroscopic method is to supply a second pulsed radiation source that can be used to ionize the excited molecule with high efficiency.

2.5.1 The Ionization Process

The requirements for the ionization wavelength are: (1) the wavelength chosen must not ionize the molecule of interest in a one-photon process, (2) the sum of the energy of the dye laser photon and the ionization photon must be sufficient to ionize the molecule, and (3) the ionization wavelength must not be resonant with a spectroscopic transition, which would allow a resonant two-photon ionization process involving this wavelength alone. With these constraints, there is no surefire method to determine whether the correct ionization wavelength for a given molecule is being used, although *ab initio* calculations can provide a good starting point. In favorable cases, it may be possible to bracket the ionization potential of the molecule of interest by scanning the spectrum using two different ionization wavelengths, and noting what spectroscopic transitions are observed with each ionization choice.

An example of this occurred when the CuCCH molecule was investigated. The optical spectrum was initially scanned using ArF (ionization photon energy 6.42 eV) starting near 19 400 cm^{-1}, eventually locating a vibronic band near 24 673 cm^{-1}. This observation placed an upper limit on the ionization energy of CuCCH as IE(CuCCH) $\leq$ 9.48 eV. To observe lower energy vibronic bands, the ionization laser gas was changed to F_2, increasing the ionization energy to 7.9 eV. This allowed many additional vibronic bands to be observed, and bracketed the ionization energy in the range between 9.40 and 9.48 eV.

The ionization source for the experiments conducted in this dissertation was a GAM model EX100 excimer laser operating with 3 different fixed output frequencies dependent upon the gas mixture used: KrF (248 nm, 5.0 eV), ArF (193 nm, 6.42 eV), and

F_2 (157 nm, 7.9 eV). Operating the excimer laser with the KrF and ArF gases is straightforward, but when switching to the F_2 radiation, modifications are required in the experimental arrangement. These changes are needed because the 157 nm output radiation lies in the vacuum ultraviolet region of the spectrum, where it is easily absorbed by O_2, as well as by fused silica. As a result, this wavelength cannot be passed through the air. The S1-UV fused silica input window that is located on one of the three sides of the A-chamber must be replaced with an MgF_2 window with a purge tube attached between the excimer aperture and the A-chamber MgF_2 window. The purge tube is flushed continuously with nitrogen gas using a very slow bleed rate, allowing the light to travel through the tube and into the ionization region in the A-chamber.

There are four ionization processes that can occur in the R2PI experiment, as illustrated in Figure 2.4. The first scheme identified in Figure 2.4 (a) is one-photon ionization, in which a single high energy photon is absorbed, ejecting an electron from the atom or molecule. Many of the species studied in the Morse group have ionization energies that can be reached by absorption of one F_2 (7.9 eV) or one ArF (6.42 eV) excimer laser photon, but such processes are not useful when attempting to map out the eigenstates of a particular molecule. This is because there is no significant enhancement in ionization probability when the molecule is in an excited state *vs.* the ground state. One photon ionization processes can prove advantageous in determining what species are present in the gas pulse, however.

Long before lasers were developed, Maria Goeppert-Mayer predicted in her 1931 dissertation that an atom can absorb two or more photons simultaneously.[11] The multiphoton absorption process that she predicted was not observed until 1961, when

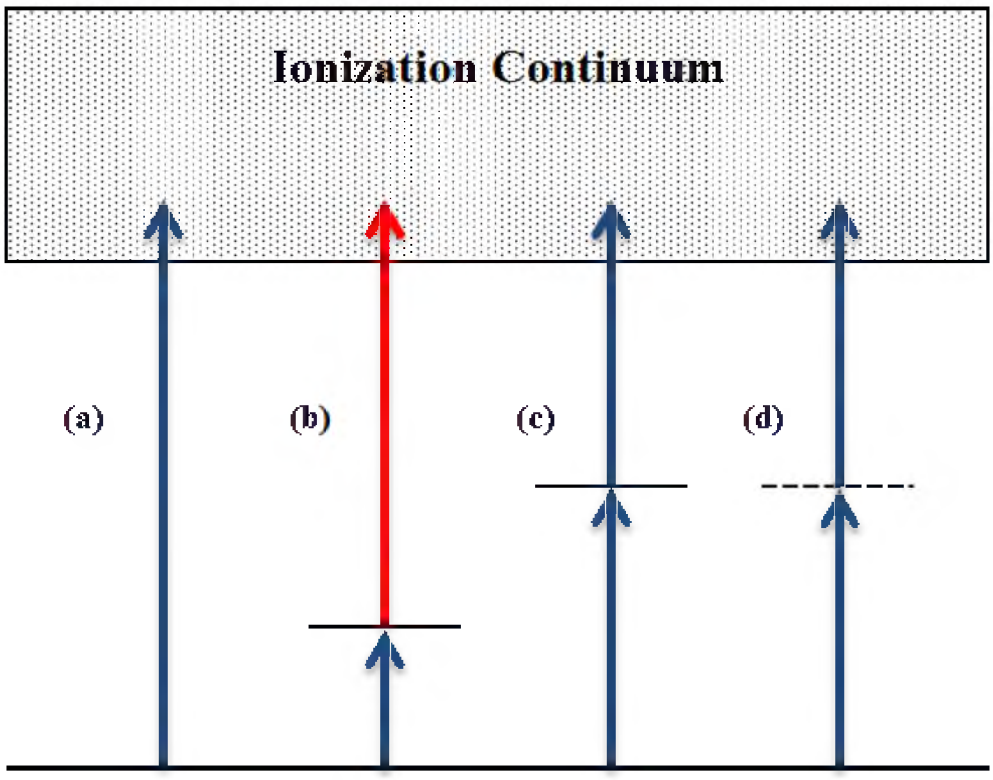

Figure 2.4 Ionization scheme for R2PI experiment. (a) One-photon ionization. (b) Two-color, two-photon ionization through a real state. (c) One-color, two-photon ionization through a real state. (d) One-color, two-photon ionization through a virtual state.

two-photon excitation of Eu^{2+}:CaF_2 was achieved using red light of wavelength 694.3 nm from a ruby optical maser.[12]

The rate of two-photon absorption is given by[13]

$$W_{f\leftarrow i} = \frac{2\pi}{\hbar^4}\sum_n \left| \frac{(E_2 \cdot \mu_{fn})(\mu_{ni} \cdot E_1)}{\omega_{ni} - \omega_1} + \frac{(E_1 \cdot \mu_{fn})(\mu_{ni} \cdot E_2)}{\omega_{ni} - \omega_2} \right|^2 \delta(\omega_{fi} - \omega_1 - \omega_2) \qquad (2.6)$$

where the subscripts *i* and *f* denote the initial and final state of the molecule with *n* representing the intermediate state. E_1 and E_2 represent the electric fields with the frequency associated these fields denoted by ω_1 and ω_2. The quantities μ_{ni} and μ_{fn} are the transition dipole integrals that couple the initial state with the intermediate state and the intermediate state with the final state. The frequency, ω_{ni}, represents the energy difference between the intermediate state and the initial state, divided by ħ. The delta function $\delta(\omega_{fi}-\omega_1-\omega_2)$specifies that the two-photon absorption is only possible when the condition $\omega_{fi}=\omega_1+\omega_2$ is satisfied. In all of the R2PI experiments, the final state lies in the ionization continuum and therefore this condition is always satisfied. The summation accounts for all the possible intermediate states, *n*. When the energy of the first photon matches the energy difference between the initial state and the first intermediate state, $\omega_1 = \omega_{ni}$, then the denominator in the first term vanishes resulting in a significant increase in the rate of ionization that leads to a resonant enhanced ion signal. The second term represents the absorption of the ionization laser photon prior to the spectroscopic photon, and is negligible in our experiments due to the delay between these two laser pulses.

In the case of Figure 2.4 (b), the resonant state lies less than halfway to the ionization continuum, requiring that the second photon must have greater energy than the

first photon in order to eject an electron and ionize the molecule. Thus, two different laser wavelengths are required, making this a resonant two-color, two-photon ionization process. In this scheme, the first photon frequency is scanned while the second is held at a fixed frequency. This is the ideal scheme for spectroscopic probing because it allows low-energy states to be investigated. States that are more than halfway to the ionization limit can be probed using a one-color two-photon ionization process, as depicted in Figure 2.4(c), but these intermediate states may lie above the dissociation threshold, where rapid predissociation will compete with the ionization step, often prohibiting the measurement of a spectrum. In addition, it is generally true that the higher one goes in energy, the more complex the electronic spectrum becomes. At energies that are more than halfway to the ionization limit, the electronic spectra of the types of molecules studied in the Morse group often become highly congested, and the high density of electronic states makes perturbations in the spectra more the rule than the exception. In order to obtain spectra that may be interpreted to provide useful information, it is generally preferable to work at lower energies. This makes a second wavelength (and generally, a second laser) necessary for the ionization step.

The two-photon process described in Figure 2.4 (d) occurs when a nonresonant condition exists such that no single intermediate state dominates the summation in equation 2.6. This is referred to as a virtual state, indicated by the dashed line in Figure 2.4 (d). The virtual state is a theoretical construct that does not correspond to any single eigenstate, but describes the superposition of a large number of pathways that constructively interfere to give a nonzero net ionization probability. This signal obtained through this nonresonant process generally results from the absorption of two excimer

laser photons, and can be minimized by reducing the intensity of the excimer laser radiation, which is usually done by inserting partially absorptive filters into the output excimer laser beam. This allows the nonresonant background signal, which is proportional at low powers to the excimer laser intensity squared, to be minimized without unduly diminishing the resonant signal, which is proportional to the tunable laser intensity times the excimer laser intensity, both to the first power. By reducing the excimer laser intensity both the nonresonant background and the resonant signal are reduced, but the ratio of the two is improved, making for a better resonant enhancement. Care must be taken not to filter the excimer laser too severely, however, because this may prevent any signal at all from being detected. In practice, this is a balancing act and the ionization laser intensity must be optimized for each individual molecule. Ultimately, the magnitude of the nonresonant background depends on how close to a resonance the excimer laser wavelength lies. If the excimer laser wavelength happens to lie at precisely the wavelength of an allowed molecular absorption, it is useless for the purposes of this experiment because the resonant two-photon ionization process will already occur with the excimer laser alone.

An experimental mass spectrum is displayed in Figure 2.5 for the four most abundant isotopes of the OsN molecule. The dye laser was tuned to a resonant frequency in Figure 2.5(a), and detuned in Figure 2.5(b). When the dye laser is detuned, the molecular signal is barely visible above the background in the mass spectrum. In contrast, the resonant signal increased is significantly larger and the masses are well defined.

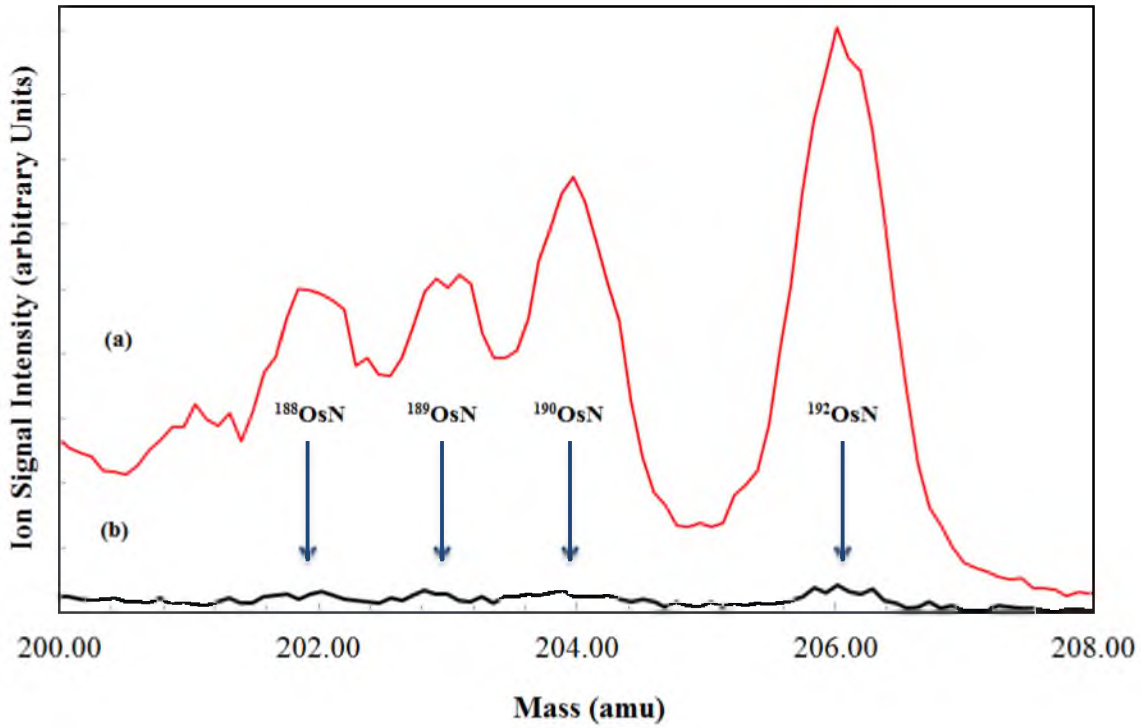

Figure 2.5 Mass spectrum of OsN: (a) dye laser tuned on resonance (b) dye laser tuned off resonance.

2.6 Time-of-Flight Mass Spectrometer

2.6.1 General Information

Time-of-flight mass spectrometry (TOF-MS) is a method by which ions are formed in the gas phase and accelerated by an electric field into a field-free drift region. Ideally, the potential used to accelerate the ions gives each ion of the same charge the same kinetic energy, but the ions travel at different velocities in the field-free zone due to their different masses. The ions with smaller masses move at higher velocities while the ions with larger masses travel more slowly, leading to a systematic variation in the ion time-of-flight that can be used to measure ion masses. For the experiments reported in this dissertation, the ions travel up a field-free drift tube, then enter a reflecting electric field and enter a second field-free drift tube before reaching the microchannel plate detector. The reflectron geometry extends the path length, in principle increasing the mass resolution. More importantly, it refocuses the ions that are produced at slightly different electrostatic potentials so that they strike the detector in a narrow time window. This also improves the mass resolution of the system.

2.6.2 The Wiley McLaren Design

A schematic of the reflectron TOF-MS and its components utilized in the Morse group is depicted in Figure 2.6. As was mentioned previously, the collimated molecular beam enters the A-chamber, where the TOF-MS is housed. The molecular beam is interrogated when it enters the region between the repeller plate and the draw-out grid (DOG), which are separated by a distance, s_0. The molecular beam is irradiated with unfocused dye laser light that is counterpropagated along the molecular beam axis.

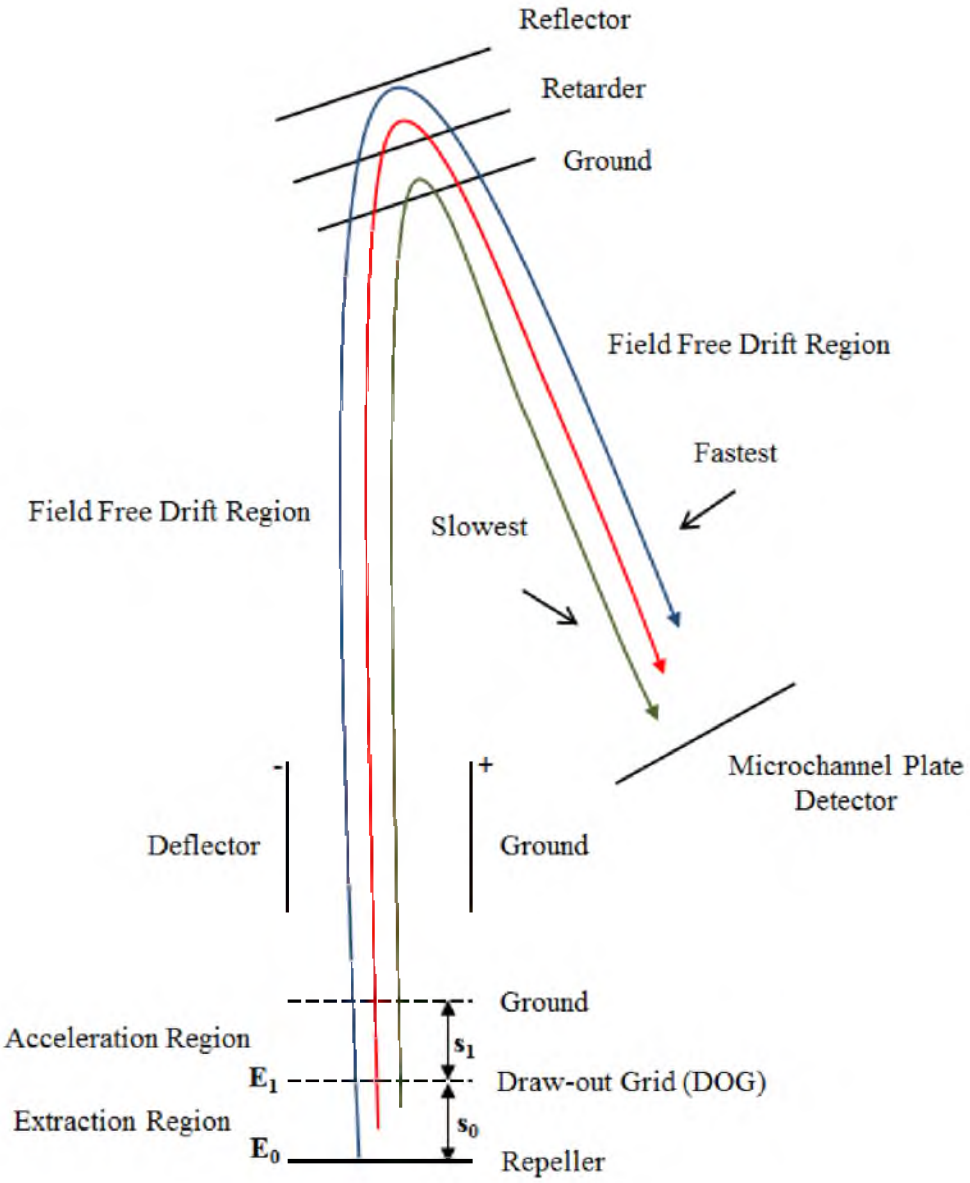

Figure 2.6 Time-of-flight mass spectrometer

Within 40 nanoseconds, the unfocused excimer laser radiation is directed across the molecular beam axis at right angles, producing ions.

A positive voltage, V_0, is continuously applied to the repeller plate in combination with a smaller positive voltage, V_1, that is continuously applied to the draw-out grid. These two voltages define the electric field in the extraction region, given by

$$E_0 = \frac{V_0 - V_1}{s_0} \tag{2.7}$$

This electric field accelerates the ions that are created in the extraction region into the acceleration region. The acceleration region is defined as lying between the draw-out grid and the ground grid, which are separated by a distance, s_1. In this region, the ions are exposed to a different electric field, given by

$$E_1 = \frac{V_1}{s_1}. \tag{2.8}$$

The acceleration region provides an additional acceleration up the flight tube. The division of the ion source into two stages of ion extraction is the hallmark of the Wiley-McLaren design.[14] Designs in which only a single extraction region is employed do not allow the position of the spatial focus to be conveniently controlled. In contrast, by adjusting the voltage on the draw-out grid, the amount of acceleration in the extraction *vs.* acceleration regions can be controlled, and this allows the spatial focus to be positioned wherever the experimenter finds it to be most convenient. In a linear time of flight instrument, no additional focusing control is required. In a reflectron instrument, additional focusing control is available through the reflecting field, as described below.

During the acceleration by the electric fields described above, the ions gain a velocity described by

$$v = \sqrt{\frac{2zeV}{m}} \tag{2.9}$$

where V is the electrostatic potential at the position where the ion is created, z is the charge on the ion, which is assumed to be unity, e is the electron charge and m is the mass of the ion.

The ions also possess a transverse velocity component due to the velocity of the molecular beam. For helium carrier gas initially at room temperature, the beam velocity is near the terminal velocity of 1.77×10^5 cm/s. Unless the transverse component of velocity is halted, or at least severely reduced, the ions will never reach the detector, instead crashing into the wall of the flight tube. In order to halt the forward motion of the ions, a pair of deflector plates is placed above the two-stage acceleration region, creating an opposing force on the ions. This halts their forward motion and allows the ions to reach the detector. The adjustable electric field on the deflector plates introduces a mild mass discrimination effect that must be optimized to obtain maximum transmission of the specific masses of interest.

2.6.3 Reflectron

At the top of the first flight tube are a second set of electrodes, creating an electrostatic ion mirror, more commonly called a reflectron.[15] These ion optics consist of a series of grids in a dual stage design. The first grid is grounded so it is at the same potential as the flight tube. It is followed by the retarder grid and a final plate, called the

reflector. These are illustrated in Figure 2.6. The purpose of this set of electrodes is to further enhance the mass resolution at the detector by increasing the path length and correcting for the kinetic energy spread of the ions. The second flight tube is set so that its axis is offset 18 degrees from the axis of the vertical flight tube, resulting in the ions being turned 162 degrees. The vector that is perpendicular to the electrodes in the reflectron (i.e., the surface normal) is oriented at a 9 degree angle relative to the vertical and second flight tubes, so that like an optical mirror, the angle of incidence (9°) equals the angle of reflection (also 9°). Finally, the planar surface of the microchannel plate detector is aligned so that its surface normal is parallel to the second flight tube.

Because the laser beams that create the ions have spatial extent, some ions are born closer to the repeller plate than others, and these ions develop a greater kinetic energy than those born closer to the draw-out grid. As the ions travel up the first flight tube, the ions produced nearer to the repeller travel faster, and eventually catch up with the ions born closer to the draw-out grid, leading to a spatial focus. Beyond this point, the faster ions are in front, and the packet of ions of the same mass begins to diverge. However, the reflectron is able to refocus the ion packet onto the detector. The faster ions, which are now farther up the flight tube, penetrate deeper into the reflecting field than the slower ions, and take longer to turn around. After reflection, the slower ions are once again in front, and the faster ions eventually catch up, forming a second spatial focus at a particular position. By adjusting the voltage on the retarder, it is possible to position the second spatial focus on the front surface of the microchannel plate detector, thereby obtaining good mass resolution.

2.7 The Detector

Located at the end of the second flight tube on the TOF-MS is a chevron configuration dual microchannel plate detector (MCP) that was purchased from Photonis (model# 25/12/10/12 D 40:1). Each microchannel plate functions as an array of tiny continuous dynode electron multipliers, where each microchannel is a small hole approximately 10 μm in diameter, etched at a 12 degree bias angle to the surface normal. The bias angle prevents particles from passing through the channels without impacting the walls. The front surface of the first plate is charged with up to -2000 volts while the back surface of the second plate is kept at -50 volts. As the ions impact the face of the MCP, they dislodge electrons, which are accelerated into the channels and collide with the wall of the channel. The surface material of the microchannels is chosen so that secondary electrons are emitted, which are further accelerated down the channel, again striking the wall, ejecting more secondary electrons and creating a cascade effect. The gain resulting from this process is approximately 10^7 for the two-plate system. The MCP is connected to a 50 Ω terminated anode[16] that is also coupled to an impedance matched 350 MHz SR445A Stanford Research preamplifier with 5× amplification per channel (4 channels total) and can be chained for a total of 625× application when operating at 50 Ω input impedance. The output signal from the MCP is converted to a voltage by the preamplifier that is sent via a BNC cable to an impedance matched 50 Ω termination on a National Instruments PCI 5112, 8 bit, 250 MHz, 250 MS/s scope card, which digitizes the waveform every 4 nanoseconds. The resulting digitized signal is then read and manipulated using a Windows 7 based PC with an i3 processor, using a program developed in the Morse group utilizing LabView software. The signal-to-noise ratio is

improved by averaging out the shot-to-shot signal fluctuations by summing 30 time-of-flight waveforms prior to measuring the intensities of the masses of interest. Given that the entire experimental cycle (pulsing the valve, firing the vaporization laser, firing the dye and excimer lasers, and recording the time of flight mass spectrum) repeats at a rate of 10 Hz, collection of the summed mass spectrum requires 3 seconds of laboratory time.

2.8 Data Collection

2.8.1 The Mass Spectrum

Prior to attempting to record an optical spectrum, the experimenter must first ensure that the molecule of interest is being made in sufficient quantity for detection. This is done by collecting a mass spectrum of the species of interest, as well as all other detectable species that appear in the mass spectrum within the limits determined by the number of digitized points. Ionization is achieved by operating the excimer laser at a high enough fluence to achieve nonresonant two-photon ionization. Monitoring atomic signals is particularly useful because they provide an indication of how stable the molecular signal may be. In addition, they can be used to align the dye laser so it overlaps well with the molecular beam and the ionization laser beam. This is done by tuning the dye laser to an atomic absorption line, and adjusting its position going into the chamber to optimize the atomic ion signal. Lastly, collecting at least one of the isotopes of an atomic signal can later allow for the calibration of the low resolution spectrum, if a sufficient number of atomic transitions occur in the spectrum.

The ability to monitor multiple peaks in the mass spectrum allows the investigator to simultaneously collect optical spectra of several different species. This is particularly useful when a molecule has several naturally occurring isotopologues, because it

eliminates the need to identify the isotopic carrier for each and every line in the spectrum. For species with many isotopic forms, this capability is a major advantage compared to methods that lack mass-specificity, such as laser-induced fluorescence. Figure 2.7 illustrates the isotopic shift of spectroscopic transitions with the example of OsN. The figure displays four mass spectra, recorded at closely spaced wavenumbers that are resonant with transitions in ^{188}OsN, ^{189}OsN, ^{190}OsN, and ^{192}OsN. It is easily seen that the enhancement moves from one isotopologue to another as the laser is tuned to the red. In cases of particularly weak transitions or poor signal-to-noise ratios, the existence of isotopes can help the experimenter to determine whether the signal that appears on the screen is real or merely noise. If it is real, it will appear in all of the isotopes, often with an isotope shift that varies regularly with isotopic mass. Measurements of the isotopic shift of the transitions in a spectrum is also useful in establishing the vibrational numbering of the upper state levels in the spectrum.

Once the experimenter is certain that all conditions have been optimized to begin the low resolution scans, the ionization laser is attenuated to reduce the nonresonant two-photon ionization background, thereby optimizing the resonance enhancement when the dye laser is tuned to an absorption.

2.8.2 Low Resolution Spectra

All the optical data in this dissertation were collected using a Lambda Physik ScanMate Pro dye laser, pumped by a Continuum Surelite III Nd:YAG laser. The low resolution vibronic scans were completed with a dye laser linewidth of about 0.15 cm^{-1}.

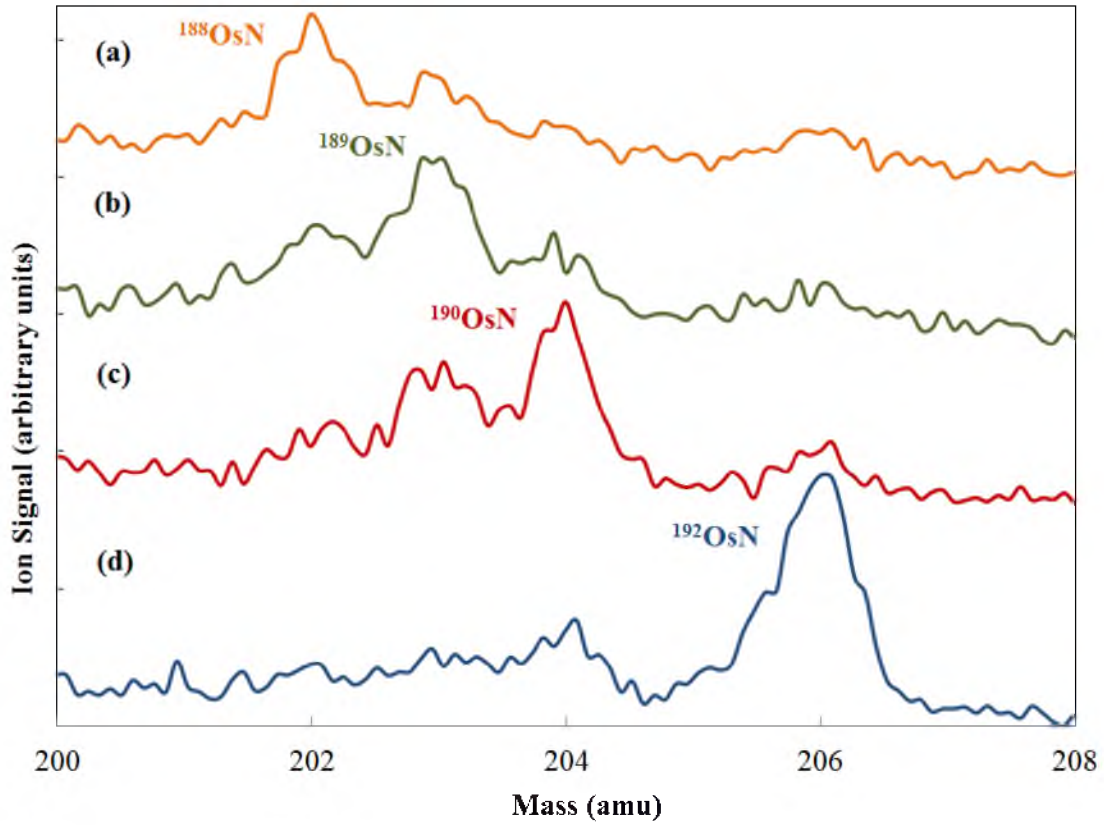

Figure 2.7 Mass spectra of OsN isotopologues, recorded with the dye laser tuned to 21019.44 cm^{-1} (a), 21019.00 cm^{-1} (b), 21018.74 cm^{-1} (c), and 21017.23 cm^{-1} (d). These wavenumbers are resonant with a transition in ^{188}OsN, ^{189}OsN, ^{190}OsN, and ^{192}OsN, respectively.

A motorized diffraction grating was computer controlled utilizing a LabView program written specifically for the R2PI experiment, using VIs provided by Lambda Physik. Vibronic spectra were collected by scanning the dye laser frequency while holding the excimer laser frequency fixed. The spectral range of the dye laser is from 11,000 to 25,000 cm^{-1}, and is covered using a variety of dyes purchased from Exciton or Lambda Physik. The spectral range available to the dye laser is subdivided into the red (543-900 nm) and blue (400-563 nm) regions, according to whether the dye employed is pumped using the Nd:YAG second harmonic (532 nm) or third harmonic (355 nm).

Figure 2.8 provides an example of a vibronically resolved spectrum for the $^{193}Ir^{28}Si$ molecule, recorded over the range 18,000-19,000 cm^{-1}, illustrating the type of data that can be obtained with this technique. This region is quite congested, with transitions that originate from the $v''=0$ and $v''=1$ levels of the ground electronic state, terminating on vibrational levels of seven different excited states, which are labeled A-G. By fitting the measured band positions to the formula

$$\nu = T_0 + v' \omega_e' - (v'^2 + v') \omega_e' - v'' \Delta G_{1/2}'', \qquad (2.10)$$

the term energy (T_0), vibrational frequency (ω_e'), and anharmonicity ($\omega_e' x_e'$) of the upper state, and the vibrational interval ($\Delta G_{1/2}''$) of the ground state may be determined.

2.8.3 High Resolution Spectra

To reveal the rotational structure of the vibronic transitions, an air spaced intracavity étalon, with a free spectral range of 1.0 cm^{-1} is introduced into the oscillator cavity where the motorized grating is located. The étalon narrows the linewidth to

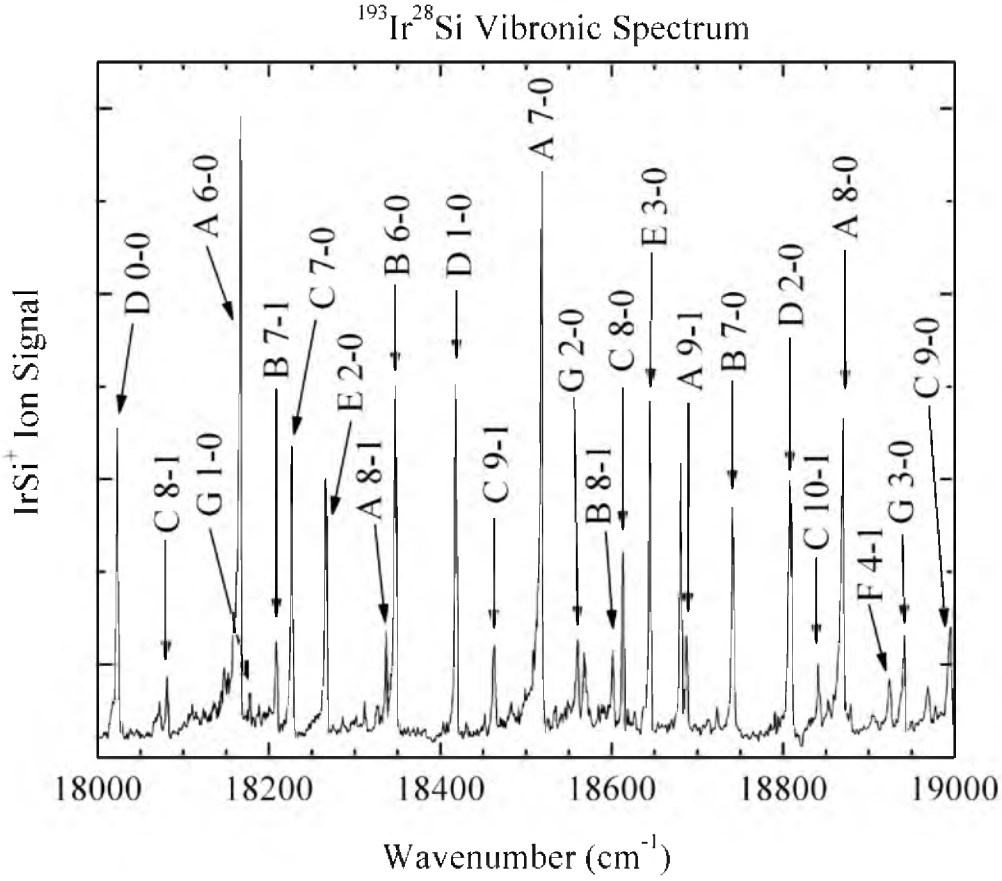

Figure 2.8 Vibronic spectrum of IrSi

approximately 0.04 cm^{-1} from the low resolution linewidth of about 0.15 cm^{-1}. The étalon is aligned in the oscillator cavity and is adjusted so that the laser operates on only a single étalon mode with a narrow linewidth by viewing the fringe pattern through a hand held étalon mounted on a small telescope as adjustments are made. When good quality fringes are obtained and the laser is operating on a single étalon mode, the cavity is closed and sealed. It is then evacuated using an Alcatel rotary vane vacuum pump to about 15 torr. After verifying that the laser is still emitting light of good optical quality at the reduced pressure, the cavity is slowly pressurized at a controlled rate back to atmosphere using sulfur hexafluoride (SF_6). During the process, the diffraction grating and étalon are held fixed in position, keeping the laser wavelength inside the oscillator cavity fixed. As the cavity is pressurized, however, the index of refraction of the medium is slowly increased from unity, causing the speed of light in the cavity to be reduced. Because of the relationship

$$\nu = \frac{c_m}{\lambda}, \qquad (2.11)$$

where c_m is the speed of light in the medium, the reduction in c_m as the cavity is pressurized leads to a reduction in ν. This technique is called pressure scanning, and SF_6 is chosen for this purpose because its index of refraction (1.000723 at 633nm, 1 atm, 300K)[17] is among the highest of the readily available gases. Generally, pressure scanning with SF_6 from a pressure of 15 to 800 Torr covers a range of about 15 cm^{-1} in the blue region, and about 10 cm^{-1} in the red region. As the pressure is increased, the laser is scanned from the blue end of the range toward the red. When the spectrum of a particular vibronic band covers a range larger than 10-15 cm^{-1}, multiple scans are collected by

advancing the grating slightly and repeating the process to cover the neighboring range. All the scans are pasted together after the calibration process is completed to provide a continuous spectrum of the entire band.

The ultimate goal in collecting high resolution data is to reveal the rotational structure of the selected vibronic band, which allows the spectroscopic constants, bond lengths, and electronic symmetries to be determined. Figure 2.9 displays a rotationally resolved spectrum of the 2-0 band of the A $[17.8]^2\Phi_{7/2} \leftarrow X^2\Delta_{5/2}$ band system of the $^{192}Os^{14}N$ molecule. The range of this scan was 23 cm^{-1}, requiring two separate scans that were individually calibrated and then combined.

2.8.4 Calibration

In order to calibrate a high resolution spectrum, a thick uncoated fused silica plate is used to pick off about 10% of the dye laser light as reflections from the first and second surfaces. One of the reflections is directed through a cell filled with a reference gas, while the other is directed through an étalon with a free spectral range of 0.22 cm^{-1}. Photodiodes are used to measure the transmission through the reference gas cell and through the monitor étalon. The étalon fringes are used to linearize the spectrum, and the absorptions of the reference gas are used to provide an absolute calibration of the spectrum. Depending on the spectral region under investigation, different reference gases are required. If the region to be scanned is between 18,500 and 24,000 cm^{-1}, a heated cell containing isotopically pure $^{130}Te_2$ may be used.[18, 19] Spectra to the red of 18,500 cm^{-1} are calibrated using I_2, which must be heated if the region lies to the red of 14,100 cm^{-1}.[20-22] In the region between 18,500 and 19,978 cm^{-1}, either calibrant may be used, although it is generally easier to use room temperature I_2.

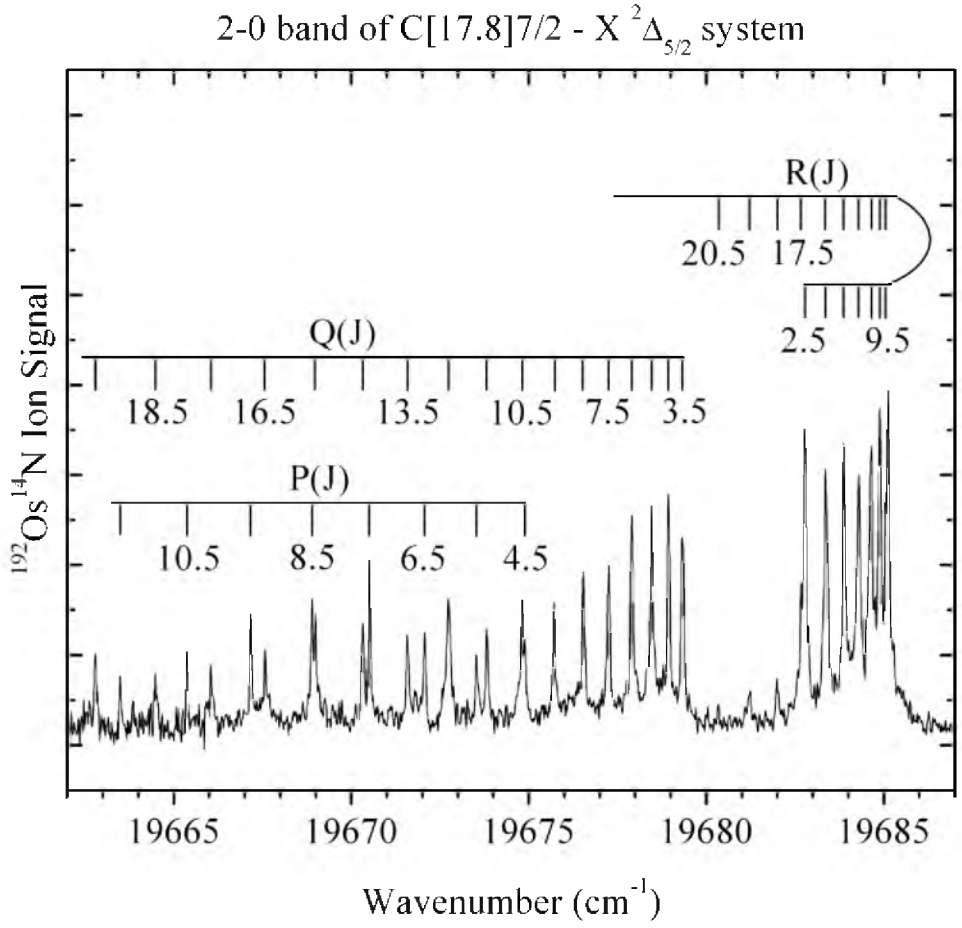

Figure 2.9 A rotationally resolved spectrum of the 2-0 band of the $C[17.8]^2\Phi_{7/2} \leftarrow X^2\Delta_{5/2}$ band system of the $^{192}Os^{14}N$ molecule.

Finally, in our experimental arrangement, the molecules move toward the light source at the beam velocity of helium (1.77×10^5 cm/s), causing them to experience the laser radiation to be blue shifted due to the Doppler effect. A correction for this effect adds an amount given by $\Delta\nu = \nu \times (v/c)$, where $v = 1.77 \times 10^5$ cm/s, $c = 2.99792458 \times 10^{10}$ cm/s to the calibrated wavenumber, ν, to obtain the wavenumber of the dye laser radiation, as experienced by the molecule. This is a minor correction, typically amounting to between 0.12 and 0.14 cm^{-1} for the studies reported in this dissertation.

2.8.5 Excited State Lifetimes

Excited state lifetimes are measured by tuning the dye laser frequency to the excitation wavelength of interest and randomly varying the time at which the dye laser fires. The ionization laser is held fixed in time, at the time of maximum signal intensity in the ionization volume. A fixed number of laser shots are accumulated for each time interval between the excitation and ionization lasers. The resulting ion signal vs. delay time curve shows an exponential decay that is fitted to extract the 1/e lifetime, τ. An example of such a decay curve is provided in Figure 2.10 for the $^{63}CuCCH^+$ molecule. The measured ion signal is plotted as a function of delay time and fitted to an exponential decay curve using the Marquardt nonlinear least-squares algorithm.[23] The measured excited state lifetime provides an additional piece of information that can be used to estimate the strength of the transition. If it is assumed that the upper state decays purely by fluorescence to the ground state, then the absorption oscillator strength is given by[24]

$$f = (1.499 \frac{s}{cm^2}) \frac{\lambda^2}{\tau} \quad . \tag{2.12}$$

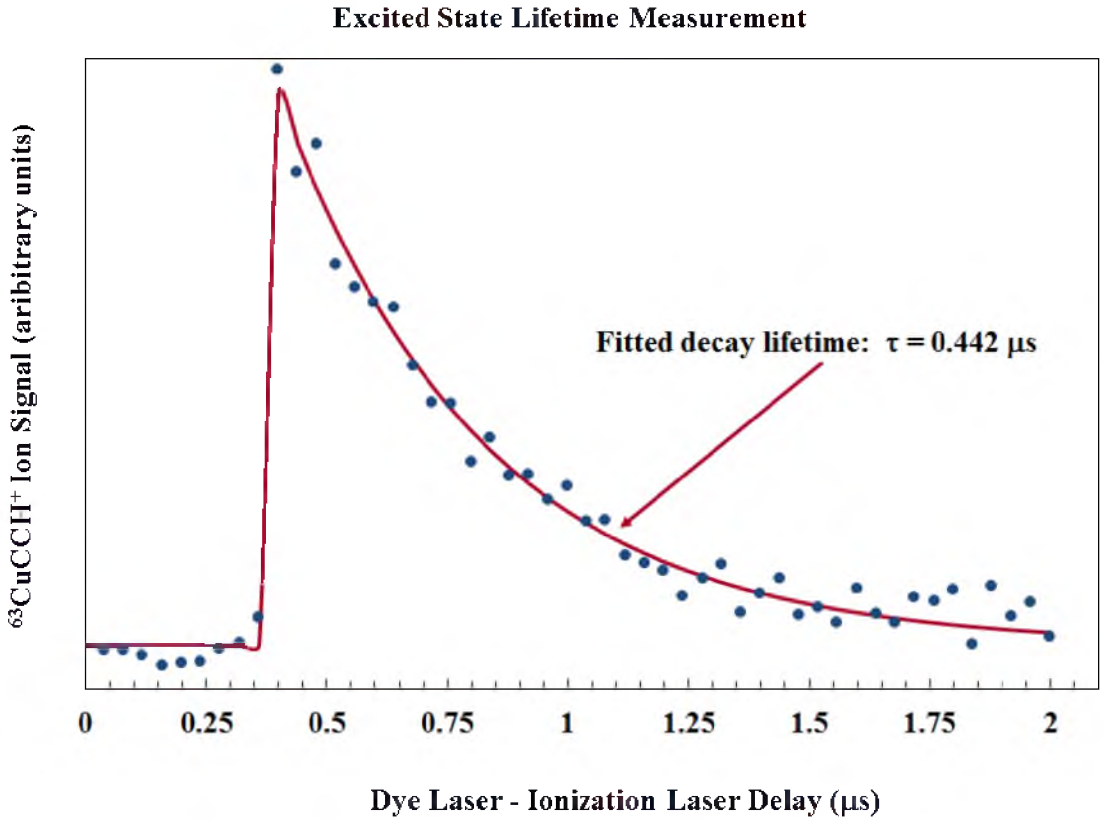

Figure 2.10 Ion signal plotted as a function of delay between the excitation and ionization laser pulses.

Of course, depending on the electronic structure of the molecule this assumption may or may not be correct. Nevertheless, the result obtained from (Figure 2.10) provides an upper limit for the absorption oscillator strength.

2.9 References

[1] M. D. Morse, in *Methods of Experimental Physics: Atomic, Molecular, and Optical Physics*, Vol. II Atoms and Molecules, edited by F. B. Dunning and R. Hulet (Academic Press, Inc., Orlando, Florida, 1996), pp. 21-47.

[2] M. A. Duncan, Rev. Sci. Instrum. **83,** 041101/1-/19 (2012).

[3] M. B. Airola and M. D. Morse, J. Chem. Phys. **116,** 1313-7 (2002).

[4] R. Nagarajan and M. D. Morse, J. Chem. Phys. **127,** 014311/1-8 (2007).

[5] O. Krechkivska and M. D. Morse, J. Chem. Phys. **128,** 084314/1-/9 (2008).

[6] M. A. Garcia and M. D. Morse, J. Chem. Phys. **135,** 114304/1-12 (2011).

[7] A. Martinez and M. D. Morse, J. Chem. Phys. **135,** 024308/1-10 (2011).

[8] A. Martinez, N. Lindholm, and M. D. Morse, J. Chem. Phys. **135,** 134308/1-8 (2011).

[9] J. F. Ready, *Industrial Applications of Lasers* (Academic Press, New York, 1978).

[10] D. H. Levy, Annual Review of Physical Chemistry **31,** 197-225 (1980).

[11] M. Goppert-Mayer, Ann. Phys. (Berlin, Ger.) **9,** 273-94 (1931).

[12] W. Kaiser and C. G. B. Garrett, Phys. Rev. Lett. **7,** 229-31 (1961).

[13] S. H. Lin, Y. Fujimora, H. J. Neusser, and E. W. Schlag, *Multiphoton Spectroscopy of Molecules* (Academic Press, Inc., Orlando, 1984).

[14] W. C. Wiley and I. H. McLaren, Rev. Sci. Instrum. **26,** 1150 - 7 (1955).

[15] B. A. Mamyrin, V. I. Karataev, D. V. Shmikk, and V. A. Zagulin, Zh. Eksp. Teor. Fiz. **64,** 82-9 (1973).

[16] G. Beck, Rev. Sci. Instrum. **47,** 849-53 (1976).

[17] M. E. Thomas and T. J. Tayag, Appl. Opt. **27,** 3317-18 (1988).

[18] J. Cariou and P. Luc, *Atlas du Spectre d'Absorption de la Molécule Tellure, Partie 5: 21,100 - 23,800 cm^{-1}* (CNRS, Paris, 1980).

[19] J. Cariou and P. Luc, *Atlas du Spectre d'Absorption de la Molécule de Tellure entre 18,500 - 23,800 cm^{-1}* (CNRS, Paris, 1980).

[20] S. Gerstenkorn and P. Luc, *Atlas du Spectre d'Absorption de la Molécule d'Iode entre 14,800-20,000 cm^{-1}* (CNRS, Paris, 1978).

[21] S. Gerstenkorn, J. Verges, and J. Chevillard, *Atlas du Spectre d'Absorption de la Molécule d'Iode entre 11,000-14,000 cm^{-1}* (CNRS, Paris, 1982).

[22] S. Gerstenkorn and P. Luc, *Atlas du Spectre d'Absorption de la Molécule d'Iode entre 14,000-15,600 cm^{-1}* (CNRS, Paris, 1978).

[23] P. R. Bevington, *Data Reduction and Error Analysis for the Physical Sciences* (McGraw-Hill, New York, 1969).

[24] J. I. Steinfeld, *Molecules and Radiation: An Introduction to Modern Molecular Spectroscopy*, Second ed. (The MIT Press, Cambridge, 1993).

CHAPTER 3

RESONANT TWO-PHOTON IONIZATION SPECTROSCOPY OF JET-COOLED OsN: 520 - 418 nm

3.1 Introduction

Transition metal molecules are of great interest and importance as catalysts in organic and organometallic chemistry.[1] Transition metal species are also of astrophysical[2, 3] importance and have been identified in the atmospheres of M and S type stars and L type dwarfs,[4-7] where their spectra play a key role in the stellar classification scheme. Transition metal nitrides, in particular, are of importance in the fixation of nitrogen[8] and in the production of metallic thin films for optical applications[9, 10] and for wear and corrosion resistance.[11-13] The interest in transition metal nitrides has prompted a number of spectroscopic investigations, with the result that spectra have now been obtained for all of the diatomic transition metal nitrides, MN, in the gas phase, with the exceptions of the 3*d* species MnN, CoN, NiN, CuN, and ZnN; the 4*d* species TcN, PdN, AgN, and CdN; and the 5*d* species AuN and HgN.[14] Infrared spectra of a large number of diatomic transition metal nitrides are also known from matrix isolation studies, including RuN and OsN.[15] It is interesting that the number of spectroscopically known species increases as one moves from the 3*d* series to the 4*d* series and on to the 5*d* series. This fact reflects the increasing ability of the transition metals to form strong π-bonds as one moves down the periodic table, due to the increasing size and accessibility of the n*d*π orbitals as n

increases from 3 to 5.

Although gas-phase spectra of OsN are known,[16] the available spectra have only located the spin-forbidden $a\ ^4\Pi_{5/2} - X\ ^2\Delta_{5/2}$, $b\ ^4\Phi_{7/2} - X\ ^2\Delta_{5/2}$, and $b\ ^4\Phi_{5/2} - X\ ^2\Delta_{5/2}$ systems in the 8 000 – 12 200 cm^{-1} region. In order to develop a more comprehensive understanding of the electronic structure of the OsN molecule, we have undertaken spectroscopic studies in the visible portion of the spectrum. In this chapter four excited states of $^2\Pi_{3/2}$ symmetry and three states of $^2\Phi_{7/2}$ symmetry are reported, all of which are thought to result from the promotion of a nonbonding 1δ or 3σ electron into the antibonding 2π orbital.

In addition to OsN, two other osmium containing diatomic molecules are known: OsO, which is known from optical emission studies,[17] and OsC, which has been studied in this group by resonant two-photon ionization methods.[18] Recent work on the other 5*d* series transition metal nitrides includes HfN,[19] TaN,[20] WN,[21] ReN,[22, 23] IrN,[24-26] and PtN.[27, 28] These molecules are all of high interest as proving grounds for theoretical methods, due to the importance of properly treating relativistic and electron correlation effects. The large magnitude of the spin-orbit interaction in these species also makes accurate calculation of their properties a significant challenge for the *ab initio* quantum chemist.

3.2 Experimental

In the present work, resonant two-photon ionization (R2PI) spectroscopy with time of flight mass spectrometric detection was used to examine the optical spectroscopy of jet-cooled diatomic OsN using a previously described instrument.[29] Briefly, the molecule was produced by focusing a pulsed Nd: YAG laser (355 nm, 15 mJ/pulse) onto a

vanadium-osmium alloy disk (45:55 mole percent V:Os), which was rotated and translated to prevent deep holes from being drilled into the sample. The laser-ablated metal atoms were entrained in a flow of helium carrier gas (120 psi) seeded with 5% ammonia. After traveling down a 1 cm long reaction zone, the gases expanded through a 2 mm orifice into a low pressure (2×10^{-4} Torr) vacuum chamber. The resulting supersonic expansion was roughly collimated by a 1 cm diameter skimmer and entered the ion source of a reflectron time of flight mass spectrometer.[30, 31] In the ion source the molecular beam was exposed to tunable dye laser radiation that counterpropagated along the molecular beam path. After a delay of 20 ns, the output of an ArF (193 nm) excimer laser intersected the molecular beam at right angles. The ions produced by this process were accelerated in a Wiley-McLaren ion source and reflected onto a microchannel plate detector. The resulting ion signal was preamplified, digitized at 100 MHz, and stored using a personal computer for further processing. The entire experimental cycle was repeated at the rate of 10 Hz.

Survey spectra (at 0.15 cm^{-1} resolution) of the four most abundant isotopomers, $^{192}Os^{14}N$ (40.78% natural abundance), $^{190}Os^{14}N$ (26.26%), $^{189}Os^{14}N$ (16.12%) and $^{188}Os^{14}N$ (13.24%), were recorded from 19 200 to 23 900 cm^{-1}, and in isolated segments as far to the red as 12 900 cm^{-1}. Rotationally resolved spectra (at 0.04 cm^{-1} resolution) were obtained for the strongest vibrational transitions by inserting an air spaced etalon into the grating cavity of the dye laser and pressure scanning using sulfur hexafluoride (SF_6). Calibration of the rotationally resolved spectrum was achieved by simultaneously measuring the absorption spectrum of I_2 or isotopically pure $^{130}Te_2$. The I_2 or Te_2 lines were identified by comparison to the corresponding atlas,[32, 33] which permitted the

absolute calibration of the OsN spectra. In the final step, the molecular spectra were corrected for the Doppler shift experienced by the molecules as they traveled toward the radiation source at the beam velocity of the helium (1.77×10^5 cm/s)[34] and for the -0.0056 cm^{-1} error in the I_2 atlas.[35] The total correction amounted to only 0.11 - 0.14 cm^{-1} for all of the examined bands.

The excited state lifetime of the principal isotopic modification, $^{192}Os^{14}N$, was measured by setting the dye laser radiation to the resonant frequency and varying the time at which it is fired. The ion signal was then recorded as a function of the excitation-ionization delay and fitted to an exponential decay curve using the Levenberg-Marquardt nonlinear least-squares algorithm.[36] For each band that was measured, three independent lifetime curves were collected and fitted, the fitted lifetimes were averaged, and the standard deviation of the three values is reported as the 1σ error limit.

3.3 Results

3.3.1 Vibronic Spectrum of OsN

Low resolution (0.15 cm^{-1}) survey scans were recorded of diatomic OsN in the 19 200 – 23 900 cm^{-1} region and at isolated wavenumber regions farther to the red using LDS 751, LDS 698, rhodamine 590, coumarin 540A, 500, 480, 460, 450, 440, and stilbene 420 laser dyes. The spectrum consists of more than 20 bands, and becomes somewhat more congested to the blue, where overlapping bands are observed. Seventeen of the bands that were observed were investigated at higher resolution and were successfully calibrated and analyzed. Figure 3.1 displays the vibronic spectrum of $^{192}Os^{14}N$, the most abundant isotope (40.85%). Seven band systems have been identified in Figure 3.1, labeled systems

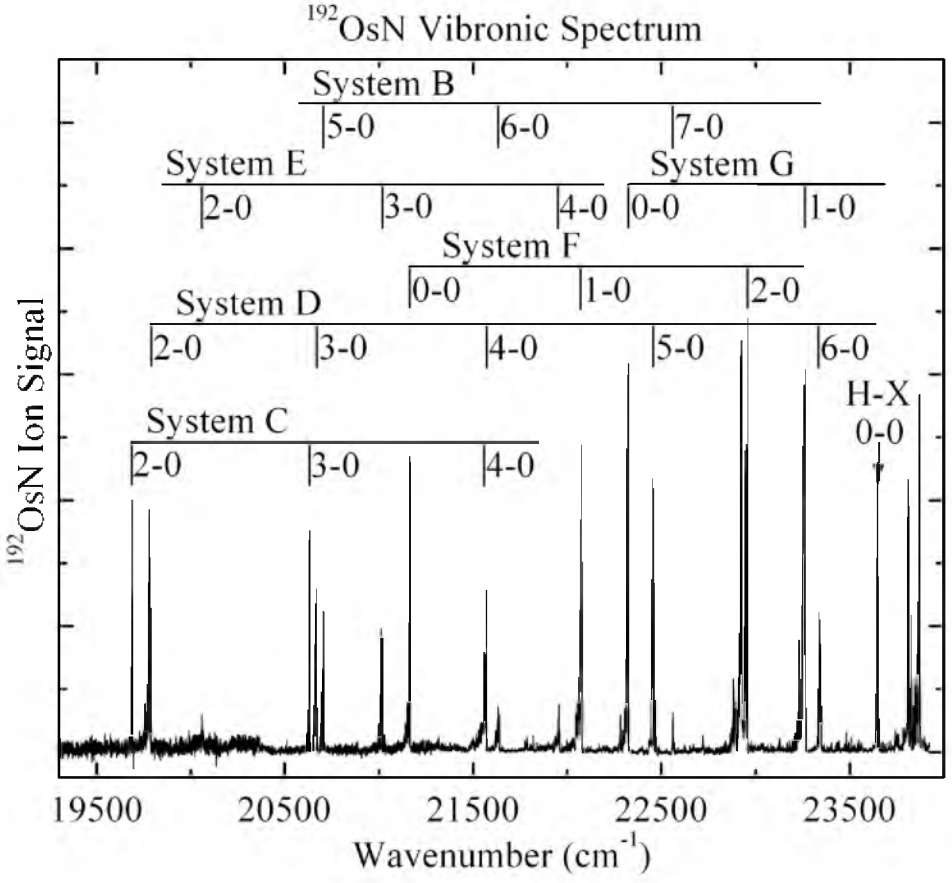

Figure 3.1 Vibronic spectrum of OsN, with assigned band systems indicated.

B-H. The letter A is reserved for the as yet unobserved $1\sigma^2\ 2\sigma^2\ 1\pi^4\ 1\delta^4\ 3\sigma^1$, $^2\Sigma^+$ term, which is predicted to lie approximately 7500 cm^{-1} above the ground level. All of these systems have been determined to originate from the $^2\Delta_{5/2}$ ground state, which arises from the $1\sigma^2\ 2\sigma^2\ 1\pi^4\ 1\delta^3\ 3\sigma^2$ electronic configuration. All bands have a band head in the R branch, with the Q and P branches strongly red degraded, consistent with an increase in bond length upon electronic excitation.

The numbering of the vibrational bands was established by varying the assignment of v′, fitting the measured bands to obtain values of T_0, ω_e', and $\omega_e'x_e'$, and then computing the transition wavenumber as a function of a continuous parameter, v′, using the equation

$$\nu = T_0 + v'\,\omega_e' - (v'^2 + v')\,\omega_e'x_e'. \qquad (3.1)$$

The corresponding isotope shift was calculated as a function of v′, as

$$\nu(^{188}Os^{14}N) - \nu(^{192}Os^{14}N)$$
$$= (\rho-1)[\omega_e'(v'+\tfrac{1}{2}) - \omega_e''(\tfrac{1}{2})] - (\rho^2-1)[\omega_e'x_e'(v'+\tfrac{1}{2})^2 - \omega_e''x_e''(\tfrac{1}{2})^2]. \qquad (3.2)$$

Here, the $^{192}Os^{14}N$ isotope was used as the reference species, and the fitted values of T_0, ω_e', $\omega_e'x_e'$, were combined with the previously reported[16] values of ω_e'' and $\omega_e''x_e''$ to generate the isotope shift *vs.* transition wavenumber plot. The parameter, ρ, is given by $[\mu(^{192}Os^{14}N)/\mu(^{188}Os^{14}N)]^{1/2}$.[37] Plots of the resulting isotope shift *vs.* transition wavenumber generally provided a definitive vibrational numbering for the band systems, as illustrated in Figure 3.2 for the C-X system. The sole exception is the weak B[16.0]3/2 ← X $^2\Delta_{5/2}$ system, for which only one band was rotationally resolved, and for which the vibrational numbering could be in error. No bands arising from any vibrational levels

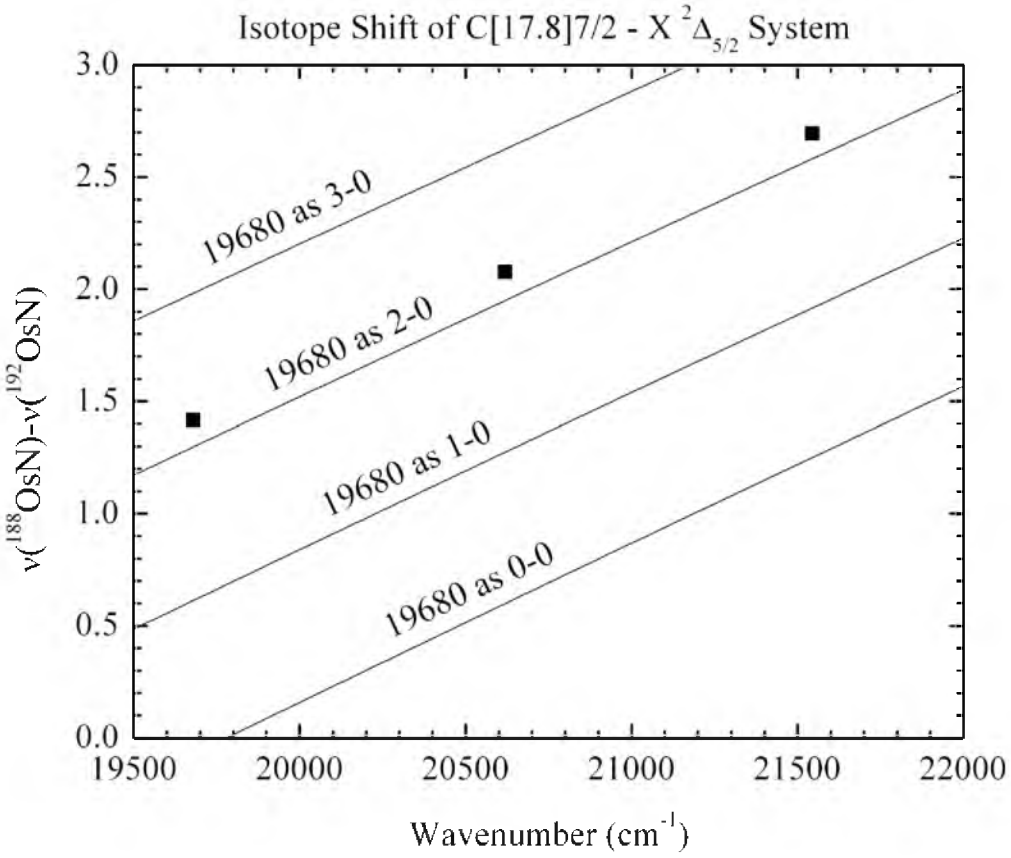

Figure 3.2 Isotope shifts and vibrational numbering of the C-X system. From this analysis, it is evident that the 19680 cm^{-1} band is the 2-0 band of the system.

other than the v″=0 level of the X $^2\Delta_{5/2}$ ground state were observed.

The next subsections provide results for each of the observed band systems. In addition to the common designation of an upper state by a letter, also used is a designation in which the energy of the v′=0 level is expressed in thousands of cm^{-1} in square brackets, along with the Ω′ value. Thus, the C[17.8]7/2 state is the state with Ω′=7/2 whose T_0 value lies near 17 800 cm^{-1}. The letter designation is retained for easy reference. The rotational structure of all of the resolved bands could be fit to the expression

$$v = v_0 + B'J'(J'+1) - B''J''(J''+1) \qquad (3.3)$$

to obtain values for ν_0, B', and B". Upper and lower state Ω values were determined by the first lines present in the spectrum.

Despite scans over the region where the 0-0 and 1-0 bands of the C[17.8]7/2 ← X $^2\Delta_{5/2}$ system were calculated to occur, these features were not observed in the spectrum Indeed, no vibronic features were observed to the red of the C[17.8]7/2 ← X $^2\Delta_{5/2}$ 2-0 band at 19 680 cm^{-1}. I believe that these features are unobserved because the combination of the dye laser photon and the ArF excimer photon falls below the ionization limit of the molecule. The absence of the C-X 1-0 band, predicted to occur at 18 728 cm^{-1} and the presence of the C-X 2-0 band at 19 680 cm^{-1} then places the ionization energy of OsN in the range 8.80 ± 0.06 eV. This is consistent with the high ionization energy of atomic osmium, IE(Os) = 8.438 eV.[38]

3.3.2 Rotationally Resolved Spectrum of OsN

3.3.2.1 The C[17.8]$^2\Phi_{7/2} \leftarrow X^2\Delta_{5/2}$ system

The 2-0, 3-0 and 4-0 vibrational bands were observed, rotationally resolved, and analyzed for this band system. Measured band origins, rotational constants, and fitted vibrational (T_0, ω_e', $\omega_e'x_e'$) and rotational (B_e', α_e', r_e') parameters for the various isotopomers of OsN are listed in Table 3.1. The rotationally resolved spectrum of the 2-0 band of $^{192}Os^{14}N$ is displayed in Figure 3.3. All of the bands of this system are characterized by an intense R branch and weaker Q and P branches. The first lines of R(2.5), Q(3.5), and P(4.5) establish the Ω-values as $\Omega''=5/2$, $\Omega'=7/2$.

With only three rotationally resolved bands, the three vibrational parameters, T_0, ω_e', and $\omega_e'x_e'$, are uniquely defined and no error estimate is possible. Ordinarily, one would expect significant errors in the extrapolation from the $v'=2$ level to determine T_0, but in this case the excellent agreement between the various isotopomers for the values of T_0, ω_e', and $\omega_e'x_e'$ gives us confidence that these values are accurate. Likewise, the values of r_e', obtained from the fit of B_2', B_3', and B_4' to extract B_e' and α_e' are in very good agreement from isotope to isotope. A weighted average of the calculated values of r_e' for the various isotopomers provides $r_e' = 1.68146(15)$ Å, which is our best estimate of the actual bond length of the C state. This value is uncorrected for any **S**- or **L**-uncoupling interactions with other states,[39] but these are not expected to be significant due to the large spin-orbit splitting expected for this molecule.

Table 3.1 Spectroscopic constants for the C[17.8]$^2\Phi_{7/2}$ – X $^2\Delta_{5/2}$ system of OsN

Band	Constant	$^{192}Os^{14}N$	$^{190}Os^{14}N$	$^{189}Os^{14}N$	$^{188}Os^{14}N$	τ (μs)
2 – 0	ν_0 (cm^{-1})	19680.0008(22)	19680.6951(27)	19681.0735(22)	19681.4181(29)	0.738(31)
	B_2' (cm^{-1})	0.448884(27)	0.449076(33)	0.449355(29)	0.449523(35)	
	r_2' (Å)	1.696324(51)	1.696569(62)	1.696350(55)	1.696345(66)	
3 - 0	ν_0 (cm^{-1})	20618.6759(21)	20619.6994(28)	20620.2285(68)	20620.7522(29)	0.808(12)
	B_3' (cm^{-1})	0.445763(34)	0.445907(30)	0.446417(50)	0.446307(27)	
	r_3' (Å)	1.702252(65)	1.702587(57)	1.701923(95)	1.702446(51)	
4 - 0	ν_0 (cm^{-1})	21544.3000(79)	21545.6608(105)	21546.3529(73)	21546.9949(143)	
	B_4' (cm^{-1})	0.442566(94)	0.441960(80)	0.442392(53)	0.442900(115)	
	r_4' (Å)	1.708389(181)	1.710173(155)	1.709648(102)	1.708982(222)	
	T_0 (cm^{-1})	17763.50	17763.56	17763.67	17763.48	
	ω_e' (cm^{-1})	977.83	978.13	978.25	978.61	
	$\omega_e' x_e'$	6.53	6.52	6.52	6.55	
	B_e' (cm^{-1})	0.45679(9)	0.45810(91)	0.45824(127)	0.45783(22)	
	α_e' (cm^{-1})	0.00316(5)	0.00356(48)	0.00348(67)	0.00331(12)	
	r_e' (Å)	1.68157(16)	1.6798(17)	1.6798(23)	1.6809(4)	
X $^2\Delta_{5/2}$	B_0'' (cm^{-1})	0.491921(34)	0.492121(36)	0.492469(42)	0.492660(36)	
	r_0'' (Å)	1.620422(56)	1.620673(59)	1.620395(69)	1.620379(59)	

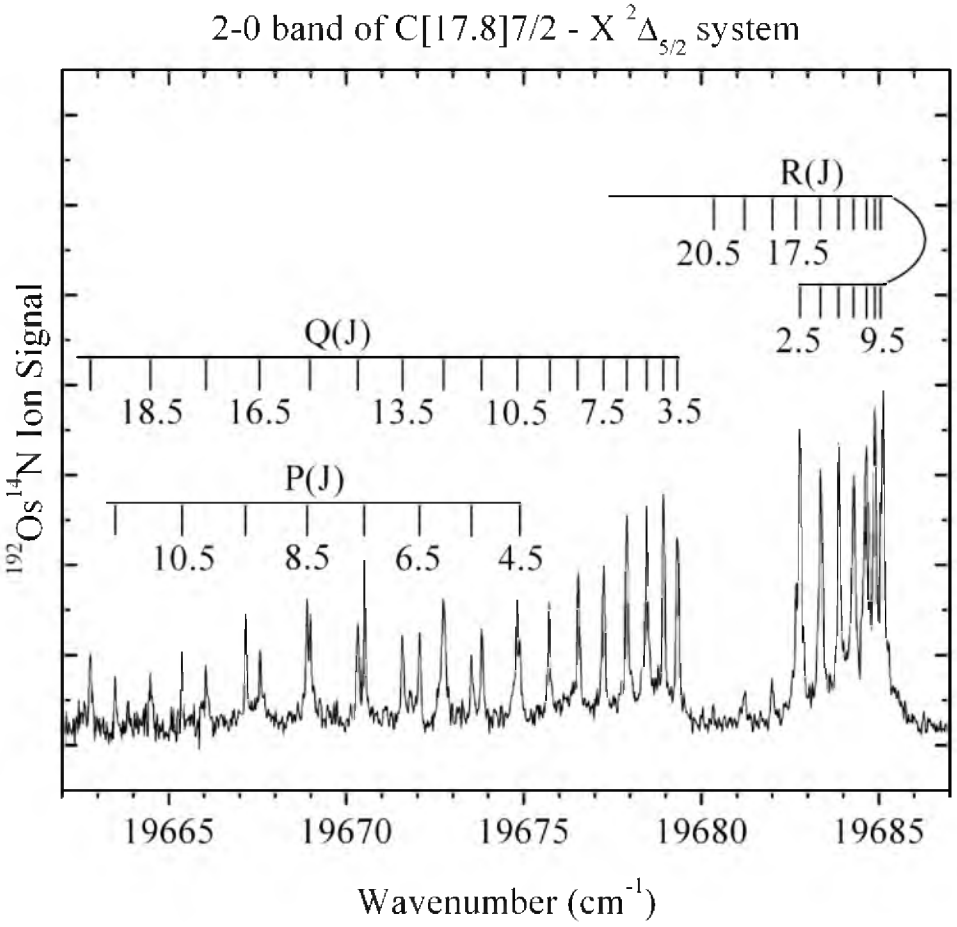

Figure 3.3 Rotationally resolved spectrum of the 2-0 band of the C $^2\Phi_{7/2} \leftarrow$ X $^2\Delta_{5/2}$ system.

The measured excited state lifetime for the v′=2 and v′=3 levels, 0.738 ± 0.031 μs and 0.808 ± 0.012 μs, respectively, is typical for excited states of transition metal molecules. If the only decay process is fluorescence to the ground electronic state, the relationship[40]

$$f = \frac{g_2}{g_1} \frac{1.51}{{v_0}^2 \tau} \tag{3.4}$$

provides an estimate of the absorption oscillator strength of the C-X system as $f \approx$ 0.004-0.005. These values suggest that the transition is an electronically allowed metal-centered excitation. If so, the assignment of the ground electronic state as $^2\Delta_{5/2}$ requires that the C[17.8]7/2 state be dominated by $^2\Phi_{7/2}$ character.

3.3.2.2 The D[18.0]$^2\Pi_{3/2} \leftarrow X^2\Delta_{5/2}$ system

Close to the bands of the C-X system, one finds another strong absorption system, the D[18.0]3/2 $\leftarrow X^2\Delta_{5/2}$ system. For this system, the 2-0, 3-0, 4-0, and 5-0 bands were rotationally resolved, calibrated, and analyzed. Although similar in intensity to the bands of the C-X system, the rotationally resolved bands of this system are somewhat different in appearance, as illustrated in Figure 3.4. All of the bands of this system are characterized by a weak R branch, a stronger Q branch, and a P branch that is quite intense. This is visible even in the low-resolution spectra, where a distinct tailing to the red is visible due to the high intensity in the P lines. The first lines R(2.5), Q(2.5), and P(2.5) identify the Ω values as Ω″=5/2, Ω′=3/2.

As was the case with the C system, the first band observed is the 2-0 band. Although one would ordinarily think that the observation and accurate fitting of 4 bands in

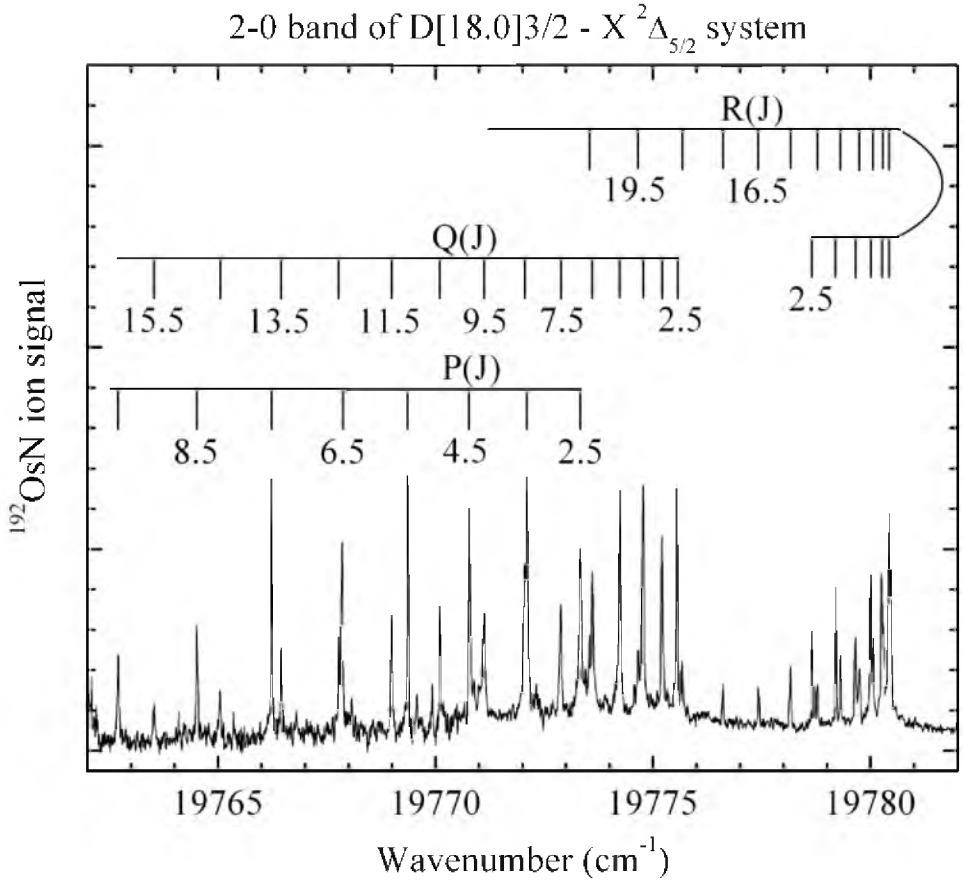

Figure 3.4 Rotationally resolved spectrum of the 2-0 band of the D $^2\Pi_{3/2} \leftarrow$ X $^2\Delta_{5/2}$ system.

this system (the 2-0, 3-0, 4-0, and 5-0) would allow an accurate determination of T_0, ω_e', and $\omega_e'x_e'$, in this case there is significant uncertainty in these parameters and significant variation in these values from isotope to isotope (see Table 3.2). The difficulties in this system stem from the fact that the 3-0 band is perturbed, with the perturber state evident in the spectra of the ^{189}OsN and ^{188}OsN isotopes. Accordingly, this level is excluded from the fit of the band origins to obtain T_0, ω_e', and $\omega_e'x_e'$, and from the fit of the B_v' values to obtain B_e', α_e', and r_e' for these isotopes. Even though perturbations in the $v'=3$ level are not apparent in the other isotopes, the fits to obtain T_0, ω_e', $\omega_e'x_e'$, B_e', α_e', and r_e' remain suspect for this state. Combining the results for all isotopes, however, a best estimate of r_e' for this state is 1.687 ± 0.003 Å.

Excited state lifetimes were measured for ^{192}OsN to be 1.17(11), 1.26(4), and 0.863(17) μs for the $v'=2$, 3, and 5 levels of the D[18.0]3/2 state. Of these, the value for the unperturbed $v'=2$ level is most likely to be representative of the electronic nature of this state. Assuming that fluorescence occurs solely to the ground $X^2\Delta_{5/2}$, $v''=0$ level, the 1.17 μs lifetime converts to an absorption oscillator strength of $f \approx 0.003$, suggesting an electronically allowed metal-based excitation. This suggests that the D[18.0]3/2 state is primarily of $^2\Pi_{3/2}$ character.

3.3.2.3 The F[21.2]$^2\Phi_{7/2} \leftarrow X^2\Delta_{5/2}$ system

Moving further to the blue, a 0-0 band is found near 21 151 cm^{-1}. The corresponding 1-0 and 2-0 bands are found near 22 062 and 22 944 cm^{-1}, respectively. This system is identified as the F [21.2]7/2 $\leftarrow X^2\Delta_{5/2}$ system on the basis of rotationally resolved spectra of all three bands. The rotationally resolved spectra are quite similar to the 2-0 band of the C-X system that is displayed in Figure 3.3. As in the C-X system, this

Table 3.2 Spectroscopic constants for the D[18.0]$^2\Pi_{3/2}$ – X $^2\Delta_{5/2}$ system of OsN

Band	Constant	$^{192}Os^{14}N$	$^{190}Os^{14}N$	$^{189}Os^{14}N$	$^{188}Os^{14}N$	τ (μs)
2 – 0	ν_0 (cm^{-1})	19775.9842(22)	19776.5575(20)	19776.8575(23)	19777.1537(18)	1.17(11)
	B_2' (cm^{-1})	0.443198(28)	0.443391(34)	0.443691(29)	0.443864(36)	
	r_2' (Å)	1.707171(54)	1.707411(65)	1.707144(56)	1.707125(69)	
3 - 0	ν_0 (cm^{-1})	20657.6998(22)	20658.9758(26)	20658.9902(56)	20659.6125(63)	1.26(4)
	B_3' (cm^{-1})	0.437158(69)	0.437205(62)	0.437150(122)	0.438055(104)	
	r_3' (Å)	1.718924(136)	1.719447(122)	1.719868(240)	1.718407(204)	
3 – 0[a]	ν_0 (cm^{-1})			20659.6166(37)	20660.2533(36)	
	B_3' (cm^{-1})			0.437498(117)	0.437678(65)	
	r_3' (Å)			1.719184(230)	1.719146(128)	
4 - 0	ν_0 (cm^{-1})	21558.0923(33)	21559.2877(38)	21559.8942(37)	21560.5073(29)	
	B_4' (cm^{-1})	0.432417(32)	0.432614(42)	0.432811(37)	0.433072(40)	
	r_4' (Å)	1.728321(64)	1.728547(84)	1.728467(74)	1.728264(80)	
5 - 0	ν_0 (cm^{-1})	22446.6492(22)	22449.0627(40)	22450.6445(59)	22447.3434(35)	0.863(17)
	B_5' (cm^{-1})	0.429767(40)	0.430360(105)	0.431275(203)	0.430365(101)	
	r_5' (Å)	1.733642(81)	1.733068(211)	1.731543(408)	1.733691(203)	

[a]A second feature was observed in the spectra of the $^{189}Os^{14}N$ and $^{188}Os^{14}N$ isotopes; this was fitted and is included in this table.

Table 3.2 (Continued)

Band	Constant	$^{192}Os^{14}N$	$^{190}Os^{14}N$	$^{189}Os^{14}N$	$^{188}Os^{14}N$	τ (μs)
	T_0 (cm^{-1})	18009.08(39.16)	18009.96(36.49)	17991.77	17980.89	
	ω_e' (cm^{-1})	877.56(27.46)	877.07(25.59)	893.31	902.97	
	$\omega_e' x_e'$ (cm^{-1})	-1.71(3.41)	-1.84(3.18)	0.256	1.61	
	B_e' (cm^{-1})	0.45365(248)	0.45337(288)	0.45394(464)	0.45505(320)	
	α_e' (cm^{-1})	0.00450(120)	0.00437(140)	0.00432(220)	0.00463(151)	
	r_e' (Å)	1.6874(46)	1.6885(54)	1.6878(86)	1.6860(59)	
$X\ ^2\Delta_{5/2}$	B_0'' (cm^{-1})	0.491921(34)	0.492121(36)	0.492469(42)	0.492660(36)	
	r_0'' (Å)	1.620422(56)	1.620673(59)	1.620395(69)	1.620379(59)	

system exhibits a strong R branch beginning with R(2.5), a somewhat weaker Q branch beginning with Q(3.5), and a much weaker P branch beginning with P(4.5). These values establish the system as an $\Omega'=7/2 \leftarrow \Omega''=5/2$ system.

The fitted spectroscopic constants listed in Table 3.3 show excellent agreement between isotopes, and display the expected trends as the reduced mass varies. The only odd aspect of this system is the extremely high anharmonicity, which probably signals some sort of global perturbation. This is reflected in a failure of the Pekeris relationship,[41] which is valid for a Morse potential, and provides

$$\alpha_e = \frac{6\left(\omega_e x_e B_e^{\,3}\right)^{1/2}}{\omega_e} - \frac{6B_e^{\,2}}{\omega_e} \quad . \tag{3.5}$$

Although this relationship predicts values of α_e that are in good agreement with the measured values for the C[17.8]7/2 state, it is in error by 26% for the F[21.2]7/2 state, indicating that the system is either perturbed by interaction with another state or that its potential energy curve departs significantly from the form of the Morse potential. Nevertheless, extrapolation of the measured B_v' values provides values of B_e' that are in good agreement between isotopes and provide an isotopically averaged value of r_e' of 1.6920(2) Å for this state.

Decay lifetimes have been measured for the v′=0 and v′=1 levels, giving values of 1.13(4) and 1.41(3) μs, respectively. Assuming fluorescence solely to the ground $X^2\Delta_{5/2}$ state, these provide estimates of the absorption oscillator strength of this system of $f \approx 0.0025$. This suggests that the system is electronically allowed, and that the F[21.2]7/2 state is dominated by $^2\Phi_{7/2}$ character.

Table 3.3 Spectroscopic constants for the F[21.2] $^2\Phi_{7/2}$ – X $^2\Delta_{5/2}$ system of OsN

Band	Constant	$^{192}Os^{14}N$	$^{190}Os^{14}N$	$^{189}Os^{14}N$	$^{188}Os^{14}N$	τ (μs)
0 – 0	ν_0 (cm^{-1})	21151.0458(25)	21151.0278(23)	21151.0312(25)	21151.0169(22)	1.13(4)
	B_0' (cm^{-1})	0.448756(20)	0.448933(23)	0.449214(33)	0.449442(30)	
	r_0' (Å)	1.696566(38)	1.696839(43)	1.696617(62)	1.696498(57)	
1 - 0	ν_0 (cm^{-1})	22061.5216(32)	22061.8169(27)	22061.9801(37)	22062.1253(31)	1.41(3)
	B_1' (cm^{-1})	0.444218(30)	0.444431(36)	0.444724(34)	0.444942(40)	
	r_1' (Å)	1.705210(58)	1.705412(69)	1.705160(65)	1.705056(77)	
2 – 0	ν_0 (cm^{-1})	22943.9328(30)	22944.5385(30)	22944.8485(33)	22945.1526(27)	
	B_2' (cm^{-1})	0.439334(32)	0.439474(51)	0.439792(41)	0.439972(26)	
	r_2' (Å)	1.714662(62)	1.715003(100)	1.714694(80)	1.714659(51)	
	T_0 (cm^{-1})	21151.04	21151.03	21151.03	21151.02	
	ω_e' (cm^{-1})	938.54	938.86	939.03	939.19	
	$\omega_e' x_e'$	14.03	14.03	14.04	14.04	
	B_e' (cm^{-1})	0.45117(21)	0.45137(28)	0.45164(27)	0.45189(29)	
	α_e' (cm^{-1})	0.00471(16)	0.00473(21)	0.00471(20)	0.00474(21)	
	r_e' (Å)	1.6920(4)	1.6922(5)	1.6920(5)	1.6919(5)	
X $^2\Delta_{5/2}$	B_0'' (cm^{-1})	0.491921(34)	0.492121(36)	0.492469(42)	0.492660(36)	
	r_0'' (Å)	1.620422(56)	1.620673(59)	1.620395(69)	1.620379(59)	

3.3.2.4 The G[22.3]$^2\Phi_{7/2} \leftarrow X^2\Delta_{5/2}$ system

Considerably further to the blue lies the intense G[22.3]7/2 $\leftarrow X^2\Delta_{5/2}$ band system. The 0-0 and 1-0 bands, which lie near 22 309 and 23248 cm^{-1}, respectively, have been rotationally resolved, calibrated and analyzed. The overall appearance of these bands is very similar to that of the 2-0 band of the C-X system, displayed in Figure 3.3. Like the C-X and F-X systems, this system displays an intense R branch beginning with R(2.5), a weaker Q branch beginning with Q(3.5), and a much weaker P branch beginning with P(4.5). These first lines establish the values Ω''=5/2, Ω'=7/2. Fitted spectroscopic constants are provided in Table 3.4.

With only two bands observed, it is impossible to extract values of ω_e' and $\omega_e'x_e'$; only $\Delta G_{1/2}'$ can be reported. However, it is possible to obtain B_e', α_e', and r_e' from the data. The signal for the 1-0 band was too weak to observe the minor isotopes ^{189}OsN and ^{188}OsN, however. A weighted average of the r_e' values for the ^{192}OsN and ^{190}OsN isotopes, provides our best estimate of r_e' for this state, r_e' = 1.6967 Å. The vibrational interval, $\Delta G_{1/2}'$, is 938.16 cm^{-1} for the ^{192}OsN isotopic modification.

The lifetime of the v'=0 level is measured to be 0.760(24) μs. Assuming a decay pathway consisting solely of fluorescence to the ground state, this converts to an absorption oscillator strength of $f \approx 0.004$. Based on the intensity of the band system it seems likely that this is again an electronically allowed absorption system, in which the G[22.3]7/2 state is dominated by $^2\Phi_{7/2}$ electronic character.

Table 3.4 Spectroscopic constants for the G[22.3] $^2\Phi_{7/2}$ – X $^2\Delta_{5/2}$ system of OsN

Band	Constant	$^{192}Os^{14}N$	$^{190}Os^{14}N$	$^{189}Os^{14}N$	$^{188}Os^{14}N$	τ (μs)
0 – 0	ν_0 (cm^{-1})	22309.4871(25)	22309.5070(24)	22309.5127(51)	22309.5316(28)	0.760(24)
	B_0' (cm^{-1})	0.447050(43)	0.447192(48)	0.447557(59)	0.447724(48)	
	r_0' (Å)	1.699800(82)	1.700139(91)	1.699754(112)	1.699750(91)	
1 - 0	ν_0 (cm^{-1})	23247.6424(24)	23247.9937(32)			
	B_1' (cm^{-1})	0.443843(12)	0.444044(18)			
	r_1' (Å)	1.705930(23)	1.706155(35)			
	T_0 (cm^{-1})	22309.49	22309.51			
	$\Delta G_{1/2}'$	938.16	938.14			
	B_e' (cm^{-1})	0.44865	0.44905			
	α_e' (cm^{-1})	0.00321	0.00372			
	r_e' (Å)	1.6968	1.6966			
X $^2\Delta_{5/2}$	B_0'' (cm^{-1})	0.491921(34)	0.492121(36)	0.492469(42)	0.492660(36)	
	r_0'' (Å)	1.620422(56)	1.620673(59)	1.620395(69)	1.620379(59)	

3.3.2.5 The E[18.1]$^2\Pi_{3/2} \leftarrow X^2\Delta_{5/2}$ system

A weaker band system than those previously described is the E[18.1]3/2 $\leftarrow X^2\Delta_{5/2}$ system. For this system, only the 3-0 band was rotationally resolved and analyzed. The band is similar in structure to the D-X 2-0 band shown in Figure 3.4. The R branch is relatively weak, the Q branch more intense, and the P branch more intense still, consistent with a $\Delta\Omega = -1$ transition. The first lines of R(2.5), Q(2.5), and P(2.5) confirm this fact, demonstrating that this is an $\Omega'=3/2 \leftarrow \Omega''=5/2$ transition.

With only a single band of the system rotationally resolved, accurate determinations of T_0, ω_e', $\omega_e'x_e'$, B_e', α_e', and r_e' are impossible. The values of r_3' determined for the four most abundant isotopes from this band are in good agreement, however, providing a weighted average value of 1.7068 Å. Low resolution measurements of the band heads of the 2-0 and 4-0 bands, along with the results of the rotationally resolved study of the 3-0 band, are reported in Table 3.5. Using the measured band heads to estimate the locations of the corresponding band origins, we have been able to estimate the values of T_0, ω_e', and $\omega_e'x_e'$ for the ^{192}OsN and ^{190}OsN isotopomers. The results for the two isotopes are in good agreement considering the indirect procedure that was employed. Finally, if we assume that the Pekeris relationship, Equation (3.5), is obeyed, the estimated values of ω_e' and $\omega_e'x_e'$ may be combined with the measured value of B_3' to provide estimates of B_e', α_e', and r_e' for the ^{192}OsN and ^{190}OsN isotopomers. The resulting values for ^{192}OsN and ^{190}OsN, 1.6828 and 1.6840 Å, are in good agreement for such an indirect method, and provide our best estimate of the equilibrium bond length of the E[18.1]3/2 state.

The lifetimes of the v′=2 and v′=3 levels of the E state were measured to be

Table 3.5 Spectroscopic constants for the E[18.1] $^2\Pi_{3/2}$ – X $^2\Delta_{5/2}$ system of OsN.[a]

Band	Constant	$^{192}Os^{14}N$	$^{190}Os^{14}N$	$^{189}Os^{14}N$	$^{188}Os^{14}N$	τ (μs)
2 – 0	Band	20061.0	20060.9			0.551(58)
3 - 0	ν_0 (cm^{-1})	21006.1985(18)	21007.1362(29)	21007.6218(33)	21008.0887	
	B_3' (cm^{-1})	0.443446(19)	0.443602(26)	0.443944(36)	0.444168(41)	0.703(52)
	r_3' (Å)	1.706693(37)	1.707005(50)	1.706657(69)	1.706541(79)	
3 – 0[b]	ν_0 (cm^{-1})			21007.1361(27)	21007.6339(34)	
	B_3' (cm^{-1})			0.443905(37)	0.444045(41)	
	r_3' (Å)			1.706732(71)	1.706777(79)	
4 - 0	Band	21950.3	21950.2	21950.9	21951.3	
	T_0 (cm^{-1})	18103.5	18107.8			
	ω_e' (cm^{-1})	995.1	992.3			
	$\omega_e x_e'$ (cm^{-1})	6.9	6.5			
	α_e' (cm^{-1})	0.003625	0.003488			
	B_e' (cm^{-1})	0.45613	0.45581			
	r_e' (Å)	1.6828	1.6840			
X $^2\Delta_{5/2}$	B_0'' (cm^{-1})	0.491921(34)	0.492121(36)	0.492469(42)	0.492660(36)	
	r_0'' (Å)	1.620422(56)	1.620673(59)	1.620395(69)	1.620379(59)	

[a] The vibrational fit to determine T_0, ω_e', and $\omega_e'x_e'$ is based on estimated band origin positions of the 2-0 and 4-0 bands, along with the fitted value of the band origin of the 3-0 band. The Pekeris relationship, Equation (3.5) was then assumed to be valid and used in conjunction with the values of ω_e', $\omega_e'x_e'$, and B_3' to estimate α_e', B_e', and r_e'. The 2-0 band was not identifiable in the spectra of the minor isotopes, $^{189}Os^{14}N$ and $^{188}Os^{14}N$. [b] A second feature was observed in spectra of the $^{189}Os^{14}N$ and $^{188}Os^{14}N$ isotopes; this was fitted and is included in this table.

0.551(58) and 0.703(52) μs, respectively, values that are comparable to that found for the much more intense G state. The fact that the E state shows up rather weakly in the spectrum but undergoes rapid fluorescence suggests that the primary decay pathway is fluorescence to a state other than the ground state. Low-lying electronic states to which the E state might fluoresce include the $1\sigma^2\ 2\sigma^2\ 1\pi^4\ 1\delta^4\ 3\sigma^1$, A $^2\Sigma^+$ state, calculated to lie near 4500 cm^{-1} (7500 cm^{-1} including the spin-orbit stabilization of the $X^2\Delta_{5/2}$ ground state) but not yet experimentally known, and the $1\sigma^2\ 2\sigma^2\ 1\pi^4\ 1\delta^3\ 3\sigma^1\ 2\pi^1$, $a\,^4\Pi$ and $b\,^4\Phi$ states, lying near 8400 and 11 000 cm^{-1}, respectively.[16] On this basis, a dispersed fluorescence study of the emission from the E[18.1]3/2 state might be useful for locating these low-lying excited states.

3.3.2.6 The F[16.0]$^2\Pi_{3/2} \leftarrow X^2\Delta_{5/2}$ system

Similar in intensity to the E[18.1]3/2 $\leftarrow X\,^2\Delta_{5/2}$ system is the weak B[16.0]3/2 $\leftarrow X\,^2\Delta_{5/2}$ system. The only member of this system to be rotationally resolved is the 20 694 cm^{-1} band, which is similar in structure to the D-X 2-0 band that is displayed in Figure 3.4. The upper level of this transition lies only 36 cm^{-1} above the D[18.0]3/2 $v'=3$ level; it is possible that some mixing of these two levels allows this band to borrow intensity from the D-X system. Alternatively, it may be that the greater intensity of this band is simply due to better Franck-Condon factors than the higher-lying bands of the B-X system. The first lines of R(2.5), Q(2.5), and P(2.5) identify the band as an $\Omega'=3/2 \leftarrow \Omega''=5/2$ transition, a fact that is confirmed by the relative intensities of the branches.

In addition to the 20 694 cm^{-1} band, the low resolution scans also show features of this system near 21 630 and 22 558 cm^{-1}, respectively. The vibrational assignment of this

system is uncertain due to limited and inconsistent isotope shift data. Although the data are best explained by assigning the 20 694 cm^{-1} band as the 5-0 band, it is possible that this numbering is in error, particularly if the band positions are shifted in an isotopically dependent manner by interactions with the D[18.0]$^2\Pi_{3/2}$ state. It is also troubling that the 4-0 band, which is predicted by the fit to lie between the C-X 2-0 and D-X 2-0 bands, is either extremely weak or completely absent. Nevertheless, assuming that the 20 694 cm^{-1} band is the 5-0 band, using the band heads of the 6-0 and 7-0 bands, and making a correction for the likely band origin positions, we are able to estimate the values of T_0, ω_e', and $\omega_e'x_e'$ for the more abundant ^{192}OsN and ^{190}OsN species, as provided in Table 3.6. These values, in combination with the measured values of B_5', were also used to estimate α_e', B_e', and r_e' using the Pekeris relationship (Equation 3.5). Although imperfect, this method allows an estimate of r_e', which when averaged over the ^{192}OsN and ^{190}OsN isotopes gives $r_e' \approx 1.706$ Å.

The measured lifetime of the v′=5 level, 1.26(12) μs, is completely in line with that found for the other band systems. Unlike the E-X system, however, the weak intensity of this band system might be explained by the fact that only the v′ = 5 -7 levels are observed. These levels have poor Franck-Condon factors due to the large change in vibrational number upon excitation. It is likely that the 0-0, 1-0, 2-0, and 3-0 bands are more intense, but fall too low in energy to be observed unless a more energetic ionization photon is employed.

These considerations do not explain why the 4-0 band is unobserved, however. The 4-0 band is predicted, based on the fit, to fall slightly to the red of the D-X 2-0 band, near 19 758 cm^{-1}. One would expect it to be more intense than the 5-0 band, on the basis

Table 3.6 Spectroscopic constants for the B[16.0] $^2\Pi_{3/2}$ – X $^2\Delta_{5/2}$ system of OsN.[a]

Band	Constant	$^{192}Os^{14}N$	$^{190}Os^{14}N$	$^{189}Os^{14}N$	$^{188}Os^{14}N$	τ (μs)
5 - 0	ν_0 (cm^{-1})	20694.0886(21)	20695.5895(26)	20696.3616(25)	20697.1415(27)	1.26(12)
	B_5' (cm^{-1})	0.436830(18)	0.437024(24)	0.437363(50)	0.437585(28)	
	r_5' (Å)	1.719569(35)	1.719803(47)	1.719449(98)	1.719329(55)	
6 - 0	Band	21629.8	21632.0	21633.2	21634.6	
7 – 0	Band	22558.1	22560.9			
	T_0 (cm^{-1})	15978.7	15974.5			
	ω_e' (cm^{-1})	954.0	955.6			
	$\omega_e'x_e'$ (cm^{-1})	1.8	1.9			
	α_e' (cm^{-1})	0.001256	0.001324			
	B_e' (cm^{-1})	0.44374	0.44430			
	r_e' (Å)	1.7061	1.7057			
X $^2\Delta_{5/2}$	B_0'' (cm^{-1})	0.491921(34)	0.492121(36)	0.492469(42)	0.492660(36)	
	r_0'' (Å)	1.620422(56)	1.620673(59)	1.620395(69)	1.620379(59)	

[a] The vibrational fit to determine T_0, ω_e', and $\omega_e'x_e'$ is based on estimated band origin positions of the 6-0 and 7-0 bands, along with the fitted value of the band origin of the 5-0 band. The Pekeris relationship, Equation (3.5) was then assumed to be valid and used in conjunction with the values of ω_e', $\omega_e'x_e'$, and B_5' to estimate α_e', B_e', and r_e'. Although this procedure is imprecise, and is compromised by errors in the determination of the vibrational parameters, particularly $\omega_e'x_e'$, it nevertheless provides an estimate of r_e'. The 7-0 band was not identifiable in the spectra of the minor isotopes, $^{189}Os^{14}N$ and $^{188}Os^{14}N$.

of Franck-Condon factors. If the B-X system is allowed, but also borrows intensity from the D-X system, however, then it is possible that the borrowed transition moment is of opposite sign to the intrinsic transition moment, and that a cancellation of the two moments causes the 4-0 band to vanish. Although such an explanation is purely hypothetical at this point, the high relative intensity of the 5-0 band is consistent with this explanation. The vibrational levels assigned as v′=4 and v′=5 lie below and above the v′=2 and v′=3 levels of the D[18.0]$^2\Pi_{3/2}$ state, respectively. Given that the first order perturbation theory correction to the wavefunction mixes in D[18.0]$^2\Pi_{3/2}$ character according to the expression

$$\Psi_{Bv_B}{}^{(1)} = \frac{H'_{Dv_D,Bv_B}}{E^{(0)}_{Bv_B} - E^{(0)}_{Dv_D}} \Psi_{Dv_D}{}^{(0)}, \tag{3.6}$$

the denominator will change sign in going from the B, v′=4 ~ D, v′=2 perturbation to the B, v′=5 ~ D, v′=3 perturbation. If the numerator retains the same sign, then the contribution for the first-order correction to the wavefunction is positive for one case and negative for the other. Thus, the intrinsic and borrowed transition moments will tend to cancel for one level (the 4-0 band) and add constructively for the other (the 5-0 band). This could explain our inability to observe the B-X 4-0 band while simultaneously observing an anomalously high intensity for the B-X 5-0 band.

For the present, we identify the B state as the B[16.0]$^2\Pi_{3/2}$ state, with the recognition that although the Ω value of this state is definite, the A-S term symbol of the leading contribution to this state could be different from $^2\Pi$.

3.3.2.7 Additional bands

Three additional bands were rotationally resolved and are listed in Table 3.7. These consist of two $\Omega'=5/2 \leftarrow \Omega''=5/2$ bands located near 22 911.5 and 22 934.0 cm^{-1} and an intense $\Omega'=3/2 \leftarrow \Omega''=5/2$ band near 23 636.5 cm^{-1}. The latter band displays a small isotope shift, 0.0942 cm^{-1} for $\nu(^{188}OsN) - \nu(^{192}OsN)$, and is presumably the 0-0 band of a system that continues beyond the range investigated here. Accordingly, it is designated as the 0-0 band of the $H[23.6]^2\Pi_{3/2} \leftarrow X\,^2\Delta_{5/2}$ system. The $H[23.6]^2\Pi_{3/2}$ state is notable for having a significantly shorter bond length than any of the other excited states reported in this study. Only the ground state and the previously reported $1\sigma^2\,2\sigma^2\,1\pi^4\,1\delta^3\,3\sigma^1\,2\pi^1$, $^4\Pi_{5/2}$ and $^4\Phi_{5/2,\,7/2}$ states have bond lengths that are shorter than that of the $H[23.6]^2\Pi_{3/2}$ state.

The two bands near 22 911.5 and 22 934.5 cm^{-1} are the only bands examined in this study that have upper states with $\Omega'=5/2$. Moreover, they are separated by only 22.5 cm^{-1} and have remarkably similar values of B': 0.44090 and 0.44089 cm^{-1}, respectively, for the ^{192}OsN isotopic form. The measured isotope shifts, $\nu(^{188}OsN) - \nu(^{192}OsN)$, are also quite similar, 0.3309 and 0.3805 cm^{-1}, for the two bands, respectively. The value of the measured isotope shift falls midway between that expected for a 0-0 band, which is typically -0.10 to -0.03 cm^{-1}, and that expected for a 1-0 band, which is typically 0.5 to 0.7 cm^{-1}.

The similarity of the upper states of these two bands suggests that they arise from a pair of $\Omega'=5/2$ levels that are coupled by a homogeneous perturbation with a J-independent coupling matrix element, H_{12}, that is much larger than the separation between the

Table 3.7 Spectroscopic constants for additional bands of OsN

Band	Constant	$^{192}Os^{14}N$	$^{190}Os^{14}N$	$^{189}Os^{14}N$	$^{188}Os^{14}N$
H[23.6] $^2\Pi_{3/2} \leftarrow X^2\Delta_{5/2}$	ν_0 (cm^{-1})	23636.5418(27)	23636.5833(28)	23636.6162(32)	23636.6360(33)
0 – 0 band	B_0' (cm^{-1})	0.465101(31)	0.465328(50)	0.465629(29)	0.465777(25)
	r_0' (Å)	1.666488(56)	1.666679(90)	1.666443(52)	1.666484(45)
$\Omega'=5/2 \leftarrow X^2\Delta_{5/2}$	ν_0 (cm^{-1})	22934.0221(36)	22934.1918(44)		22934.4026(41)
22934 band	B′ (cm^{-1})	0.440888(28)	0.441115(32)		0.441394(42)
	r′ (Å)	1.711637(54)	1.711810(62)		1.711895(81)
$\Omega'=5/2 \leftarrow X^2\Delta_{5/2}$	ν_0 (cm^{-1})	22911.4990(43)	22911.6572(37)	22911.6825(92)	22911.8299(42)
22911 band	B′ (cm^{-1})	0.440896(32)	0.441353(32)	0.442478(118)	0.442087(60)
	r′ (Å)	1.711622(62)	1.711348(62)	1.709482(228)	1.710552(116)
$X\ ^2\Delta_{5/2}$	B_0'' (cm^{-1})	0.491921(34)	0.492121(36)	0.492469(42)	0.492660(36)
	r_0'' (Å)	1.620422(56)	1.620673(59)	1.620395(69)	1.620379(59)

interacting states. In such a case, examination of the two-state perturbation model shows that the effective band origins (ν_0) and effective rotational constants (B) of the two states are related to the term energies (T_0^+ and T_0^-) and rotational constants (B^+ and B^-) of the upper (+) and lower (−) of the states prior to interaction according to:

$$\nu_0 = \tfrac{1}{2}(T_0^+ + T_0^-) \pm H_{12} \pm (T_0^+ - T_0^-)^2/8H_{12} + \ldots \quad (3.7)$$

and $$B = \tfrac{1}{2}(B^+ + B^-) \pm (T_0^+ - T_0^-)(B^+ - B^-)/4H_{12} + \ldots \quad (3.8)$$

In the limit that $|H_{12}| >> |T_0^+ - T_0^-|$, these results predict that the two measured states will have the same effective value of B, which will be the average of the B values of the two states prior to interaction. In the same limit, the two band origins will be separated by $2H_{12}$, suggesting that in our case $H_{12} \approx 11$ cm^{-1}. Further, since the two measured band origins are displaced by $\pm H_{12}$ from the average of T^+ and T^-, they will display an isotope shift that is the average of the two states prior to interaction. This suggests that our two interacting states are v′=0 and v′=1 levels, leading to isotope shifts that are midway between that expected for levels with v′=0 and v′=1, as found. The fact that no $\Omega'=5/2 \leftarrow X^2\Delta_{5/2}$ transition is observed where the 0-0 transition would be expected, roughly 800-1000 cm^{-1} to the red of these bands, suggests that v′=1 level belongs to a dark state that gains its intensity via mixing with the v′=0 level of a bright state. If this is true, dispersed fluorescence from these strongly mixed bands could terminate on both the doublet and the quartet manifolds, allowing the electronic structure of OsN to be probed more deeply.

3.4 Discussion

3.4.1 Assignment of Observed States to Configurations and Terms

With the spectroscopic data described in the previous section in hand, it is appropriate to try to identify the observed states with electronic configurations in the OsN molecule. Toward this end, a discussion of the molecular orbital structure of the molecule is useful. Figure 3.5 presents a qualitative molecular orbital diagram that is consistent with what was obtained via CASSCF calculations in a previous study.[16] Ignoring the core-like 1σ orbital, which is primarily nitrogen 2*s* in character, the remaining orbitals fall into three categories: (1) strongly bonding combinations of 2*p* orbitals on nitrogen and 5*d* orbitals on osmium, giving rise to the 2σ and 1π orbitals; (2) nonbonding orbitals consisting primarily of the 5*d*δ orbitals of osmium (forming the 1δ molecular orbital) and the 6*s* orbital of osmium (forming, with some admixture of the 5*d*σ and 6*p*σ osmium orbitals, the 3σ molecular orbital); and (3) strongly antibonding combinations of 2*p* orbitals on nitrogen and 5*d* orbitals on osmium, giving rise to the 2π and 4σ antibonding molecular orbitals.

The ground electronic configuration, $1\sigma^2\ 2\sigma^2\ 1\pi^4\ 1\delta^3\ 3\sigma^2$, places a single hole in the nonbonding 1δ set of orbitals, leading only to an inverted $^2\Delta$ term with a $^2\Delta_{5/2}$ ground level. If the hole is instead placed in the nonbonding 3σ orbital, a $1\sigma^2\ 2\sigma^2\ 1\pi^4\ 1\delta^4\ 3\sigma^1$, $^2\Sigma^+$ state is obtained. This is predicted to be the first excited state of the molecule, calculated to lie 4465 cm^{-1} above the average of the $X_1\ ^2\Delta_{5/2}$ and $X_2\ ^2\Delta_{3/2}$ levels.[16] The spin-orbit interaction, which is quite significant in heavy atoms such as Os, shifts the $X_1\ ^2\Delta_{5/2}$ level to lower energies by the amount –A, where A is approximately given by $\zeta_{5d}(Os) \approx 3045\ cm^{-1}$;

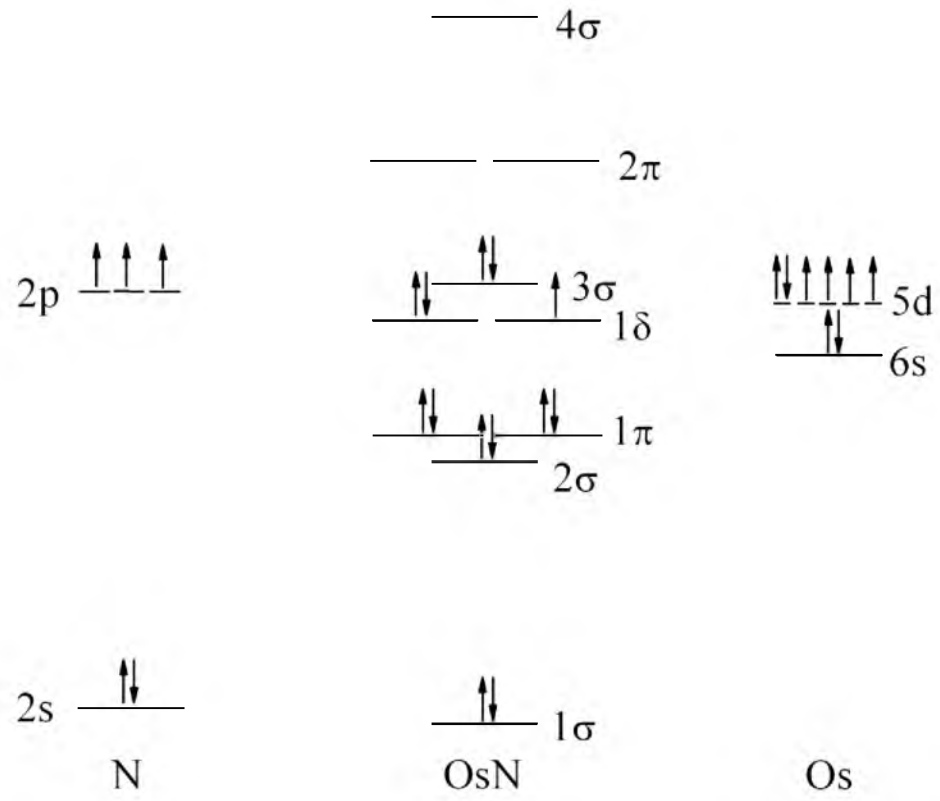

Figure 3.5 Qualitative molecular orbital diagram for OsN.

thus the $^2\Sigma^+$ state may be expected to lie approximately 7500 cm^{-1} above the $X_1\ ^2\Delta_{5/2}$ ground level. This prediction, of course, ignores any inaccuracies in the calculation as well as off-diagonal spin-orbit interactions, which are important in second order perturbation theory.

The next higher energy configurations arise from the ground state by promotion of either a 3σ or 1δ nonbonding electron to the 2π antibonding orbital, giving the $1\sigma^2\ 2\sigma^2\ 1\pi^4\ 1\delta^3\ 3\sigma^1\ 2\pi^1$ and $1\sigma^2\ 2\sigma^2\ 1\pi^4\ 1\delta^2\ 3\sigma^2\ 2\pi^1$ configurations. The former configuration leads to the *a* $^4\Pi$ and *b* $^4\Phi$ states that have been identified by Fourier transform emission spectroscopy,[16] along with two $^2\Pi$ and two $^2\Phi$ terms. Both $^2\Pi$ and $^2\Phi$ states are accessible under electric dipole-allowed transitions from the X $^2\Delta$ ground state. Similarly, the $1\sigma^2\ 2\sigma^2\ 1\pi^4\ 1\delta^2\ 3\sigma^2\ 2\pi^1$ configuration generates one $^4\Pi$ term, two $^2\Pi$ terms, one $^2\Phi$ term, and one ^{2}H term. Thus, the promotion of a nonbonding 1δ or 3σ electron to the antibonding 2π orbital will lead to four $^2\Pi$ terms and three $^2\Phi$ terms that may be accessed in fully allowed optical transitions. In transitions from the $X_1\ ^2\Delta_{5/2}$ level, transitions to the four $^2\Pi_{3/2}$ and three $^2\Phi_{7/2}$ levels are allowed under electric dipole selection rules.

With these facts in hand, it is no surprise that the observed transitions nearly all terminate on upper states with $\Omega' = 3/2$ or 7/2. In fact, it is likely that the four observed upper states with $\Omega'=3/2$ (the B[16.0] $^2\Pi_{3/2}$, D[18.0]$^2\Pi_{3/2}$, E[18.1] $^2\Pi_{3/2}$, and H[23.6] $^2\Pi_{3/2}$ states) are the four $^2\Pi_{3/2}$ states expected from these excitations. It is also likely that the three observed upper states with $\Omega'=7/2$ (the C[17.8]$^2\Phi_{7/2}$, F[21.2] $^2\Phi_{7/2}$, and G[22.3] $^2\Phi_{7/2}$ states) are the three expected $^2\Phi_{7/2}$ levels. All of these states are generated by excitation of a nonbonding 1δ or 3σ electron to the antibonding 2π orbital, consistent with the increase in bond length of 0.05 to 0.09 Å that is found.

To facilitate a direct comparison to the *ab initio* calculation that was previously reported,[16] Table 3.8 collects all of the experimentally known information about the electronic states of OsN, which is compared to the previous computational study. It is difficult to directly compare the experimental excitation energies, T_0, with the calculated ones, since the calculation omitted spin-orbit interactions, which are quite significant in this molecule. It is easy to estimate the effects of the spin-orbit operator on the ground $^2\Delta_{5/2}$ level, since this contains only a single hole in an orbital that is nearly purely 5*d*δ on osmium. Estimating the spin-orbit effects on the excited states is much more difficult, however, since there are multiple $^2\Pi$ and $^2\Phi$ states that derive from the $1\sigma^2\ 2\sigma^2\ 1\pi^4\ 1\delta^3\ 3\sigma^1\ 2\pi^1$ and $1\sigma^2\ 2\sigma^2\ 1\pi^4\ 1\delta^2\ 3\sigma^2\ 2\pi^1$ configurations, and these are strongly mixed by configuration interaction.[16] Thus, disagreements between theory and experiment in the T_0 values could be due to spin-orbit effects. As is commonly found in *ab initio* work on transition metal systems, the calculated bond lengths of the various states are too long, by 0.014 Å on average. The calculated vibrational frequencies tend to be a bit low for the excited electronic states, but the calculated ω_e is in nearly perfect agreement with the measured value for the ground state.

In addition to these $^2\Pi$ and $^2\Phi$ excited states, we also observe one strong band with $\Omega' = 5/2$, which mixes with a nearby dark $\Omega' = 5/2$ state. A fully allowed $\Omega'=5/2 \leftarrow X\ ^2\Delta_{5/2}$ transition can only occur to another $^2\Delta_{5/2}$ upper state. Thus, there is good evidence of a $^2\Delta_{5/2}$ excited state lying near 22 911.5 cm^{-1}. Such a term cannot arise from promotion of a nonbonding 1δ or 3σ electron to the antibonding 2π orbital. It could arise from the promotion of the nonbonding 3σ electron into the strongly antibonding 4σ orbital, leading

Table 3.8 Summary of all experimentally known states of $^{192}Os^{14}N$

	Experiment				Theory[c]		
State	T_0 (cm^{-1})	r_e (Å)	ω_e (cm^{-1})	$\omega_e x_e$ (cm^{-1})	T_0 (cm^{-1})	r_e (Å)	ω_e (cm^{-1})
$X\ ^2\Delta_{5/2}$	0.00	1.6180[c]	1147.95[c]	5.460[c]	0.00	1.627	1146
$a\ ^4\Pi_{5/2}$	8 381.75[c]	1.6552[c]	1045.61[a, c]		8 445	1.677	1003
$b\ ^4\Phi_{7/2}$	11 147.93[c]	1.6679[b, c]			10 245	1.675	1004
$b\ ^4\Phi_{5/2}$	12 127.19[c]	1.6591[b, c]			10 245	1.675	1004
$B\ ^2\Pi_{3/2}$	15 979 [d]	1.706	954	1.8	16 000	1.720	841
$C\ ^2\Phi_{7/2}$	17 763.50	1.681	977.83	6.53	15 337	1.697	940
$D\ ^2\Pi_{3/2}$	18 009	1.687	878		18 016	1.703	843
$E\ ^2\Pi_{3/2}$	18 104	1.683	995.1	6.9			
$F\ ^2\Phi_{7/2}$	21151.04	1.6920	938.54	14.03	20 116	1.704	933
$G\ ^2\Phi_{7/2}$	22 309.49	1.6968	938.16[a]				
$H^2\Pi_{3/2}$	23 636.54	1.6665[b]					

[a] This value represents the vibrational interval, $\Delta G_{1/2}$, not ω_e. [b] This value represents r_0, not r_e. [c] From reference [16].
[d] Vibrational numbering is uncertain in the B-X system. This introduces uncertainty into the parameters ω_e, $\omega_e x_e$, r_e, and especially T_0.

to a $1\sigma^2\ 2\sigma^2\ 1\pi^4\ 1\delta^3\ 3\sigma^1\ 4\sigma^1$ configuration, or by promotion of a 1π bonding electron into the antibonding 2π orbital, leading to a $1\sigma^2\ 2\sigma^2\ 1\pi^3\ 1\delta^3\ 3\sigma^2\ 2\pi^1$ configuration. Although the energy, bond length, and vibrational frequency were not tabulated, the previous computational study of OsN did report that the $2\ ^2\Delta$ term of OsN derives primarily (69%) from the $1\pi \rightarrow 2\pi$ excitation. Thus, we suspect that the strongly allowed $\Omega'=5/2 \leftarrow X\ ^2\Delta_{5/2}$ transition near 22 911.5 cm^{-1} is the 0-0 band of this $2\ ^2\Delta_{5/2} \leftarrow X\ ^2\Delta_{5/2}$ transition. Unfortunately, due to strong coupling to the other $\Omega'=5/2$ level near 22 934 cm^{-1}, it is impossible to provide an accurate estimate of the bond length of this state.

3.4.2 Comparison to Related Molecules

The isoelectronic 5*d* transition metal molecules, ReO,[22, 42-45] OsN,[16] and IrC,[25, 46-49] have now all been spectroscopically investigated to varying degrees, and have been shown to have a $^2\Delta_{5/2}$ ground state deriving from the $1\sigma^2\ 2\sigma^2\ 1\pi^4\ 1\delta^3\ 3\sigma^2$ configuration. Of these three molecules, the manifold of excited states is now best known for OsN. Although a large number of band systems are known for ReO,[44] our understanding of this molecule is hampered by the fact that the Ω values of the upper states are mostly unknown. An exception is the [14.0]7/2 – $X^2\Delta_{5/2}$ band, which has been investigated at 50 MHz resolution, demonstrating that the upper state has an unpaired electron in the 3σ orbital, resulting in a large Fermi contact contribution to the hyperfine splitting.[45] For IrC, upper states in the 14 000-18 000 cm^{-1} range have been reassigned to the $a\ ^4\Phi_{7/2}$, $a\ ^4\Phi_{5/2}$, and $b\ ^4\Pi_{3/2}$ states, all arising from the $1\sigma^2\ 2\sigma^2\ 1\pi^4\ 1\delta^3\ 3\sigma^1\ 2\pi^1$ configuration.[16, 47] The analogues of these states are known in OsN from Fourier transform emission spectroscopy.[16] In addition, three excited states of IrC with $\Omega=3/2$ and one with $\Omega=7/2$

have been observed in the 19 000 – 23 000 cm^{-1} range.[46, 48, 49] These are undoubtedly analogues of some of the $^2\Pi_{3/2}$ and $^2\Phi_{7/2}$ states observed in OsN in the present study, although it is impossible to draw a precise correlation.

It is also interesting to compare the 5*d*, $1\sigma^2\ 2\sigma^2\ 1\pi^4\ 1\delta^3\ 3\sigma^2$, X $^2\Delta_{5/2}$ molecules, ReO, OsN, and IrC, to their isovalent 3*d* and 4*d* counterparts. Both MnO[50] and TcO[51] have $1\sigma^2\ 2\sigma^2\ 1\pi^4\ 1\delta^2\ 2\pi^2\ 3\sigma^1$, X $^6\Sigma^+$ ground states, while RuN,[52] CoC,[53] and RhC[54] all have $1\sigma^2\ 2\sigma^2\ 1\pi^4\ 1\delta^4\ 3\sigma^1$, X $^2\Sigma^+$ ground states. Only FeN shares the same $1\sigma^2\ 2\sigma^2\ 1\pi^4\ 1\delta^3\ 3\sigma^2$, X $^2\Delta_{5/2}$ ground state that is found in ReO, OsN, and IrC.[55] Hyperfine splitting measurements in CoC, RuN, and RhC show that the 3σ orbital is primarily composed of the transition metal (n+1)*s* orbital, containing 89% Co 4*s*,[53] 63% Ru 5*s*,[56] and 70% Rh 5*s* character,[57] respectively. The double occupancy of this 3σ orbital in the 5*d* molecules, ReO, OsN, and IrC, is favored by the relativistic stabilization of the 6*s* orbital in these heavy atoms. Another important factor in the emergence of $1\sigma^2\ 2\sigma^2\ 1\pi^4\ 1\delta^3\ 3\sigma^2$, $^2\Delta_{5/2}$ as the ground state in these 5*d* molecules is the spin-orbit interaction, which stabilizes the Ω=5/2 component of this state by $-\zeta_{5d}(M)$, which amounts to -2545, -3045, and -3617 cm^{-1} in Re, Os, and Ir, respectively.[39] Typically, the magnitude of the spin-orbit stabilization is reduced by a factor of 3 in the 4*d* series, and by a factor of 7 in the 3*d* series,[39] making the spin-orbit stabilization of the $^2\Delta_{5/2}$ level far less significant in the 3*d* and 4*d* series.

The $^6\Sigma^+$ ground states that are found for MnO and TcO are stabilized because the atomic orbitals of the electronegative oxygen atom lie far below those of the metal atom, resulting in significant ionic character and reducing the splitting of the metal n*d* orbitals. Because the resulting molecular orbitals are little changed from the n*d* orbitals of the atom, they lie close in energy, favoring the high-spin $^6\Sigma^+$ term. The emergence of the high-spin

$^6\Sigma^+$ ground term for highly ionic species is also found for the isovalent transition metal fluoride CrF,[58] and is calculated to be the ground term for MoF and WF as well.[59, 60] High spin states are often found for transition metal hydrides for similar reasons: the lack of orbitals of suitable π or δ symmetry on hydrogen prevents the dπ and dδ orbitals from splitting significantly, making it more favorable to place electrons in different orbitals with high-spin coupling, resulting in $^6\Sigma^+$ terms for CrH,[61] MoH,[62] and WH.[63]

3.5 Conclusion

The electronic spectrum of diatomic OsN has been investigated in the range from 19 200 to 23 900 cm^{-1} using resonant two-photon ionization spectroscopy. The study confirms the ground state of OsN to be $^2\Delta_{5/2}$, arising from the $1\sigma^2\ 2\sigma^2\ 1\pi^4\ 1\delta^3\ 3\sigma^2$ electronic configuration. Rotational analysis of 17 bands has revealed four excited states of $^2\Pi_{3/2}$ symmetry and three excited states of $^2\Phi_{7/2}$ symmetry, as expected to arise from the $1\sigma^2\ 2\sigma^2\ 1\pi^4\ 1\delta^3\ 3\sigma^1\ 2\pi^1$ and $1\sigma^2\ 2\sigma^2\ 1\pi^4\ 1\delta^2\ 3\sigma^2\ 2\pi^1$ excited configurations. In addition, one state of $^2\Delta_{5/2}$ symmetry, likely originating from the $1\sigma^2\ 2\sigma^2\ 1\pi^3\ 1\delta^3\ 3\sigma^2\ 2\pi^1$ configuration, has also been found. Spectroscopic constants have been reported and the OsN molecule has been compared to related species.

3.6 References

1 *The Chemical Physics of Solid Surfaces and Heterogeneous Catalyst, Vol 4*, Vol., edited by M. Grunze (Elsevier, New York, 1982).

2 D. N. Davis, Astrophys. J. **106,** 28 (1949).

3 H. Spinard and R. F. Wing, Annu. Rev. Astron. Astrophys. **7,** 269 (1969).

4 *The Behavior of Chemical Elements in Stars*, Vol., edited by C. J. a. M. Jascheck (Cambridge University Press, Cambridge, 1995).

5 Y. Yerle, Astron. Astrophys. **73,** 346 (1979).

6 B. Lindgren and G. Olofsson, Astron. Astrophys. **84,** 209 (1980).

7 R. S. Ram, P. F. Bernath, and L. Wallace, Astrophys. J., Suppl. Ser. **107,** 443-9 (1996).

8 R. H. Crabtree, *The Organometallic Chemistry of the Transition Metals*, 5th ed. (Wiley, Hoboken, NJ, 2009).

9 K. E. Andersson, M. Veszelei, and A. Roos, Sol. Energy Mater. Sol. Cells **32,** 199-212 (1994).

10 C. G. Ribbing and A. Roos, Proc. SPIE-Int. Soc. Opt. Eng. **3133,** 148-62 (1997).

11 E. C. Samano, A. Clemente, J. A. Diaz, and G. Soto, Vacuum **85,** 69-77 (2010).

12 T. H. Randle, J. Gopalakrishna, and E. D. Doyle, in *Proc. - Corros. Prev.* (2001), pp. 47/1-/8.

13 F. Levy, P. Hones, P. E. Schmid, R. Sanjines, M. Diserens, and C. Wiemer, Surf. Coat. Technol. **120-121,** 284-90 (1999).

14 P. F. Bernath and S. McLeod, J. Mol. Spectrosc. **207,** 287 (2001).

15 A. Citra and L. Andrews, J. Phys. Chem. A **104,** 1152-61 (2000).

16 R. S. Ram, J. Liévin, and P. F. Bernath, J. Chem. Phys. **111,** 3449-56 (1999).

17 W. J. Balfour and R. S. Ram, J. Mol. Spectrosc. **105,** 360-8 (1984).

18 O. Krechkivska and M. D. Morse, J. Chem. Phys. **128,** 084314/1-/9 (2008).

[19] R. S. Ram and P. F. Bernath, J. Mol. Spectrosc. **184,** 401-12 (1997).

[20] R. S. Ram, J. Lievin, and P. F. Bernath, J. Mol. Spectrosc. **215,** 275-84 (2002).

[21] R. S. Ram and P. F. Bernath, J. Opt. Soc. Am. B **11,** 225-30 (1994).

[22] W. J. Balfour, J. Cao, C. X. W. Qian, and S. J. Rixon, J. Mol. Spectrosc. **183,** 113-8 (1997).

[23] R. S. Ram, P. F. Bernath, and W. J. Balfour, J. Mol. Spectrosc. **246,** 192-7 (2007).

[24] R. S. Ram, J. Liévin, and P. F. Bernath, J. Mol. Spectrosc. **197,** 133-46 (1999).

[25] A. J. Marr, M. E. Flores, and T. C. Steimle, J. Chem. Phys. **104,** 8183-96 (1996).

[26] T. C. Steimle, A. J. Marr, S. A. Beaton, and J. M. Brown, J. Chem. Phys. **106,** 2073-7 (1997).

[27] E. J. Friedman-Hill and R. W. Field, J. Chem. Phys. **100,** 6141-52 (1994).

[28] T. C. Steimle, K. Y. Jung, and B.-Z. Li, J. Chem. Phys. **103,** 1767-72 (1995).

[29] D. J. Brugh and M. D. Morse, J. Chem. Phys. **107,** 9772-82 (1997).

[30] W. C. Wiley and I. H. McLaren, Rev. Sci. Instrum. **26,** 1150 - 7 (1955).

[31] B. A. Mamyrin, V. I. Karataev, D. V. Shmikk, and V. A. Zagulin, Zh. Eksp. Teor. Fiz. **64,** 82-9 (1973).

[32] S. Gerstenkorn and P. Luc, *Atlas du Spectre d'Absorption de la Molécule d'Iode entre 14,800-20,000 cm^{-1}* (CNRS, Paris, 1978).

[33] J. Cariou and P. Luc, *Atlas du Spectre d'Absorption de la Molécule de Tellure entre 18,500 - 23,800 cm^{-1}* (CNRS, Paris, 1980).

[34] M. D. Morse, in *Methods of Experimental Physics: Atomic, Molecular, and Optical Physics*, Vol. II Atoms and Molecules, edited by F. B. Dunning and R. Hulet (Academic Press, Inc., Orlando, Florida, 1996), pp. 21-47.

[35] S. Gerstenkorn and P. Luc, Rev. Phys. Appl. **14,** 791-4 (1979).

[36] P. R. Bevington, *Data Reduction and Error Analysis for the Physical Sciences* (McGraw-Hill, New York, 1969).

[37] G. Herzberg, *Molecular Spectra and Molecular Structure I. Spectra of Diatomic Molecules*, 2nd ed. (Van Nostrand Reinhold, New York, 1950).

[38] P. Colarusso, M.-A. Lebeault-Dorget, and B. Simard, Physical Review A **55,** 1526-9 (1997).

[39] H. Lefebvre-Brion and R. W. Field, *The Spectra and Dynamics of Diatomic Molecules* (Elsevier, Amsterdam, 2004).

[40] J. I. Steinfeld, *Molecules and Radiation: An Introduction to Modern Molecular Spectroscopy*, Second ed. (The MIT Press, Cambridge, 1993).

[41] P. F. Bernath, *Spectra of Atoms and Molecules* (Oxford University Press, New York, 1995).

[42] W. J. Balfour and F. B. Orth, J. Mol. Spectrosc. **84,** 424-30 (1980).

[43] W. J. Balfour and R. S. Ram, J. Mol. Spectrosc. **100,** 164-73 (1983).

[44] W. J. Balfour and R. S. Ram, Can. J. Phys. **62,** 1524-37 (1984).

[45] M. A. Roberts, C. G. Alfonzo, K. J. Manke, W. M. Ames, D. B. Ron, and T. D. Varberg, Mol. Phys. **105,** 917-21 (2007).

[46] K. Jansson, R. Scullman, and B. Yttermo, Chem. Phys. Lett. **4,** 188-90 (1969).

[47] K. Jansson and R. Scullman, J. Mol. Spectrosc. **36,** 248 - 67 (1970).

[48] T. Ma, J. W. H. Leung, and A. S. C. Cheung, Chem. Phys. Lett. **385,** 259-62 (2004).

[49] H. F. Pang and A. S. C. Cheung, Chem. Phys. Lett. **471,** 194-7 (2009).

[50] R. M. Gordon and A. J. Merer, Can. J. Phys. **58,** 642-56 (1980).

[51] S. R. Langhoff, C. W. Bauschlicher, Jr., L. G. M. Pettersson, and P. E. M. Siegbahn, Chem. Phys. **132,** 49-58 (1989).

[52] R. S. Ram, J. Liévin, and P. F. Bernath, J. Chem. Phys. **109,** 6329-37 (1998).

[53] M. Barnes, A. J. Merer, and G. F. Metha, J. Chem. Phys. **103,** 8360-71 (1995).

[54] A. Lagerqvist and R. Scullman, Arkiv för Fysik **32,** 479 - 508 (1966).

[55] K. Aiuchi and K. Shibuya, J. Mol. Spectrosc. **204,** 235-61 (2000).

[56] T. C. Steimle and W. Virgo, J. Chem. Phys. **119,** 12965-72 (2003).

[57] J. M. Brom, Jr., W. R. M. Graham, and W. Weltner, Jr., J. Chem. Phys. **57,** 4116-24 (1972).

[58] O. Launila, J. Mol. Spectrosc. **169,** 373-95 (1995).

[59] L. Cheng, M. Y. Wang, Z. J. Wu, and Z. M. Su, J. Comput. Chem. **28,** 2190-202 (2007).

[60] K. G. Dyall, J. Phys. Chem. A **104,** 4077-83 (2000).

[61] R. S. Ram, C. N. Jarman, and P. F. Bernath, J. Mol. Spectrosc. **161,** 445-54 (1993).

[62] K. Balasubramanian and J. Li, J. Phys. Chem. **94,** 4415-19 (1990).

[63] Z. Ma and K. Balasubramanian, Chem. Phys. Lett. **181,** 467-73 (1991).

CHAPTER 4

ELECTRONIC SPECTROSCOPY AND ELECTRONIC STRUCTURE OF DIATOMIC IrSi

4.1 Introduction

Transition metal silicides have been of interest in the electronics industry for a number of years, owing to their hardness, resistance to oxidation, useful electronic properties, and compatibility with silicon-based microelectronics. In particular, several transition metal silicides have potential uses as Schottky-barrier infrared detection devices, including NiSi[1] and PtSi.[2] Iridium silicide has also been studied for purposes of infrared detection in Schottky barrier devices.[3] Another potential use for IrSi is in cold cathode field emission displays, where its ability to be annealed at low temperatures is key.[4]

Because of these potential uses, information about the fundamental interactions between transition metals and silicon is desired, and significant efforts have been made to elucidate the properties of the diatomic transition metal silicides. Bond dissociation energies of ScSi,[5] YSi,[6] FeSi,[7] RuSi,[8] CoSi,[7] RhSi,[8] IrSi,[8] NiSi,[7] PdSi,[8, 9] PtSi,[8] CuSi,[10] AgSi,[10] and AuSi[8, 11] have been measured using Knudsen effusion mass spectrometry, and guided ion beam studies have determined the bond energies of the cations $ScSi^+$,[12] YSi^+,[12] $LaSi^+$,[12] $LuSi^+$,[12] $TiSi^+$,[13] VSi^+,[13] $CrSi^+$,[13] $FeSi^+$,[14] $CoSi^+$,[14] $NiSi^+$,[14] $CuSi^+$,[15] and $ZnSi^+$.[15] Diatomic VSi and NbSi have been investigated by matrix isolation ESR

spectroscopy.[16] Gas phase spectroscopic information is also available for some of these species. Cavity ringdown spectra have been recorded for CuSi,[17] AgSi,[18] AuSi,[19] and PtSi,[20] and emission spectra have been measured and analyzed for CuSi.[21] The pure rotational spectrum of PtSi has also been recorded, enabling a precise measurement of its bond length and dipole moment.[22]

Previous resonant two-photon ionization spectra collected in this group have provided the first spectroscopic characterizations of gas phase diatomic NiSi,[23] PdSi,[24] and RuSi,[25] and have identified two excited states of PtSi.[26] In this chapter these investigations are extended to IrSi, providing the first spectroscopic observation of this molecule.

4.2 Experimental

In the present study, diatomic IrSi was investigated using resonant two-photon ionization spectroscopy (R2PI). The instrument employed in this work is identical to that used in many previous studies,[23-26] and is therefore only briefly described. Diatomic IrSi is produced by focusing the third harmonic radiation from a Q-switched Nd:YAG laser (355 nm, 6-8 mJ/pulse, measured at the sample) onto an Ir sample in the throat of a pulsed supersonic expansion of helium (160 psi backing pressure) that is seeded with 0.05% SiH_4. Higher concentrations of silane proved ineffective in making the diatomic IrSi molecule. The sample is in the form of a disk that is rotated and translated to maintain a nearly constant concentration of IrSi in the molecular beam, and to avoid drilling a hole into the sample. The carrier gas and products of ablation flow down a 1 mm channel for approximately 1.3 cm prior to supersonic expansion. After supersonic expansion, the molecular beam passes through a skimmer (50° inside angle, 1 cm

diameter) that provides a roughly collimated beam in the second chamber, which is the ionization region of a reflectron time-of-flight mass spectrometer.[27]

In the second chamber, the molecular beam is exposed to unfocussed radiation emitted by a Nd:YAG pumped dye laser that is counterpropagated along the molecular beam axis. After a few tens of nanoseconds, the unfocused output radiation of an ArF excimer laser (193 nm) is directed across the molecular beam axis at right angles. Neither wavelength is capable of ionizing the molecule in a one-photon process, but the absorption of one dye laser photon and one ArF photon can ionize the molecule. The resulting ions are accelerated in a two-stage Wiley-McLaren ion extraction assembly[28] and travel up a flight tube to a microchannel plate. The output signal is then preamplified (350 MHz) and digitized for processing in a personal computer. By recording the signal for specific masses of interest as a function of the dye laser wavenumber, the spectra for those species are obtained.

To reveal the rotational structure of the observed vibronic bands, an air-spaced intracavity étalon is inserted into the dye laser, which is then pressure scanned using SF_6. For calibration, a portion of the dye laser output radiation is sent through a cell containing room temperature I_2 vapor. For transitions to the blue of 20 000 cm^{-1}, a heated cell containing $^{130}Te_2$ is used. Another portion of the output radiation is sent through a 0.22 cm^{-1} free spectral range étalon. The transmitted intensities are recorded and are used to provide an absolute calibration of the spectrum using the precisely known wavenumbers taken from the I_2 or $^{130}Te_2$ atlas.[29-31] Because in our instrument the IrSi molecules travel at the beam velocity of helium (1.77×10^5 cm/s)[32] toward the dye laser, a small correction for the Doppler shift experienced by the molecules is required. At the same

time, a correction for the error in the I_2 atlas (-0.0056 cm^{-1}) is also made.[33] Together, these corrections amount to less than 0.15 cm^{-1} for all of the bands reported here.

Excited state lifetimes were also measured for the bands that were rotationally resolved. This was accomplished by firing the ionization laser at the time of greatest IrSi signal intensity, and monitoring the $IrSi^+$ ion signal as the dye laser was scanned in time. The measured ion signal as a function of delay time was then fitted to an exponential decay curve using the Marquardt nonlinear least-squares algorithm.[34]

4.3 Results

4.3.1 Low Resolution Spectrum

Spectra of both $^{191}Ir^{28}Si$ (34.4% natural abundance) and $^{193}Ir^{28}Si$ (57.8%) were recorded over the range from 17 220 to 23 825 cm^{-1}, resulting in the observation of 207 vibronic bands. A portion of the low-resolution spectrum of $^{193}Ir^{28}Si$ is displayed in Figure 4.1, illustrating the high density of vibronic bands observed in this molecule. Progressions of bands belonging to the same electronic state were identified by finding bands of similar intensity separated by nearly constant intervals, ultimately allowing 107 of the more intense bands to be grouped into transitions to 14 excited electronic states. These excited states were labeled as the A through N electronic states.

To identify hot bands in the spectrum, the band difference histogram method was employed.[35, 36] The method works best when a dense vibronic spectrum is observed, and has been successfully applied in this research group to ZrF,[36] ZrCl,[36] and ZrFe.[35] First, band heads are measured and compiled into a list, in the case of IrSi amounting to 207 heads. Then, differences between all measured band heads are calculated and compiled into a much larger list (21 321 differences for IrSi). For each measured band head

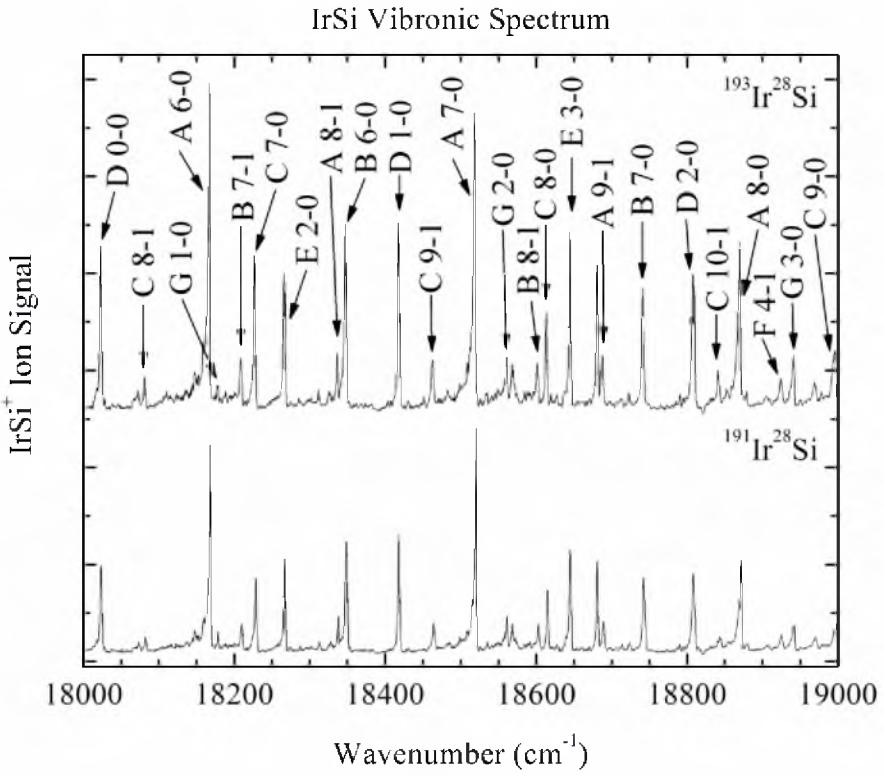

Figure 4.1 Vibronically resolved spectrum of $^{193}Ir^{28}Si$, over the 18 000-19 000 cm^{-1} range. In this range, bands from the A-X, B-X, C-X, D-X, E-X, F-X, and G-X systems have been identified.

difference, a Gaussian function is constructed with a height of unity and a width of 1 cm^{-1}, centered on the band head difference frequency. The Gaussians are then summed to generate a continuous function that can be plotted and further investigated. Since all hot bands are separated from their corresponding cold band by the fixed vibrational interval, $\Delta G_{1/2}''$, ignoring the small differences between band heads and band origins, the Gaussians corresponding to cold band-hot band differences add in phase and lead to an easily identifiable peak in the band difference histogram plot. This is illustrated in Figure 4.2 for $^{193}Ir^{28}Si$, where the value of $\Delta G_{1/2}''$ is identified as 533.4 cm^{-1}. When the corresponding plot was constructed for $^{191}Ir^{28}Si$, which was separately monitored in the mass spectrum, the peak was found at 534.0 cm^{-1}, close to the expected value based on the molecular reduced masses of 533.75 cm^{-1}. Based on this correspondence, we believe the value of $\Delta G_{1/2}''$ is accurate to better than 1 cm^{-1}.

To assign vibrational numbers to the observed vibrational progressions, we attempted to use the isotope shifts between the band heads of $^{191}Ir^{28}Si$ and $^{193}Ir^{28}Si$, but the measurements obtained from the low-resolution spectra were not sufficiently accurate. The bands that were investigated in high resolution mode, however, provided accurate isotope shifts that were quite helpful in assigning vibrational numbers. The method employed was to assume a vibrational numbering and fit the band origins of $^{193}Ir^{28}Si$ to the expression[37]

$$\nu_{v'-0} = T_0 + \upsilon' \omega_e' - (\upsilon'^2 + \upsilon') \omega_e' x_e'. \qquad (4.1)$$

The fitted spectroscopic constants ω_e' and $\omega_e' x_e'$ could then be used to calculate the predicted isotope shift using the formula[37]

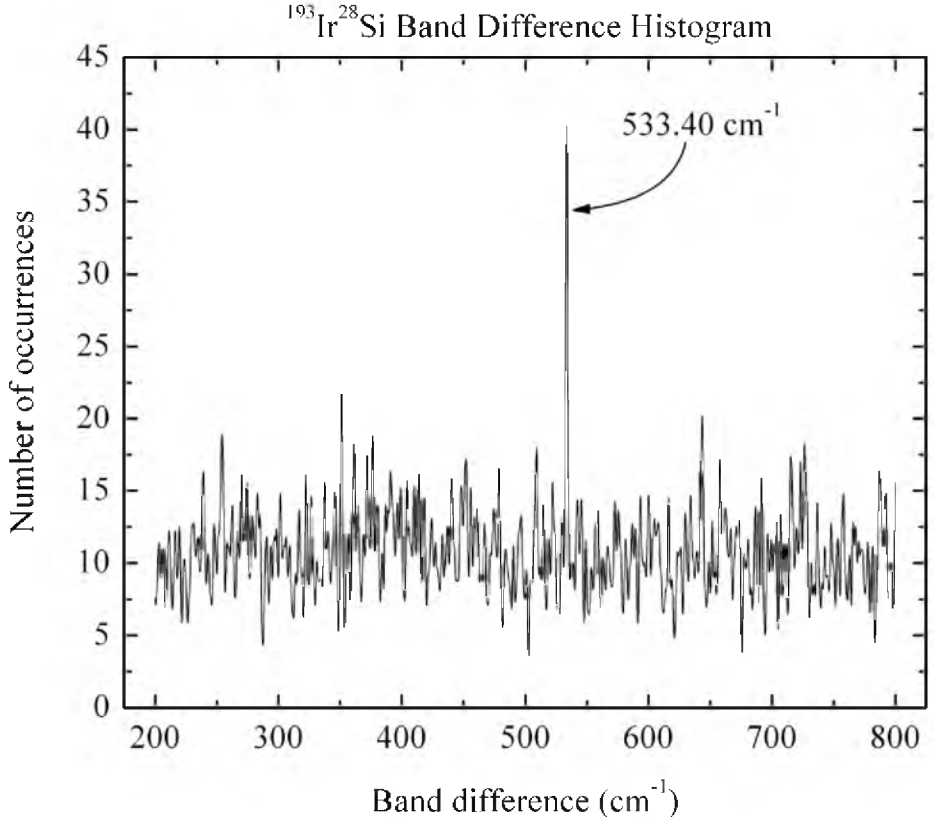

Figure 4.2 Band difference histogram plot for $^{193}Ir^{28}Si$, showing the constructive accumulation of band differences at 533.4 cm^{-1}, which is identified as $\Delta G_{1/2}''$ for this isotopic combination.

$$\nu(^{191}Ir^{28}Si) - \nu(^{193}Ir^{28}Si) =$$

$$(\rho\text{-}1)[\omega_e'(\upsilon'+½)-\omega_e''(½)]-(\rho^2\text{-}1)[\omega_e'x_e'(\upsilon'+½)^2-\omega_e''x_e''(½)^2\,], \qquad (4.2)$$

where the dimensionless parameter, ρ, is given as $\rho = \sqrt{\frac{\mu(^{193}Ir^{28}Si)}{\mu(^{191}Ir^{28}Si)}} = 1.000664.$ By treating equations (1) and (2) as functions of a continuous parameter, υ′, it was possible to plot the predicted isotope shift, $\nu(^{191}Ir^{28}Si) - \nu(^{193}Ir^{28}Si)$, as a function of the band frequency, $\nu_{v'\text{-}0}$, for various assignments of the bands. The resulting curves were then compared to the measured isotope shifts to identify the correct vibrational numbering. To do so, the ground state vibrational frequency, ω_e'' was taken as 533 cm^{-1} from the band difference histogram result, and the anharmonicity, $\omega_e''x_e''$, was neglected. An example of the results of this method is provided in Figure 4.3 for the B-X system. In general, this method provided a reliable vibrational assignment, although in some cases there is a possibility that the assignment could be in error by ±1 unit. Isotope shift plots for all of the band systems that were rotationally resolved are provided in appendix B for this chapter.

4.3.2 Rotationally Resolved Spectra

Rotationally resolved investigations allowed the Ω values of the ground and excited states to be determined from the first lines in the spectra, and allowed the rotational constants B′ and B″ to be determined from fits to the expression[37]

$$\nu = \nu_0 + B'J'(J'+1) - B''J''(J''+1). \qquad (4.3)$$

All of the bands examined for which the first R line could be determined had R(2.5) as the first line, implying that Ω″=2.5. Further, all of the fitted bands had the same value of

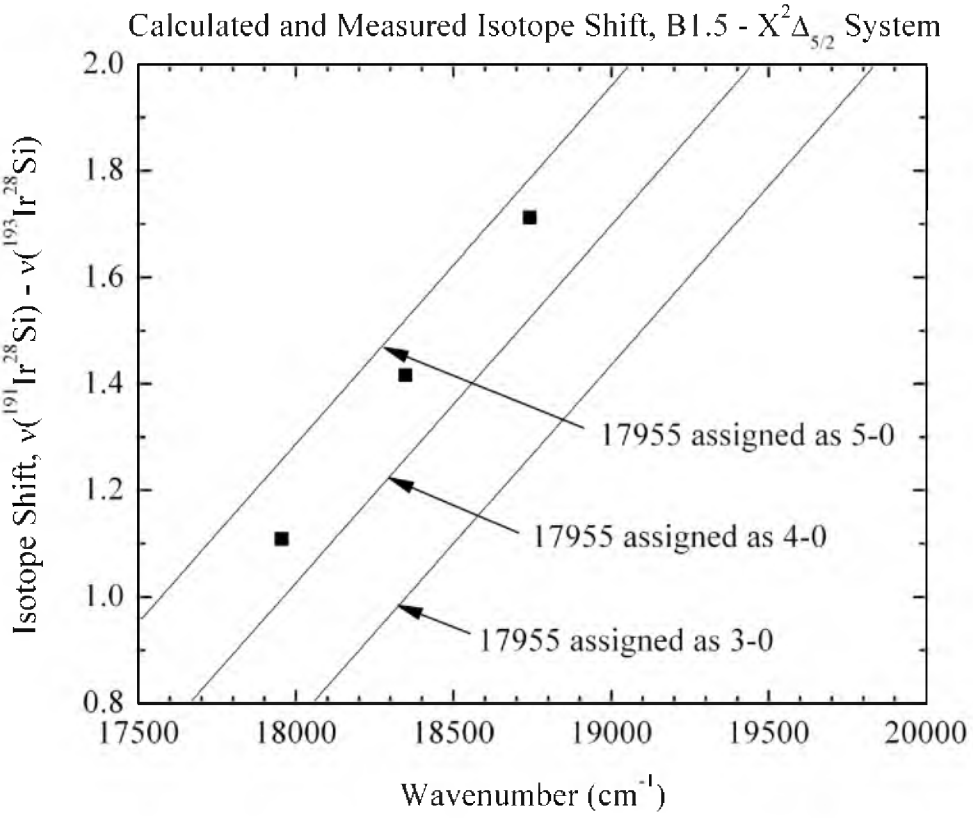

Figure 4.3 Isotope shift plot for the B-X system. Based on this plot, we believe the 17955 cm^{-1} band is the 5-0 band, but it is possible that it is the 4-0 band. Some of the other isotope shift plots for other band systems are more definitive, but this plot is not atypical.

B″. These facts establish that all 31 rotationally resolved bands originate from the same lower level, which must be the ground vibronic level of the molecule. Given that the only reasonable candidates for the ground state are the $1\sigma^2\ 1\pi^4\ 2\sigma^2\ 1\delta^4 3\sigma^1, {}^2\Sigma^+$ and $1\sigma^2\ 1\pi^4\ 2\sigma^2\ 1\delta^3\ 3\sigma^2, {}^2\Delta_{5/2}$ states, the determination that $\Omega''=2.5$ establishes the ground state as $1\sigma^2\ 1\pi^4\ 2\sigma^2\ 1\delta^3\ 3\sigma^2, {}^2\Delta_{5/2}$.

Excited states were observed with all three of the values of Ω' that are allowed in transitions from an $\Omega''=2.5$ level, namely $\Omega' = 1.5$, 2.5, and 3.5. In most cases, the first lines of the Q and P branches were observed and this enabled Ω' to be deduced; in a few cases, the determination of Ω' was based on the observed branch intensities. It is well-known that in cases of heterogeneous perturbations, branch intensities can be misleading.[38] In IrSi, however, the small value of B′ (typically close to 0.14 cm^{-1}) implies that a perturber would have to lie within a few cm^{-1} of the state in order to appreciably mix and distort the branch intensities. Therefore, we believe that the branch intensities generally provide a reliable determination of Ω' for IrSi.

Figures 4.4, 4.5, and 4.6 display rotationally resolved spectra for the 4-0 band of the A[16.0]3.5-$X^2\Delta_{5/2}$ system ($\Omega'=3.5$), the 0-0 band of the K[21.1]2.5-$X^2\Delta_{5/2}$ system ($\Omega'=2.5$), and the 7-0 band if the B[16.0]1.5-$X^2\Delta_{5/2}$ system ($\Omega'=1.5$), respectively. These illustrate the differences in branch intensities that are observed. The A-X system, exemplified by the band displayed in Figure 4.4, exhibits a particularly intense R branch, a strong Q branch beginning at Q(3.5) and extending to high J, and a weak P branch beginning at P(4.5). All of these are characteristic features of an $\Omega'=3.5 \leftarrow \Omega''=2.5$ transition. In contrast, the K-X system, exemplified by the band shown in Figure 4.5, has a Q branch that begins at Q(2.5) but which

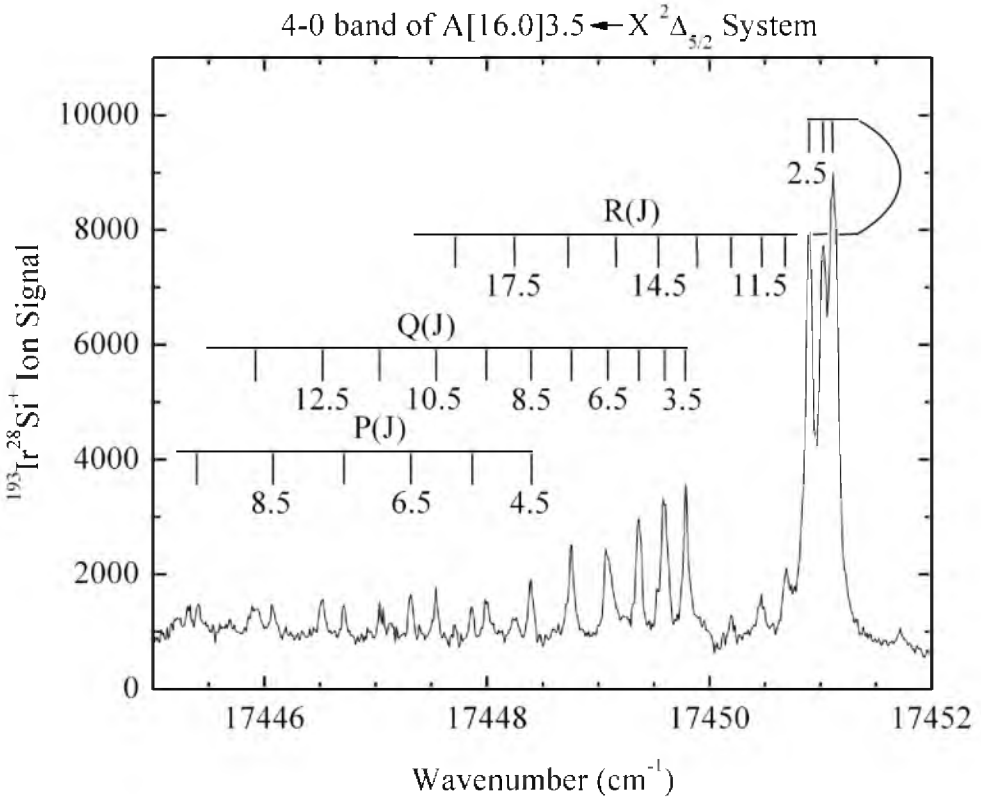

Figure 4.4 Rotationally resolved spectrum of the 4-0 band of the A[16.0]3.5 ← $X^2\Delta_{5/2}$ system.

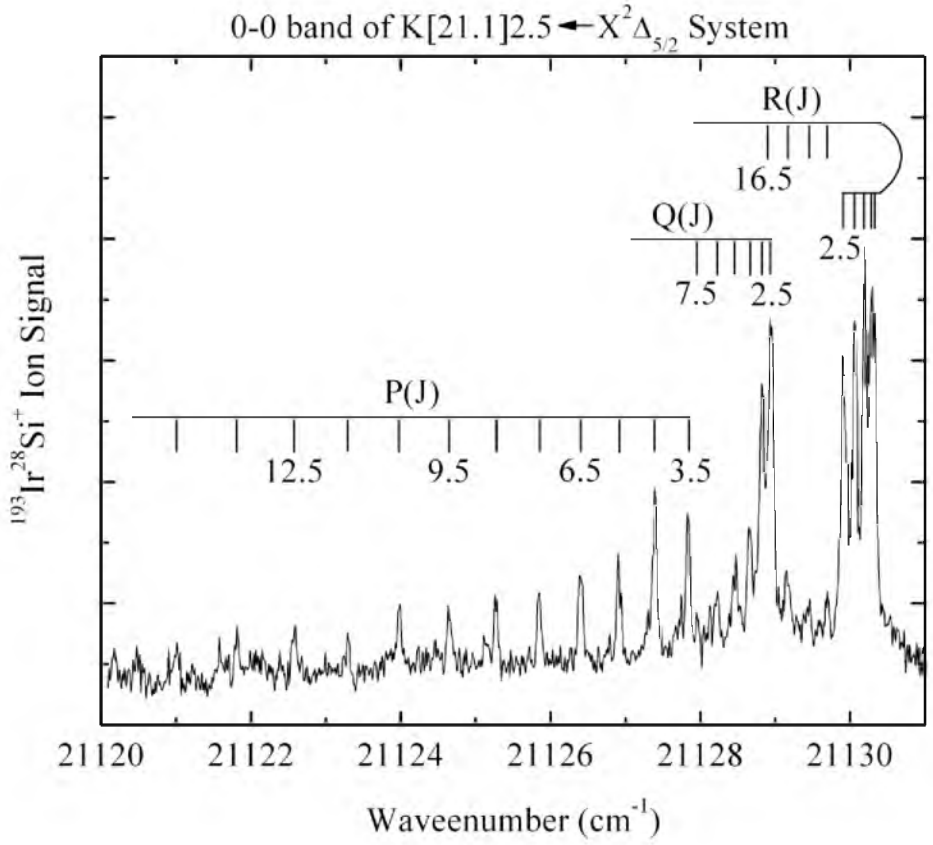

Figure 4.5 Rotationally resolved spectrum of the 0-0 band of the K[21.1]2.5 ← $X^2\Delta_{5/2}$ system.

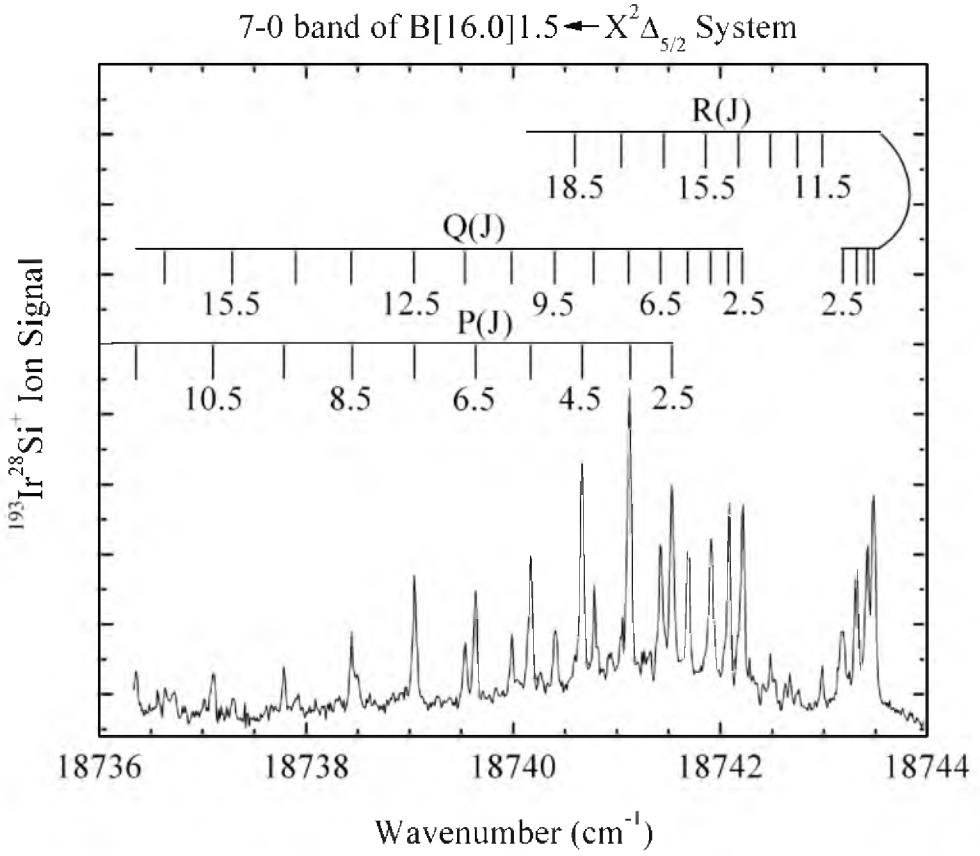

Figure 4.6 Rotationally resolved spectrum of the 7-0 band of the B[16.0]1.5 ← $X^2\Delta_{5/2}$ system.

rapidly diminishes in intensity, a P branch that begins at P(3.5) and proceeds to higher J with similar intensities as the R branch, which begins with R(2.5). These are characteristic of an $\Omega'=2.5 \leftarrow \Omega''=2.5$ transition. In this figure, the R branch appears stronger than the P branch because of overlapping returning R lines. Finally, the B-X system, exemplified by the band shown in Figure 4.6, displays the characteristics expected for an $\Omega'=1.5 \leftarrow \Omega''=2.5$ transition: first lines of R(2.5), Q(2.5), and P(2.5), with strong P and Q branches and a significantly weaker R branch. Analyses of the other rotationally resolved bands established the values of Ω' for all of the rotationally resolved band systems.

With 107 bands grouped into 14 band systems, of which 31 bands have been rotationally resolved and analyzed, it is impossible to present any significant fraction of the data in the body of this chapter. Instead, in Table 4.1 a summary of the results is presented for the various band systems and direct the interested reader to Appendix B for further details.

4.3.3 Comments Regarding Specific Electronic States

This work establishes the ground state of IrSi as having $\Omega=2.5$, with $r_0 = 2.090$ Å (1σ error limit is less than 0.001 Å) and $\Delta G_{1/2} = 533$ cm^{-1}. This is undoubtedly the $^2\Delta_{5/2}$ state that is calculated and is found to be the ground state in the isovalent IrC[39-42] and OsN[43, 44] molecules.

All of the excited electronic states that are observed have bond lengths that are significantly lengthened as compared to the ground state, and vibrational frequencies that are significantly reduced. Moving either a nonbonding 3σ or 1δ electron into the antibonding 2π orbital or moving a bonding 1π electron into the nonbonding 1δ orbital

Table 4.1 Fitted spectroscopic constants for the observed band systems of $^{193}Ir^{28}Si$

State	Ω	T_0 (cm^{-1})	r_e(Å)	ω_e (cm^{-1})	$\omega_e x_e$ (cm^{-1})	τ(μs)
$X\ ^2\Delta_{5/2}$	2.5	0	r_0= 2.090	$\Delta G_{1/2}$ = 533	---	---
A[16.0]3.5	3.5	16007(14)	2.244(14)	365.8(4.7)	0.7(3)	2.6
B[16.0]1.5	1.5	16001	2.210(2)	389	-0.38	1.30
C[15.4]1.5	1.5	15399	r_7 = 2.232	421	2.15	5
D[18.0]1.5	1.5	18024.3(2.5)	2.187(3)	393(5)	-0.14(1.3)	6
E[17.5]1.5	1.5	17493	r_2=2.200	397	3.0	8.5
F[17.8]1.5	1.5	17845	2.169(1)	403		6
G[17.8]2.5	2.5	17793	r_4=2.269	389	1.58	---
H	---	<19900	---	>399	1.2	---
I	---	<19615	---	>421	1.1	---
J[20.9]3.5	3.5	20946.5793(8)	2.2038(2)	416.976(2)	1.730	6.4
K[21.1]2.5	2.5	21129.08	2.2156(2)	393.5	1.640	2.62
L[22.1]2.5	2.5	22122.66	2.1913(3)	452.07		2.4
M[21.2]1.5	1.5	21192	r_2=2.238	363	0.1	2.24
N[23.3]2.5	2.5	23347.86	2.1956(3)	$\Delta G_{1/2}$= 433.64		0.82

results in the lengthening of the bond. Consequently, the bond order of the molecule is reduced by roughly 0.5 in the electronic excitation. For a few of the excited states, a bonding 2σ or 1π electron is moved into the 2π antibonding orbital, reducing the bond order by roughly 1, again lengthening the bond and reducing the vibrational frequency. The resulting excited configurations generate a large number of states that are optically allowed in transitions from the $X\,^2\Delta_{5/2}$ ground state, as shown in Table 4.2. Indeed, the states generated by excitations of a nonbonding 3σ or 1δ electron into the antibonding 2π orbital generate 7 Ω'=1.5, 6 Ω'=2.5, and 4 Ω'=3.5 states.

Due to time restrictions and the diminishing returns associated with further work on this project, limitations exist in our knowledge of some of the excited electronic states that were observed. These are discussed briefly here. Here we identify the upper states by letter (A, B, C, *etc.*), followed by [T_0/1000] and the value of Ω' for the state. In a system in which spin-orbit mixing can be quite extensive, this system of nomenclature is useful and unambiguous.

4.3.3.1 The A[16.0]3.5 state

The vibrational numbering of this state is slightly uncertain. It is possible that v′ should be decreased by one unit. The revised values would then be: T_0 = 16370 cm^{-1}, ω_e=363 cm^{-1}, $\omega_e x_e$ = 0.7 cm^{-1}, and r_e = 2.247 Å. The measured upper state lifetimes drop smoothly with increasing v′: τ(v′=4) = 2.84(12) μs; τ(v′=5) = 2.63(4) μs; τ(v′=6) = 2.45(16) μs; and τ(v′=7) = 2.30(19) μs. If this state fluoresces exclusively to the ground state, these lifetimes imply an absorption oscillator strength of $f \approx 0.002$.

Table 4.2 Ground and excited electronic configurations and states of IrSi

	Configuration	Λ-S States	Λ-S-Ω Levels	Allowed Ω levels
Ground	$1\sigma^2\ 1\pi^4\ 2\sigma^2\ 1\delta^3\ 3\sigma^2$	$^2\Delta$	$^2\Delta_{5/2}$, $^2\Delta_{3/2}$	
$3\sigma\rightarrow1\delta$	$1\sigma^2\ 1\pi^4\ 2\sigma^2\ 1\delta^4\ 3\sigma^1$	$^2\Sigma^+$	$^2\Sigma^+_{1/2}$	
$3\sigma\rightarrow2\pi$	$1\sigma^2\ 1\pi^4\ 2\sigma^2\ 1\delta^3\ 3\sigma^1\ 2\pi^1$	$^2\Pi(2)$, $^4\Pi$, $^2\Phi(2)$, $^4\Phi$	$^2\Pi_{3/2}(2)$, $^2\Pi_{1/2}(2)$, $^4\Pi_{5/2}$, $^4\Pi_{3/2}$, $^4\Pi_{1/2}$, $^4\Pi_{-1/2}$, $^2\Phi_{7/2}(2)$, $^2\Phi_{5/2}(2)$, $^4\Phi_{9/2}$, $^4\Phi_{7/2}$, $^4\Phi_{5/2}$, $^4\Phi_{3/2}$	1.5 (4) 2.5 (4) 3.5 (3)
$1\delta\rightarrow2\pi$	$1\sigma^2\ 1\pi^4\ 2\sigma^2\ 1\delta^2\ 3\sigma^2\ 2\pi^1$	$^2\Pi(2)$, $^2\Phi$, ^2H, $^4\Pi$	$^2\Pi_{3/2}(2)$, $^2\Pi_{1/2}(2)$, $^2\Phi_{7/2}$, $^2\Phi_{5/2}$, $^2H_{11/2}$, $^2H_{9/2}$, $^4\Pi_{5/2}$, $^4\Pi_{3/2}$, $^4\Pi_{1/2}$, $^4\Pi_{-1/2}$	1.5 (3) 2.5 (2) 3.5 (1)
$1\pi\rightarrow1\delta$	$1\sigma^2\ 1\pi^3\ 2\sigma^2\ 1\delta^4\ 3\sigma^2$	$^2\Pi$	$^2\Pi_{3/2}$, $^2\Pi_{1/2}$	1.5 (1)
$2\sigma\rightarrow2\pi$	$1\sigma^2\ 1\pi^4\ 2\sigma^1\ 1\delta^3\ 3\sigma^2\ 2\pi^1$	$^2\Pi(2)$, $^4\Pi$, $^2\Phi(2)$, $^4\Phi$	$^2\Pi_{3/2}(2)$, $^2\Pi_{1/2}(2)$, $^4\Pi_{5/2}$, $^4\Pi_{3/2}$, $^4\Pi_{1/2}$, $^4\Pi_{-1/2}$, $^2\Phi_{7/2}(2)$, $^2\Phi_{5/2}(2)$, $^4\Phi_{9/2}$, $^4\Phi_{7/2}$, $^4\Phi_{5/2}$, $^4\Phi_{3/2}$	1.5 (4) 2.5 (4) 3.5 (3)
$1\pi\rightarrow2\pi$	$1\sigma^2\ 1\pi^3\ 2\sigma^2\ 1\delta^3\ 3\sigma^2\ 2\pi^1$	$^2\Sigma^+(2)$, $^2\Sigma^-(2)$, $^2\Delta(4)$, $^2\Gamma(2)$, $^4\Sigma^+$, $^4\Sigma^-$, $^4\Delta(2)$, $^4\Gamma$	$^2\Sigma^+_{1/2}(2)$, $^2\Sigma^-_{1/2}(2)$, $^2\Delta_{3/2}(4)$, $^2\Delta_{5/2}(4)$, $^2\Gamma_{7/2}(2)$, $^2\Gamma_{9/2}(2)$, $^4\Sigma^+_{3/2}$, $^4\Sigma^+_{1/2}$, $^4\Sigma^-_{3/2}$, $^4\Sigma^-_{1/2}$, $^4\Delta_{1/2}(2)$, $^4\Delta_{3/2}(2)$, $^4\Delta_{5/2}(2)$, $^4\Delta_{7/2}(2)$, $^4\Gamma_{5/2}$, $^4\Gamma_{7/2}$, $^4\Gamma_{9/2}$, $^4\Gamma_{11/2}$	1.5 (8) 2.5 (7) 3.5 (5)

4.3.3.2 The B[16.0]1.5 state

It is possible that v′ should be decreased by one unit for this state. The revised values would then be: T_0 = 16390 cm^{-1}, ω_e=389 cm^{-1}, $\omega_e x_e$ = -0.38 cm^{-1}, and r_e = 2.213 Å. Excited state lifetimes increase with increasing v′: τ(v′=5) = 1.16(6) μs; τ(v′=6) = 1.26(2) μs; and τ(v′=7)= 1.49(6) μs. If this state fluoresces exclusively to the ground state, these lifetimes imply an absorption oscillator strength of $f \approx 0.004$.

4.3.3.3 The C[15.4]1.5 state

It is possible that v′ should be decreased by one unit for this state. The revised values would then be: T_0 = 15816 cm^{-1}, ω_e= 417 cm^{-1}, and $\omega_e x_e$ = 2.15 cm^{-1}. Measured excited state lifetimes are τ(v′=6) = 6.17(10) μs and τ(v′=7) = 4.20(13) μs. If this state fluoresces exclusively to the ground state, these lifetimes imply an absorption oscillator strength of $f \approx 0.001$.

4.3.3.4 The D[18.0]1.5 state

It is possible that v′ should be increased by one unit for this state. The revised values would then be: T_0 = 17632 cm^{-1}, ω_e=392 cm^{-1}, $\omega_e x_e$ = -0.135 cm^{-1} and r_e = 2.181 Å. The D state lifetimes generally increase with v′: τ(v′=0) = 5.23(20) μs; τ(v′=1) = 5.24(21) μs; τ(v′=2) = 6.57(13) μs; and τ(v′=3) = 8.83(21) μs. If this state fluoresces exclusively to the ground state, these lifetimes imply an absorption oscillator strength of $f \approx 0.0008$.

4.3.3.5 The E[17.5]1.5 state

It is possible that v′ should be decreased or increased by one unit for this state. The revised values would then be: T_0 = 17884 cm^{-1}, ω_e=390 cm^{-1}, and $\omega_e x_e$ = 3 cm^{-1} or T_0

= 17097 cm^{-1}, ω_e=403 cm^{-1}, and $\omega_e x_e$ = 3 cm^{-1}, respectively. The measured lifetimes are $\tau(v'=2)$ = 8.50(23) μs and $\tau(v'=3)$ = 8.42(74) μs. If this state fluoresces exclusively to the ground state, these lifetimes imply an absorption oscillator strength of $f \approx 0.0006$.

4.3.3.6 The F[17.8]1.5 state

The vibrational numbering of this state and the associated constants seem to be correct. The lifetime of the v'=3 level is $\tau(v'=3)$ = 6.00(20) μs. If this state fluoresces exclusively to the ground state, this lifetime implies an absorption oscillator strength of $f \approx 0.0008$.

4.3.3.7 The G[17.8]2.5 state

The vibrational numbering of this state is slightly uncertain. It is possible that v' should be decreased or increased by one unit. The revised values would then be: T_0 = 18179 cm^{-1}, ω_e=386 cm^{-1}, and $\omega_e x_e$ = 1.58 cm^{-1} or T_0 = 17403 cm^{-1}, ω_e=393 cm^{-1}, and $\omega_e x_e$ = 1.58 cm^{-1}. The value of r_4 listed is the expectation value $\langle 1/r^2 \rangle^{-1/2}$ for the v=4 level.

4.3.3.8 The H state

We have not rotationally resolved any of the bands of the H state, so the vibrational numbering could be wrong. Also, we do not know the value of Ω for this state.

4.3.3.9 The I state

None of the bands of the I state have been rotationally resolved, so the vibrational numbering could be wrong. Again, the value of Ω for this state is unknown.

4.3.3.10 The J[20.9]3.5, K[21.1]2.5, L[22.1]2.5, and N[23.3]2.5 states

The vibrational numbering of these states and the associated constants are definite. The excited state lifetimes for the J[20.9]3.5 state decrease with increasing v′: $\tau(v'=0) = 7.25(30)$ μs; $\tau(v'=1) = 6.39(24)$ μs; $\tau(v'=2) = 6.11(5)$ μs; and $\tau(v'=3) = 5.72(28)$ μs. If this state fluoresces exclusively to the ground state, these lifetimes imply an absorption oscillator strength of $f \approx 0.0005$. The excited state lifetimes of the K[21.1]2.5 state show a slight increase with increasing v′: $\tau(v'=0) = 2.38(16)$ μs; $\tau(v'=1) = 2.61(6)$ μs; $\tau(v'=2) = 2.59(1)$ μs; $\tau(v'=3) = 2.79(14)$ μs; and $\tau(v'=4)=2.75(4)$ μs. If this state fluoresces exclusively to the ground state, these lifetimes imply an absorption oscillator strength of $f \approx 0.001$. Excited state lifetimes of the L[22.1]2.5 state are $\tau(v'=0) = 2.06(5)$ μs and $\tau(v'=2) = 2.66(9)$ μs. If this state fluoresces exclusively to the ground state, these lifetimes imply an absorption oscillator strength of $f \approx 0.001$. Excited state lifetimes of the N[23.3]2.5 state are quite short compared to the other states investigated in this work: $\tau(v'=0) = 0.93(2)$ μs and $\tau(v'=1) = 0.71(16)$ μs. If this state fluoresces exclusively to the ground state, these lifetimes imply an absorption oscillator strength of $f \approx 0.003$.

4.3.3.11 The M[21.1]1.5 state

The vibrational numbering is a bit uncertain; it is possible that v′ should be increased by one unit. This would result in new values of $T_0 = 20829$ cm^{-1}, $\omega_e=363$ cm^{-1}, and $\omega_e x_e = -0.135$ cm^{-1}. Excited state lifetimes drop slightly with increasing v′: $\tau(v'=1) = 2.38(8)$ μs; $\tau(v'=2) = 2.23(9)$ μs; and $\tau(v'=3) = 2.10(18)$ μs. If this state fluoresces exclusively to the ground state, these lifetimes imply an absorption oscillator strength of $f \approx 0.001$.

4.4 Discussion and Conclusion

In this experimental study, we report the first spectroscopic investigation of diatomic IrSi. The molecule is found to have a triple bond, which is consistent with its high measured (4.76±0.22 eV)[8] and previously calculated (4.98 eV)[45] bond dissociation energy. The ground state is well-described as a single configuration $1\sigma^2\ 1\pi^4\ 2\sigma^2\ 1\delta^3\ 3\sigma^2$, $^2\Delta_{5/2}$ state. This ground term is consistent with that found for the isovalent IrC[40-42, 46] and OsN[43, 44] molecules, but differs from the $^2\Sigma^+$ ground term of the isovalent 4d molecules RhC,[47-49] RhSi,[50] and RuN.[51] The emergence of $^2\Delta_{5/2}$ as the ground level of the 5d molecules IrC, IrSi, and OsN results from two effects. First, the relativistic stabilization of the 6s orbital causes the 3σ orbital to lie much lower in energy in the 5d metal molecules, causing it to be doubly-occupied in the ground state. Second, these heavy metal atoms have large spin-orbit constants for the 5d orbitals, with ζ_{5d}(Os) and ζ_{5d}(Ir) tabulated as 3045 and 3617 cm^{-1}, respectively.[38] In contrast, the corresponding constants for Ru and Rh are 1038 cm^{-1} and 1253 cm^{-1}, respectively.[38] The spin-orbit interaction stabilizes the Ω=5/2 component of the $^2\Delta$ state by approximately ζ_{nd}, which is a more significant effect in the 5d molecules than in the 4d molecules.

Diatomic IrSi exhibits strong similarities to its neighbor in the periodic table, PtSi. The bond length of PtSi (r_0 = 2.063 Å)[26] is only slightly smaller than that of IrSi (r_0 = 2.090 Å). Similarly, the measured bond energies of PtSi (5.15 ± 0.19 eV) and IrSi (4.76 ±0.22 eV) are quite strong and similar in magnitude.[8] Both PtSi[52] and IrSi are triply-bonded, with one σ bond and two π bonds. The additional electron in PtSi goes into the nonbonding 1δ orbital, resulting in a ground state of $^1\Sigma^+$ symmetry and a much simpler optical spectrum than is found for IrSi.

4.5 References

1 J. Kurianski, J. Van Damme, J. Vermeiren, K. Maex, and C. Claeys, Proc. SPIE-Int. Soc. Opt. Eng. **1308,** 27-35 (1990).

2 J. L. Gates, W. G. Connelly, T. D. Franklin, R. E. Mills, F. W. Price, and T. Y. Wittwer, Proceedings of SPIE - International Society of Optical Engineering **1540,** 262-73 (1991).

3 X. Ma, Thin Solid Films **484,** 257-60 (2005).

4 Y. J. Hu, ((Micron Technology, Inc., USA), Application: US US, 2001), pp. 7 pp.

5 J. E. Kingcade, Jr. and K. A. Gingerich, J. Chem. Soc. Faraday Trans. 2 **85,** 195-200 (1989).

6 J. E. Kingcade, Jr. and K. A. Gingerich, J. Chem. Phys. **84,** 4574-8 (1986).

7 A. V. Auwera-Mahieu, N. S. McIntyre, and J. Drowart, Chem. Phys. Lett. **4,** 198-200 (1969).

8 A. Vander Auwera-Mahieu, R. Peeters, N. S. McIntyre, and J. Drowart, Trans. Faraday Soc. **66,** 809-16 (1970).

9 I. Shim, J. E. Kingcade, and K. A. Gingerich, Zeitschrift fur Physik D **7,** 261-9 (1987).

10 G. Riekert, P. Lamparter, and S. Steeb, Z. Metallkd. **72,** 765-8 (1981).

11 K. A. Gingerich, R. Haque, and J. E. Kingcade, Jr., Thermochim. Acta **30,** 61-71 (1979).

12 B. L. Kickel and P. B. Armentrout, J. Am. Chem. Soc. **117,** 4057-70 (1995).

13 B. L. Kickel and P. B. Armentrout, J. Am. Chem. Soc. **116,** 10742-50 (1994).

14 B. L. Kickel and P. B. Armentrout, J. Am. Chem. Soc. **117,** 764-73 (1995).

15 B. L. Kickel and P. B. Armentrout, J. Phys. Chem. **99,** 2024-32 (1995).

16 Y. M. Hamrick and W. Weltner, Jr., J. Chem. Phys. **94,** 3371-80 (1991).

17 J. J. Scherer, J. B. Paul, C. P. Collier, and R. J. Saykally, J. Chem. Phys. **102,** 5190-9 (1995).

[18] J. J. Scherer, J. B. Paul, C. P. Collier, and R. J. Saykally, J. Chem. Phys. **103,** 113-20 (1995).

[19] J. J. Scherer, J. B. Paul, C. P. Collier, A. O'Keefe, and R. J. Saykally, J. Chem. Phys. **103,** 9187-92 (1995).

[20] J. B. Paul, J. J. Scherer, C. P. Collier, and R. J. Saykally, J. Chem. Phys. **104,** 2782-8 (1996).

[21] Y. Lefebvre and J. Schamps, J. Mol. Spectrosc. **201,** 128-33 (2000).

[22] S. A. Cooke, M. C. L. Gerry, D. J. Brugh, and R. D. Suenram, J. Mol. Spectrosc. **223,** 185-94 (2004).

[23] N. F. Lindholm, D. J. Brugh, G. K. Rothschopf, S. M. Sickafoose, and M. D. Morse, J. Chem. Phys. **118,** 2190-6 (2003).

[24] A. Martinez, N. Lindholm, and M. D. Morse, J. Chem. Phys. **135,** 134308/1-8 (2011).

[25] N. Lindholm and M. D. Morse, J. Chem. Phys. **127,** 084317/1-5 (2007).

[26] L. Shao, S. M. Sickafoose, J. D. Langenberg, D. J. Brugh, and M. D. Morse, J. Chem. Phys. **112,** 4118-23 (2000).

[27] B. A. Mamyrin, V. I. Karataev, D. V. Shmikk, and V. A. Zagulin, Zh. Eksp. Teor. Fiz. **64,** 82-9 (1973).

[28] W. C. Wiley and I. H. McLaren, Rev. Sci. Instrum. **26,** 1150 - 7 (1955).

[29] S. Gerstenkorn and P. Luc, *Atlas du Spectre d'Absorption de la Molécule d'Iode entre 14,800-20,000 cm^{-1}* (CNRS, Paris, 1978).

[30] J. Cariou and P. Luc, *Atlas du Spectre d'Absorption de la Molécule Tellure, Partie 5: 21,100 - 23,800 cm^{-1}* (CNRS, Paris, 1980).

[31] J. Cariou and P. Luc, *Atlas du Spectre d'Absorption de la Molécule de Tellure entre 18,500 - 23,800 cm^{-1}* (CNRS, Paris, 1980).

[32] M. D. Morse, in *Methods of Experimental Physics: Atomic, Molecular, and Optical Physics*, Vol. II Atoms and Molecules, edited by F. B. Dunning and R. Hulet (Academic Press, Inc., Orlando, Florida, 1996), pp. 21-47.

[33] S. Gerstenkorn and P. Luc, Rev. Phys. Appl. **14,** 791-4 (1979).

[34] P. R. Bevington, *Data Reduction and Error Analysis for the Physical Sciences* (McGraw-Hill, New York, 1969).

[35] O. Krechkivska and M. D. Morse, J. Phys. Chem. A **117,** 992-1000 (2013).

[36] A. Martinez and M. D. Morse, J. Chem. Phys. **135,** 024308/1-10 (2011).

[37] G. Herzberg, *Molecular Spectra and Molecular Structure I. Spectra of Diatomic Molecules*, 2nd ed. (Van Nostrand Reinhold, New York, 1950).

[38] H. Lefebvre-Brion and R. W. Field, *The Spectra and Dynamics of Diatomic Molecules* (Elsevier, Amsterdam, 2004).

[39] K. Jansson, R. Scullman, and B. Yttermo, Chem. Phys. Lett. **4,** 188-90 (1969).

[40] K. Jansson and R. Scullman, J. Mol. Spectrosc. **36,** 248 - 67 (1970).

[41] T. Ma, J. W. H. Leung, and A. S. C. Cheung, Chem. Phys. Lett. **385,** 259-62 (2004).

[42] H. F. Pang and A. S. C. Cheung, Chem. Phys. Lett. **471,** 194-7 (2009).

[43] R. S. Ram, J. Liévin, and P. F. Bernath, J. Chem. Phys. **111,** 3449-56 (1999).

[44] M. A. Garcia and M. D. Morse, J. Chem. Phys. **135,** 114304/1-12 (2011).

[45] Z. J. Wu and Z. M. Su, J. Chem. Phys. **124,** 184306/1-/15 (2006).

[46] H. Tan, M. Liao, and K. Balasubramanian, Chem. Phys. Lett. **280,** 219-26 (1997).

[47] B. Kaving and R. Scullman, J. Mol. Spectrosc. **32,** 475 - 500 (1969).

[48] H. Tan, M. Liao, and K. Balasubramanian, Chem. Phys. Lett. **280,** 423-9 (1997).

[49] W. J. Balfour, S. G. Fougère, R. F. Heuff, C. X. W. Qian, and C. Zhou, J. Mol. Spectrosc. **198,** 393-407 (1999).

[50] A. G. Adam, A. D. Granger, W. J. Balfour, and R. Li, J. Mol. Spectrosc. **258,** 35-41 (2009).

[51] R. S. Ram, J. Liévin, and P. F. Bernath, J. Chem. Phys. **109,** 6329-37 (1998).

[52] M. Barysz and P. Pyykko, Chem. Phys. Lett. **368,** 538-41 (2003).

CHAPTER 5

ELECTRONIC SPECTROSCOPY AND ELECTRONIC STRUCTURE OF COPPER ACETYLIDE, CuCCH

5.1 Introduction

Organometallics and, more specifically, organocopper reagents[1, 2] are extremely useful in synthetic organic chemistry. Commonly, these reagents make use of the weak sigma bond that exists between the metal atom and an organic radical to activate the organic species for subsequent reactions. One of the earliest known organometallic reactions, the Grignard reaction, employs an alkyl- or aryl-magnesium halide to form carbon-carbon bonds, and has been used in organic synthesis since the early 1900s.[3] The Gilman reagent, a lithium diorganylcuprate(I) salt, $Li^+[R\text{-}Cu\text{-}R]^-$, reacts with organic halides, R′X, to form new carbon-carbon bonds as well, producing R-R′ compounds.[4] The Ullman reaction is another copper catalyzed reaction that has been used to homocouple two aryl iodides to form a biaryl compound.[5]

Copper acetylides, Cu-C≡C-R, are also frequently employed in synthetic organic chemistry. Despite the danger of explosion, a well-known hazard when acetylene comes into contact with copper, copper alloys, or copper(I) compounds, copper acetylides readily undergo the Castro-Stephens cross coupling reaction when combined with aryl halides, leading to a convenient synthesis of disubstituted alkynes.[6] This reaction was modified in 1973 by combining the copper (I) halide catalyst with a zerovalent palladium

catalyst in the Sonogashira cross coupling reaction.[7-10] In this synthetically useful reaction, a terminal acetylene is combined with an aryl or a vinyl halide to form an aryl or vinyl alkyne. The exact mechanism by which this reaction occurs is unknown, but it is thought that a copper acetylide, Cu-C≡C-R, is an important intermediate. Finally, the formation of copper acetylides has been show to be a useful test for acetylene in air, in concentrations as low as 10 ppb.[11] The goal of the present study is to develop an improved understanding of the electronic structure and spectroscopy of the synthetically important copper acetylides, concentrating on the simplest example, CuCCH.

There has been a great deal of spectroscopic work on metal acetylides, although most of this has involved the *s*-block metals. Unlike the metal cyanides NaCN and KCN,[12, 13] all of the known metal acetylides are linear molecules in the MCCH geometry. The alkaline earth acetylides MgCCH,[14-18] CaCCH,[19-28] and SrCCH[19, 29-31] have been studied extensively through optical spectroscopy and Fourier transform microwave and millimeter wave techniques. Although technically a lanthanide acetylide, YbCCH is more analogous to the alkaline earth acetylides, owing to the $4f^{14}\,6s^2$ closed shell structure of atomic Yb. This molecule has been studied by laser-induced fluorescence and resonant two-photon ionization methods.[32] Similarly, the closed d-subshell molecule, ZnCCH, which is also similar to the alkaline earth acetylides, has been studied by microwave and millimeter wave spectroscopy.[33] Fourier transform microwave studies of the alkali acetylides LiCCH,[34-36] NaCCH,[17, 34, 36, 37] and KCCH [34, 36] have also been reported. Among the *p*-block metals, AlCCH has been studied through matrix isolation,[38] optical[39] and FT microwave spectroscopy,[40] as well as through computational work.[41-43] Among the *d*-block metal acetylides, a Fourier transform microwave study of AgCCH

has been reported.[40] The Morse group has investigated CrCCH through the resonant two-photon ionization (R2PI) and laser induced fluorescence (LIF) techniques.[44] Finally, CuCCH has been studied by millimeter and submillimeter wave spectroscopy, establishing the ground state as $\tilde{X}\ ^1\Sigma^+$ and determining the rotational constants for several isotopologues and thereby, the bond lengths.[45] In this chapter the optical spectra of CuCCH in the blue region of the spectrum are reported, collected using the resonant two-photon ionization method.

5.2 Experimental

In the present work, copper acetylide, CuCCH, was investigated using resonant two-photon ionization spectroscopy (R2PI). The instrument employed is identical to that used in many previous studies.[46-49] The CuCCH molecule is produced by focusing the third harmonic radiation from a Q-switched Nd:YAG laser (355 nm, 3-6 mJ/pulse, measured at the sample) onto a copper sample in the throat of a pulsed supersonic expansion of helium (60-120 psig backing pressure) that is seeded with a small percentage of acetylene. The copper sample is a disk that is rotated and translated to prevent the ablation laser from drilling a hole in the sample. This provides a nearly constant concentration of CuCCH in the molecular beam. The metal-containing plasma then flows down a thermalization channel that is approximately 1.3 cm in length prior to expansion into vacuum. Following supersonic expansion into vacuum, the molecular beam is roughly collimated by a 1 cm diameter skimmer, which admits the molecules into a second chamber that houses the ionization region of a reflectron time-of-flight mass spectrometer.[50]

In the second chamber, the molecular beam is exposed to unfocussed radiation emitted by a Nd:YAG pumped dye laser that is counterpropagated along the molecular beam axis. After a delay of about 40 nanoseconds, the unfocused output radiation of an ArF or F_2 excimer laser is directed across the molecular beam axis at right angles. Neither wavelength is capable of ionizing the molecule in a one-photon process, but it was hoped that the absorption of one dye laser photon and one excimer laser photon could ionize the molecule. The resulting ions are accelerated in a two-stage Wiley-McLaren ion extraction assembly,[51] travel up a flight tube, and enter a reflectron[50] that reverses their motion and directs them down a second flight tube to a dual microchannel plate detector. The output signal is then preamplified and digitized for processing by a personal computer. By recording the signal for specific masses of interest as a function of the dye laser wavenumber, the spectra for those species are obtained. Experiments were conducted using both the ArF excimer (193 nm, 6.42 eV) and the F_2 excimer (157 nm, 7.87 eV) lasers for the ionization photon.

Initial attempts to produce CuCCH used helium carrier gas seeded with 5% acetylene and used a 1 mm diameter thermalization channel. Although the vaporization laser power, vaporization timing relative to the gas pulse, backing pressure, nozzle voltage, and pulse duration were varied, CuCCH could not be detected in the mass spectrum, even at the highest available excimer laser fluences. A new vaporization block was constructed and installed with a 5 mm diameter channel and expansion orifice, and this was used with the 5% acetylene in helium gas mixture. With the larger diameter channel, CuCCH was detected in the mass spectrum with considerable intensity. After optimizing the molecular signal, the excimer laser intensity was reduced in order to

decrease the nonresonant 2-photon ionization signal due to this wavelength alone, and low-resolution survey scans were collected. Attempts to rotationally resolve the observed vibronic transitions were unsuccessful, however, due to the high rotational temperature obtained with the large diameter expansion orifice.

The key to resolving the rotational structure of the observed vibronic transitions was to rotationally cool the molecule. This increases the population in the low J levels, making the lines more intense, while at the same time preventing returning R and Q lines from overlapping with P lines and increasing the spectral congestion. By reinstalling the 1 mm diameter channel, diluting the concentration of the acetylene to 0.0013%, and increasing the backing pressure to 140 psig, the molecular signal was once again detected weakly in the mass spectrum. The low rotational temperature obtained with the smaller expansion orifice then permitted rotationally resolved spectra to be recorded.

To reveal the rotational structure of the bands, an air-spaced intracavity étalon was inserted into the dye laser, which was then pressure scanned using SF_6. Calibration of the rotationally resolved spectra was accomplished by simultaneously collecting a $^{130}Te_2$ absorption spectrum and comparing the line positions to the $^{130}Te_2$ atlas of Cariou and Luc.[52] A correction for the Doppler shift experienced by the molecules as they approach the dye laser radiation source at the beam velocity of helium (1.77×10^5 cm/s)[53] was included in all measured line positions.

Excited state lifetimes were measured for selected bands by firing the ionization laser at the time of greatest CuCCH signal intensity, and monitoring the $CuCCH^+$ ion signal as the dye laser was scanned in time. The measured ion signal as a function of delay time was then fitted to an exponential decay curve using the Marquardt nonlinear

least-squares algorithm.[54] In order to measure decay curves for states with long lifetimes, the dye laser was counterpropagated along the molecular beam axis, allowing molecules to be excited upstream of the ionization region. For a few of the bands, however, the lifetime was too long to be properly characterized even with this method. For these features, which belong to the $\tilde{a}\ 1 \leftarrow \tilde{X}\ ^1\Sigma^+$ band system, I can only conclude that the upper state lifetime exceeds 150 μs.

5.3 Results

5.3.1 Ionization Energy of CuCCH

Low resolution (0.15 cm^{-1}) survey scans were recorded for ^{63}CuCCH (69.6% natural abundance) and ^{65}CuCCH (30.1% natural abundance) in the 19400 – 25200 cm^{-1} region. The optical spectrum was initially scanned using ArF (6.42 eV) excimer radiation as the ionization laser, beginning at 19,400 cm^{-1} and proceeding toward the blue. Eventually, a vibronic band was found near 24673 cm^{-1}. Additional features were found near 25100 cm^{-1}. The 24673 cm^{-1} band establishes an upper bound on the ionization energy given by the sum of the dye laser and ArF photon energies as IE(CuCCH) $\leq$ 9.48 eV. A follow-up scan over the same region using the F_2 excimer laser for ionization (7.87 eV) revealed numerous vibronic bands farther to the red. A prominent feature near 24069 cm^{-1} was observed using F_2 radiation for ionization, but was not observed using ArF radiation. This suggests that the combination of a 24069 cm^{-1} dye laser photon and a 6.42 eV ArF photon is insufficient to ionize the molecule, placing IE(CuCCH) $\geq$ 9.40 eV. Together, these two observations place the ionization energy of CuCCH in the range of 9.40-9.48 eV.

In mass resolved optical R2PI studies conducted in our laboratory, the spectra of individual masses can be collected simultaneously, allowing separate spectra to be collected for the different isotopologues. The precise isotope shifts that are obtained are especially helpful in vibrational assignments. Unfortunately, in this particular study we ran into a problem during the rotationally resolved studies because the 1 mm diameter vaporization fixture had been used in a previous study of Zr-containing molecules, and was contaminated with zirconium. While this would not be a problem with many choices of ionization wavelength, atomic Zr is one-photon ionized at the F_2 laser wavelength, leading to a large, fluctuating signal at mass 90. Because of this difficulty, it was impossible to record rotationally resolved spectra for the ^{65}CuCCH isotopologue, which also lies at mass 90.

5.3.2 Computations on CuCCH

In order to understand the normal modes of CuCCH to aid in the assignment of the spectra, a density functional calculation for the lowest energy singlet ($\widetilde{X}\ ^1\Sigma^+$), lowest energy triplet ($^3\Sigma^+$), and lowest energy doublet cation states was performed. The calculation was performed using the Gaussian 03W suite of programs[55] with the B3LYP method, in combination with the 6-311+G basis set. The $^3\Sigma^+$ state is calculated to lie approximately 20,800 cm^{-1} above the $\widetilde{X}\ ^1\Sigma^+$ ground state. The calculated ionization energy, 9.34 eV, is in quite good agreement with the bracketed value noted above, 9.44 ± 0.04 eV. For all three electronic states, CuCCH is linear with three stretching normal modes of σ^+ symmetry (ν_1, C-H stretch; ν_2, C≡C stretch; and ν_3, Cu-C stretch) and two doubly-degenerate bending modes of π symmetry (ν_4, C≡C-H bend; and ν_5, Cu-C≡C

bend). The calculated frequencies for the 5 modes, listed in Table 5.1 along with other calculated data, are similar in all electronic and charge states and fall in the same order as the corresponding modes of AlCCH.[42, 43]

A total of 24 bands were identified and assigned after scanning the 19400 – 25200 cm^{-1} region using the F_2 ionization laser. Of these, 4 bands were successfully rotationally resolved, calibrated, and fitted. No attempt was made to rotationally resolve bands above 23800 cm^{-1} due to the lack of $^{130}Te_2$ calibration lines in this region. None of the bands that were analyzed exhibited detectable hyperfine splitting or broadening of the lines. Table 5.2 presents a list of all observed bands, along with isotope shifts, excited state lifetimes, and fitted rotational constants, when determined.

5.3.3 The [20.2] $\tilde{a}1 \leftarrow \tilde{X}\,^1\Sigma^+$ Band System

Between 19400 and 23000 cm^{-1}, only two bands were observed; these are assigned as belonging to the [20.2] $\tilde{a}1 \leftarrow \tilde{X}\,^1\Sigma^+$ system. The low resolution scan is displayed in Figure 5.1. The more intense band near 20249 cm^{-1} is the only feature of significant intensity in the system, and is therefore identified as the 0_0^0 band; a much weaker band near 20729 cm^{-1} is assigned as the 3_0^1 band, corresponding to excitation of one quantum in the Cu-C stretching mode, giving ν_3 = 480 cm^{-1} for this excited electronic state. The large gap between these features and those further to the blue (nearly 2900 cm^{-1}) shows that these bands belong to a different band system than those further to the blue. This is also borne out by the vastly different lifetimes of the $\tilde{a}$ state and the states further to the blue.

Table 5.1 Computed results on $^{63}CuCCH$[a]

Property	$\tilde{X}\,^1\Sigma^+$	$^3\Sigma^+$	$^{63}CuCCH^+$
T_e	0	20812 cm^{-1}	9.34 eV
ν_1 (σ^+, C-H stretch)	3444 cm^{-1}	3441 cm^{-1}	3362 cm^{-1}
ν_2 (σ^+, C≡C stretch)	2049 cm^{-1}	2057 cm^{-1}	1870 cm^{-1}
ν_3 (σ^+, Cu-C stretch)	488 cm^{-1}	452 cm^{-1}	461 cm^{-1}
ν_4 (π, C≡C-H bend)	715 cm^{-1}	617 cm^{-1}	720 cm^{-1}
ν_5 (π, Cu-C≡C bend)	249 cm^{-1}	200 cm^{-1}	251 cm^{-1}
r(Cu-C)	1.834 Å	1.909 Å	1.841 Å
r(C≡C)	1.221 Å	1.219 Å	1.261 Å
r(C-H)	1.063 Å	1.064 Å	1.072 Å

[a] As described in the text, all computations were done using density functional theory, employing the B3LYP functional and using a 6-311+G basis set.

Table 5.2 Bands measured for CuCCH

System	Band	ν_0(cm^{-1})	Isotope shift $\nu(^{63}$CuCCH)-$\nu(^{65}$CuCCH) (cm^{-1})	B′ (cm^{-1})	τ(μs)
$\widetilde{a}\ ^1\Pi \leftarrow \widetilde{X}\ ^1\Sigma^+$	0_0^0	20248.8981(29)[d]	0.0	0.130864(20)[d]	197(13)[b,d]
	3_0^1	20728[a]	1.6		137(4)[b,d]
$\widetilde{A}\ ^1\Sigma^+ \leftarrow \widetilde{X}\ ^1\Sigma^+$	0_0^0	23130.3185(11)[d]	-0.6	0.129504(8)[d]	0.442(21)[d]
	5_1^1	23169[a]	0.0		
	5_0^1	23412.8008(31)[d]	-0.1	0.129533(39)[d]	
	$4_0^1 5_1^0$	23541[a]	1.0		
	3_1^2	23581[a]	-0.3		
	3_0^1	23595.6509(23)[d]	0.8	0.129164(32)[d]	0.495(57)[d]
	$3_0^1 5_1^1$	23631[a]	0.5		
	$3_0^1 5_0^1$	23873[a]	1.5		
	$3_0^1 4_0^1 5_1^0$	24011[a]	2.6		
	3_1^3	24047[a]	2.1		
	3_0^2	24059[a]	3.1		
	$3_0^2 4_0^1 5_1^0$	24478[a]	2.3		
	3_1^4	24507[a]	4.4		
	3_0^3	24521[a]	4.4		
	3_1^5	24965[a]	6.2		
	3_0^4	24982[a]	5.6		
$\widetilde{B} \leftarrow \widetilde{X}\ ^1\Sigma^+$	U	24597[a]	-0.1		
	3_1^1	24654[a]	---		
	0_0^0	24664[a]	-0.1		0.818(73)[d]
	5_1^1	24688[a]	-0.2		
	U[c]	24849[a]	0.1		
	5_0^1	24931[a]	1.8		
	$4_0^1 5_1^0$	25092[a]	0.1		
	3_0^1	25126[a]	0.5		
	U[c]	25134[a]	0.4		

[a] Measured in low resolution, expected accuracy ± 2 cm^{-1}. [b] Not well characterized.
[c] Unidentified band. [d] Error limits (1σ) are provided in parentheses.

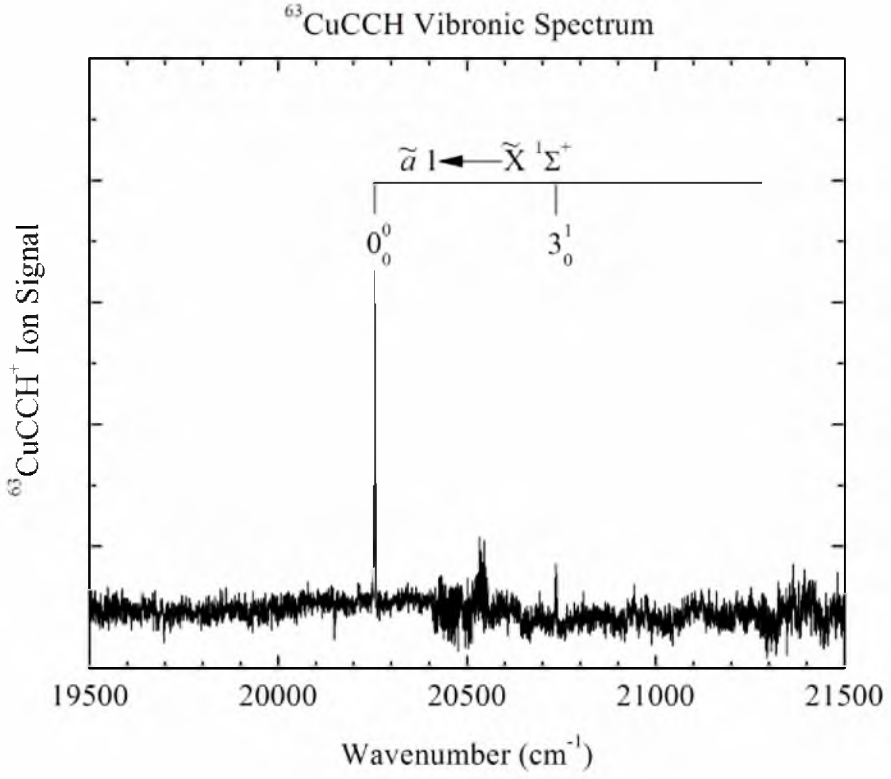

Figure 5.1. Low resolution scan over the $\tilde{a}\ 1 \leftarrow \tilde{X}^1\Sigma^+$ band system of ^{63}CuCCH.

Attempts were made to measure lifetimes for both bands of this system, but the lifetimes were so long that a complete decay curve could not be recorded. The fitted lifetimes of 197 μs for the 20249 cm^{-1} band and 137 μs for the 20729 cm^{-1} band nevertheless indicate that the band system is electronically forbidden. Despite the long upper state lifetime and forbidden nature of the system, a rotationally resolved scan over the 0_0^0 band at 20249 cm^{-1} was successful (Figure 5.2). The band displays an intense Q-branch with unresolved Q lines, but nicely resolved R and P branches. An unconstrained fit of the P and R lines to the formula

$$\nu = \nu_0 + B'J'(J'+1) - B''J''(J''+1) \qquad (5.1)$$

gives a value of B″ of 0.137342(11) cm^{-1} (1σ error limit) for ^{63}CuCCH, consistent with the far more precise value, B″ = 0.13745471(30) cm^{-1} measured by Fourier transform microwave and millimeter/submillimeter wave methods.[45] Accordingly, for this band and all other rotationally resolved features, the final B′ values reported are obtained from fits in which B″ is constrained to the microwave/millimeter wave value. Table 5.3 provides a list of measured line positions and fitted rotational constants for all rotationally resolved bands.

The $\tilde{X}\ ^1\Sigma^+$ ground state is a mixture of a covalent structure, in which the copper 4s electron is spin-paired with the unpaired σ electron of the CCH radical, and an ionic structure, in which the copper 4s electron is transferred to the CCH fragment to form a CCH^- anion. Regardless of whether the bond is primarily covalent, ionic, or intermediate between these limiting cases, the assignment of the ground state as $^1\Sigma^+$ is the only reasonable possibility, and is in agreement with microwave data.[45] The presence of a Q

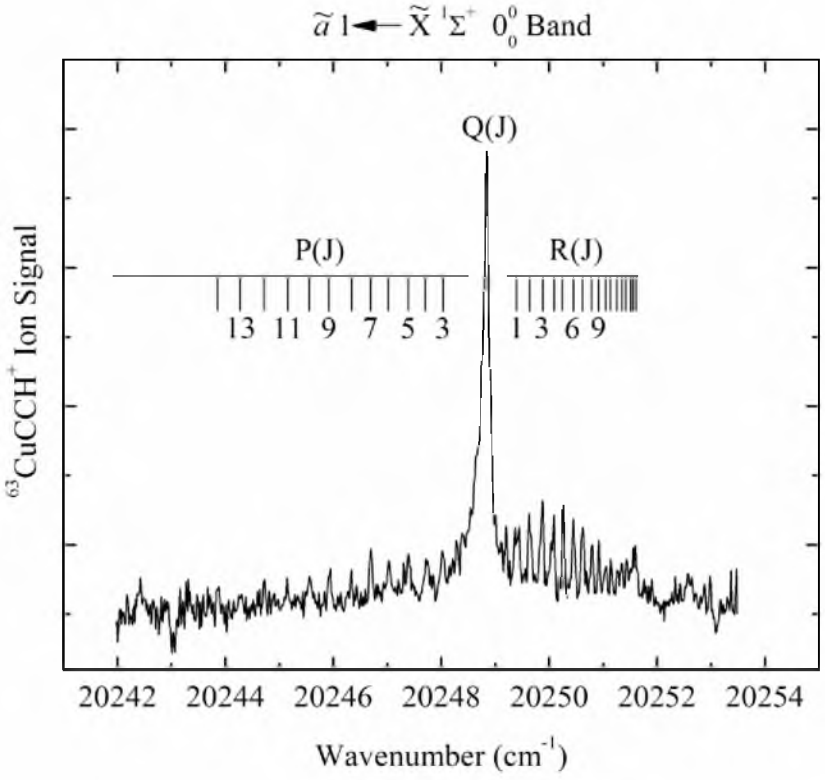

Figure 5.2. Rotationally resolved scan over the 0_0^0 band of the $\tilde{a}\ 1 \leftarrow \tilde{X}\,^1\Sigma^+$ system of ^{63}CuCCH.

Table 5.3. Rotational lines of resolved bands of ^{63}CuCCH.[a]

Rotational Line	$\tilde{a}\ ^1\Sigma^+ \leftarrow \tilde{X}\ ^1\Sigma^+$ 0_0^0 band	$\tilde{A}\ ^1\Sigma^+ \leftarrow \tilde{X}\ ^1\Sigma^+$ 0_0^0 band	$\tilde{A}\ ^1\Sigma^+ \leftarrow \tilde{X}\ ^1\Sigma^+$ 5_0^1 band	$\tilde{A}\ ^1\Sigma^+ \leftarrow \tilde{X}\ ^1\Sigma^+$ 3_0^1 band
P(15)		23124.523(2)		
P(14)	20243.859(-9)	23125.028(-6)		
P(13)	20244.304(-8)	23125.506(-2)		23590.789(-6)
P(12)	20244.723(6)	23125.974(-5)		
P(11)	20245.145(4)	23126.426(-7)	23408.896(9)	23591.707(8)
P(10)	20245.562(-6)	23126.855(-1)	23409.342(-3)	23592.136(20)
P(9)	20245.949(1)	23127.264(8)	23409.757(-1)	23592.580(-1)
P(8)	20246.341(-11)	23127.678(-4)	23410.166(-9)	23592.996(-8)
P(7)	20246.701(-4)	23128.061(-1)	23410.544(0)	23593.382(-4)
P(6)	20247.033(18)	23128.434(-3)	23410.912(2)	23593.764(-11)
P(5)	20247.396(-4)	23128.786(-1)	23411.263(4)	23594.112(-2)
P(4)	20247.738(-19)	23129.116(7)		23594.451(1)
P(3)	20248.026(8)	23129.447(-1)		23594.774(3)
P(2)		23129.753(-1)		23595.087(-3)
P(1)		23130.049(-5)		
Q(12)			23411.558(6)	
Q(11)			23411.753(2)	
Q(10)			23411.933(-4)	
Q(9)			23412.111(-23)	
Q(8)			23412.218(13)	
Q(7)			23412.361(-4)	
Q(6)			23412.467(1)	
Q(5)			23412.575(-12)	
Q(4)			23412.646(-4)	
Q(3)			23412.717(-11)	
R(0)		23130.573(5)		23595.910(-1)
R(1)	20249.405(3)	23130.814(7)	23413.306(-3)	23596.156(-5)
R(2)	20249.627(17)	23131.048(0)	23413.521(9)	23596.377(-1)
R(3)	20249.879(-13)	23131.262(-3)	23413.726(16)	23596.585(0)
R(4)	20250.087(-12)	23131.454(0)	23413.937(0)	23596.766(11)
R(5)	20250.261(10)	23131.635(-1)	23414.110(8)	23596.951(1)
R(6)	20250.448(6)	23131.800(-3)	23414.290(-9)	23597.102(9)
R(7)	20250.622(1)	23131.945(0)	23414.430(0)	23597.253(0)
R(8)	20250.795(-16)	23132.079(-2)	23414.555(7)	23597.381(-2)
R(9)	20250.920(2)	23132.191(2)	23414.663(15)	23597.492(-4)
R(10)	20251.053(-1)	23132.283(10)		
R(11)	20251.150(19)	23132.375(2)		23597.663(-6)
R(12)	20251.271(2)		23414.942(-9)	

[a] All values are in cm^{-1} units; residuals in the fit (calculated – measured) are provided in parentheses, in units of 0.001 cm^{-1}. Error limits in the fitted spectroscopic constants (1σ) are provided in parentheses after each constant, in units of the last digits quoted.

Table 5.3. (Continued)

Rotational Line	$\tilde{a}\ ^1\Sigma^+ \leftarrow \tilde{X}\ ^1\Sigma^+$ 0_0^0 band	$\tilde{A}\ ^1\Sigma^+ \leftarrow \tilde{X}\ ^1\Sigma^+$ 0_0^0 band	$\tilde{A}\ ^1\Sigma^+ \leftarrow \tilde{X}\ ^1\Sigma^+$ 5_0^1 band	$\tilde{A}\ ^1\Sigma^+ \leftarrow \tilde{X}\ ^1\Sigma^+$ 3_0^1 band
R(13)	20251.349(14)			
R(14)	20251.432(7)			
R(15)	20251.507(-3)			
R(16)	20251.558(-4)			
R(17)	20251.599(-7)	23132.544(3)		
R(19)		23132.478(-1)		
Fitted spectroscopic constants (cm^{-1})				
T_0	20248.8982(29)	23130.3184(11)	23412.8008(31)	23595.6509(23)
B′	0.130864(20)	0.129504(8)	0.129533(39)	0.129164(32)
B″ (held fixed)	0.137456	0.137456	0.137456	0.137456

[a] All values are in cm^{-1} units; residuals in the fit (calculated – measured) are provided in parentheses, in units of 0.001 cm^{-1}. Error limits in the fitted spectroscopic constants (1σ) are provided in parentheses after each constant, in units of the last digits quoted.

branch then identifies the $\tilde{a}$ state as having Ω=1, and the long fluorescence lifetime shows that the system is spin-forbidden. Accordingly, the upper state is labeled as the [20.2] $\tilde{a}1$ state, where the [20.2] symbol provides the energy of the ground vibrational level of the state, relative to the ground level of the ground state, in thousands of cm^{-1}. Likely candidates for the [20.2] $\tilde{a}1$ state are states of $^3\Sigma_1^+$ or $^3\Pi_1$ symmetry (see below), which can gain intensity through spin-orbit coupling to an excited $^1\Pi$ state that has significant oscillator strength in absorption from the ground state. Assuming the [20.2] $\tilde{a}1$ state decays purely by fluorescence to the ground state, the fluorescence lifetime converts to an absorption oscillator strength of $f \approx 2 \times 10^{-5}$, an exceptionally weak absorption system.

5.3.4 The [23.1] $\tilde{A}^1\Sigma^+ \leftarrow \tilde{X}^1\Sigma^+$ Band System

5.3.4.1. Cold bands

Approximately 2880 cm^{-1} to the blue of the $\tilde{a}1 \leftarrow \tilde{X}^1\Sigma^+$ system lies a much more intense and extensive system, displayed in Figure 5.3. The bands between 23130 cm^{-1} and 24550 cm^{-1} are assigned, on the basis of details presented below, as belonging to the $\tilde{A}^1\Sigma^+ \leftarrow \tilde{X}^1\Sigma^+$ system, while most of those lying further to the blue are assigned to the $\tilde{B} \leftarrow \tilde{X}^1\Sigma^+$ system. The lowest energy strong band, near 23130 cm^{-1}, is quite intense and no bands of significant intensity are found to lower energy. Accordingly, this is assigned as the 0_0^0 band. A series of strong bands spaced by 465 cm^{-1} proceed to higher energy. Based on the computed vibrational frequencies, this is a progression in the Cu-C stretching mode, ν_3. The bands in this progression are therefore identified as the 3_0^1, 3_0^2,

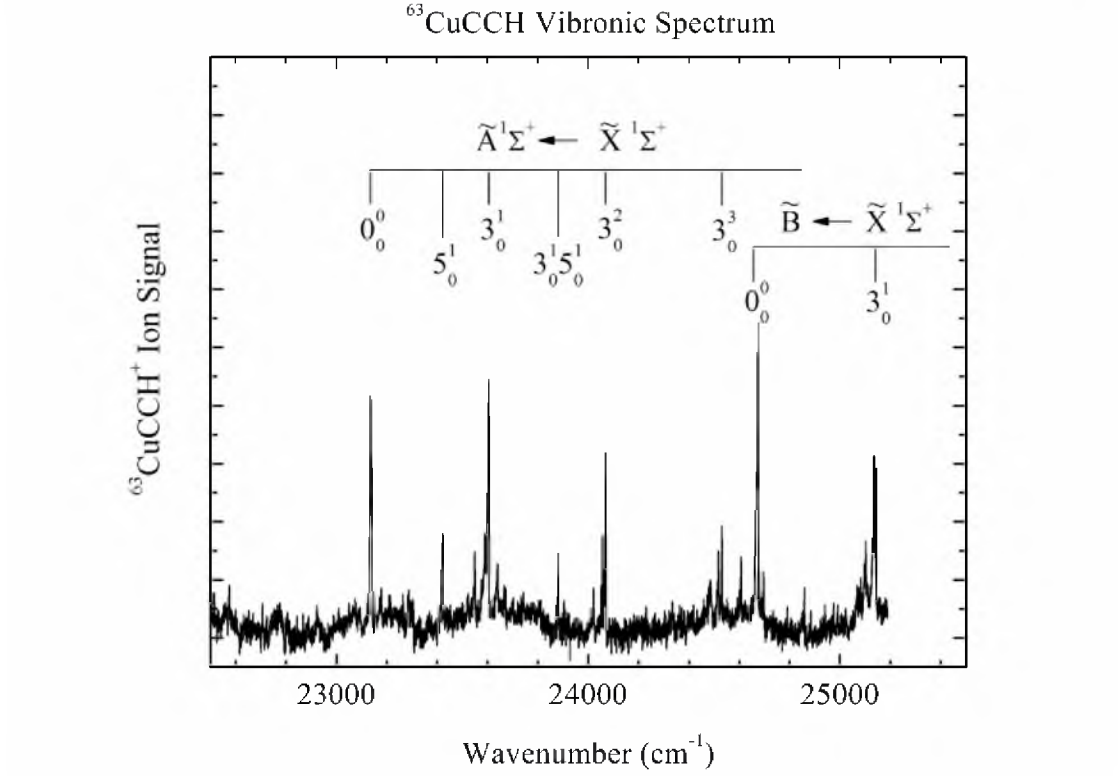

Figure 5.3. Low resolution scan over the $\tilde{A}^1\Sigma^+ \leftarrow \tilde{X}^1\Sigma^+$ and $\tilde{B} \leftarrow \tilde{X}^1\Sigma^+$ band systems of ^{63}CuCCH.

3_0^3, and 3_0^4 bands. Somewhat surprisingly, a pair of moderately intense features is found about 280 cm^{-1} above the 0_0^0 and 3_0^1 bands. The only calculated vibrational mode that could correspond to this interval is the ν_5 Cu-C≡C bending mode. However excitation of this motion is forbidden in the absence of vibronic coupling. On the basis of rotationally resolved work described below, these features are assigned as the vibronically-induced 5_0^1 and $3_0^1 5_0^1$ bands.

Rotationally resolved studies of the 0_0^0 and 3_0^1 bands, displayed in Figures 5.4 and 5.5, show that these bands lack a Q-branch and begin with R(0) and P(1). This establishes that both states involved in the transition have $\Omega = 0$. Further, the short upper state lifetimes, 442(21) ns for excitation of the 0_0^0 band and 495(57) ns for excitation of the 3_0^1 band, show that this excitation is spin-allowed. On this basis, the upper state is assigned as the [23.1]$\tilde{A}\,^1\Sigma^+$ state, where the symbol [23.1] again identifies the energy of the vibrationless level of the $\tilde{A}$ state. Assuming the decay rate is due to fluorescence to the ground state alone, the measured lifetimes correspond to an absorption oscillator strength of $f \approx 6 \times 10^{-3}$, making the [23.1]$\tilde{A}\,^1\Sigma^+ \leftarrow \tilde{X}\,^1\Sigma^+$ system about a factor of 200 more intense than the $\tilde{a}1 \leftarrow \tilde{X}\,^1\Sigma^+$ system. A rotationally resolved scan over the weak band near 23413 cm^{-1}, tentatively identified as the 5_0^1 band, is displayed in Figure 5.6. Unlike the 0_0^0 and 3_0^1 bands, this feature is a perpendicular transition exhibiting R, Q, and P branches.

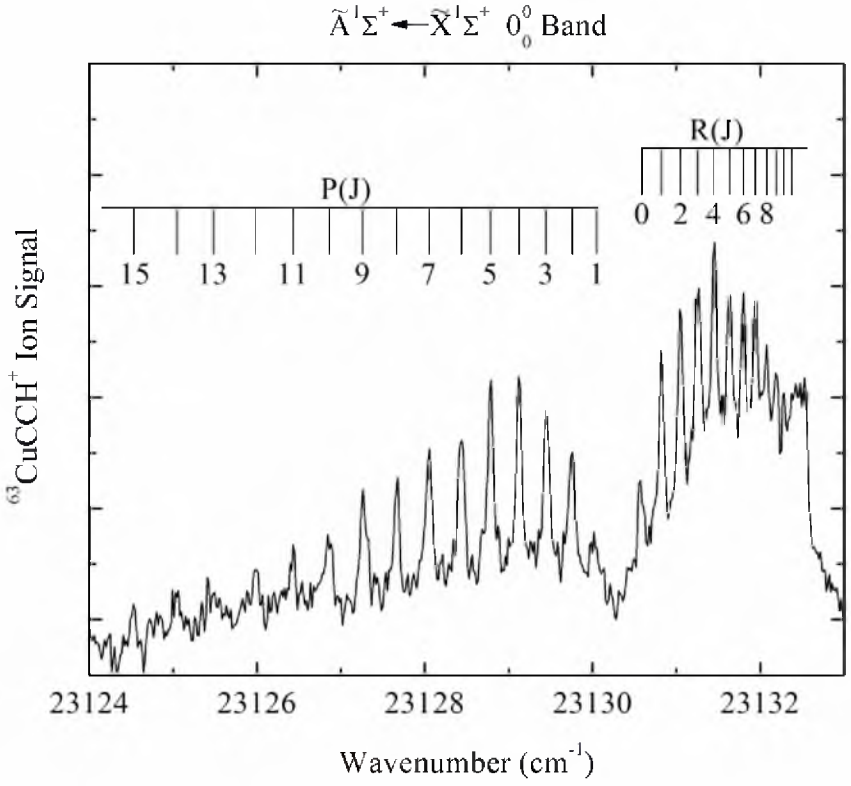

Figure 5.4. Rotationally resolved scan over the 0_0^0 band of the $\tilde{A}\,^1\Sigma^+ \leftarrow \tilde{X}\,^1\Sigma^+$ system of ^{63}CuCCH.

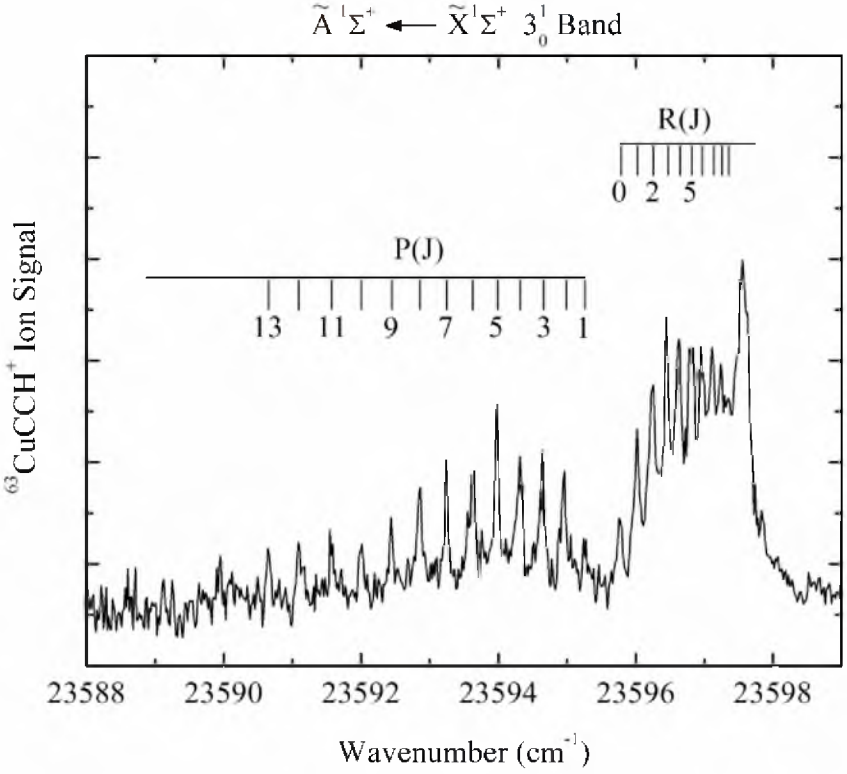

Figure 5.5. Rotationally resolved scan over the 3_0^1 band of the $\tilde{A}\,^1\Sigma^+ \leftarrow \tilde{X}\,^1\Sigma^+$ system of ^{63}CuCCH.

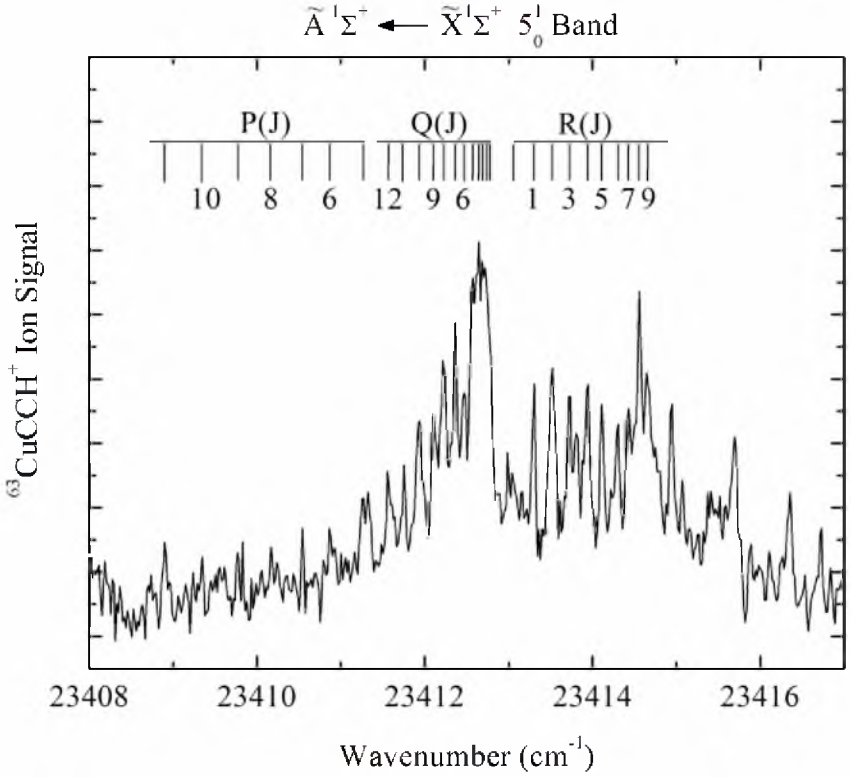

Figure 5.6. Rotationally resolved scan over the 5_0^1 band of the $\tilde{A}\,^1\Sigma^+ \leftarrow \tilde{X}\,^1\Sigma^+$ system of ^{63}CuCCH.

This indicates that the upper state has a total angular momentum along the axis of 1, which is consistent with excitation of a bending mode (v_5=1, ℓ_5=1) within a $^1\Sigma^+$ electronic state. This confirms the assignment of the band as the 5_0^1 band, and establishes the value of $v_5(\tilde{A}\ ^1\Sigma^+)$ as 282.5 cm^{-1}. By analogy, the band near 23873 cm^{-1} is assigned as the $3_0^1 5_0^1$ combination band. These perpendicular bands derive their intensity by a different mechanism than the other bands of this system, via vibronic coupling with a $^1\Pi$ state that has a fully allowed transition with the ground $\tilde{X}\ ^1\Sigma^+$ state.

The spectrum of the 5_0^1 band displayed in Figure 5.6 also shows additional lines that have not been assigned. These originate from a second vibronic level that lies close in energy. Because of the overlap between these two features, we have been unable to obtain a clean measurement of the lifetime of the 5^1 level of the $\tilde{A}\ ^1\Sigma^+$ state.

5.3.4.2. Hot Bands

In addition to the bands described above, there are a number of weaker bands that arise from vibrationally excited molecules in the molecular beam. One would expect that the lowest frequency vibration, the v_5 Cu-C≡C bending mode calculated at 249 cm^{-1}, would be populated in the molecular beam. The 5_1 level has Π vibronic symmetry, so parallel transitions to upper states of Π vibronic symmetry would be electronically allowed. Upper states with the most favorable Franck-Condon factors would also excite the v_5 mode with 1 vibrational quantum, leading to transitions such as 5_1^1 and $3_0^1 5_1^1$. Using the calculations as a guide, these transitions should occur roughly 200 to 250 cm^{-1} below the corresponding 5_0^1 and $3_0^1 5_0^1$ bands.

Weak features near 23169 and 23631 cm^{-1} satisfy these requirements, and are therefore assigned to the 5_1^1 and $3_0^1 5_1^1$ bands. These establish the value of $\nu_5(\tilde{X}\,^1\Sigma^+)$ as 243 ± 1 cm^{-1}.

The other parallel transition that can arise from the 5_1 level is excitation of ν_4' with one quantum, leading to vibronic bands of Π-Π symmetry such as $4_0^1 5_1^0$ and $3_0^1 4_0^1 5_1^0$. Based on the computed values of ν_4, the C≡C-H bending mode, in the various states, we expect these transitions to lie roughly 410-470 cm^{-1} ($\nu_4' - \nu_5'$) above the corresponding 5_1^1 and $3_0^1 5_1^1$ bands. Bands at 23541 and 24011 cm^{-1} are close to the expected positions, falling 372 and 380 cm^{-1} above the 5_1^1 and $3_0^1 5_1^1$ bands, respectively. Another band in this progression, the $3_0^2 4_0^1 5_1^0$ band, falls at 24478 cm^{-1}.

In addition to the 5_1 level, the 3_1 level is also populated in the experiments performed with the 5 mm expansion orifice. According to the computed results, hot bands arising from this level should appear about 488 cm^{-1} to the red of the corresponding cold bands. A set of weak bands fitting this description appear 475 ± 3 cm^{-1} to the red of the 3_0^2, 3_0^3, and 3_0^4 bands, and are assigned as the 3_1^2, 3_1^3, and 3_1^4 bands. An additional band fitting into this progression is the 3_1^5 band. These observations establish the value of $\nu_3(\tilde{X}\,^1\Sigma^+)$ as 475 ± 3 cm^{-1}.

The assigned vibronic bands of the $\tilde{A}\,^1\Sigma^+ \leftarrow \tilde{X}\,^1\Sigma^+$ system have been fitted to the expression

$$\nu = T_0 + \sum_{i=3}^{5} \omega_i' v_i' + x_{33}'(v_3'^2 + v_3') + x_{34}'(v_3' v_4' + (v_3' + v_4')/2) +$$

$$x_{35}'(v_3' v_5' + (v_3' + v_5')/2) - \omega_3'' v_3'' - \omega_5'' v_3'' \ . \qquad (5.2)$$

The resulting vibrational constants are reported in Table 5.4, along with results from the other band systems.

5.3.5 The [24.7] $\widetilde{B} \leftarrow \widetilde{X}\ ^1\Sigma^+$ Band System

Further to the blue, an intense band is found near 24664 cm^{-1}, and an associated strong feature is found near 25126 cm^{-1}. These features do not fit into a progression involving any of the known vibrational modes of the [23.1]$\widetilde{A}\ ^1\Sigma^+ \leftarrow \widetilde{X}\ ^1\Sigma^+$ system. One might think that the 24664 cm^{-1} band corresponds to excitation of the C≡C stretching mode in the [23.1]$\widetilde{A}\ ^1\Sigma^+$ state, but this would place the value of ν_2' at 1534 cm^{-1}, a value that is lower than the calculated values (Table 5.1) by about 500 cm^{-1}, and is even lower than the 1623 cm^{-1} C=C stretching frequency of ground state ethylene, C_2H_4.[56] Such a low value of ν_2' seems unreasonable. In addition, the fluorescence lifetime (820 ns) of the 24664 cm^{-1} band is about 75% greater than that of the 0^0 and 3^1 levels of the $\widetilde{A}\ ^1\Sigma^+$ state. These facts show that another band system is present in this region. Attempts were not made to rotationally resolve these features, so the symmetry of this upper state is unknown at this time; it is designated simply as the [24.7] $\widetilde{B}$ state. Arguments presented below suggest that the $\widetilde{B}$ state is a $^1\Pi$ state.

Assuming that the lifetime is dominated by fluorescence to the ground state, the [24.7] $\widetilde{B} \leftarrow \widetilde{X}\ ^1\Sigma^+$ band system is an allowed transition with an absorption oscillator

strength of $f \approx 3 \times 10^{-3}$. This implies that the $\widetilde{B}$ state is either a $^1\Sigma^+$ or $^1\Pi$ state. Using the results obtained for the hot band frequencies, and assuming similar frequencies for the ν_3, ν_4, and ν_5 modes of the $\widetilde{B}$ state as were found for the $\widetilde{A}\ ^1\Sigma^+$ state, it is straightforward to identify the 3_0^1, 3_1^1, 5_0^1, 5_1^1, and $4_0^1 5_1^0$ bands in the spectrum. These assigned bands are listed in Table 5.2, and the resulting vibrational constants for the $\widetilde{B}$ state are given in Table 5.4.

5.4 Discussion

The electronic structure of CuCCH is best understood by comparing the molecule to better known related species. The ethynyl radical, CCH, is highly electronegative, with an electron affinity of 2.968(6) eV.[57] This is comparable to the electron affinity of the halogen atoms F (3.401 eV), Cl (3.613 eV), Br (3.364 eV), and I (3.059 eV),[58] suggesting that CuCCH may be understood as an ionic molecule. Therefore, it is appropriate to compare the electronic spectra of CuCCH to those of the copper halides. The copper halides have a rich spectroscopic history, dating to Mulliken's 1925 study of CuF, CuCl, CuBr and CuI.[59] All of the copper halides have been spectroscopically studied, but the focus of our discussion is on CuF, for which some of the most detailed and extensive calculations are available.[60] In CuF, the $X\ ^1\Sigma^+$ ground state is ionic, correlating diabatically to Cu^+ ($3d^{10}$, ^1S) + F^- ($2p^6$, ^1S) and adiabatically to Cu ($3d^{10}4s^1$, ^2S) + F ($2p^5$, ^2P).[60] The lowest group of excited states, lying in the range 14000-25000 cm^{-1}, is also primarily ionic, correlating diabatically to $Cu^+(3d^9 4s^1, {}^{1,3}D) + F^-(2p^6, {}^1S)$ and adiabatically to Cu ($3d^9\ 4s^2$, ^2D) + F ($2p^5$, ^2P).[60] The separated ion limit, $Cu^+(3d^9 4s^1, {}^{1,3}D) + F^-(2p^6, {}^1S)$, generates states of $^1\Sigma^+$, $^3\Sigma^+$, $^1\Pi$, $^3\Pi$, $^1\Delta$, and $^3\Delta$ symmetry.

Table 5.4. Fitted vibrational constants and other results for ^{63}CuCCH

Parameter	$\tilde{X}^1\Sigma^+$ state	$\tilde{a}$ 1 state	$\tilde{A}^1\Sigma^+$ state	$\tilde{B}$ state
T_0 (cm^{-1})	0	20248.8981(29)	23130.3185(11)	24664
ω_3 (cm^{-1})	476.1(0.9)	479	466.8(1.8)	462
ω_4 (cm^{-1})	---	---	652.1(2.2)	671
ω_5 (cm^{-1})	242.9(1.1)	---	284.4(2.0)	267
x_{33} (cm^{-1})	---	---	-0.73(0.17)	---
x_{34} (cm^{-1})	---	---	4.0(1.0)	---
x_{35} (cm^{-1})	---	---	-4.2(1.4)	---
B_0 (cm^{-1})	0.137456[a]	0.130864(20)	0.129504(8)	---
R_{Cu-C} (C≡CH)[b]	1.800 Å	1.867 Å	1.884 Å	---
R_{Cu-C} ($C\equiv CH^-$)[c]	1.791 Å	1.859 Å	1.874 Å	---
Microwave R_{Cu-C}	1.820(2)Å	---	---	---
R_{Cu-C} (best estimate)[d]	1.820(2)Å	1.887±0.03 Å	1.904±0.03 Å	---
Ionization energy	9.44(4) eV			

[a] Held fixed at the microwave value, from Reference 45.

[b] Calculated from the moment of inertia, assuming a rigid C≡C-H structure with the geometry of the C_2H radical.

[c] Calculated from the moment of inertia, assuming a rigid C≡C-H structure with the geometry of the C_2H^- anion.

[d] Estimated Cu-C bond length is obtained from the values based on rigid C≡C-H structures, corrected by the difference between the ground state microwave result and these estimates.

Of these, all have been spectroscopically observed in CuF except for $^1\Delta$. The $^1\Sigma^+$ and $^1\Pi$ states are accessible from the $X^1\Sigma^+$ state in electronically allowed transitions, while the $^3\Sigma^+$, $^3\Pi_{0^+,1}$, and $^3\Delta_1$ states become allowed through spin-orbit mixing with the $^1\Sigma^+$ and $^1\Pi$ states. *Ab initio* calculations on CuCl, CuBr, and CuI confirm these general statements, with both the ground state and the lowest group of excited states dominated by ionic configurations of $Cu^+(3d^{10}) + F^-(2p^6)$ and $Cu^+(3d^9 4s^1) + F^-(2p^6)$, respectively.[61, 62] The ionic character of these states of CuCl, CuBr, and CuI is displayed very clearly in the calculated nearly linear increase in dipole moment as a function of internuclear distance.[62] The known electronic states of CuF,[63, 64] CuCl,[65-67] CuBr,[68-72] and CuI[70, 73-75] are summarized in Table 5.5, where they are compared to our results and the microwave results on CuCCH.[45] Many more studies on the copper halides have been carried out than are listed here; however, these are the more useful references for the construction of Table 5.5. It is worth mentioning that the names of these states (A, B, etc.) as given in the literature vary from molecule to molecule, and have been changed over time as the electronic structure has become better understood.

An interesting observation is that the transitions to the excited $^1\Sigma^+$ state become more intense, with a shorter fluorescence lifetime, as one proceeds down the periodic table from CuF (τ = 1.5 μs) to CuI (τ = 0.16 μs). In a purely ionic limit, this transition is completely centered on the Cu^+ ion, and corresponds to the Cu^+ $3d^9 4s^1$, ^1D $|3d^{10}$, ^1S fluorescence, which is electric dipole forbidden.[76] The admixture of covalent character, which is greater in the heavier halides, allows the transition to become allowed.[76] This accounts for the shortening of the lifetime as the atomic number of the halogen increases. The electronic structure of CuCCH is expected to be similar to that of the copper halides.

Table 5.5. Comparison of CuCCH to the copper halides[a]

	$^{63}Cu^{19}F$	$^{63}Cu^{35}Cl$	$^{63}Cu^{79}Br$	^{63}CuI	$^{63}CuCCH$
$X^1\Sigma^+$	ω_e 621.55[b] r_e 1.7450 Å[b]	ω_e 417.64[d] r_e 2.051 Å[d]	ω_e 314.82[g] r_e 2.173 Å[g]	ω_e 264.31[l] r_e 2.338 Å[l]	ω_3 476.1 r(Cu-C) 1.82 Å
$a^3\Sigma^+$	T_0 14606.68[b] ω_e 674.20[b] r_e 1.7379 Å[b]	T_0 18994.46[d] --- r_0 2.099 Å[d] τ 60 μs[e]	T_0 19820.19[i] ω_e 294.49[h] r_0 2.261 Å[i]		
$b^3\Pi_1$	T_0 17556.52[b] ω_e 647.08[b] r_e 1.7512 Å[b]	T_0 20476.08[d] $\Delta G_{1/2}$ 398.29[d] r_e 2.097 Å[d] τ 3.3 μs[e]	T_0 20487.18[j] $\Delta G_{1/2}$ 293.97[j] r_e 2.234 Å[j] τ 3.5 μs[k]	T_0 19705[m] $\Delta G_{1/2}$ 209.48[m] r_e 2.444 Å[m] τ 1.9 μs[k]	T_0 20248.90 ω_3 479 r(Cu-C) 1.89 Å τ > 150 μs
$b^3\Pi_{0^+}$	T_0 17612.63[b] ω_e 647.08[b] r_e 1.7512 Å[b] τ = 7.3 μs[c]	T_0 20621.84[d] $\Delta G_{1/2}$ 396.09[d] r_e 2.0945 Å[d] τ 3.2 μs[e]		T_0 21851.3[n] r_0 2.423 Å[n] τ 1.0 μs[k]	
$A^1\Sigma^+$	T_0 19734.69[b] ω_e 656.04[b] r_e 1.7638 Å[b] τ = 1.2 μs[c]	T_0 23068.26[d] $\Delta G_{1/2}$ 402.23[d] r_e 2.1117 Å[d] τ 0.43 μs[e]	T_0 23303.46[g] ω_e 294.94[g] r_e 2.260 Å[g] τ 0.23 μs[k]	T_0 23869.7[n] ω_e 229.5[n] r_e 2.472 Å[n] τ 0.16 μs[k]	T_0 23130.32 ω_3 466.8 r(Cu-C) 1.90 Å τ 0.47 μs
$B^1\Pi$	T_0 20269.75[b] ω_e 643.73[b] r_e 1.7539 Å[b] τ = 0.60 μs[c]	T_0 22958.48[d] $\Delta G_{1/2}$ 391.51[d] r_e 2.1045 Å[d] τ 0.45 μs[e]	T_0 23027.41[g] ω_e 284.69[g] r_e 2.237 Å[g] τ 0.45 μs[k]	T_0 22929.371[l] $\Delta G_{1/2}$ 212.26[l] r_e 2.445 Å[l] τ 0.5 μs[k]	T_0 24664 ω_3 462 τ 0.82 μs
$c^3\Delta_1$	T_0 22802.63[b] ω_e 616.42[b] r_e 1.7928 Å[b]	T_0 25480[f] ω_e 386.8[f] τ 6.3 μs[e]			
$C^1\Delta$	Unobserved	Unobserved	Unobserved	Unobserved	Unobserved

Table 5.5. (continued)

[a] All quantities are given in cm^{-1} unless otherwise specified.
[b] Reference 63
[c] Reference 64
[d] Reference 65
[e] Reference 66
[f] Reference 67
[g] Reference 68
[h] Reference 72
[i] Reference 69
[j] Reference 71
[k] Reference 70
[l] Reference 73
[m] Reference 75
[n] Reference 74

The ground $\widetilde{X}\,^1\Sigma^+$ term combines ionic character from the $Cu^+(3d^{10}, {}^1S) + CCH^-$ ($\widetilde{X}\,^1\Sigma^+$) ionic limit and covalent character coming from the $Cu(3d^{10}4s^1, {}^2S) + CCH$ ($\widetilde{X}\,^2\Sigma^+$) neutral limit.

Excited terms of $^1\Sigma^+$, $^3\Sigma^+$, $^1\Pi$, $^3\Pi$, $^1\Delta$, and $^3\Delta$ symmetry are expected from the combination of the Cu^+ ($3d^94s^1$, $^{1,3}D$) + CCH^- ($\widetilde{X}\,^1\Sigma^+$) ions and the Cu ($3d^94s^2$, ^2D) + CCH ($\widetilde{X}\,^2\Sigma^+$) neutral fragments. Thus, it is expected that the same lowest-lying group of excited states as are found in the copper halides.

In terms of the Cu-X vibrational frequency, CuCCH falls in an intermediate position between CuF and CuCl in all of the observed electronic states. This is unsurprising, given that the mass of CCH (25 amu) falls between that of F (19 amu) and ^{35}Cl (35 amu). Likewise, for all of the measured states, the Cu-CCH bond length falls between the corresponding Cu-F and Cu-Cl bond lengths. The electronic excitation energy for the $\widetilde{A}\,^1\Sigma^+ \leftarrow \widetilde{X}\,^1\Sigma^+$ transition falls very close to the corresponding transitions in the heavier copper halides, differing from the CuCl transition frequency by only 62 cm^{-1}. Similarly, the measured lifetime of the $\widetilde{A}\,^1\Sigma^+$ state is within experimental error equal to that measured for this state in CuCl.

The other electronically allowed transition expected in this region is to the $\widetilde{B}\,^1\Pi$ state, which lies near 23,000 cm^{-1} in CuCl, CuBr, and CuI. Based on the strength of our $\widetilde{B} \leftarrow \widetilde{X}\,^1\Sigma^+$ transition, its radiative lifetime, and its location (T_0 = 24,662 cm^{-1}), I am convinced that the CuCCH $\widetilde{B}$ state is the $\widetilde{B}\,^1\Pi$ state. Of course, this can only be confirmed through rotationally resolved investigations or computational work. The

location of the $\widetilde{B}\,^1\Pi$ state is only 1534 cm^{-1} above the $\widetilde{A}$ state, thereby providing a source of oscillator strength for the vibronic coupling that is required to give the 5_0^1 and $3_0^1 5_0^1$ transitions their intensity. It also provides a mechanism, through spin-orbit mixing, for the $\widetilde{a}\,1$ state to gain intensity as well.

The nature of the $\widetilde{a}\,1$ state is more uncertain. Both the $^3\Sigma_1^+$ and $^3\Pi_1$ states are expected in this general region. These two states should be distinguishable by their rotational structure, but this requires resolution of the Q branch, which could not be resolved in our experiments. Specifically, the $\widetilde{X}\,^1\Sigma^+$ state has only *e* levels, while the $^3\Sigma^+$ state has $\Omega=0^-$ (*f* levels only) and $\Omega = 1$ (*e* and *f* levels). Likewise, the $^3\Pi_1$ state has *e* and *f* levels. In the $^3\Pi_1$ state, the *e*/*f* splitting arises from Λ-doubling, and is expected to be small, while in the $^3\Sigma_1^+$ state the *e*/*f* splitting arises from spin-uncoupling interactions between the nearby $\Omega = 0^- f$ levels and the $\Omega = 1f$ levels, and is expected to be much larger. Regardless of whether the upper state is a $^3\Sigma_1^+$ or a $^3\Pi_1$ state, the P and R lines follow the $e \leftarrow e$ selection rule, while the Q lines follow the $f \leftarrow e$ selection rule.[77] Thus, if the Q lines were resolved, this would enable the ability to deduce the upper state *e*/*f* splitting, and this would establish the upper state electronic symmetry. A simulation of the spectrum assuming no *e*/*f* splitting, however, displays a Q branch that is close to what is observed in our spectrum. On this basis, I tentatively assign the $\widetilde{a}\,1$ state as having $^3\Pi_1$ symmetry. This also places the $^3\Pi_1$ state within 250 cm^{-1} of the corresponding $^3\Pi_1$ state in CuCl and CuBr.

The most serious mystery remaining in our data concerns the lifetime of the $\tilde{a}1$ state. The long lifetime measured for this state, approximately 150 μs, is not consistent with the values (τ = 1.9 – 3.5 μs) measured for the $^3\Pi_1$ state in CuCl, CuBr, and CuI. To shed light on this issue, we have investigated the expected spin-orbit interactions in these species, since both the $^3\Pi_1$ state and the $^3\Sigma^+$ state gain oscillator strength by spin-orbit mixing with the $^1\Pi_1$ state. If we assume that the electronic structure of the excited states consists of a $3d^9 4s^1$, ^{1,3}D Cu^+ ion and a closed shell, ^{1}S or $^1\Sigma^+$ X^- ion, then the molecular states generated when the two ions combine consist of two $\Omega=0^+$ states ($^1\Sigma_{0^+}^+$ and $^3\Pi_{0^+}$), two $\Omega=0^-$ states ($^3\Sigma_{0^-}^+$ and $^3\Pi_{0^-}$), four $\Omega=1$ states ($^1\Pi_1$, $^3\Sigma_1^+$, $^3\Pi_1$, and $^3\Delta_1$), three $\Omega=2$ states ($^1\Delta_2$, $^3\Pi_2$, and $^3\Delta_2$), and one $\Omega=3$ state ($^3\Delta_3$). After constructing wavefunctions in terms of dδ, dπ, dσ, and sσ orbitals, I have derived the matrices of the spin-orbit interaction for the optically accessible $\Omega=0^+$ and $\Omega=1$ states as:

$$\boldsymbol{H}^{SO}(\Omega=1) = \begin{array}{c} \begin{matrix} {}^1\Pi_1 & {}^3\Delta_1 & {}^3\Pi_1 & {}^3\Sigma_1^+ \end{matrix} \\ \begin{pmatrix} 0 & \frac{\zeta}{\sqrt{2}} & -\frac{\zeta}{2} & -\frac{\sqrt{3}\zeta}{2} \\ \frac{\zeta}{\sqrt{2}} & \zeta & \frac{\zeta}{\sqrt{2}} & 0 \\ -\frac{\zeta}{2} & \frac{\zeta}{\sqrt{2}} & 0 & \frac{\sqrt{3}\zeta}{2} \\ -\frac{\sqrt{3}\zeta}{2} & 0 & \frac{\sqrt{3}\zeta}{2} & 0 \end{pmatrix} \end{array} \quad \text{and}$$

$$\boldsymbol{H}^{SO}(\Omega=0^+) = \begin{array}{c} \begin{matrix} {}^1\Sigma^+ & {}^3\Pi_{0^+} \end{matrix} \\ \begin{pmatrix} 0 & \sqrt{\frac{3}{2}}\zeta \\ \sqrt{\frac{3}{2}}\zeta & \frac{\zeta}{2} \end{pmatrix} \end{array}. \qquad (5.3)$$

The ζ in these matrices is the atomic spin-orbit parameter, $\zeta_{3d}(Cu^+, 3d^9 4s^1)$, which is obtained by numerical Hartree-Fock methods as $\zeta = 821.76$ cm^{-1}.[78] These matrices, combined with estimated term values of the $^1\Pi$, $^3\Delta$, $^3\Pi$, $^3\Sigma^+$, and $^1\Sigma^+$ terms, allow the amount of mixing of the $^1\Pi_1$ and $^1\Sigma^+$ states into the spin-forbidden triplet states to be quantified, and thereby allows the approximate ratio of the fluorescence lifetimes to be estimated.

To make this estimate, approximate term energies of the various states are added to the diagonals of the matrices above, the value ζ=821.76 cm^{-1} is employed, and the matrices are diagonalized. In the resulting Ω=1 eigenvectors, if the coefficient of the $^1\Pi$ basis function in the eigenfunction that is dominated by $^3\Pi$ character is designated as c($^1\Pi$; $^3\Pi$), for example, then the ratio of the fluorescence lifetimes may be estimated as

$$\frac{\tau(^3\Pi_1)}{\tau(^1\Pi_1)} = \frac{|c(\,^1\Pi;\ ^1\Pi)|^2}{|c(\,^1\Pi;\ ^3\Pi)|^2}\,\frac{(T_0(\,^1\Pi))^3}{(T_0(\,^3\Pi))^3}\ . \qquad (5.4)$$

Here we have used the fact that for both the $^1\Pi_1$ and $^3\Pi_1$ states the source of oscillator strength for the transition to or from the $\widetilde{X}\ ^1\Sigma^+$ ground state is the amount of $^1\Pi$ character in the wavefunction.

By choosing term energies of T($^3\Sigma^+$) = 19000, T($^3\Pi$) = 20063, T($^1\Pi$) = 24735, and T($^3\Delta$) = 25000 cm^{-1}, we are able to reproduce the measured locations of the $\widetilde{a}1$ (assumed $^3\Pi_1$) and $\widetilde{B}$ (assumed $^1\Pi_1$) states. Further, the calculation of the ratio of the lifetimes according to equation (4) provides $\tau(^3\Pi_1)/\tau(^1\Pi_1) = 56.7$, which compares to a measured ratio of $\tau(\widetilde{a}1)/\tau(\widetilde{B}) \approx 183$. While these two values seem somewhat different, they are in much better agreement than the measured lifetime ratio, $\tau(^3\Pi_1)/\tau(^1\Pi_1)$, found for the

copper halides: 7.3 for CuCl; 7.8 for CuBr, and 3.8 for CuI, which have similar state energies as CuCCH. This suggests that either the halogen assists in the spin-orbit coupling, giving the triplet states greater oscillator strength or that there might be a systematic error in the lifetime measurements that were conducted previously. As regards the previous measurements, it is worth noting that these measurements were performed using a Broida oven and that for at least some of the states biexponential decays were observed due to collisional processes.[64, 66, 70] Further, the biexponential decays were most evident for the $^1\Pi$ and $^1\Sigma^+$ states, which have the shortest lifetimes.[70] I surmise that the $^3\Pi_1$ state may be collisionally deactivated to the lower-lying $^3\Pi_2$ or $^3\Sigma^+$ state more rapidly than it fluoresces, leading to an erroneously short measurement of its fluorescence lifetime in the Broida oven. Due to the long lifetime of these triplet states, it is possible that these collisional processes may not have been evident in the measured decay curves. Our measurements, conducted far downstream from the expansion orifice in a supersonic beam, are not subject to collisional effects.

5.5 Conclusion

In this investigation, the optical spectrum of CuCCH has been investigated. Three excited electronic states have been found, and have been identified as the [20.2] $\tilde{a}1$, $\tilde{A}$ $^1\Sigma^+$, and the [24.7] $\tilde{B}$ $^1\Pi$ states. The [20.2] $\tilde{a}1$ state is thought to be of $^3\Pi_1$ symmetry, becoming optically allowed in transitions from the ground $\tilde{X}$ $^1\Sigma^+$ state via spin-orbit mixing with the [24.7] $\tilde{B}$ $^1\Pi$ state. A close correspondence with the electronic structure of the copper halides is noted, leading to the conclusion that CuCCH can be described as primarily an ionic molecule, in both the ground and the lowest group of excited states.

5.6 References

1 R. D. Rieke and M. V. Hanson, Tetrahedron **53,** 1925-56 (1997).

2 R. D. Rieke, Science (Washington, D. C., 1883-) **246,** 1260-4 (1989).

3 M. S. Kharasch and P. O. Tawney, Journal of the American Chemical Society **63,** 2308-15 (1941).

4 H. Gilman, R. G. Jones, and L. A. Woods, J. Org. Chem. **17,** 1630-4 (1952).

5 J. Hassan, M. Sevignon, C. Gozzi, E. Schulz, and M. Lemaire, Chem. Rev. (Washington, D. C.) **102,** 1359-469 (2002).

6 R. D. Stephens and C. E. Castro, J. Org. Chem. **28,** 3313-15 (1963).

7 K. Sonogashira, Y. Tohda, and N. Hagihara, Tetrahedron Lett., 4467-70 (1975).

8 K. Sonogashira, J. Organomet. Chem. **653,** 46-9 (2002).

9 R. Chinchilla and C. Najera, Chem. Rev. (Washington, DC, U. S.) **107,** 874-922 (2007).

10 R. Chinchilla and C. Najera, Chem. Soc. Rev. **40,** 5084-121 (2011).

11 E. E. Hughes and R. Gordon, Jr., Anal. Chem. **31,** 94-8 (1959).

12 H. S. P. Mueller, D. T. Halfen, and L. M. Ziurys, J. Mol. Spectrosc. **272,** 23-6 (2012).

13 J. J. Van Vaals, W. L. Meerts, and A. Dymanus, Journal of Molecular Spectroscopy **106,** 280-98 (1984).

14 M. A. Anderson and L. M. Ziurys, Astrophys. J. **439,** L25-L8 (1995).

15 G. K. Corlett, A. M. Little, and A. M. Ellis, Chemical Physics Letters **249,** 53-8 (1996).

16 G. K. Corlett, M. S. Beardah, and A. M. Ellis, Journal of Molecular Spectroscopy **185,** 202-3 (1997).

17 M. A. Brewster, A. J. Apponi, J. Xin, and L. M. Ziurys, Chem. Phys. Lett. **310,** 411-22 (1999).

18 D. W. Tokaryk, A. G. Adam, and W. S. Hopkins, Journal of Molecular Spectroscopy **230,** 54-61 (2005).

[19] A. M. R. P. Bopegedera, C. R. Brazier, and P. F. Bernath, Chem. Phys. Lett. **136,** 97-100 (1987).

[20] A. M. R. P. Bopegedera, C. R. Brazier, and P. F. Bernath, J. Mol. Spectrosc. **129,** 268-75 (1988).

[21] M. A. Anderson and L. M. Ziurys, Astrophys. J. **444,** L57-L60 (1995).

[22] A. J. Marr, J. Perry, and T. C. Steimle, J. Chem. Phys. **103,** 3861-3 (1995).

[23] M. Li and J. A. Coxon, Journal of Molecular Spectroscopy **180,** 287-97 (1996).

[24] M. Li and J. A. Coxon, Journal of Molecular Spectroscopy **176,** 206-10 (1996).

[25] M. Li and J. A. Coxon, Journal of Molecular Spectroscopy **184,** 395-400 (1997).

[26] M. Li and J. A. Coxon, Journal of Molecular Spectroscopy **183,** 250-62 (1997).

[27] M. Li and J. A. Coxon, Journal of Molecular Spectroscopy **196,** 14-9 (1999).

[28] D. W. Tokaryk, A. G. Adam, and M. E. Slaney, Chemical Physics Letters **433,** 264-7 (2007).

[29] B. P. Nuccio, A. J. Apponi, and L. M. Ziurys, Chem. Phys. Lett. **247,** 283-8 (1995).

[30] G. M. Greetham and A. M. Ellis, Journal of Molecular Spectroscopy **206,** 198-9 (2001).

[31] M. J. Dick, P. M. Sheridan, J. G. Wang, and P. F. Bernath, Journal of Molecular Spectroscopy **233,** 197-202 (2005).

[32] H.-P. Loock, A. Bérces, B. Simard, and C. Linton, J. Chem. Phys. **107,** 2720-6 (1997).

[33] J. Min, D. T. Halfen, M. Sun, B. Harris, and L. M. Ziurys, J. Chem. Phys. **136,** 244310/1-10 (2012).

[34] D. B. Grotjahn, A. J. Apponi, M. A. Brewster, J. Xin, and L. M. Ziurys, Angew. Chem., Int. Ed. **37,** 2678-81 (1998).

[35] A. J. Apponi, M. A. Brewster, and L. M. Ziurys, Chem. Phys. Lett. **298,** 161-9 (1998).

[36] P. M. Sheridan, M. K. L. Binns, M. Sun, J. Min, M. P. Bucchino, D. T. Halfen, and L. M. Ziurys, J. Mol. Spectrosc. **269,** 231-5 (2011).

[37] B. Z. Li and L. M. Ziurys, Astrophys. J. **482,** L215-L7 (1997).

[38] G. V. Chertihin, L. Andrews, and P. R. Taylor, J. Am. Chem. Soc. **116,** 3513-18 (1994).

[39] C. Apetrei, H. Ding, and J. P. Maier, Physical Chemistry Chemical Physics **9,** 3897-901 (2007).

[40] C. Cabezas, S. Mata, A. M. Daly, A. Martin, J. L. Alonso, and J. Cernicharo, Journal of Molecular Spectroscopy **278,** 31-4 (2012).

[41] N. E. Schultz and D. G. Truhlar, J. Chem. Theory Comput. **1,** 42-54 (2005).

[42] X. Guo, S. Wang, J. Li, L. Jiang, and J. Zhang, J. Mol. Spectrosc. **256,** 242-6 (2009).

[43] Y.-J. Liu, Z.-X. Zhao, M.-X. Song, H.-X. Zhang, and C.-C. Sun, J. Phys. Chem. A **114,** 5035-40 (2010).

[44] D. J. Brugh, R. S. DaBell, and M. D. Morse, J. Chem. Phys. **121,** 12379-85 (2004).

[45] M. Sun, D. T. Halfen, J. Min, B. Harris, D. J. Clouthier, and L. M. Ziurys, J. Chem. Phys. **133,** 174301/1-8 (2010).

[46] L. Shao, S. M. Sickafoose, J. D. Langenberg, D. J. Brugh, and M. D. Morse, J. Chem. Phys. **112,** 4118-23 (2000).

[47] N. F. Lindholm, D. J. Brugh, G. K. Rothschopf, S. M. Sickafoose, and M. D. Morse, J. Chem. Phys. **118,** 2190-6 (2003).

[48] N. Lindholm and M. D. Morse, J. Chem. Phys. **127,** 084317/1-5 (2007).

[49] A. Martinez, N. Lindholm, and M. D. Morse, J. Chem. Phys. **135,** 134308/1-8 (2011).

[50] B. A. Mamyrin, V. I. Karataev, D. V. Shmikk, and V. A. Zagulin, Zh. Eksp. Teor. Fiz. **64,** 82-9 (1973).

[51] W. C. Wiley and I. H. McLaren, Rev. Sci. Instrum. **26,** 1150 - 7 (1955).

[52] J. Cariou and P. Luc, *Atlas du Spectre d'Absorption de la Molécule de Tellure entre 18,500 - 23,800 cm^{-1}* (CNRS, Paris, 1980).

[53] M. D. Morse, in *Methods of Experimental Physics: Atomic, Molecular, and Optical Physics*, Vol. II Atoms and Molecules, edited by F. B. Dunning and R. Hulet (Academic Press, Inc., Orlando, Florida, 1996), pp. 21-47.

[54] P. R. Bevington, *Data Reduction and Error Analysis for the Physical Sciences* (McGraw-Hill, New York, 1969).

[55] Gaussian 03, Revision B.02, M. J. Frisch, G. W. Trucks, H. B. Schlegel, G. E. Scuseria, M. A. Robb, J. R. Cheeseman, J. A. J. Montgomery, T. Vreven, K. N. Kudin, J. C. Burant, J. M. Millam, S. S. Iyengar, J. Tomasi, V. Barone, B. Mennucci, M. Cossi, G. Scalmani, N. Rega, G. A. Petersson, H. Nakatsuji, M. Hada, M. Ehara, K. Toyota, R. Fukuda, J. Hasegawa, M. Ishida, T. Nakajima, Y. Honda, O. Kitao, H. Nakai, M. Klene, X. Li, J. E. Knox, H. P. Hratchian, J. B. Cross, C. Adamo, J. Jaramillo, R. Gomperts, R. E. Stratmann, O. Yazyev, A. J. Austin, R. Cammi, C. Pomelli, J. W. Ochterski, P. Y. Ayala, K. Morokuma, G. A. Voth, P. Salvador, J. J. Dannenberg, V. G. Zakrzewski, S. Dapprich, A. D. Daniels, M. C. Strain, O. Farkas, D. K. Malick, A. D. Rabuck, K. Raghavachari, J. B. Foresman, J. V. Ortiz, Q. Cui, A. G. Baboul, S. Clifford, J. Cioslowski, B. B. Stefanov, G. Liu, A. Liashenko, P. Piskorz, I. Komaromi, R. L. Martin, D. J. Fox, T. Keith, M. A. Al-Laham, C. Y. Peng, A. Nanayakkara, M. Challacombe, P. M. W. Gill, B. R. Johnson, W. Chen, M. W. Wong, C. Gonzalez, and J. A. Pople, Gaussian, Inc., Pittsburgh PA, (2003).

[56] R. G. Dickinson, R. T. Dillon, and F. Rasetti, Phys. Rev. **34,** 582-90 (1929).

[57] K. M. Ervin and W. C. Lineberger, Journal of Physical Chemistry **95,** 1167-77 (1991).

[58] H. Hotop and W. C. Lineberger, Journal of Physical and Chemical Reference Data **14,** 731-50 (1985).

[59] R. S. Mulliken, Physical Review **26,** 1-32 (1925).

[60] C. Koukounas and A. Mavridis, Journal of Physical Chemistry A **112,** 11235-50 (2008).

[61] C. Sousa, W. A. De Jong, R. Broer, and W. C. Nieuwpoort, Mol. Phys. **92,** 677-86 (1997).

[62] M. Guichemerre, G. Chambaud, and H. Stoll, Chem. Phys. **280,** 71-102 (2002).

[63] F. Ahmed, R. F. Barrow, A. H. Chojnicki, C. Dufour, and J. Schamps, Journal of Physics B **15,** 3801-18 (1982).

[64] R. E. Steele and H. P. Broida, J. Chem. Phys. **69,** 2300-5 (1978).

[65] T. Parekunnel, L. C. O'Brien, T. L. Kellerman, T. Hirao, M. Elhanine, and P. F. Bernath, J. Mol. Spectrosc. **206,** 27-32 (2001).

[66] J. M. Delaval, Y. Lefebvre, H. Bocquet, P. Bernage, and P. Niay, Chem. Phys. **111,** 129-36 (1987).

[67] P. R. Rao and J. K. Brody, J. Chem. Phys. **35,** 776-87 (1961).

[68] T. Hirao and P. F. Bernath, Can. J. Phys. **79,** 299-343 (2001).

[69] I. Hikmet, C. Dufour, and B. Pinchemel, Chemical Physics **172,** 147-52 (1993).

[70] Y. Lefebvre, J. M. Delaval, P. Bernage, and P. Niay, Chem. Phys. Lett. **139,** 212-14 (1987).

[71] G. P. Mishra, R. Tripathi, S. B. Rai, K. N. Upadhya, and D. K. Rai, J. Mol. Spectrosc. **85,** 245-7 (1981).

[72] P. Kowalczyk, I. Hikmet, and N. Sadeghi, Chem. Phys. **160,** 73-83 (1992).

[73] G. P. Mishra, V. B. Singh, and S. B. Rai, Can. J. Phys. **70,** 764-71 (1992).

[74] K. P. R. Nair, Chem. Phys. Lett. **92,** 271-2 (1982).

[75] G. P. Mishra, S. B. Rai, and K. N. Upadhya, Can. J. Phys. **57,** 824-7 (1979).

[76] J. M. Delaval, J. Schamps, A. Ramirez-Solis, and J. P. Daudey, J. Chem. Phys. **97,** 6588-92 (1992).

[77] H. Lefebvre-Brion and R. W. Field, *The Spectra and Dynamics of Diatomic Molecules* (Elsevier, Amsterdam, 2004).

[78] C. F. Fischer, *The Hartree-Fock Method for Atoms* (John Wiley & Sons, New York, 1977).

APPENDIX A

ROTATIONALLY RESOLVED SPECTRA, TABULATED LINE POSITIONS AND FITTED PARAMETERS OF OsN

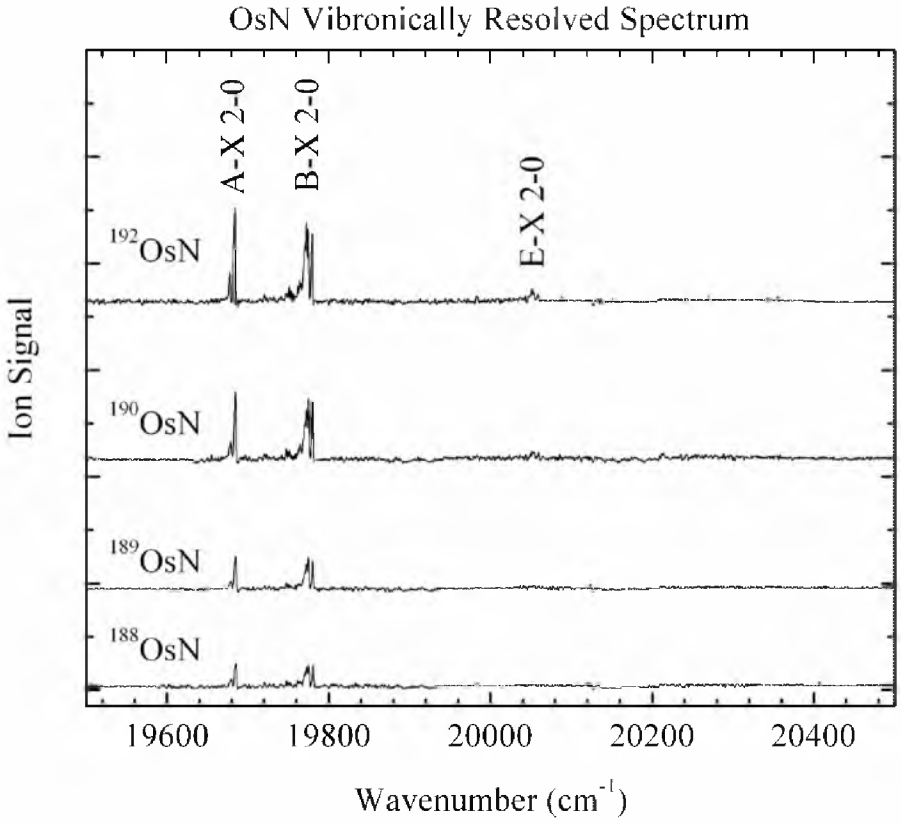

Figure A.1 Vibronically resolved spectrum of OsN, over the 19500-20500 cm^{-1} range.

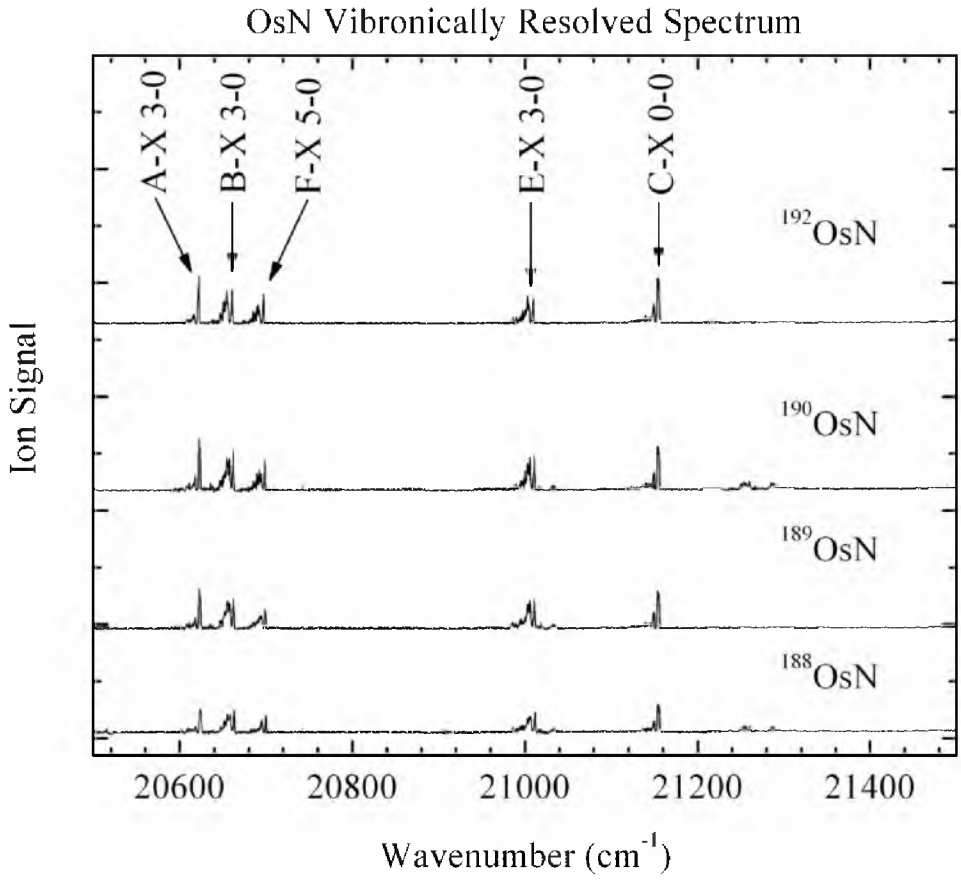

Figure A.2 Vibronically resolved spectrum of OsN, over the 20500-21500 cm^{-1} range.

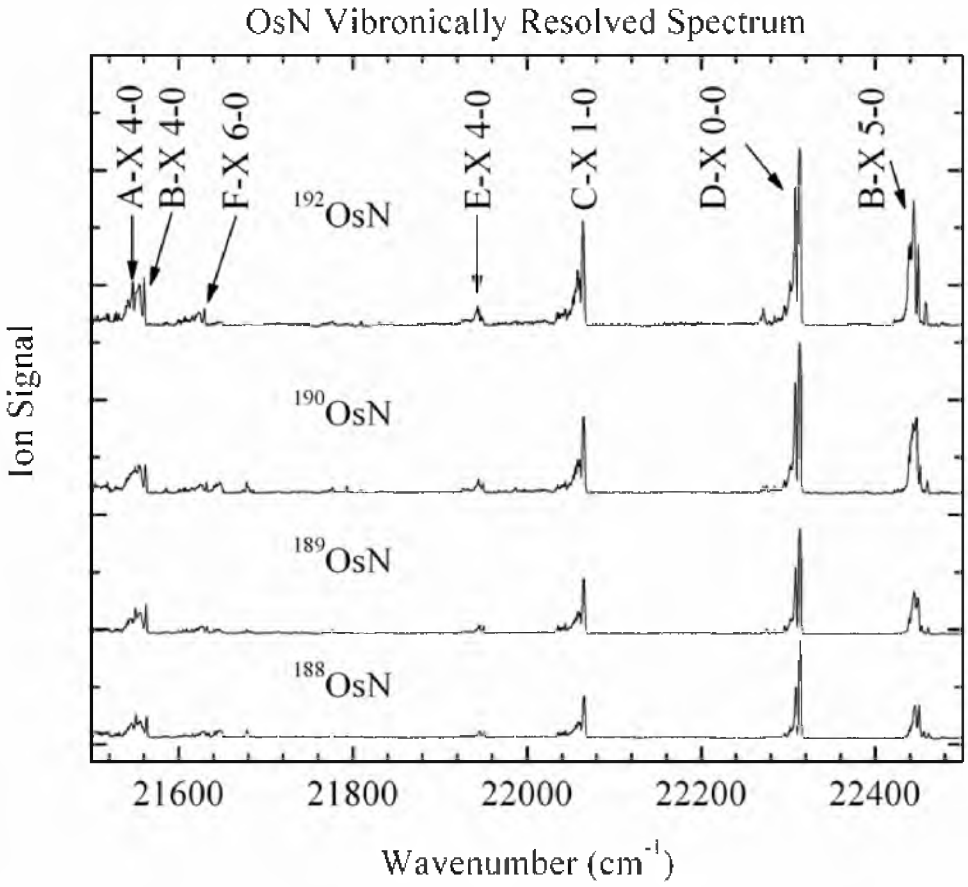

Figure A.3 Vibronically resolved spectrum of OsN, over the 21500-22500 cm^{-1} range.

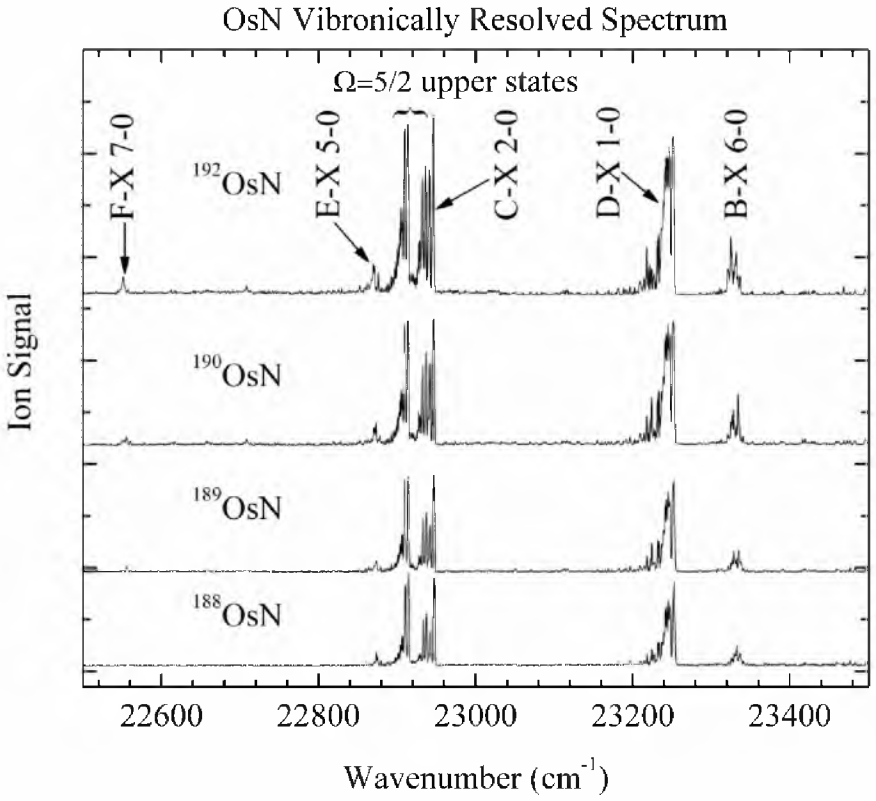

Figure A.4 Vibronically resolved spectrum of OsN, over the 22500-23500 cm^{-1} range.

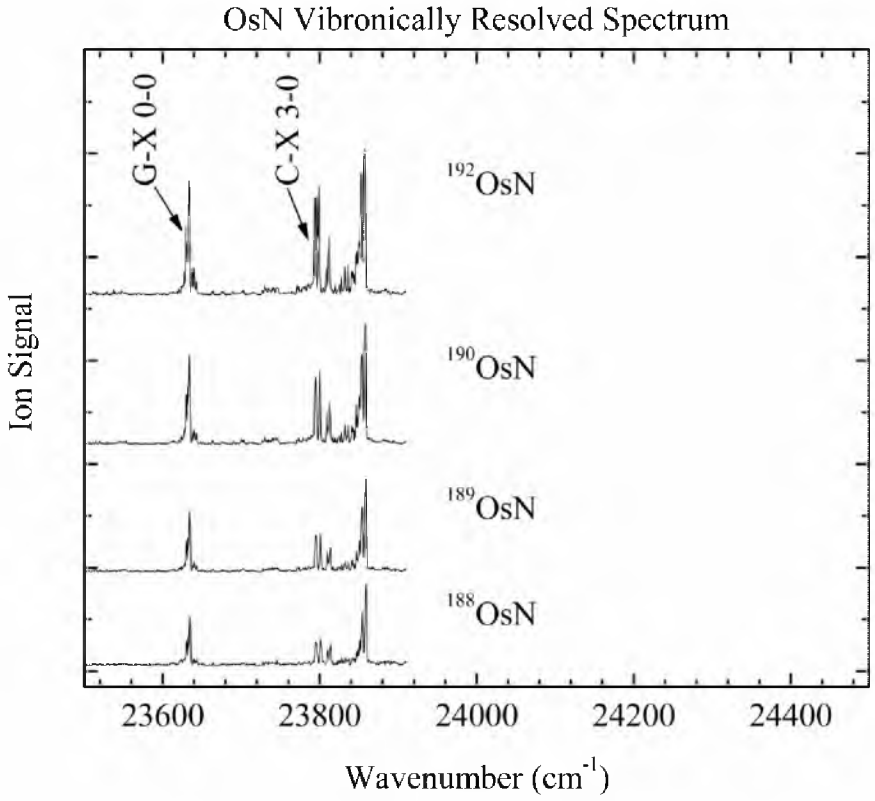

Figure A.5 Vibronically resolved spectrum of OsN, over the 23500-24500 cm^{-1} range.

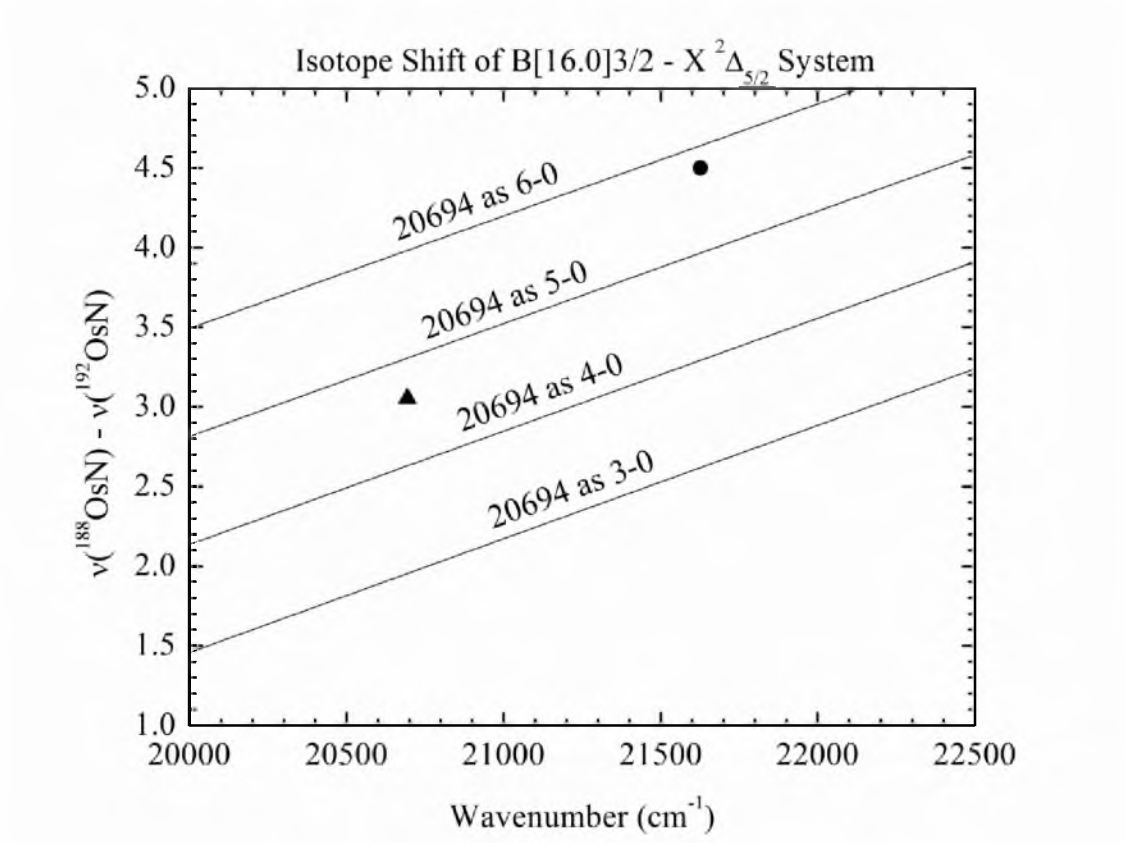

Figure A.6 Isotope shifts, $\nu(^{188}Os^{14}N) - \nu(^{192}Os^{14}N)$, measured in high resolution (solid triangle) and low resolution (solid circle), *vs.* band origin for the B $^2\Pi_{3/2} \leftarrow$ X $^2\Delta_{5/2}$ system. The solid lines provide calculated isotope shifts for the various assignments of the vibrational bands. It appears likely that the 20694 cm^{-1} band is the 5-0 band of the system, but this vibrational numbering is not as definite as that determined for the other band systems. The remaining bands that were observed were too weak to be identified in the spectrum of the minor isotope, $^{188}Os^{14}N$.

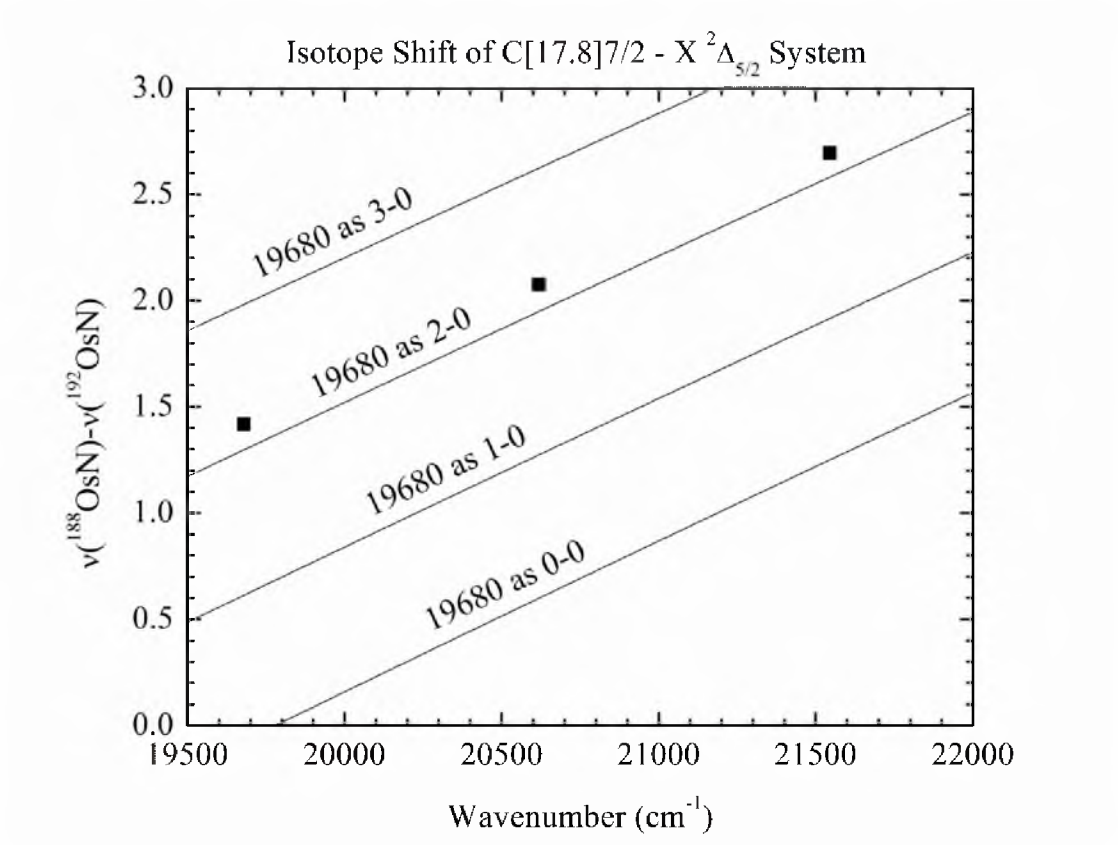

Figure A.7 Isotope shifts, $\nu(^{188}Os^{14}N) - \nu(^{192}Os^{14}N)$, measured in high resolution (solid squares), *vs.* band origin for the C $^2\Phi_{7/2} \leftarrow X\,^2\Delta_{5/2}$ system. The solid lines provide calculated isotope shifts for the various assignments of the vibrational bands. From the close correspondence, it is evident that the 19680 cm^{-1} band is the 2-0 band of the system.

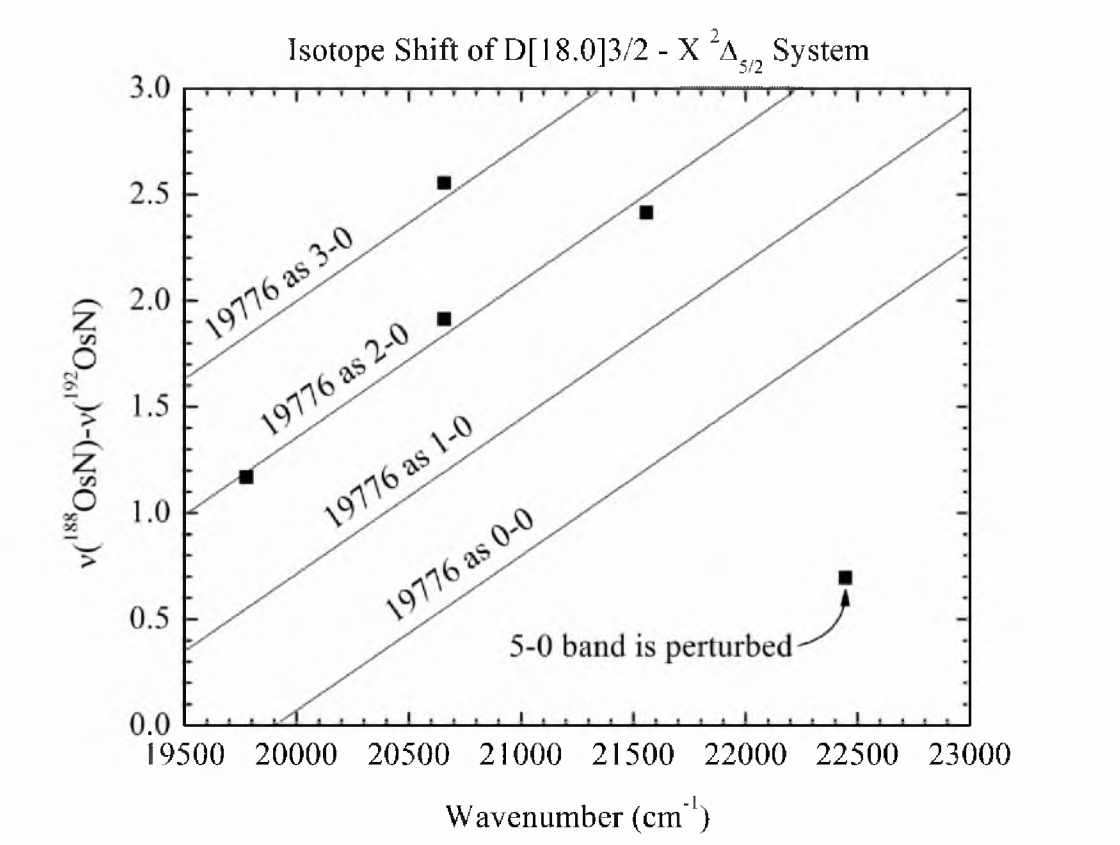

Figure A.8 Isotope shifts, $\nu(^{188}Os^{14}N) - \nu(^{192}Os^{14}N)$, measured in high resolution (solid squares), *vs.* band origin for the D $^2\Pi_{3/2} \leftarrow$ X $^2\Delta_{5/2}$ system. Two bands are found near 20660 cm^{-1} in the $^{188}Os^{14}N$ isotope; both are plotted in the figure, although it is evident that one fits into the system and the other is an interloper. The solid lines provide calculated isotope shifts for the various assignments of the vibrational bands. From the close correspondence, it is evident that the 19776 cm^{-1} band is the 2-0 band of the system.

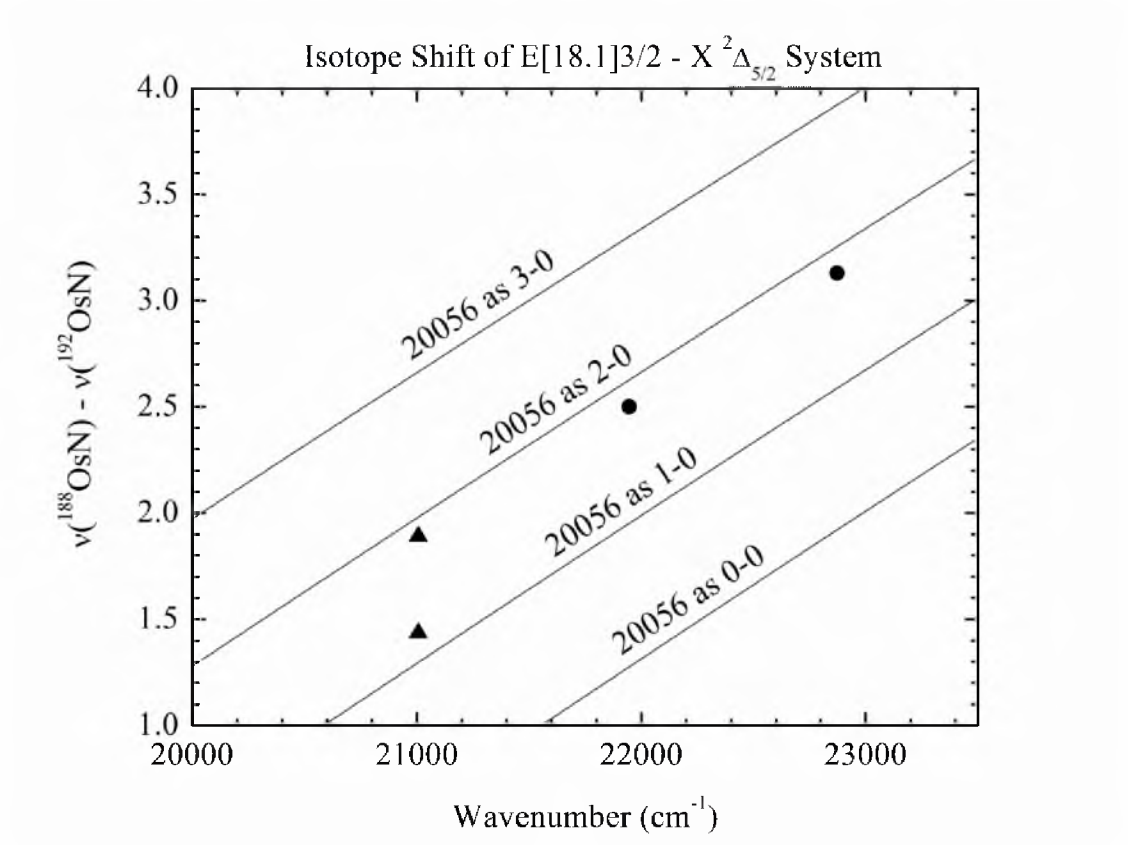

Figure A.9 Isotope shifts, $\nu(^{188}Os^{14}N) - \nu(^{192}Os^{14}N)$, measured in high resolution (solid triangles) and in low resolution (solid circles), *vs.* band origin for the E $^2\Pi_{3/2} \leftarrow$ X $^2\Delta_{5/2}$ system. The $^{188}Os^{14}N$ isotopic modification displays two bands near the 21006 cm^{-1} feature, which was examined in high resolution. Both isotope shifts are plotted, although it seems evident that one belongs to this system and the second is an interloper. The solid lines provide calculated isotope shifts for the various assignments of the vibrational bands. From the close correspondence, it is evident that the 20056 cm^{-1} band is the 2-0 band of the system, and that the 21006 cm^{-1} feature that was rotationally resolved is the 3-0 band.

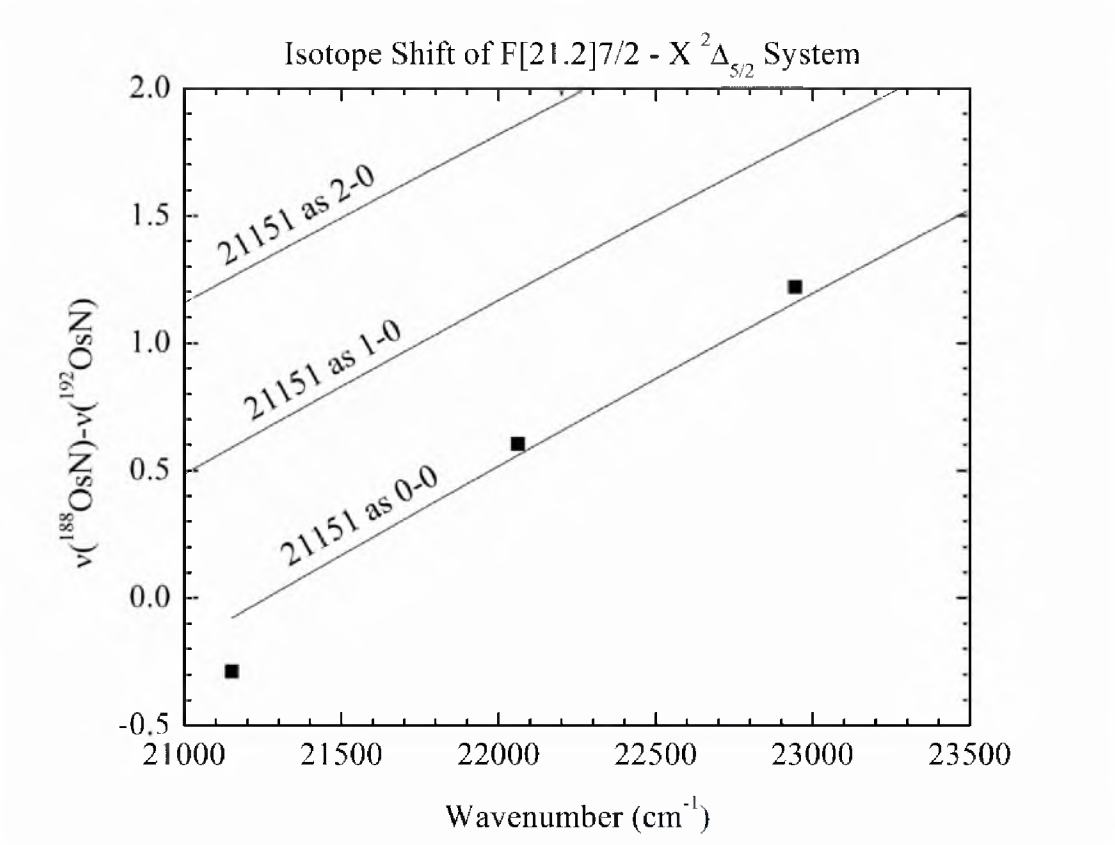

Figure A.10 Isotope shifts, $\nu(^{188}Os^{14}N) - \nu(^{192}Os^{14}N)$, measured in high resolution (solid squares), *vs.* band origin for the F $^2\Phi_{7/2} \leftarrow$ X $^2\Delta_{5/2}$ system. The solid lines provide calculated isotope shifts for the various assignments of the vibrational bands. From the close correspondence, it is evident that the 21151 cm^{-1} band is the 0-0 band of the system.

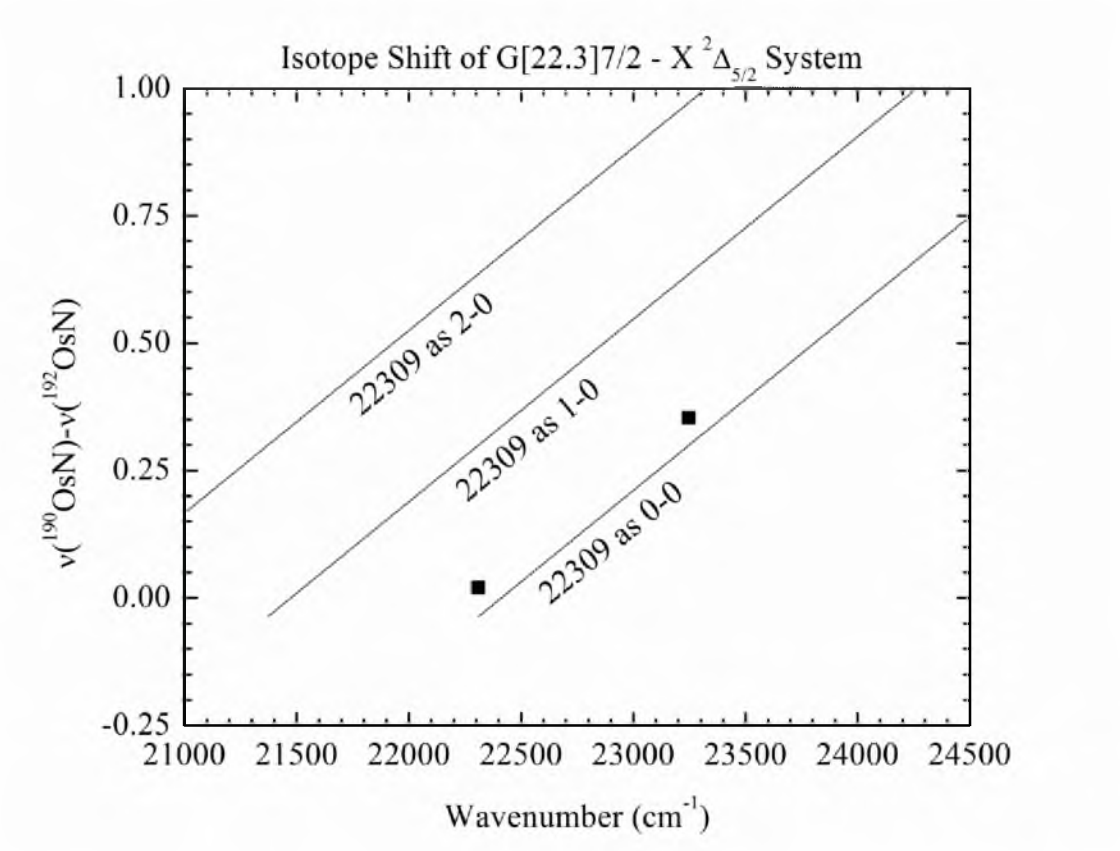

Figure A.11 Isotope shifts, $\nu(^{190}Os^{14}N) - \nu(^{192}Os^{14}N)$, measured in high resolution (solid squares), *vs.* band origin for the G $^2\Phi_{7/2} \leftarrow$ X $^2\Delta_{5/2}$ system. The solid lines provide calculated isotope shifts for the various assignments of the vibrational bands. From the close correspondence, it is evident that the 22309 cm^{-1} band is the 0-0 band of the system.

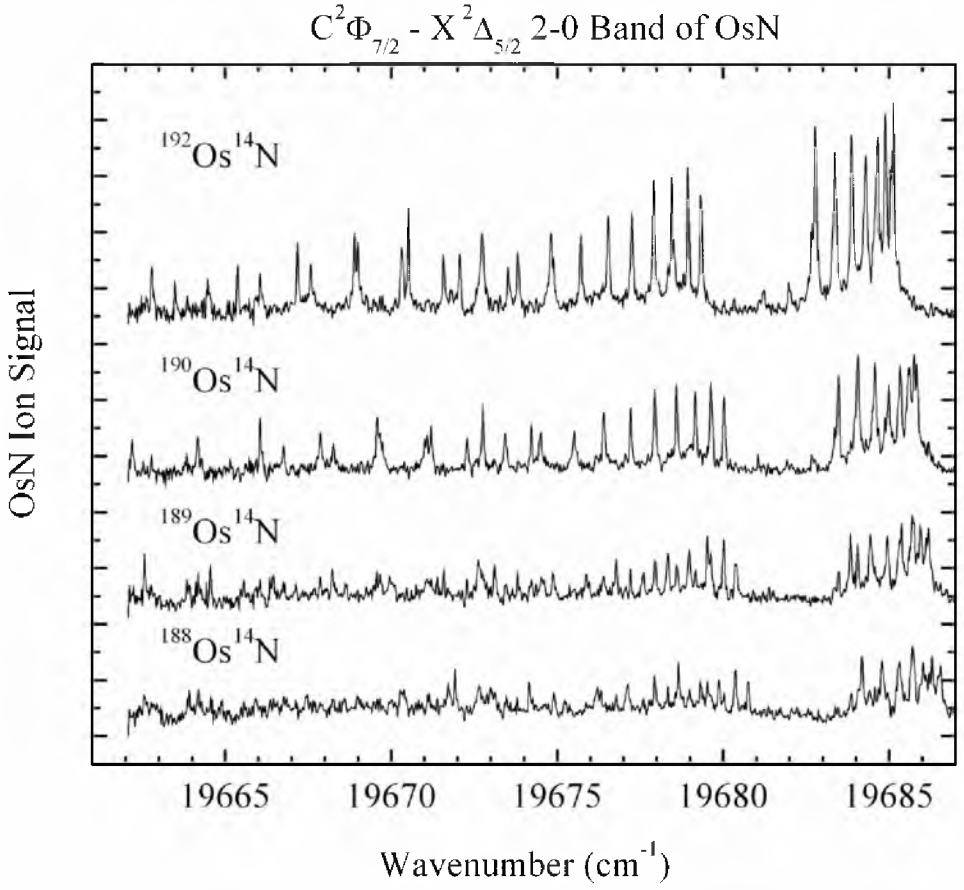

Figure A.12 Rotationally resolved scan over the C $^2\Phi_{7/2} \leftarrow$ X $^2\Delta_{5/2}$ 2-0 band of OsN, showing the isotopes $^{192}Os^{14}N$, $^{190}Os^{14}N$, $^{189}Os^{14}N$, and $^{188}Os^{14}N$.

Table A.1 Fitted rotational lines of the C[17.8] $\frac{7}{2} \leftarrow$ X $^2\Delta_{5/2}$ 2-0 band.

Line	$^{192}Os^{14}N$	$^{190}Os^{14}N$	$^{189}Os^{14}N$	$^{188}Os^{14}N$
P(4.5)	19674.886(9)	19675.592(-4)	19675.959(3)	19676.315(-10)
P(5.5)	19673.525(0)	19674.221(-5)	19674.600(-10)	19674.904(27)
P(6.5)	19672.068(-1)	19672.758(1)	19673.116(14)	19673.466(5)
P(7.5)	19670.516(8)	19671.209(6)	19671.586(-1)	19671.929(-4)
P(8.5)	19668.898(-3)	19669.580(5)	19669.947(6)	19670.274(19)
P(9.5)	19667.174(5)	19667.869(0)	19668.227(8)	
P(10.5)	19665.373(5)	19666.049(18)	19666.425(6)	19666.765(5)
P(11.5)	19663.485(4)	19664.173(6)	19664.549(-9)	19664.876(2)
P(12.5)		19662.189(15)	19662.571(-7)	
Q(3.5)	19679.329(-6)	19680.028(-11)	19680.403(-9)	19680.762(-23)
Q(4.5)	19678.935(1)	19679.633(-3)	19680.019(-12)	19680.365(-14)
Q(5.5)	19678.462(0)	19679.164(-8)	19679.523(9)	19679.875(1)
Q(6.5)	19677.906(-3)	19678.593(3)	19678.977(-6)	19679.314(1)
Q(7.5)	19677.251(6)	19677.943(8)	19678.331(-6)	19678.659(10)
Q(8.5)	19676.535(-9)	19677.214(5)	19677.592(0)	19677.939(-4)
Q(9.5)	19675.715(-8)	19676.404(-2)	19676.782(-9)	19677.112(3)
Q(10.5)	19674.811(-7)	19675.508(-10)	19675.872(-5)	19676.211(-2)
Q(11.5)	19673.817(-2)	19674.508(0)	19674.877(-1)	19675.225(-8)
Q(12.5)	19672.739(0)	19673.427(5)	19673.815(-17)	19674.152(-13)
Q(13.5)	19671.580(-4)	19672.288(-19)	19672.634(0)	19672.985(-10)
Q(14.5)	19670.320(9)		19671.384(-1)	19671.721(2)
Q(15.5)	19668.988(6)			19670.380(6)
Q(16.5)	19667.574(0)	19668.259(7)	19668.624(1)	19668.979(-17)
Q(17.5)	19666.049(19)	19666.755(4)	19667.123(-8)	
Q(18.5)	19664.486(-11)	19665.151(16)		
Q(19.5)	19662.785(11)	19663.470(18)	19663.838(0)	
R(2.5)	19682.767(0)	19683.472(-10)	19683.840(2)	19684.178(9)
R(3.5)	19683.366(-3)	19684.061(-2)	19684.434(4)	19684.785(0)
R(4.5)	19683.867(6)	19684.569(0)	19684.942(7)	19685.298(-3)
R(5.5)	19684.296(1)	19684.994(0)	19685.372(2)	19685.711(9)
R(6.5)	19684.644(-8)	19685.332(1)	19685.707(5)	

Table A.1 (continued)

R(7.5)	19684.904(-16)		19685.946(18)	19686.288(22)
R(8.5)	19685.048(6)	19685.750(2)	19686.126(4)	19686.497(-22)
R(9.5)	19685.116(18)	19685.830(2)	19686.193(16)	19686.553(3)
R(10.5)	19685.116(12)	19685.830(-4)	19686.193(9)	19686.553(-4)
R(11.5)	19685.048(-12)	19685.750(-15)	19686.126(-16)	19686.461(-6)
R(12.5)	19684.879(-21)	19685.574(-18)	19685.946(-15)	19686.288(-12)
R(13.5)		19685.283(10)		19686.020(-10)
R(14.5)	19684.230(14)	19684.949(-7)	19685.312(2)	19685.644(15)
R(15.5)		19684.493(13)	19684.873(3)	19685.222(-2)
R(16.5)	19683.303(-18)	19683.969(14)		19684.687(8)
R(17.5)	19682.669(8)	19683.363(12)	19683.746(-5)	19684.071(14)
R(18.5)	19681.992(-10)	19682.680(1)		19683.381(7)
R(19.5)	19681.215(-14)	19681.929(-29)		
R(20.5)	19680.332(2)	19681.057(-24)	19681.377(16)	19681.739(-4)
R(21.5)				
R(22.5)	19678.337(5)			
Fitted Spectroscopic Constants				
ν_0	19680.0008(22)	19680.6951(27)	19681.0735(22)	19681.4181(29)
B_2'	0.448884(27)	0.449076(33)	0.449355(29)	0.449523(35)
r_2' (Å)	1.696324(51)	1.696569(62)	1.696350(55)	1.696345(66)
B_0''	0.491921(34)	0.492121(36)	0.492469(42)	0.492660(36)
r_0'' (Å)	1.620422(56)	1.620673(59)	1.620395(69)	1.620379(59)

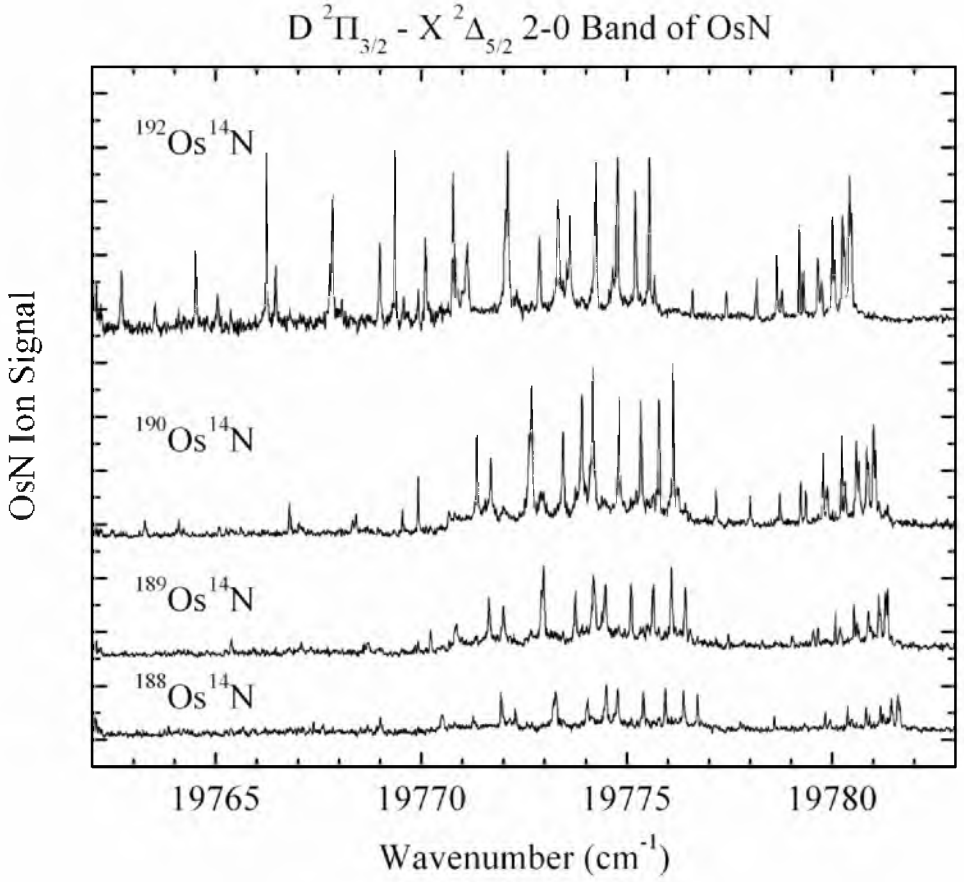

Figure A.13 Rotationally resolved scan over the D $^2\Pi_{3/2} \leftarrow$ X $^2\Delta_{5/2}$ 2-0 band of OsN, showing the isotopes $^{192}Os^{14}N$, $^{190}Os^{14}N$, $^{189}Os^{14}N$, and $^{188}Os^{14}N$.

Table A.2 Fitted rotational lines of the B[18.0] $\frac{3}{2} \leftarrow$ X $^2\Delta_{5/2}$ 2-0 band.

Line	$^{192}Os^{14}N$	$^{190}Os^{14}N$	$^{189}Os^{14}N$	$^{188}Os^{14}N$
P(2.5)	19773.328(14)	19773.907(7)	19774.195(17)	19774.502(6)
P(3.5)	19772.103(12)	19772.680(6)	19772.973(11)	19773.280(-1)
P(4.5)	19770.781(8)	19771.353(8)	19771.650(7)	19771.943(8)
P(5.5)	19769.361(6)	19769.921(18)	19770.227(6)	19770.513(14)
P(6.5)	19767.850(-3)	19768.419(-1)	19768.706(5)	19769.005(0)
P(7.5)	19766.233(-3)	19766.791(9)	19767.083(9)	19767.387(-2)
P(8.5)	19764.514(2)	19765.100(-15)	19765.384(-8)	19765.665(3)
P(9.5)	19762.707(-4)	19763.279(-7)		19763.849(4)
P(10.5)		19761.374(-12)		
Q(2.5)	19775.549(9)	19776.125(6)	19776.430(1)	19776.723(4)
Q(3.5)	19775.207(10)	19775.784(6)	19776.091(-2)	19776.384(1)
Q(4.5)	19774.772(6)	19775.346(6)	19775.642(8)	19775.938(8)
Q(5.5)	19774.239(3)	19774.811(4)	19775.113(1)	19775.406(4)
Q(6.5)	19773.606(3)	19774.179(3)	19774.480(-1)	19774.775(0)
Q(7.5)	19772.876(2)	19773.453(-2)	19773.752(-4)	19774.052(-9)
Q(8.5)	19772.062(-12)	19772.622(1)	19772.923(-4)	
Q(9.5)	19771.119(5)	19771.695(1)	19772.002(-10)	19772.293(-6)
Q(10.5)	19770.122(-21)	19770.676(-3)		19771.265(-3)
Q(11.5)	19768.990(-9)	19769.548(5)	19769.852(-6)	
Q(12.5)	19767.773(-11)	19768.336(-2)		19768.916(3)
Q(13.5)	19766.455(-8)			
Q(14.5)	19765.048(-14)		19765.923(-29)	
Q(15.5)	19763.527(-4)			
R(2.5)	19778.652(8)	19779.231(4)	19779.545(-8)	19779.834(-1)
R(3.5)	19779.202(4)	19779.781(-1)	19780.079(3)	19780.378(1)
R(4.5)	19779.656(-2)	19780.227(1)	19780.534(-3)	19780.825(4)
R(5.5)	19780.002(2)	19780.586(-7)	19780.880(1)	19781.178(1)
R(6.5)	19780.259(-2)	19780.838(-5)	19781.136(-1)	19781.433(0)
R(7.5)	19780.428(-15)	19781.007(-18)	19781.299(-9)	19781.600(-11)
R(8.5)	19780.471(-1)	19781.052(-5)	19781.351(-2)	19781.656(-9)
R(9.5)	19780.428(3)	19781.007(1)		19781.628(-21)

Table A.2 (continued)

R(10.5)	19780.293(1)	19780.873(-1)	19781.173(-1)	19781.473(-3)
R(11.5)	19780.067(-7)	19780.647(-10)	19780.936(2)	19781.243(-7)
R(12.5)	19779.740(-11)	19780.317(-11)	19780.605(1)	19780.905(-1)
R(13.5)	19779.306(-7)	19779.884(-7)	19780.190(-13)	19780.478(-3)
R(14.5)	19778.782(-9)	19779.358(-8)	19779.656(-7)	19779.955(-8)
R(15.5)	19778.157(-8)	19778.729(-3)	19779.026(-2)	19779.322(0)
R(16.5)	19777.423(5)	19778.002(3)	19778.297(5)	19778.589(10)
R(17.5)	19776.601(8)	19777.171(15)	19777.473(9)	19777.765(14)
R(18.5)	19775.674(18)	19776.258(13)	19776.542(23)	
R(19.5)	19774.657(22)			
Fitted Spectroscopic Constants				
ν_0	19775.9842(22)	19776.5575(20)	19776.8575(23)	19777.1537(18)
$B_2^{'}$	0.443198(28)	0.443391(34)	0.443691(29)	0.443864(36)
$r_2^{'}$ (Å)	1.707171(54)	1.707411(65)	1.707144(56)	1.707125(69)
$B_0^{''}$	0.491921(34)	0.492121(36)	0.492469(42)	0.492660(36)
$r_0^{''}$ (Å)	1.620422(56)	1.620673(59)	1.620395(69)	1.620379(59)

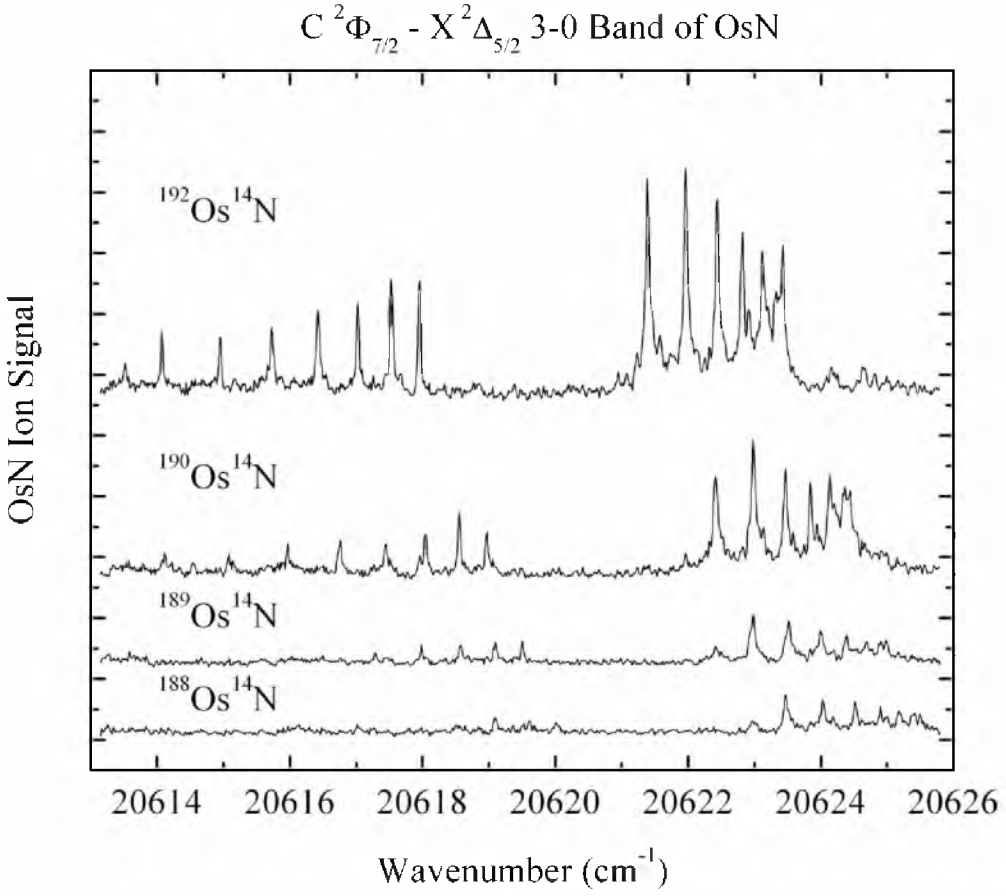

Figure A.14 Rotationally resolved scan over the C $^2\Phi_{7/2} \leftarrow$ X $^2\Delta_{5/2}$ 3-0 band of OsN, showing the isotopes $^{192}Os^{14}N$, $^{190}Os^{14}N$, $^{189}Os^{14}N$, and $^{188}Os^{14}N$.

Table A.3 Fitted rotational lines of the C[17.8] $\frac{7}{2} \leftarrow$ X $^2\Delta_{5/2}$ 3-0 band.

Line	$^{192}Os^{14}N$	$^{190}Os^{14}N$	$^{189}Os^{14}N$	$^{188}Os^{14}N$
P(4.5)	20613.521(1)	20614.547(-5)		20615.571(17)
Q(3.5)	20617.954(-5)	20618.967(4)	20619.500(4)	20620.016(6)
Q(4.5)	20617.532(2)	20618.551(5)	20619.095(-7)	20619.610(-5)
Q(5.5)	20617.023(2)	20618.043(4)	20618.572(10)	20619.097(-2)
Q(6.5)	20616.423(3)	20617.444(3)	20617.980(4)	20618.508(-16)
Q(7.5)	20615.726(7)	20616.760(-7)	20617.284(8)	20617.794(3)
Q(8.5)	20614.948(0)	20615.969(-2)	20616.492(17)	20617.018(-8)
Q(9.5)	20614.071(1)	20615.082(7)		20616.132(-3)
Q(10.5)		20614.115(4)	20614.665(3)	
R(2.5)	20621.390(3)	20622.413(3)	20622.970(-20)	20623.467(3)
R(3.5)	20621.964(-3)	20622.984(1)	20623.523(-2)	20624.032(7)
R(4.5)	20622.437(0)	20623.466(-6)	20624.003(-4)	20624.519(-4)
R(5.5)	20622.817(4)	20623.843(1)	20624.387(-1)	20624.899(-2)
R(6.5)	20623.119(-7)	20624.136(-1)	20624.692(-12)	20625.178(9)
R(7.5)	20623.308(3)	20624.364(-30)	20624.902(-20)	20625.392(-7)
R(8.5)	20623.425(-7)	20624.440(0)	20624.987(5)	20625.495(-6)
R(9.5)	20623.425(7)	20624.440(14)	20624.987(23)	20625.495(6)
R(10.5)	20623.362(-7)	20624.364(11)	20624.902(33)	20625.417(3)
R(11.5)	20623.204(-19)	20624.204(0)	20624.779(-9)	
R(12.5)	20622.914(9)	20623.945(-5)	20624.542(-31)	20624.992(-12)
R(13.5)		20623.584(0)		20624.614(8)
R(14.5)		20623.133(3)		20624.181(-11)
R(15.5)	20621.578(3)			
R(16.5)	20620.948(2)	20621.966(-4)		20622.976(13)
Fitted Spectroscopic Constants				
ν_0	20618.6759(21)	20619.6994(28)	20620.2285(68)	20620.7522(29)
B_3'	0.445763(34)	0.445907(30)	0.446417(50)	0.446307(27)
r_3' (Å)	1.702252(65)	1.702587(57)	1.701923(95)	1.702446(51)
B_0''	0.491921(34)	0.492121(36)	0.492469(42)	0.492660(36)
r_0'' (Å)	1.620422(56)	1.620673(59)	1.620395(69)	1.620379(59)

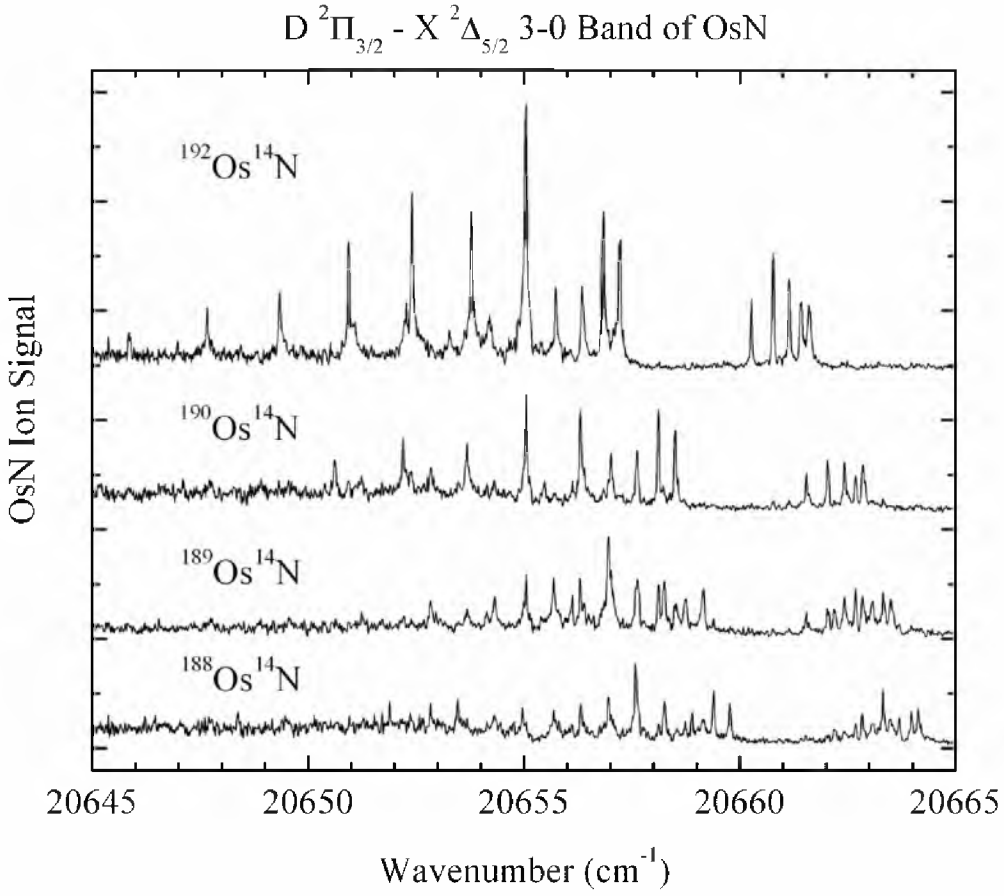

Figure A.15 Rotationally resolved scan over the D $^2\Pi_{3/2} \leftarrow$ X $^2\Delta_{5/2}$ 3-0 band of OsN, showing the isotopes $^{192}Os^{14}N$, $^{190}Os^{14}N$, $^{189}Os^{14}N$, and $^{188}Os^{14}N$.

Table A.4 Fitted rotational lines of the D[18.0] $\frac{3}{2} \leftarrow X\ ^2\Delta_{5/2}$ 3-0 band.

Line	$^{192}Os^{14}N$	$^{190}Os^{14}N$	$^{189}Os^{14}N$	$^{188}Os^{14}N$
P(2.5)	20655.038(-3)	20656.307(2)		20656.956(-11)
P(3.5)	20653.777(0)	20655.047(4)	20655.050(9)	20655.691(-5)
P(4.5)	20652.410(0)	20653.682(0)	20653.686(1)	20654.315(4)
P(5.5)	20650.934(-1)	20652.196(7)	20652.222(-18)	20652.835(7)
P(6.5)	20649.340(7)	20650.618(-3)		20651.282(-26)
P(7.5)	20647.662(-11)		20648.904(3)	
P(8.5)	20645.855(-9)			
Q(2.5)	20657.220(1)	20658.503(-8)	20658.519(-13)	20659.135(0)
Q(3.5)	20656.841(-4)	20658.114(-3)	20658.117(2)	20658.736(16)
Q(4.5)	20656.347(-2)	20657.619(-2)	20657.635(-14)	20658.261(1)
Q(5.5)	20655.738(4)	20657.016(-3)	20657.016(-4)	20657.651(10)
Q(6.5)	20655.038(-8)	20656.307(-8)	20656.303(-10)	20656.956(-5)
Q(7.5)	20654.206(3)	20655.477(-2)		20656.110(21)
Q(8.5)	20653.269(8)			
R(2.5)	20660.273(7)	20661.546(10)	20661.546(20)	20662.206(-5)
R(3.5)	20660.777(-6)	20662.057(-12)	20662.048(5)	20662.683(12)
R(4.5)	20661.146(7)	20662.427(-1)	20662.429(1)	20663.078(1)
R(5.5)	20661.425(0)	20662.680(16)	20662.680(16)	
R(6.5)	20661.581(7)	20662.852(4)	20662.842(8)	20663.540(-18)
R(7.5)	20661.635(5)	20662.903(5)	20662.902(-6)	
R(8.5)	20661.581(3)	20662.852(-4)		
R(9.5)	20661.425(-8)	20662.680(-1)		
Fitted Spectroscopic Constants				
ν_0	20657.6998(22)	20658.9758(26)	20658.9902(56)	20659.6125(63)
B_3'	0.437158(69)	0.437205(62)	0.437150(122)	0.438055(104)
r_3' (Å)	1.718924(136)	1.719447(122)	1.719868(240)	1.718407(204)
B_0''	0.491921(34)	0.492121(36)	0.492469(42)	0.492660(36)
r_0'' (Å)	1.620422(56)	1.620673(59)	1.620395(69)	1.620379(59)

Table A.5 Fitted rotational lines of the extra band that appears in the $^{189}Os^{14}N$ and $^{188}Os^{14}N$ masses in the scan over the $D[18.0]\frac{3}{2} \leftarrow X\ ^2\Delta_{5/2}$ 3-0 band.

Line	$^{192}Os^{14}N$	$^{190}Os^{14}N$	$^{189}Os^{14}N$	$^{188}Os^{14}N$
P(2.5)			20656.956(-7)	20657.587(-3)
P(3.5)			20655.690(-2)	20656.316(7)
P(4.5)			20654.318(1)	20654.970(-17)
P(5.5)			20652.838(1)	20653.468(5)
P(6.5)			20651.245(4)	20651.886(-3)
P(7.5)			20649.559(-9)	20650.186(-3)
P(8.5)			20647.731(9)	20648.366(7)
P(9.5)				20646.460(-7)
P(10.5)				20644.428(-5)
Q(2.5)			20659.155(-19)	20659.773(-1)
Q(3.5)			20658.744(7)	20659.395(-7)
Q(4.5)			20658.258(-2)	20658.897(-5)
Q(5.5)			20657.635(16)	20658.261(27)
Q(6.5)			20656.956(-19)	20657.587(-14)
Q(7.5)			20656.119(-6)	20656.761(-13)
Q(8.5)				20655.812(2)
Q(9.5)			20654.136(-3)	20654.764(5)
R(2.5)			20662.204(-6)	20662.836(0)
R(3.5)			20662.680(8)	20663.321(5)
R(4.5)			20663.055(14)	20663.697(10)
R(5.5)			20663.322(16)	20663.979(-1)
R(6.5)			20663.498(1)	20664.127(11)
R(7.5)			20663.546(4)	20664.193(-4)
R(8.5)			20663.498(-8)	20664.127(3)
R(9.5)			20663.322(-2)	
Fitted Spectroscopic Constants				
ν_0			20659.6166(37)	20660.2533(36)
B'			0.437498(117)	0.437678(65)
r'(Å)			1.719184(230)	1.719146(128)
B_0''	0.491921(34)	0.492121(36)	0.492469(42)	0.492660(36)
r_0''(Å)	1.620422(56)	1.620673(59)	1.620395(69)	1.620379(59)

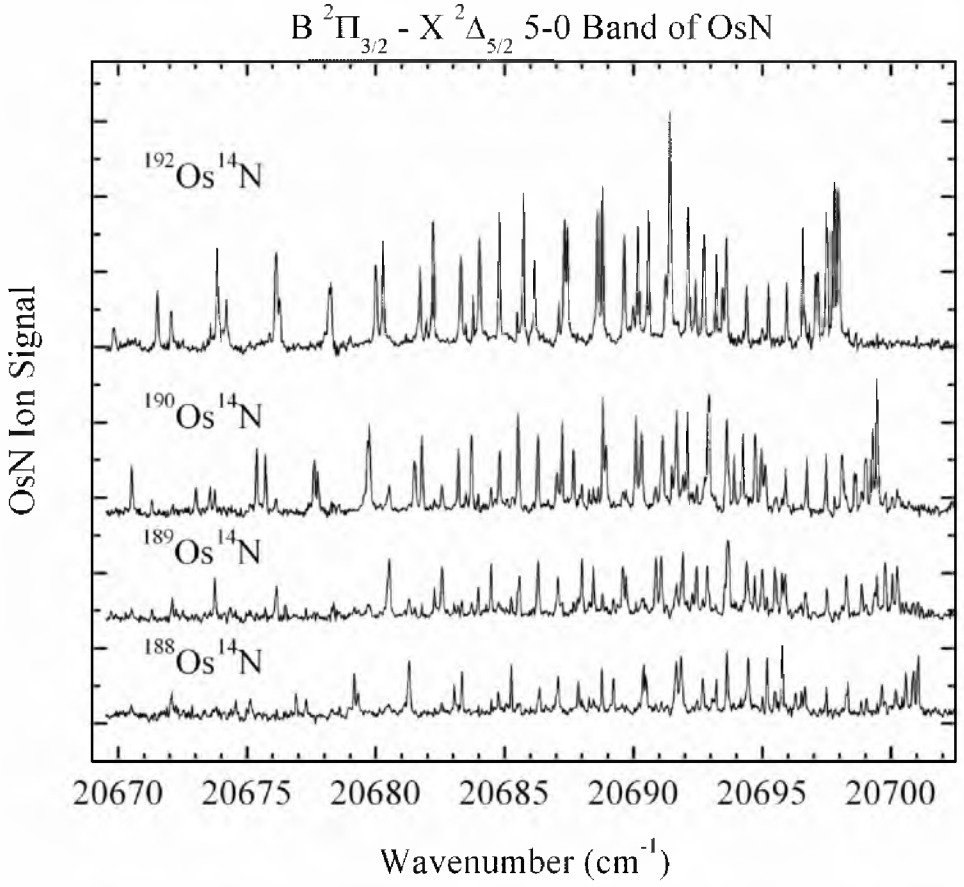

Figure A.16 Rotationally resolved scan over the B $^2\Pi_{3/2} \leftarrow$ X $^2\Delta_{5/2}$ 5-0 band of OsN, showing the isotopes $^{192}Os^{14}N$, $^{190}Os^{14}N$, $^{189}Os^{14}N$, and $^{188}Os^{14}N$.

Table A.6 Fitted rotational lines of the B[16.0] $\frac{3}{2} \leftarrow X\ ^2\Delta_{5/2}$ 5-0 band.

Line	$^{192}Os^{14}N$	$^{190}Os^{14}N$	$^{189}Os^{14}N$	$^{188}Os^{14}N$
P(2.5)	20691.414(8)	20692.927(-5)	20693.698(-5)	20694.458(13)
P(3.5)	20690.176(-13)	20691.673(-11)	20692.445(-13)	20693.216(-5)
P(4.5)	20688.807(-13)	20690.315(-22)	20691.070(-8)	20691.852(-12)
P(5.5)	20687.320(-6)	20688.817(-4)	20689.585(-4)	20690.384(-25)
P(6.5)	20685.732(-8)	20687.228(-6)	20687.997(-8)	20688.783(-15)
P(7.5)	20684.032(-8)	20685.525(-4)	20686.286(2)	20687.074(-8)
P(8.5)	20682.221(-7)	20683.712(-1)	20684.474(3)	20685.257(-2)
P(9.5)	20680.293(0)	20681.795(-4)	20682.562(-7)	20683.342(-8)
P(10.5)	20678.260(3)	20679.748(12)	20680.520(3)	20681.296(6)
P(11.5)	20676.131(-9)	20677.618(0)		20679.164(-4)
P(12.5)	20673.855(17)	20675.375(-9)	20676.140(-12)	20676.900(8)
P(13.5)	20671.524(-14)	20673.013(-8)	20673.754(12)	20674.567(-21)
P(14.5)			20671.309(-16)	20672.072(1)
Q(2.5)	20693.610(-3)	20695.119(-11)	20695.875(4)	20696.652(8)
Q(3.5)	20693.223(-3)	20694.727(-6)	20695.491(3)	20696.279(-5)
Q(4.5)	20692.735(-10)	20694.239(-13)	20694.991(7)	20695.772(7)
Q(5.5)	20692.125(-6)	20693.627(-8)	20694.389(3)	20695.182(-9)
Q(6.5)	20691.414(-12)	20692.892(12)	20693.658(17)	20694.458(-2)
Q(7.5)	20690.581(-5)	20692.081(-4)	20692.867(-19)	20693.629(1)
Q(8.5)	20689.638(2)	20691.136(4)	20691.914(-3)	20692.696(-2)
Q(9.5)	20688.600(-6)	20690.098(-4)	20690.864(1)	20691.662(-15)
Q(10.5)	20687.428(8)	20688.936(1)	20689.711(-3)	20690.487(4)
Q(11.5)	20686.164(5)	20687.671(-2)	20688.449(-9)	20689.220(5)
Q(12.5)	20684.791(0)	20686.287(5)	20687.062(1)	20687.865(-17)
Q(13.5)	20683.299(5)	20684.802(2)	20685.572(3)	20686.361(0)
Q(14.5)	20681.711(-4)		20683.972(4)	20684.759(5)
Q(15.5)	20679.999(0)		20682.278(-10)	20683.045(11)
Q(16.5)	20678.188(-7)			20681.246(-8)
Q(17.5)	20676.269(-16)			20679.311(0)
Q(18.5)	20674.202(12)		20676.494(-11)	20677.298(-24)
Q(19.5)	20672.062(4)		20674.335(-1)	20675.136(-11)
Q(20.5)	20669.832(-25)		20672.089(-15)	20672.857(10)
Q(21.5)			20669.705(-1)	20670.512(-13)

Table A.7 Fitted rotational lines of the B[16.0] $\frac{3}{2} \leftarrow X\ ^2\Delta_{5/2}$ 5-0 band.

R(2.5)	20696.647(18)	20698.172(-6)		
R(3.5)	20697.156(-4)	20698.634(21)	20699.439(-9)	20700.206(6)
R(4.5)	20697.516(14)	20699.028(5)	20699.792(16)	20700.567(25)
R(5.5)	20697.790(8)	20699.279(22)	20700.058(19)	20700.857(5)
R(6.5)	20697.954(1)	20699.439(20)	20700.238(-3)	20701.010(10)
R(7.5)	20697.998(4)		20700.282(2)	20701.047(23)
R(8.5)	20697.954(-14)	20699.439(5)	20700.238(-17)	20701.010(-2)
R(9.5)	20697.754(12)	20699.279(-8)	20700.058(-9)	20700.841(-4)
R(10.5)	20697.489(-6)	20698.992(-4)	20699.758(9)	20700.567(-11)
R(11.5)	20697.072(17)	20698.579(16)	20699.357(17)	20700.163(1)
R(12.5)	20696.571(16)	20698.100(-8)	20698.857(14)	20699.638(24)
R(13.5)	20695.951(22)	20697.476(2)	20698.262(-3)	20699.048(3)
R(14.5)	20695.242(6)	20696.735(20)	20697.502(33)	20698.321(8)
R(15.5)	20694.391(23)	20695.896(25)	20696.683(18)	20697.491(6)
R(16.5)	20693.460(10)	20694.965(11)	20695.768(-10)	20696.532(22)
R(17.5)	20692.411(4)	20693.907(15)	20694.705(-1)	20695.492(10)
R(18.5)	20691.248(3)	20692.767(-9)	20693.537(2)	
R(19.5)	20689.981(-5)	20691.490(-7)	20692.284(-19)	
R(20.5)	20688.600(-9)	20690.098(0)	20690.864(17)	
R(21.5)	20687.110(-14)	20688.628(-26)	20689.381(4)	
R(22.5)	20685.488(2)	20687.023(-26)		
R(23.5)	20683.777(-2)			
R(24.5)	20681.960(-11)			
R(25.5)	20679.999(14)	20681.502(18)		
Fitted Spectroscopic Constants				
ν_0	20694.0886(21)	20695.5895(26)	20696.3616(25)	20697.1415(27)
B_5'	0.436830(18)	0.437024(24)	0.437363(50)	0.437585(28)
r_5' (Å)	1.719569(35)	1.719803(47)	1.719449(98)	1.719329(55)
B_0''	0.491921(34)	0.492121(36)	0.492469(42)	0.492660(36)
r_0'' (Å)	1.620422(56)	1.620673(59)	1.620395(69)	1.620379(59)

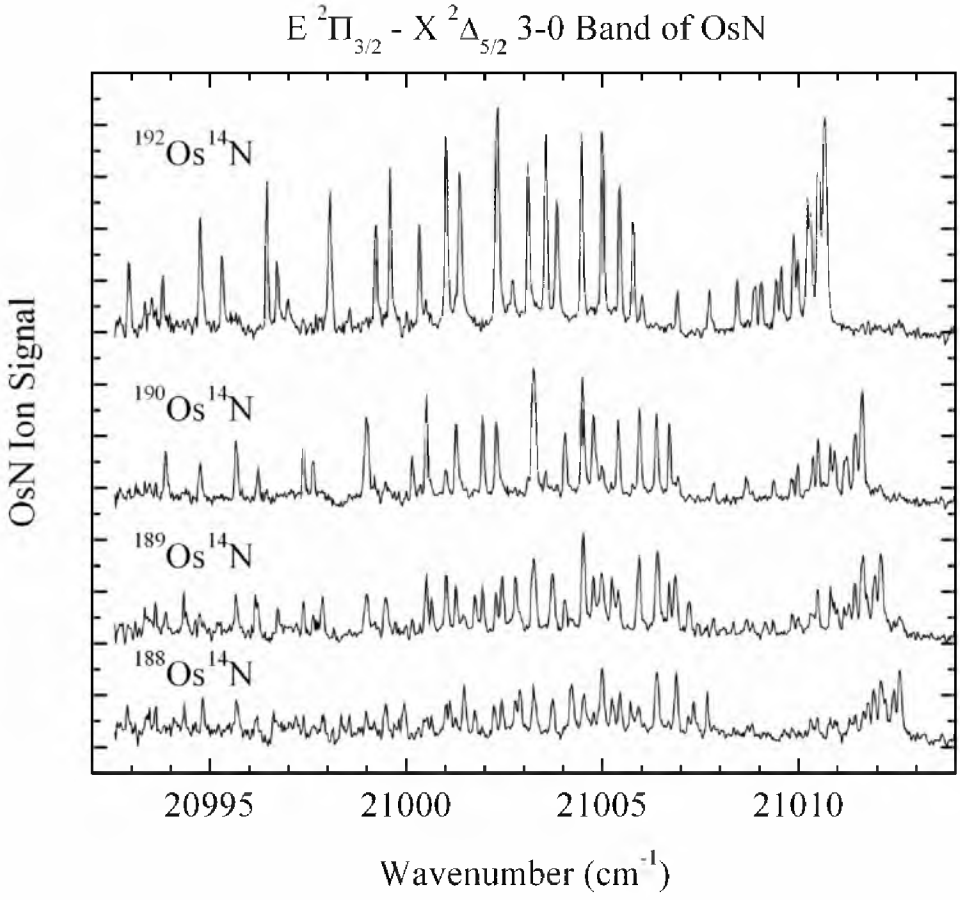

Figure A.17 Rotationally resolved scan over the E $^2\Pi_{3/2} \leftarrow$ X $^2\Delta_{5/2}$ 3-0 band of OsN, showing the isotopes $^{192}Os^{14}N$, $^{190}Os^{14}N$, $^{189}Os^{14}N$, and $^{188}Os^{14}N$.

Table A.8 Fitted rotational lines of the E[18.1] $^{3}_{2}$ ← X $^{2}\Delta_{5/2}$ 3-0 band.

Line	$^{192}Os^{14}N$	$^{190}Os^{14}N$	$^{189}Os^{14}N$	$^{188}Os^{14}N$
P(2.5)	21003.556(1)	21004.490(3)	21004.508(-16)	21004.998(-9)
P(3.5)	21002.329(2)	21003.263(4)	21003.253(11)	21003.754(5)
P(4.5)	21001.016(-8)	21001.950(-7)	21001.945(-6)	21002.437(-3)
P(5.5)	20999.589(-1)	21000.514(9)	21000.514(3)	21001.014(-3)
P(6.5)	20998.060(10)	20999.018(-14)	20998.996(2)	20999.482(9)
P(7.5)	20996.446(10)	20997.380(9)	20997.382(-1)	20997.896(-22)
P(8.5)	20994.749(-3)		20995.656(12)	20996.179(-19)
P(9.5)	20992.930(7)		20993.869(-12)	20994.341(6)
Q(2.5)	21005.778(-4)	21006.709(3)	21006.702(9)	21007.195(13)
Q(3.5)	21005.439(-4)	21006.376(-4)	21006.375(-4)	21006.882(-14)
Q(4.5)	21004.994(4)	21005.947(-11)	21005.933(1)	21006.419(12)
Q(5.5)	21004.466(-1)	21005.405(-4)	21005.404(-4)	21005.921(-25)
Q(6.5)	21003.840(-4)	21004.772(-1)	21004.770(-2)	21005.267(-3)
Q(7.5)	21003.107(2)	21004.047(-4)	21004.046(-6)	21004.527(8)
Q(8.5)	21002.295(-10)	21003.224(-6)	21003.201(13)	21003.718(-10)
Q(9.5)	21001.363(0)	21002.296(0)	21002.287(5)	21002.784(0)
Q(10.5)	21000.335(10)	21001.268(10)	21001.264(9)	21001.752(11)
Q(11.5)	20999.229(1)	21000.153(8)	21000.158(-3)	21000.642(3)
Q(12.5)	20998.028(-10)	20998.964(-16)	20998.951(-10)	20999.443(-13)
Q(13.5)	20996.710(0)	20997.627(11)	20997.629(1)	20998.122(-4)
Q(14.5)	20995.304(-1)	20996.225(6)	20996.207(14)	20996.685(23)
Q(15.5)	20993.793(8)	20994.752(-25)	20994.730(-14)	20995.208(-7)
Q(16.5)				20993.618(-22)
R(2.5)	21008.883(-4)	21009.812(5)	21009.827(-8)	21010.309(8)
R(3.5)	21009.427(-1)	21010.363(1)	21010.364(2)	21010.856(9)
R(4.5)	21009.877(0)	21010.813(2)	21010.823(-6)	21011.305(10)
R(5.5)	21010.228(2)	21011.162(6)	21011.166(5)	21011.657(12)
R(6.5)	21010.505(-18)	21011.448(-23)	21011.434(-7)	
R(7.5)	21010.666(-19)			
R(8.5)		21011.620(27)	21011.654(-5)	
R(9.5)	21010.666(10)	21011.620(-8)		

Table A.8 Fitted rotational lines of the E[18.1] $\frac{3}{2} \leftarrow X\ ^2\Delta_{5/2}$ 3-0 band.

R(10.5)				
R(11.5)	21010.297(19)	21011.231(21)		
R(12.5)	21009.981(10)	21010.923(3)	21010.908(18)	
R(13.5)	21009.561(9)	21010.500(3)	21010.482(21)	21010.982(13)
R(14.5)	21009.053(-2)	21009.984(-1)	21009.988(-6)	21010.476(-2)
R(15.5)	21008.435(0)	21009.369(-3)	21009.358(6)	21009.838(16)
R(16.5)	21007.726(-4)	21008.675(-23)	21008.678(-28)	21009.123(15)
R(17.5)	21006.911(1)	21007.834(7)	21007.833(5)	21008.348(-23)
R(18.5)	21006.010(-4)	21006.922(11)		21007.409(5)
R(19.5)				
R(20.5)				
R(21.5)	21002.712(-8)			
Fitted Spectroscopic Constants				
ν_0	21006.1985(18)	21007.1362(29)	21007.1361(27)	21007.6339(34)
B_3'	0.443446(19)	0.443602(26)	0.443905(37)	0.444045(41)
r_3' (Å)	1.706693(37)	1.707005(50)	1.706732(71)	1.706777(79)
B_0''	0.491921(34)	0.492121(36)	0.492469(42)	0.492660(36)
r_0'' (Å)	1.620422(56)	1.620673(59)	1.620395(69)	1.620379(59)

Table A.9 Fitted rotational lines of the extra band that appears in the $^{189}Os^{14}N$ and $^{188}Os^{14}N$ masses in the scan over the E[18.1] $\frac{3}{2} \leftarrow X\ ^2\Delta_{5/2}$ 3-0 band.

Line	$^{192}Os^{14}N$	$^{190}Os^{14}N$	$^{189}Os^{14}N$	$^{188}Os^{14}N$
P(2.5)			21004.981(-4)	21005.443(1)
P(3.5)			21003.729(21)	21004.205(10)
P(4.5)			21002.441(-16)	21002.898(-7)
P(5.5)			21001.021(-17)	21001.472(-2)
P(6.5)			20999.491(-6)	20999.951(-1)
P(7.5)			20997.868(1)	20998.335(-1)
P(8.5)			20996.154(2)	20996.614(8)
P(9.5)			20994.328(18)	20994.819(-7)
P(10.5)				20992.886(20)
Q(2.5)			21007.210(-12)	21007.671(-6)
Q(3.5)			21006.857(0)	21007.323(2)
Q(4.5)			21006.405(16)	21006.882(6)
Q(5.5)				21006.388(-33)
Q(6.5)			21005.243(14)	21005.722(3)
Q(7.5)				21004.998(0)
Q(8.5)				21004.184(-11)
Q(9.5)			21002.785(-3)	21003.242(10)
Q(10.5)			21001.756(6)	21002.240(-7)
Q(11.5)			21000.648(-2)	21001.116(2)
Q(12.5)			20999.458(-25)	20999.907(-1)
Q(13.5)			20998.156(-33)	
Q(14.5)			20996.721(-5)	20997.183(7)
Q(15.5)				20995.677(10)
Q(16.5)			20993.610(1)	20994.085(1)
R(2.5)			21010.322(-17)	21010.764(10)
R(3.5)			21010.853(0)	21011.305(17)
R(4.5)			21011.285(19)	21011.772(2)
R(5.5)			21011.654(4)	21012.128(1)
R(6.5)			21011.924(-9)	21012.406(-19)
R(7.5)			21012.078(-2)	

Table A.9 (continued)

R(8.5)			21012.127(11)	
R(9.5)			21012.104(1)	
R(10.5)			21011.953(20)	
R(11.5)			21011.743(2)	21012.216(6)
R(12.5)			21011.434(-15)	21011.917(-19)
R(13.5)			21010.986(11)	
R(14.5)			21010.482(-4)	21010.953(6)
R(15.5)			21009.843(18)	
R(16.5)			21009.153(-5)	21009.641(-8)
R(17.5)			21008.338(0)	21008.811(13)
R(18.5)			21007.423(8)	21007.931(-13)
Fitted Spectroscopic Constants				
ν_0			21007.6218(33)	21008.0887(27)
B'			0.443944(36)	0.444168(41)
r'(Å)			1.706657(69)	1.706733(79)
B_0''	0.491921(34)	0.492121(36)	0.492469(42)	0.492660(36)
r_0'' (Å)	1.620422(56)	1.620673(59)	1.620395(69)	1.620379(59)

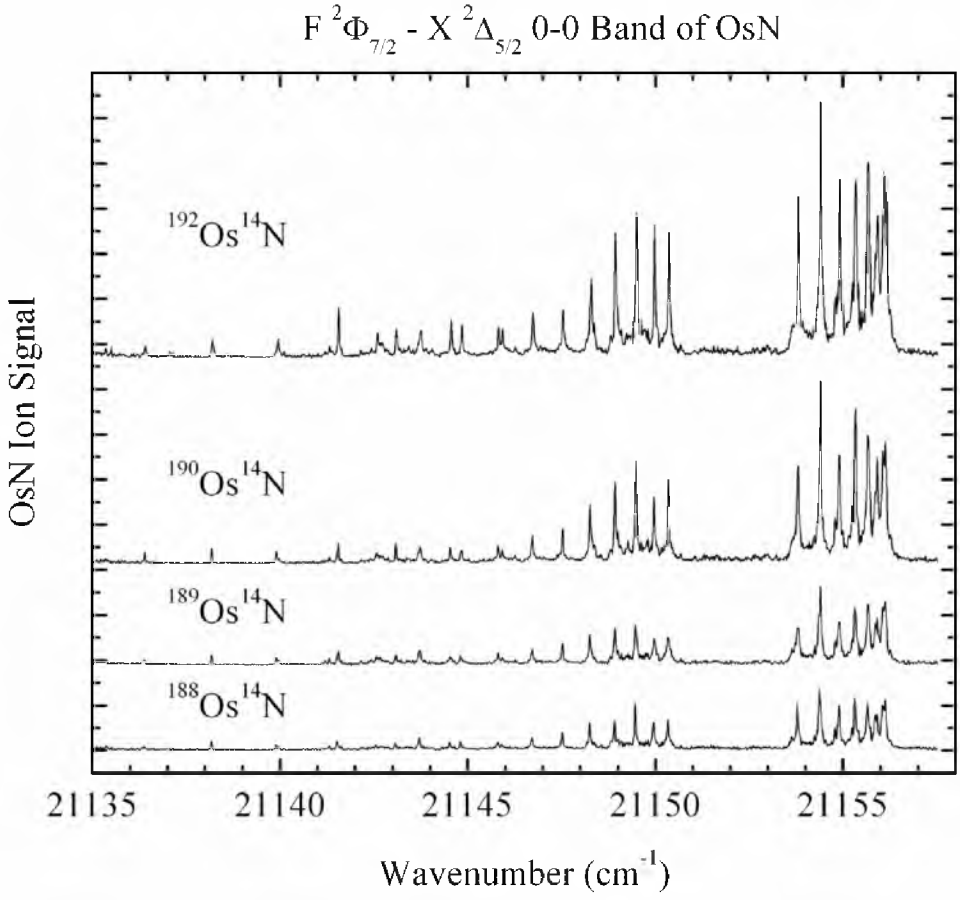

Figure A.18 Rotationally resolved scan over the $F^2\Phi_{7/2} \leftarrow X\ ^2\Delta_{5/2}$ 0-0 band of OsN, showing the isotopes $^{192}Os^{14}N$, $^{190}Os^{14}N$, $^{189}Os^{14}N$, and $^{188}Os^{14}N$.

Table A.10 Fitted rotational lines of the F[21.2] $\frac{7}{2} \leftarrow$ X $^2\Delta_{5/2}$ 0-0 band.

Line	$^{192}Os^{14}N$	$^{190}Os^{14}N$	$^{189}Os^{14}N$	$^{188}Os^{14}N$
P(4.5)	21145.930(8)	21145.919(-1)	21145.918(0)	21145.905(-3)
P(5.5)	21144.567(0)	21144.540(6)	21144.545(-1)	21144.518(10)
P(6.5)	21143.103(4)	21143.080(6)	21143.085(-2)	21143.071(-4)
P(7.5)	21141.562(1)	21141.548(-8)	21141.548(-13)	21141.521(-1)
P(8.5)	21139.943(-12)	21139.899(9)	21139.898(4)	21139.886(0)
P(9.5)	21138.207(7)	21138.175(15)	21138.175(6)	21138.169(-3)
P(10.5)	21136.415(-6)	21136.396(-10)	21136.379(-5)	21136.377(-17)
Q(3.5)	21150.371(-5)	21150.343(4)	21150.339(11)	21150.335(1)
Q(4.5)	21149.984(-7)	21149.962(-3)	21149.976(-15)	21149.952(-5)
Q(5.5)	21149.498(5)	21149.482(2)	21149.473(12)	21149.465(6)
Q(6.5)	21148.936(5)	21148.924(-2)	21148.923(0)	21148.916(-6)
Q(7.5)	21148.292(2)	21148.266(8)	21148.261(13)	21148.252(10)
Q(8.5)	21147.545(15)	21147.539(1)	21147.525(13)	21147.522(5)
Q(9.5)	21146.738(2)	21146.723(-3)	21146.725(-8)	21146.714(-9)
Q(10.5)	21145.824(9)	21145.812(1)	21145.815(-7)	21145.797(1)
Q(11.5)	21144.849(-8)	21144.810(10)	21144.807(7)	21144.805(-1)
Q(12.5)	21143.748(14)	21143.728(12)	21143.720(11)	21143.714(10)
Q(13.5)	21142.600(-4)	21142.574(0)	21142.571(-7)	21142.554(3)
Q(14.5)	21141.321(24)	21141.312(9)	21141.304(5)	21141.312(-8)
Q(15.5)		21139.970(12)	21139.977(-8)	21139.965(-1)
Q(16.5)		21138.569(-12)		
Q(17.5)		21137.054(-8)	21137.028(-1)	21137.018(8)
R(2.5)	21153.812(-2)	21153.799(-7)	21153.799(-1)	21153.779(6)
R(3.5)	21154.412(-8)	21154.403(-15)	21154.410(-17)	21154.375(6)
R(4.5)	21154.921(-8)	21154.905(-8)	21154.903(-1)	21154.897(-6)
R(5.5)	21155.338(-2)	21155.324(-4)	21155.319(6)	21155.315(0)
R(6.5)	21155.674(-1)	21155.666(-9)	21155.669(-8)	21155.656(-4)
R(7.5)	21155.924(-1)	21155.907(-1)	21155.907(3)	21155.908(-5)
R(8.5)	21156.090(-4)	21156.060(10)	21156.062(11)	21156.051(15)
R(9.5)	21156.164(0)	21156.159(-12)	21156.161(-11)	21156.157(-12)
R(10.5)	21156.164(-9)	21156.129(9)	21156.128(12)	21156.128(8)

Table A.10 (continued)

R(11.5)	21156.066(-6)			
R(12.5)	21155.866(12)	21155.862(-1)	21155.862(-1)	21155.863(-4)
R(13.5)	21155.623(-13)			
R(14.5)	21155.258(-2)	21155.251(-13)	21155.254(-19)	21155.248(-11)
R(15.5)		21154.795(2)	21154.798(-5)	21154.789(7)
R(16.5)	21154.299(-11)		21154.246(17)	
R(17.5)			21153.650(-2)	21153.635(20)
R(18.5)				
R(19.5)				21152.182(-15)
Fitted Spectroscopic Constants				
ν_0	21151.0458(25)	21151.0278(23)	21151.0312(25)	21151.0169(22)
B_0'	0.448756(20)	0.448933(23)	0.449214(33)	0.449442(30)
r_0' (Å)	1.696566(38)	1.696839(43)	1.696617(62)	1.696498(57)
B_0''	0.491921(34)	0.492121(36)	0.492469(42)	0.492660(36)
r_0'' (Å)	1.620422(56)	1.620673(59)	1.620395(69)	1.620379(59)

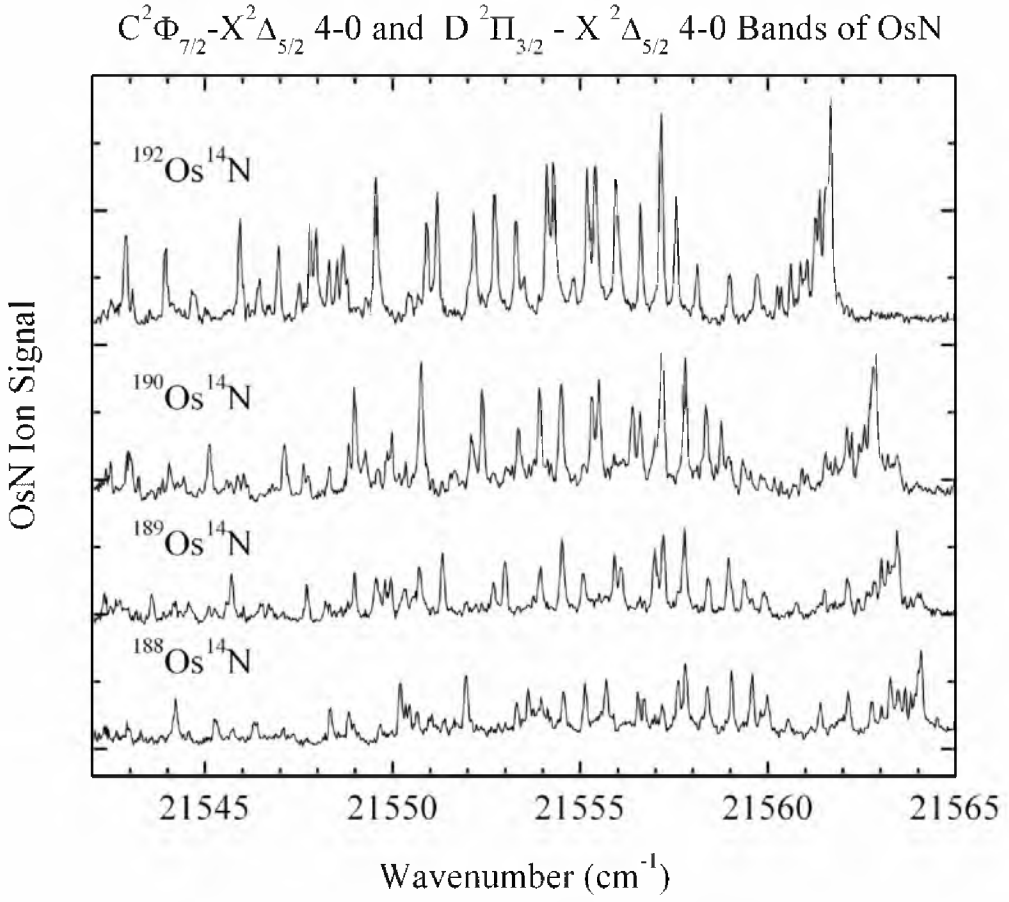

Figure A.19 Rotationally resolved scan over the C $^2\Phi_{7/2} \leftarrow$ X $^2\Delta_{5/2}$ 4-0 and D $^2\Pi_{3/2} \leftarrow$ X $^2\Delta_{5/2}$ 4-0 bands of OsN, showing the isotopes ^{192}Os^{14}N, ^{190}Os^{14}N, ^{189}Os^{14}N, and ^{188}Os^{14}N.

Table A.11 Fitted rotational lines of the C[17.8] $\frac{7}{2} \leftarrow X\ ^2\Delta_{5/2}$ 4-0 band.

Line	$^{192}Os^{14}N$	$^{190}Os^{14}N$	$^{189}Os^{14}N$	$^{188}Os^{14}N$
Q(3.5)	21543.530(-8)	21544.853(17)	21545.577(-13)	
Q(4.5)	21543.065(13)	21544.442(-22)	21545.107(6)	21545.725(39)
Q(5.5)		21543.863(4)	21544.560(3)	21545.249(-33)
Q(6.5)	21541.895(-1)	21543.227(-11)	21543.892(20)	21544.563(6)
Q(7.5)		21542.489(-26)	21543.166(-5)	
Q(8.5)			21542.316(-7)	21542.965(12)
R(2.5)	21546.954(12)	21548.317(-1)	21548.985(26)	21549.661(-1)
R(3.5)	21547.515(-9)	21548.825(23)	21549.568(-22)	21550.203(-5)
R(4.5)	21547.958(-11)	21549.278(3)	21549.951(28)	21550.642(-7)
R(5.5)	21548.295(-6)	21549.612(1)	21550.319(-6)	21550.973(1)
R(6.5)	21548.517(15)	21549.855(-10)	21550.548(-1)	
R(7.5)	21548.682(-4)	21549.981(-5)	21550.717(-36)	21551.378(-26)
R(8.5)		21549.981(27)	21550.717(-3)	21551.378(14)
R(14.5)			21548.802(10)	
Fitted Spectroscopic Constants				
ν_0	21544.3000(79)	21545.6608(105)	21546.3529(73)	21546.9949(143)
B_4'	0.442566(94)	0.441960(80)	0.442392(53)	0.442900(115)
r_4' (Å)	1.708389(181)	1.710173(155)	1.709648(102)	1.708982(222)
B_0''	0.491921(34)	0.492121(36)	0.492469(42)	0.492660(36)
r_0'' (Å)	1.620422(56)	1.620673(59)	1.620395(69)	1.620379(59)

Table A.12 Fitted rotational lines of the D[18.0] $\frac{3}{2} \leftarrow X\ ^2\Delta_{5/2}$ 4-0 band.

Line	$^{192}Os^{14}N$	$^{190}Os^{14}N$	$^{189}Os^{14}N$	$^{188}Os^{14}N$
P(2.5)	21555.410(0)	21556.601(3)	21557.215(-7)	21557.806(14)
P(3.5)	21554.108(21)	21555.317(5)	21555.918(7)	21556.541(-4)
P(4.5)	21552.721(7)	21553.922(-1)	21554.514(9)	21555.130(4)
P(5.5)	21551.190(19)	21552.395(6)	21552.995(6)	21553.615(-1)
P(6.5)	21549.553(17)	21550.757(6)	21551.335(24)	21551.955(17)
P(7.5)	21547.806(7)	21548.993(12)	21549.568(31)	21550.203(10)
P(8.5)	21545.930(6)	21547.121(7)	21547.713(6)	21548.340(-6)
P(9.5)	21543.947(-6)	21545.122(10)	21545.710(10)	21546.313(22)
P(10.5)		21542.990(28)	21543.579(23)	21544.215(2)
Q(2.5)	21557.561(11)	21558.761(6)	21559.372(1)	21559.988(-2)
Q(3.5)	21557.154(1)	21558.355(-4)	21558.954(0)	21559.580(-11)
Q(4.5)	21556.606(14)	21557.801(14)	21558.419(-1)	21559.035(-2)
Q(5.5)	21555.959(6)	21557.180(-20)	21557.779(-17)	21558.390(-13)
Q(6.5)	21555.192(0)	21556.392(-5)	21556.986(0)	21557.611(-9)
Q(7.5)	21554.286(13)	21555.496(-2)	21556.088(3)	21556.699(10)
Q(8.5)	21553.297(-10)	21554.497(-15)	21555.087(-10)	21555.696(0)
Q(9.5)	21552.171(-14)	21553.351(1)	21553.939(4)	21554.555(8)
Q(10.5)	21550.908(-1)	21552.118(-15)	21552.689(2)	21553.311(1)
Q(11.5)	21549.553(-14)	21550.757(-23)	21551.335(-17)	21551.955(-13)
Q(12.5)		21549.278(-32)	21549.800(27)	21550.452(-1)
Q(13.5)	21546.458(-13)	21547.628(11)	21548.222(-6)	21548.833(10)
Q(14.5)	21544.738(-20)	21545.888(26)	21546.475(11)	21547.089(26)
Q(15.5)	21542.880(-6)	21544.054(15)		21545.286(-19)
Q(16.5)				21543.289(13)
R(2.5)	21560.610(-12)	21561.797(-2)	21562.409(-7)	21563.027(-10)
R(3.5)	21561.045(2)	21562.239(5)	21562.842(7)	21563.470(-4)
R(4.5)	21561.375(1)	21562.571(3)	21563.203(-24)	21563.811(-15)
R(5.5)	21561.583(4)	21562.793(-8)	21563.442(-54)	21564.008(-1)
R(6.5)	21561.676(1)	21562.874(2)	21563.495(-17)	21564.085(13)
R(7.5)		21562.874(-25)	21563.442(7)	21564.085(-15)
R(8.5)	21561.534(-30)	21562.711(-9)	21563.310(-10)	21563.926(-2)

Table A.12 (continued)

R(9.5)	21561.267(-29)	21562.443(-6)	21563.028(5)	21563.662(-4)
R(10.5)	21560.871(-18)		21562.664(-19)	21563.265(8)
R(11.5)	21560.358(-9)	21561.537(12)	21562.128(10)	21562.773(-5)
R(12.5)	21559.714(13)	21560.910(16)	21561.513(0)	21562.144(0)
R(13.5)	21558.978(6)	21560.170(15)	21560.765(3)	21561.404(-2)
R(14.5)	21558.121(3)	21559.349(-24)	21559.903(0)	21560.540(0)
R(15.5)	21557.154(-10)	21558.355(-10)		21559.580(-21)
R(16.5)				
R(17.5)	21554.809(18)		21556.596(-2)	
R(18.5)	21553.494(-4)			
R(19.5)				
R(20.5)	21550.431(28)		21552.219(-8)	
Fitted Spectroscopic Constants				
ν_0	21558.0923(33)	21559.2877(38)	21559.8942(37)	21560.5073(29)
B_4'	0.432417(32)	0.432614(42)	0.432811(37)	0.433072(40)
r_4' (Å)	1.728321(64)	1.728547(84)	1.728467(74)	1.728264(80)
B_0''	0.491921(34)	0.492121(36)	0.492469(42)	0.492660(36)
r_0'' (Å)	1.620422(56)	1.620673(59)	1.620395(69)	1.620379(59)

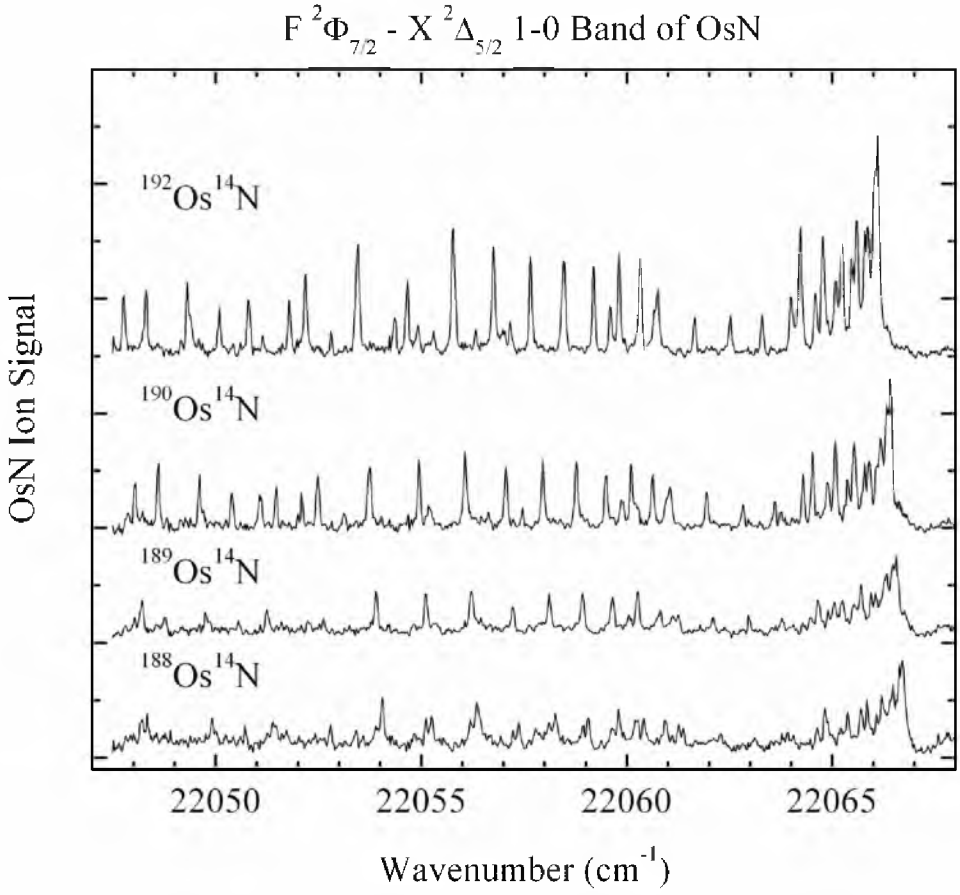

Figure A.20 Rotationally resolved scan over the F $^2\Phi_{7/2} \leftarrow$ X $^2\Delta_{5/2}$ 1-0 band of OsN, showing the isotopes $^{192}Os^{14}N$, $^{190}Os^{14}N$, $^{189}Os^{14}N$, and $^{188}Os^{14}N$.

Table A.13 Fitted rotational lines of the F[21.2] $\frac{7}{2} \leftarrow$ X $^2\Delta_{5/2}$ 1-0 band.

Line	$^{192}Os^{14}N$	$^{190}Os^{14}N$	$^{189}Os^{14}N$	$^{188}Os^{14}N$
P(4.5)	22056.326(17)	22056.636(1)		22056.934(6)
P(5.5)	22054.922(7)	22055.200(23)	22055.349(33)	22055.535(-10)
P(6.5)	22053.424(-3)	22053.721(-7)	22053.879(-8)	22054.029(-14)
P(7.5)	22051.790(27)	22052.097(14)	22052.244(22)	22052.423(-14)
P(8.5)	22050.088(30)	22050.393(18)	22050.555(10)	22050.709(-1)
P(9.5)	22048.308(15)	22048.603(13)	22048.761(6)	22048.893(18)
Q(3.5)	22060.752(18)	22061.056(10)	22061.257(-29)	22061.379(-5)
Q(4.5)	22060.331(10)	22060.626(11)	22060.817(-19)	22060.943(1)
Q(5.5)	22059.814(2)	22060.110(2)	22060.266(7)	22060.414(6)
Q(6.5)	22059.190(6)	22059.499(-7)	22059.656(-4)	22059.802(-3)
Q(7.5)	22058.471(10)	22058.773(3)	22058.924(12)	22059.064(19)
Q(8.5)	22057.661(9)	22057.961(5)	22058.114(11)	22058.267(5)
Q(9.5)	22056.759(4)	22057.061(-1)	22057.233(-16)	22057.367(-1)
Q(10.5)	22055.775(-13)	22056.068(-9)	22056.219(-4)	22056.356(7)
Q(11.5)	22054.662(2)	22054.951(11)	22055.110(6)	22055.257(9)
Q(12.5)	22053.475(-3)	22053.767(2)	22053.915(8)	22054.058(15)
Q(13.5)	22052.179(4)	22052.488(-7)	22052.625(9)	22052.797(-12)
Q(14.5)	22050.798(2)	22051.092(7)	22051.241(8)	22051.394(7)
Q(15.5)	22049.306(16)	22049.603(18)	22049.758(11)	22049.912(9)
Q(16.5)	22047.761(-13)	22048.036(10)	22048.160(34)	22048.334(13)
R(2.5)	22064.225(-11)	22064.524(-13)	22064.659(16)	22064.822(1)
R(3.5)	22064.773(-5)	22065.074(-8)	22065.240(-9)	22065.376(2)
R(4.5)	22065.233(-6)	22065.536(-10)	22065.699(-8)	22065.847(-9)
R(5.5)	22065.599(-8)	22065.897(-8)	22066.065(-11)	22066.206(-3)
R(6.5)	22065.856(3)	22066.182(-24)	22066.320(3)	22066.480(-7)
R(7.5)	22066.045(-13)	22066.326(6)	22066.482(14)	22066.638(9)
R(8.5)	22066.100(9)	22066.419(-9)		22066.714(12)
R(9.5)	22066.100(-9)	22066.380(12)	22066.556(1)	22066.714(-5)
R(10.5)	22066.012(-34)		22066.445(-1)	
R(11.5)	22065.793(-24)	22066.081(-9)	22066.267(-32)	22066.409(-19)
R(12.5)	22065.481(-15)	22065.789(-20)	22065.948(-17)	22066.081(6)

Table A.13 (continued)

R(13.5)	22065.082(-16)	22065.375(-5)	22065.528(3)	22065.704(-16)
R(14.5)	22064.592(-21)	22064.891(-15)	22065.055(-19)	22065.211(-17)
R(15.5)	22063.993(-12)	22064.289(-3)	22064.473(-27)	22064.623(-18)
R(16.5)	22063.299(-3)	22063.609(-8)	22063.782(-23)	22063.910(10)
R(17.5)	22062.523(-9)	22062.834(-12)	22062.985(-8)	
R(18.5)	22061.654(-16)	22061.946(0)	22062.101(0)	
R(19.5)	22060.669(-3)	22060.972(2)	22061.125(2)	
R(20.5)	22059.601(-3)	22059.916(-8)	22060.052(7)	
R(22.5)	22057.168(10)		22057.634(3)	
R(24.5)	22054.352(23)	22054.673(16)	22054.826(6)	
R(25.5)	22052.814(16)			
Fitted Spectroscopic Constants				
ν_0	22061.5216(32)	22061.8169(27)	22061.9801(37)	22062.1253(31)
B_1'	0.444218(30)	0.444431(36)	0.444724(34)	0.444942(40)
r_1' (Å)	1.705210(58)	1.705412(69)	1.705160(65)	1.705056(77)
B_0''	0.491921(34)	0.492121(36)	0.492469(42)	0.492660(36)
r_0'' (Å)	1.620422(56)	1.620673(59)	1.620395(69)	1.620379(59)

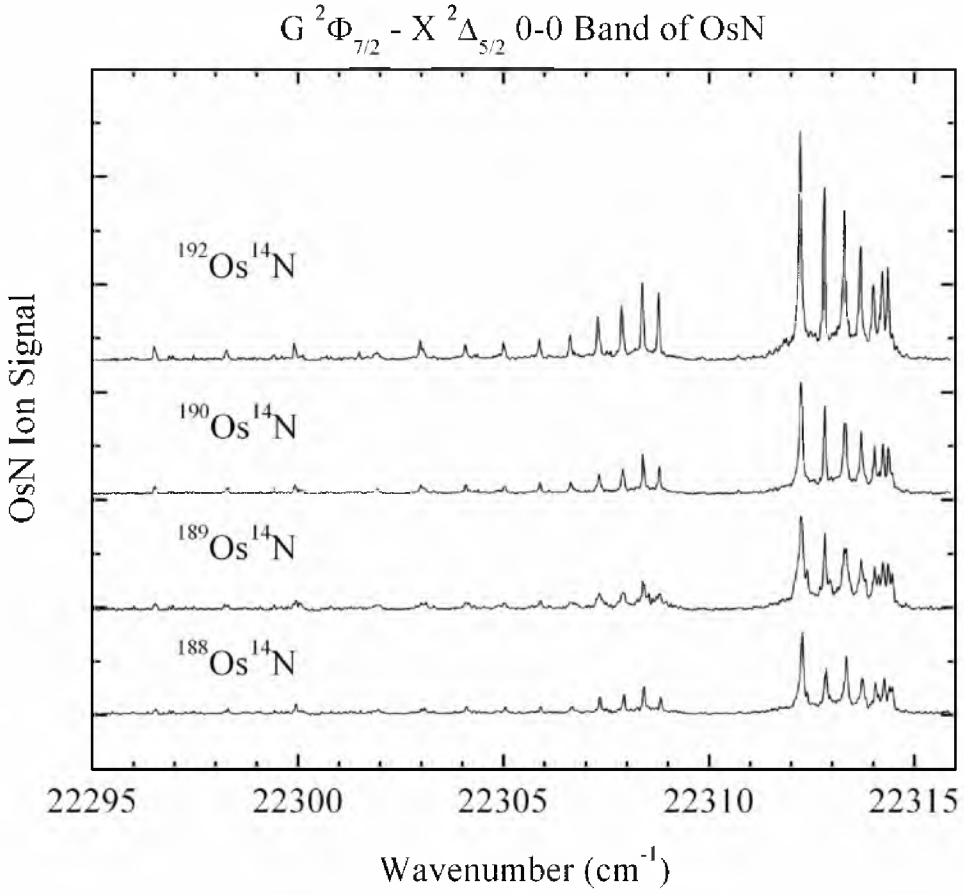

Figure A.21 Rotationally resolved scan over the G $^2\Phi_{7/2} \leftarrow$ X $^2\Delta_{5/2}$ 0-0 band of OsN, showing the isotopes $^{192}Os^{14}N$, $^{190}Os^{14}N$, $^{189}Os^{14}N$, and $^{188}Os^{14}N$.

Table A.14 Fitted rotational lines of the G[22.3] $\frac{7}{2} \leftarrow$ X $^2\Delta_{5/2}$ 0-0 band.

Line	$^{192}Os^{14}N$	$^{190}Os^{14}N$	$^{189}Os^{14}N$	$^{188}Os^{14}N$
P(4.5)	22304.361(-8)	22304.382(-12)		
P(5.5)	22302.973(-7)	22302.983(-1)	22303.002(-19)	22303.005(-5)
P(6.5)	22301.492(-4)	22301.500(3)		
P(7.5)	22299.927(-6)	22299.932(3)	22299.954(-17)	22299.955(-4)
P(8.5)	22298.262(2)	22298.288(-12)	22298.298(-20)	22298.298(-6)
P(9.5)	22296.513(4)	22296.521(7)	22296.533(-4)	22296.541(2)
P(10.5)	22294.682(-1)	22294.688(3)	22294.693(-2)	22294.698(5)
Q(3.5)	22308.772(8)	22308.797(2)	22308.804(1)	22308.826(-3)
Q(4.5)	22308.377(-1)	22308.399(-4)	22308.407(-6)	22308.416(4)
Q(5.5)	22307.879(4)	22307.907(-6)	22307.915(-8)	22307.938(-13)
Q(6.5)	22307.296(4)	22307.329(-12)	22307.334(-11)	22307.349(-8)
Q(7.5)	22306.624(3)	22306.641(2)		22306.667(0)
Q(8.5)	22305.881(-18)	22305.891(-12)	22305.898(-12)	22305.904(-1)
Q(9.5)	22305.002(9)	22305.032(-7)	22305.027(6)	22305.047(2)
Q(10.5)	22304.072(-3)	22304.086(-4)	22304.088(1)	22304.103(3)
Q(11.5)	22303.034(3)	22303.048(1)		22303.081(-9)
Q(12.5)	22301.917(-2)	22301.920(5)		22301.965(-17)
Q(13.5)		22300.702(10)		
Q(14.5)		22299.425(-16)	22299.426(-7)	22299.428(4)
Q(15.5)		22298.013(4)		
Q(17.5)				22294.991(-7)
R(2.5)	22312.220(3)	22312.237(7)	22312.249(3)	22312.271(2)
R(3.5)	22312.809(-5)	22312.816(8)	22312.817(16)	22312.856(-2)
R(4.5)	22313.296(-2)	22313.313(1)	22313.317(8)	22313.347(-3)
R(5.5)	22313.689(6)	22313.702(12)	22313.705(20)	22313.733(13)
R(6.5)	22314.001(4)	22314.023(1)	22314.025(11)	22314.051(6)
R(7.5)	22314.213(14)	22314.235(10)	22314.234(24)	22314.261(17)
R(8.5)	22314.357(0)	22314.369(7)	22314.374(16)	22314.393(17)
R(9.5)				22314.463(-11)
R(10.5)	22314.357(-6)	22314.369(-1)		
R(14.5)				22313.293(19)
R(15.5)				22312.820(-5)

Table A.14 (continued)

Fitted Spectroscopic Constants				
ν_0	22309.4871(25)	22309.5070(24)	22309.5127(51)	22309.5316(28)
B_0'	0.447050(43)	0.447192(48)	0.447557(59)	0.447724(48)
r_0' (Å)	1.699800(82)	1.700139(91)	1.699754(112)	1.699750(91)
B_0''	0.491921(34)	0.492121(36)	0.492469(42)	0.492660(36)
r_0'' (Å)	1.620422(56)	1.620673(59)	1.620395(69)	1.620379(59)

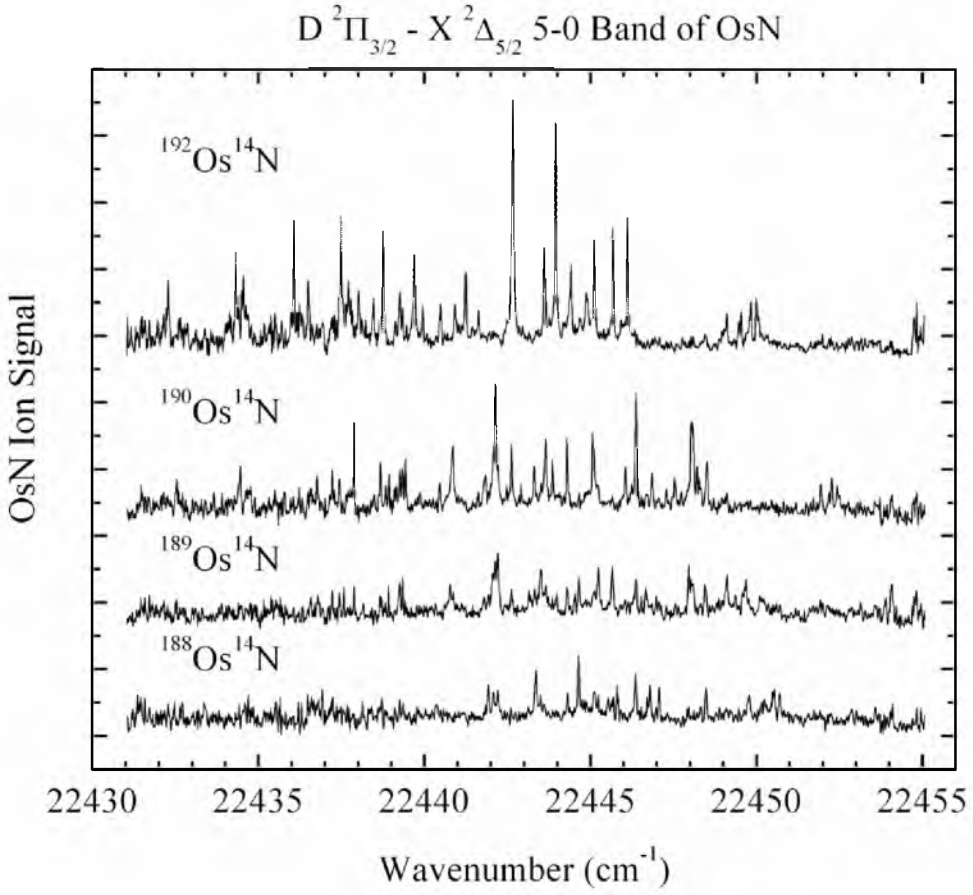

Figure A.22 Rotationally resolved scan over the D $^2\Pi_{3/2} \leftarrow$ X $^2\Delta_{5/2}$ 5-0 band of OsN, showing the isotopes $^{192}Os^{14}N$, $^{190}Os^{14}N$, $^{189}Os^{14}N$, and $^{188}Os^{14}N$.

Table A.15 Fitted rotational lines of the D[18.0] $\frac{3}{2} \leftarrow X\ ^2\Delta_{5/2}$ 5-0 band.

Line	$^{192}Os^{14}N$	$^{190}Os^{14}N$	$^{189}Os^{14}N$	$^{188}Os^{14}N$
P(2.5)	22443.959(-2)	22446.372(-2)	22447.968(-15)	22444.645(2)
P(3.5)	22442.669(-7)	22445.082(-5)	22446.664(-2)	22443.358(-8)
P(4.5)	22441.242(1)	22443.655(6)	22445.232(17)	22441.923(5)
P(5.5)	22439.697(3)	22442.130(-9)		22440.366(16)
P(6.5)	22438.020(12)	22440.458(-1)	22442.054(1)	22438.714(-2)
P(7.5)		22438.680(-11)		22436.930(-14)
P(8.5)	22434.317(7)	22436.765(-6)		
P(9.5)	22432.276(8)			
P(10.5)		22432.546(22)		
Q(2.5)	22446.103(3)	22448.514(8)	22450.098(11)	22446.797(1)
Q(3.5)	22445.671(-1)	22448.076(14)	22449.684(-3)	22446.360(2)
Q(4.5)	22445.111(0)	22447.544(-9)	22449.115(15)	22445.797(4)
Q(5.5)	22444.425(2)	22446.856(-1)	22448.466(-9)	22445.114(2)
Q(6.5)	22443.613(7)	22446.051(1)	22447.651(10)	22444.318(-12)
Q(8.5)	22441.627(3)			22442.302(11)
Q(9.5)	22440.453(-4)	22442.910(-8)		
Q(10.5)	22439.138(6)			
Q(11.5)	22437.706(9)			
Q(13.5)	22434.488(-5)			
R(2.5)	22449.117(-3)		22453.130(-2)	
R(3.5)	22449.551(-13)	22451.952(11)	22453.569(-7)	22450.238(-2)
R(4.5)	22449.844(-6)	22452.272(-4)	22453.885(-11)	22450.538(-2)
R(5.5)	22450.004(10)	22452.445(4)	22454.068(-4)	22450.704(7)
R(6.5)	22450.073(-8)	22452.519(-12)		
R(7.5)	22450.004(-11)			22450.704(-16)
R(8.5)	22449.796(0)			22450.493(-3)
R(9.5)	22449.484(-10)			22450.157(11)

Table A.15 (continued)

Fitted Spectroscopic Constants				
ν_0	22446.6492(22)	22449.0627(40)	22450.6445(59)	22447.3434(35)
B_5'	0.429767(40)	0.430360(105)	0.431275(203)	0.430365(101)
r_5' (Å)	1.733642(81)	1.733068(211)	1.731543(408)	1.733691(203)
B_0''	0.491921(34)	0.492121(36)	0.492469(42)	0.492660(36)
r_0'' (Å)	1.620422(56)	1.620673(59)	1.620395(69)	1.620379(59)

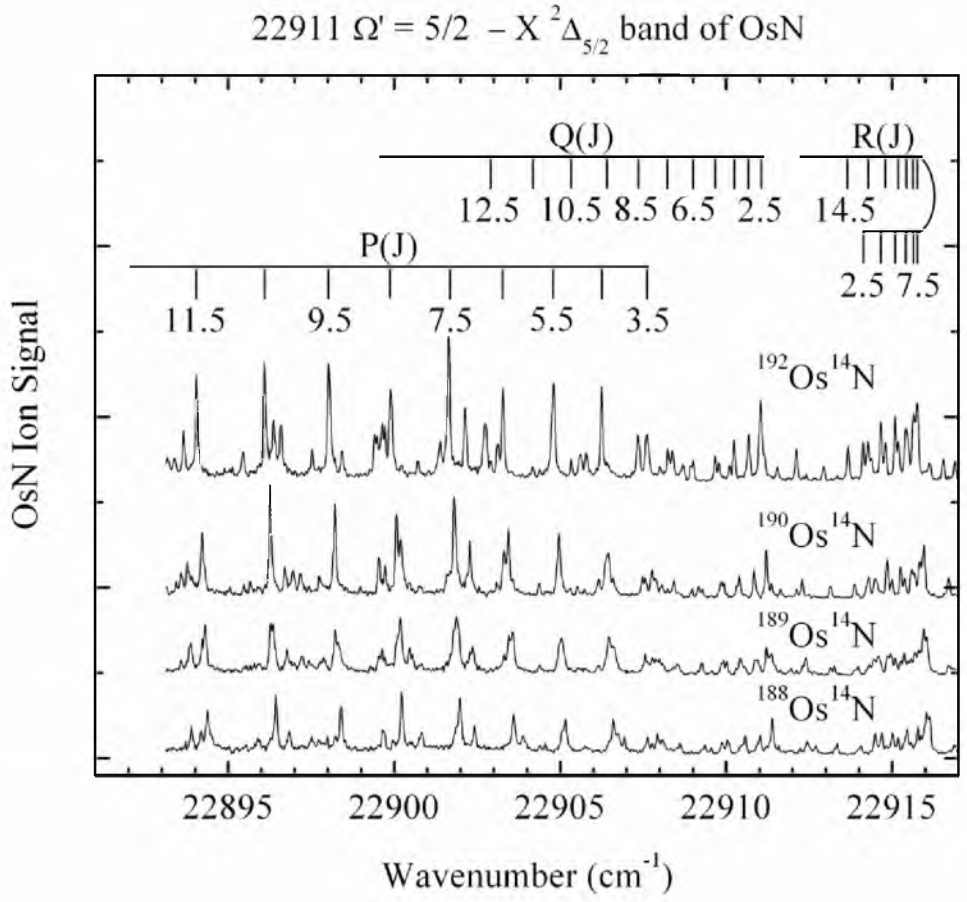

Figure A.23 Rotationally resolved scan over the 22911 Ω′ = 5/2 ← X $^2\Delta_{5/2}$ band of OsN, showing the isotopes $^{192}Os^{14}N$, $^{190}Os^{14}N$, $^{189}Os^{14}N$, and $^{188}Os^{14}N$. Marked line positions refer to the $^{192}Os^{14}N$ isotopomer. Additional features are from the nearly overlapping 22934 Ω′ = 5/2 ← X $^2\Delta_{5/2}$ and F $^2\Phi_{7/2}$ ← X $^2\Delta_{5/2}$ 2-0 bands.

Table A.16 Fitted rotational lines of the 22911 cm^{-1} $\Omega' = \frac{5}{2} \leftarrow X\ ^2\Delta_{5/2}$ band.

Line	$^{192}Os^{14}N$	$^{190}Os^{14}N$	$^{189}Os^{14}N$	$^{188}Os^{14}N$
P(3.5)	22907.607(2)	22907.762(6)		22907.932(6)
P(4.5)	22906.248(20)	22906.446(-18)	22906.471(-9)	22906.599(1)
P(5.5)	22904.801(24)	22904.964(23)	22905.041(-13)	22905.158(1)
P(6.5)	22903.271(8)	22903.442(3)	22903.496(-3)	22903.600(17)
P(7.5)	22901.646(-13)	22901.807(-6)	22901.876(-17)	22901.977(-2)
P(8.5)	22899.897(-14)	22900.069(-14)	22900.108(16)	22900.217(14)
P(9.5)	22898.030(3)	22898.215(-8)	22898.302(-13)	22898.392(-7)
P(10.5)	22896.102(-23)	22896.261(-3)	22896.348(6)	22896.440(-1)
P(11.5)	22894.048(-25)	22894.211(-3)	22894.303(16)	22894.374(18)
Q(2.5)	22911.041(11)	22911.209(4)	22911.215(30)	22911.385(3)
Q(3.5)	22910.680(15)	22910.846(11)	22910.906(-10)	22911.021(12)
Q(4.5)	22910.232(4)	22910.396(4)	22910.424(21)	22910.574(4)
Q(5.5)	22909.672(3)	22909.852(-10)	22909.923(-28)	22910.040(-18)
Q(6.5)	22909.011(1)	22909.175(7)	22909.270(-25)	22909.361(3)
Q(7.5)	22908.245(2)	22908.424(-3)		22908.606(0)
Q(8.5)	22907.395(-17)	22907.564(-6)		22907.766(-20)
Q(9.5)	22906.394(15)	22906.592(1)		
Q(10.5)	22905.336(1)	22905.522(5)		22905.749(-26)
Q(11.5)	22904.172(-8)	22904.369(-10)		22904.556(4)
Q(12.5)	22902.903(-15)	22903.085(5)		
Q(13.5)		22901.695(24)		
Q(14.5)		22900.275(-28)		
R(2.5)	22914.125(14)	22914.289(14)	22914.314(28)	22914.485(-3)
R(3.5)	22914.660(3)	22914.845(-16)		22915.009(3)
R(4.5)	22915.089(-3)	22915.259(-3)		22915.451(-10)
R(5.5)	22915.427(-21)	22915.582(-2)		22915.780(-11)
R(6.5)	22915.646(-21)	22915.821(-18)		
R(7.5)	22915.754(-13)	22915.908(15)		22916.134(-13)
R(8.5)	22915.754(2)	22915.960(-17)		22916.134(11)
R(9.5)		22915.846(15)		22916.077(-8)
R(10.5)	22915.487(-9)	22915.664(14)		22915.870(21)

Table A.16 (continued)

R(11.5)	22915.184(3)	22915.378(15)		
R(12.5)	22914.799(-6)	22915.000(6)		
R(13.5)	22914.272(24)	22914.526(-8)		
R(14.5)	22913.670(29)			
Fitted Spectroscopic Constants				
ν_0	22911.4990(43)	22911.6572(37)	22911.6825(92)	22911.8299(42)
B′	0.440896(32)	0.441353(32)	0.442478(118)	0.442087(60)
r′(Å)	1.711622(62)	1.711348(62)	1.709482(228)	1.710552(116)
B_0''	0.491921(34)	0.492121(36)	0.492469(42)	0.492660(36)
r_0''(Å)	1.620422(56)	1.620673(59)	1.620395(69)	1.620379(59)

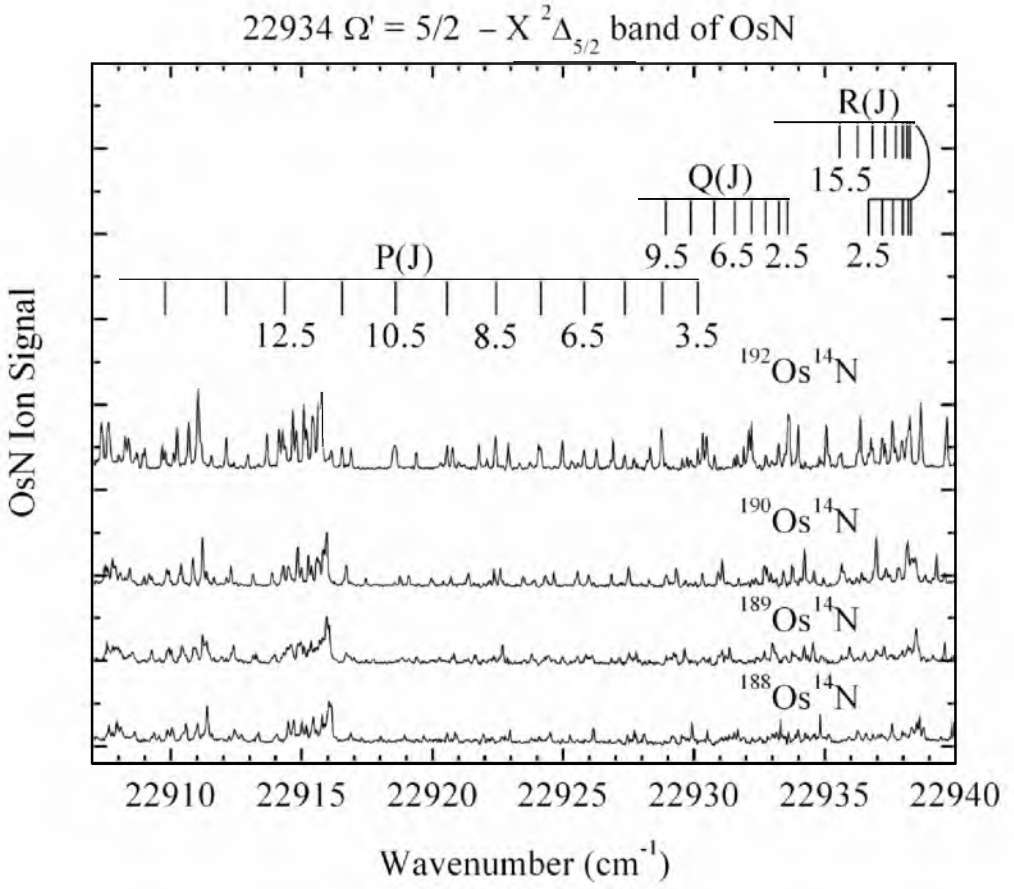

Figure A.24 Rotationally resolved scan over the 22934 Ω′ = 5/2 ← X $^2\Delta_{5/2}$ band of OsN, showing the isotopes ^{192}Os^{14}N, ^{190}Os^{14}N, ^{189}Os^{14}N, and ^{188}Os^{14}N. Marked line positions refer to the ^{192}Os^{14}N isotopomer. Additional features are from the nearly overlapping 22911 Ω′ = 5/2 ← X $^2\Delta_{5/2}$ and F $^2\Phi_{7/2}$ ← X $^2\Delta_{5/2}$ 2-0 bands.

Table A.17 Fitted rotational lines of the 22934 cm^{-1} $\Omega' = \frac{5}{2} \leftarrow X\ ^2\Delta_{5/2}$ band.

Line	$^{192}Os^{14}N$	$^{190}Os^{14}N$	$^{189}Os^{14}N$	$^{188}Os^{14}N$
P(3.5)	22930.147(-15)	22930.318(-18)		22930.509(-4)
P(4.5)	22928.790(1)			22929.157(4)
P(5.5)	22927.351(-3)	22927.503(13)		22927.713(2)
P(6.5)	22925.789(13)	22925.958(13)		22926.159(7)
P(7.5)	22924.132(24)	22924.321(3)		22924.499(15)
P(8.5)	22922.415(-9)	22922.569(6)		22922.783(-24)
P(9.5)	22920.557(-3)	22920.712(11)		22920.873(29)
P(10.5)	22918.581(21)	22918.763(6)		22918.943(0)
P(11.5)	22916.544(2)	22916.702(12)		22916.873(8)
P(12.5)	22914.374(14)			22914.694(23)
P(13.5)	22912.116(12)	22912.292(5)		22912.432(18)
P(14.5)	22909.779(-12)	22909.935(0)		22910.089(-9)
P(15.5)				22907.629(-21)
Q(2.5)	22933.599(-23)	22933.754(-9)		22933.973(-19)
Q(3.5)	22933.233(-14)	22933.407(-18)		22933.611(-16)
Q(4.5)	22932.748(11)	22932.948(-18)		22933.140(-6)
Q(5.5)	22932.202(-4)	22932.360(8)		22932.576(-6)
Q(6.5)	22931.542(-8)	22931.707(-2)		22931.893(10)
Q(7.5)	22930.785(-16)	22930.919(21)		
Q(8.5)	22929.877(24)	22930.063(10)		
Q(9.5)	22928.919(12)	22929.109(-5)		
Q(10.5)		22927.999(34)		
R(2.5)	22936.670(-8)	22936.860(-27)		22937.049(-6)
R(3.5)	22937.196(-10)	22937.343(15)		22937.575(-7)
R(4.5)	22937.589(20)	22937.796(-14)		22937.977(12)
R(5.5)	22937.958(-28)			22938.326(-18)
R(6.5)	22938.137(10)	22938.336(-14)		22938.526(-2)
R(7.5)	22938.261(3)	22938.450(-10)		22938.630(8)
R(8.5)	22938.261(17)	22938.450(5)		22938.630(20)
R(9.5)	22938.193(-3)			
R(11.5)	22937.714(-6)			22938.070(-2)

Table A.17 (continued)

R(12.5)	22937.307(8)	22937.483(11)		22937.672(-3)
R(13.5)	22936.824(-6)			22937.161(6)
R(14.5)	22936.231(-11)	22936.415(-12)		22936.582(-19)
R(15.5)	22935.534(-14)	22935.729(-25)		
R(17.5)	22933.812(1)			
Fitted Spectroscopic Constants				
ν_0	22934.0221(36)	22934.1918(44)		22934.4026(41)
B'	0.440888(28)	0.441115(32)		0.441394(42)
r'(Å)	1.711637(54)	1.711810(62)		1.711895(81)
B_0''	0.491921(34)	0.492121(36)	0.492469(42)	0.492660(36)
r_0'' (Å)	1.620422(56)	1.620673(59)	1.620395(69)	1.620379(59)

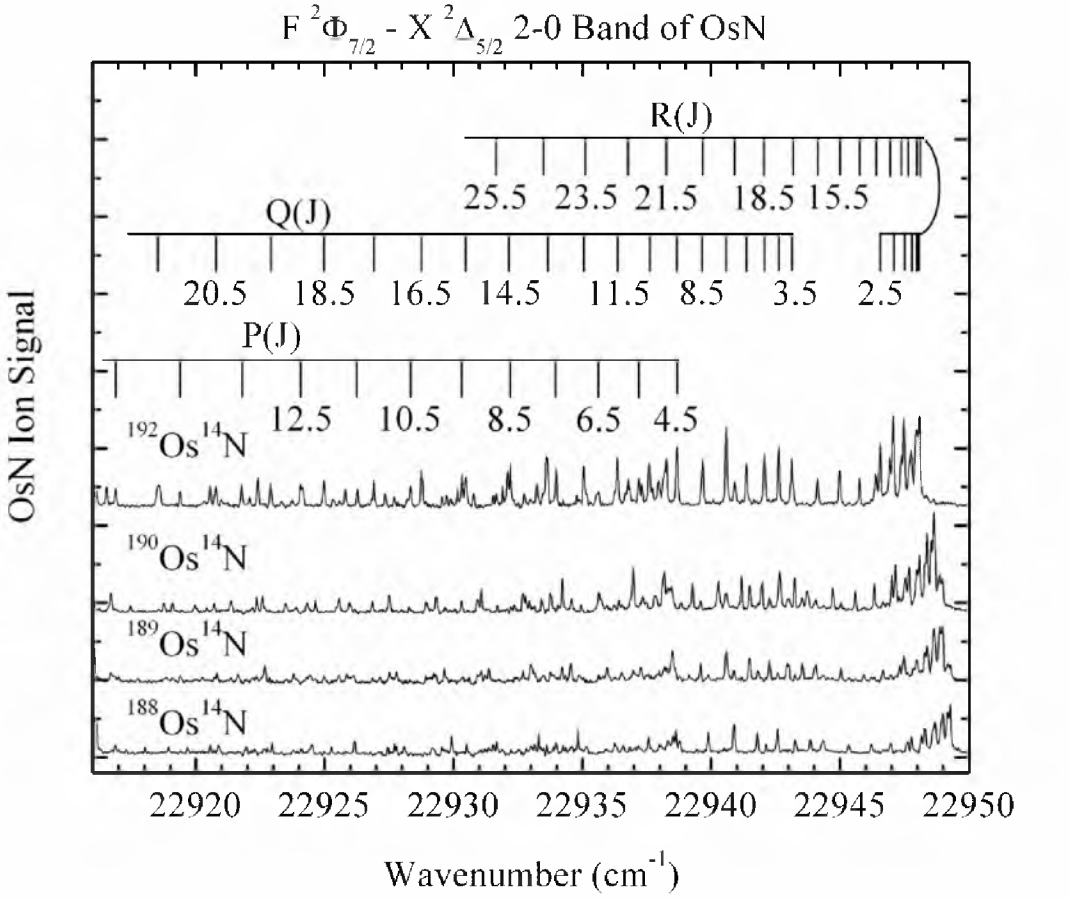

Figure A.25 Rotationally resolved scan over the F $^2\Phi_{7/2} \leftarrow$ X $^2\Delta_{5/2}$ 2-0 band of OsN, showing the isotopes $^{192}Os^{14}N$, $^{190}Os^{14}N$, $^{189}Os^{14}N$, and $^{188}Os^{14}N$. Marked line positions refer to the $^{192}Os^{14}N$ isotopomer. Additional features are from the nearly overlapping 22911 $\Omega' = 5/2 \leftarrow$ X $^2\Delta_{5/2}$ and 22934 $\Omega' = 5/2 \leftarrow$ X $^2\Delta_{5/2}$ bands.

Table A.18 Fitted rotational lines of the C[21.2] $\frac{7}{2} \leftarrow$ X $^2\Delta_{5/2}$ 2-0 band.

Line	$^{192}Os^{14}N$	$^{190}Os^{14}N$	$^{189}Os^{14}N$	$^{188}Os^{14}N$
P(4.5)	22938.672(5)	22939.280(1)	22939.575(11)	22939.887(2)
P(5.5)	22937.196(24)	22937.818(5)		
P(6.5)	22935.629(28)	22936.241(18)	22936.531(33)	22936.849(15)
P(7.5)	22933.980(10)	22934.584(6)	22934.885(8)	22935.171(24)
P(8.5)	22932.202(16)	22932.788(28)	22933.133(-15)	22933.401(18)
P(9.5)	22930.336(4)	22930.919(18)	22931.214(24)	22931.540(-3)
P(10.5)	22928.329(28)	22928.939(14)	22929.228(24)	22929.534(17)
P(11.5)	22926.266(3)	22926.853(9)	22927.155(6)	22927.450(9)
P(12.5)	22924.057(18)	22924.640(27)	22924.970(-6)	22925.261(1)
P(13.5)	22921.779(-2)	22922.356(11)	22922.678(-16)	22922.962(-2)
P(14.5)	22919.377(-4)	22919.965(-4)	22920.264(-8)	22920.559(-7)
P(15.5)	22916.885(-21)	22917.461(-10)	22917.743(0)	22918.033(5)
P(16.5)	22914.272(-22)	22914.845(-11)	22915.099(26)	
P(17.5)	22911.542(-11)	22912.126(-14)	22912.398(3)	22912.700(-4)
P(18.5)	22908.694(13)	22909.282(4)	22909.577(-4)	22909.868(-2)
P(19.5)	22905.784(-7)	22906.375(-22)	22906.611(28)	22906.941(-10)
P(20.5)	22902.747(-5)	22903.318(-2)	22903.581(19)	22903.882(9)
P(21.5)	22899.632(-30)	22900.194(-21)	22900.462(-8)	22900.756(-10)
P(22.5)	22896.366(-8)	22896.950(-25)	22897.224(-19)	22897.516(-21)
P(23.5)		22893.573(-1)	22893.855(-5)	
Q(3.5)	22943.123(-19)	22943.726(-17)		22944.326(-3)
Q(4.5)	22942.628(3)	22943.236(0)	22943.543(2)	22943.837(11)
Q(5.5)	22942.071(-18)	22942.655(1)	22942.957(8)	22943.258(11)
Q(6.5)	22941.364(6)	22941.975(-3)	22942.266(15)	22942.571(13)
Q(7.5)	22940.582(-2)	22941.174(8)	22941.484(7)	22941.788(6)
Q(8.5)	22939.660(26)	22940.278(9)	22940.580(15)	22940.884(15)
Q(9.5)	22938.672(15)	22939.280(7)	22939.575(19)	22939.887(10)
Q(10.5)	22937.589(-6)	22938.178(3)	22938.495(-7)	22938.780(10)
Q(11.5)	22936.359(14)	22936.970(1)	22937.261(15)	22937.575(4)
Q(12.5)	22935.051(7)	22935.647(7)	22935.956(3)	22936.255(6)
Q(13.5)	22933.632(7)	22934.223(10)	22934.550(-13)	22934.828(11)

Table A.18 (continued)

Q(14.5)	22932.103(11)	22932.694(12)	22933.006(3)	22933.310(1)
Q(15.5)	22930.472(12)	22931.082(-8)	22931.364(13)	22931.668(10)
Q(16.5)	22928.748(0)	22929.327(9)	22929.635(3)	22929.924(15)
Q(17.5)	22926.908(0)	22927.503(-9)	22927.787(7)	22928.088(7)
Q(18.5)	22924.965(-3)	22925.555(-9)	22925.856(-11)	22926.159(-13)
Q(19.5)	22922.902(9)	22923.473(20)	22923.795(-5)	22924.090(1)
Q(20.5)	22920.773(-19)	22921.359(-24)	22921.636(-5)	22921.954(-24)
Q(21.5)	22918.529(-36)	22919.089(-19)	22919.390(-24)	22919.666(-1)
Q(22.5)	22916.132(-5)	22916.702(-1)	22917.010(-14)	22917.294(-1)
Q(23.5)	22913.670(-14)	22914.235(-8)	22914.549(-30)	22914.825(-8)
Q(24.5)		22911.641(6)	22911.960(-21)	22912.235(1)
Q(25.5)	22908.381(16)	22908.977(-14)	22909.270(-18)	22909.553(-5)
Q(26.5)	22905.609(1)	22906.165(7)	22906.471(-11)	22906.742(14)
Q(27.5)	22902.747(-29)	22903.318(-41)	22903.563(0)	22903.869(-11)
Q(28.5)	22899.717(3)	22900.275(1)	22900.546(14)	22900.825(30)
Q(29.5)	22896.586(31)	22897.175(-6)	22897.425(28)	22897.728(18)
Q(30.5)			22894.218(20)	
R(2.5)	22946.551(-3)	22947.152(3)	22947.482(-16)	22947.762(10)
R(3.5)	22947.059(-1)	22947.674(-10)	22947.975(2)	22948.293(-11)
R(4.5)	22947.479(-15)	22948.080(-10)	22948.384(-1)	22948.683(5)
R(5.5)	22947.754(10)	22948.377(-7)	22948.671(11)	22948.989(0)
R(6.5)	22947.954(6)	22948.544(20)	22948.875(3)	22949.189(-5)
R(7.5)	22948.068(-19)	22948.643(11)	22948.984(-17)	22949.275(-2)
R(8.5)	22948.046(-12)	22948.643(-6)	22948.984(-33)	22949.275(-18)
R(9.5)	22947.923(-10)	22948.544(-28)		22949.168(-31)
R(10.5)	22947.693(-6)	22948.296(-7)		22948.946(-36)
R(11.5)	22947.378(-21)	22947.983(-25)	22948.295(-24)	22948.601(-23)
R(12.5)	22946.926(-5)	22947.535(-15)	22947.840(-7)	22948.156(-15)
R(13.5)	22946.383(-3)	22947.013(-35)	22947.312(-22)	22947.628(-30)
R(14.5)	22945.759(-26)	22946.335(-6)	22946.664(-21)	22946.970(-20)
R(15.5)	22944.984(-2)	22945.594(-17)	22945.926(-37)	22946.205(-9)
R(16.5)	22944.123(2)	22944.713(5)	22945.039(-9)	22945.333(5)

Table A.18 (continued)

R(17.5)	22943.186(-23)		22944.059(7)	22944.371(3)
R(18.5)			22943.020(-23)	22943.299(6)
R(19.5)	22940.914(10)	22941.498(13)	22941.809(13)	22942.124(6)
R(20.5)			22939.133(23)	22940.862(-13)
R(21.5)	22938.261(3)	22938.836(11)	22937.659(7)	22939.450(13)
R(22.5)	22936.774(2)	22937.343(13)	22936.061(9)	22937.977(-5)
R(23.5)	22935.166(17)	22935.729(32)	22934.345(22)	
R(24.5)	22933.467(18)	22934.055(6)		
R(25.5)	22931.654(28)	22932.220(34)		
R(26.5)		22930.318(25)		
R(27.5)		22928.310(16)		
Fitted Spectroscopic Constants				
ν_0	22943.9328(30)	22944.5385(30)	22944.8485(33)	22945.1526(27)
B_2'	0.439334(32)	0.439474(51)	0.439792(41)	0.439972(26)
r_2' (Å)	1.714662(62)	1.715003(100)	1.714694(80)	1.714659(51)
B_0''	0.491921(34)	0.492121(36)	0.492469(42)	0.492660(36)
r_0'' (Å)	1.620422(56)	1.620673(59)	1.620395(69)	1.620379(59)

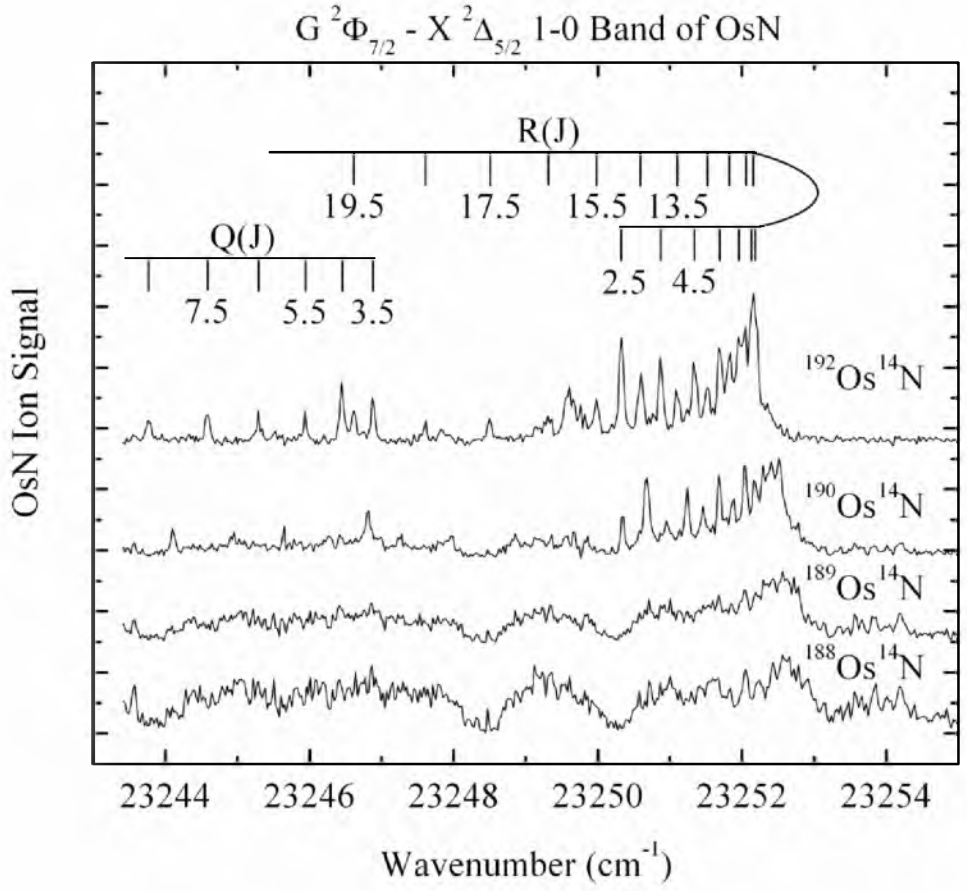

Figure A.26 Rotationally resolved scan over the G $^2\Phi_{7/2} \leftarrow$ X $^2\Delta_{5/2}$ 1-0 band of OsN, showing the isotopes $^{192}Os^{14}N$, $^{190}Os^{14}N$, $^{189}Os^{14}N$, and $^{188}Os^{14}N$. Marked line positions refer to the $^{192}Os^{14}N$ isotopomer. Lines could not be picked out in the spectra of the minor isotopes $^{189}Os^{14}N$ and $^{188}Os^{14}N$.

Table A.19 Fitted rotational lines of the G[22.3] $\frac{7}{2}$ ← X $^2\Delta_{5/2}$ 1-0 band.[a]

Line	$^{192}Os^{14}N$	$^{190}Os^{14}N$	$^{189}Os^{14}N$	$^{188}Os^{14}N$
Q(3.5)	23246.879(6)	23247.260(-24)		
Q(4.5)	23246.444(9)	23246.809(-5)		
Q(5.5)	23245.937(-13)	23246.271(4)		
Q(6.5)	23245.288(10)	23245.643(7)		
Q(7.5)	23244.580(-3)	23244.950(-21)		
Q(8.5)	23243.774(-14)	23244.107(5)		
R(2.5)	23250.325(4)	23250.677(4)		
R(3.5)	23250.872(7)	23251.240(-7)		
R(4.5)	23251.338(-3)	23251.685(3)		
R(5.5)	23251.689(4)	23252.041(6)		
R(6.5)	23251.951(5)	23252.296(14)		
R(7.5)	23252.125(-2)	23252.477(1)		
R(8.5)	23252.204(-11)	23252.538(11)		
R(9.5)	23252.171(-3)	23252.514(9)		
R(10.5)	23252.038(7)	23252.403(-1)		
R(11.5)	23251.826(1)	23252.175(9)		
R(12.5)	23251.524(-11)	23251.877(-7)		
R(13.5)	23251.102(1)	23251.462(-2)		
R(14.5)	23250.599(-3)	23250.955(-1)		
R(15.5)	23249.981(13)	23250.344(7)		
R(16.5)	23249.306(-11)	23249.669(-15)		
R(17.5)	23248.498(1)	23248.855(3)		
R(18.5)	23247.607(1)	23247.968(0)		
R(19.5)	23246.615(6)			
Fitted Spectroscopic Constants				
ν_0	23247.6424(24)	23247.9937(32)		
B_1'	0.443843(12)	0.444044(18)		
r_1' (Å)	1.705930(23)	1.706155(35)		
B_0''	0.491921(34)	0.492121(36)	0.492469(42)	0.492660(36)
r_0'' (Å)	1.620422(56)	1.620673(59)	1.620395(69)	1.620379(59)

[a] This band was particularly difficult to calibrate using the Te_2 absorption spectrum. Because we were not 100% confident that the calibration was correct, it was omitted from the combined fit. The fitted etalon free spectral range was in line with our other fits, however. The ground state rotational constant was constrained to be equal to that obtained in the combined fit.

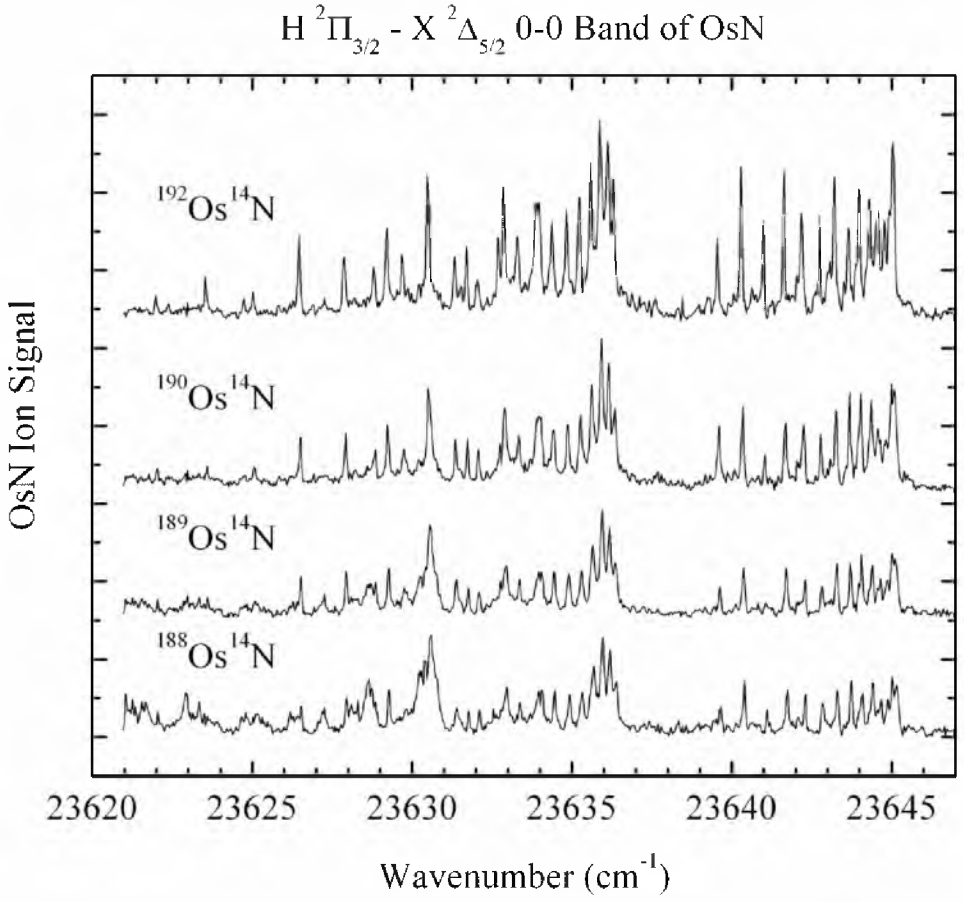

Figure A.27 Rotationally resolved scan over the H $^2\Pi_{3/2} \leftarrow$ X $^2\Delta_{5/2}$ 0-0 band of OsN, showing the isotopes $^{192}Os^{14}N$, $^{190}Os^{14}N$, $^{189}Os^{14}N$, and $^{188}Os^{14}N$.

Table A.20 Fitted rotational lines of the H[23.6] $\frac{3}{2} \leftarrow X\ ^2\Delta_{5/2}$ 0-0 band.

Line	$^{192}Os^{14}N$	$^{190}Os^{14}N$	$^{189}Os^{14}N$	$^{188}Os^{14}N$
P(2.5)	23633.968(14)	23633.983(40)	23634.053(0)	23634.064(8)
P(3.5)	23632.859(5)	23632.895(9)	23632.932(2)	23632.953(-1)
P(4.5)	23631.701(-9)	23631.734(-2)	23631.758(3)	23631.767(11)
P(5.5)	23630.491(-24)	23630.522(-15)	23630.559(-24)	23630.575(-24)
P(6.5)	23629.208(-20)	23629.236(-8)	23629.263(-9)	23629.271(-1)
P(7.5)	23627.870(-14)	23627.927(-32)	23627.940(-19)	23627.949(-14)
P(8.5)	23626.464(5)	23626.508(2)	23626.520(13)	23626.532(15)
P(9.5)	23625.028(1)	23625.065(4)	23625.083(9)	23625.141(-36)
P(10.5)	23623.544(-8)	23623.594(-17)	23623.604(-7)	
P(11.5)	23621.978(11)	23622.023(7)	23622.042(6)	
Q(2.5)	23636.292(15)	23636.344(4)	23636.354(27)	23636.390(11)
Q(3.5)	23636.118(1)	23636.157(4)	23636.180(13)	23636.190(22)
Q(4.5)	23635.884(-6)	23635.927(-7)	23635.954(-2)	23635.967(4)
Q(5.5)	23635.582(1)	23635.621(4)	23635.657(0)	23635.684(-9)
Q(6.5)	23635.229(5)	23635.269(8)	23635.302(6)	23635.320(6)
Q(7.5)	23634.826(6)	23634.867(8)	23634.908(-3)	23634.927(-4)
Q(8.5)	23634.376(0)	23634.412(7)	23634.446(3)	23634.459(6)
Q(9.5)	23633.889(-22)	23633.900(11)	23633.961(-22)	23633.962(-7)
Q(10.5)	23633.295(9)	23633.337(12)	23633.365(10)	23633.377(13)
Q(11.5)	23632.696(-9)	23632.752(-20)	23632.763(-5)	23632.797(-25)
Q(12.5)	23632.040(-24)	23632.067(-5)	23632.097(-10)	23632.111(-12)
Q(13.5)	23631.326(-34)	23631.354(-15)	23631.382(-19)	23631.398(-24)
Q(14.5)	23630.491(23)	23630.584(-22)	23630.646(-62)	23630.575(19)
Q(15.5)	23629.692(-9)	23629.745(-14)	23629.768(-16)	23629.788(-27)
Q(16.5)	23628.805(-8)	23628.847(0)		23628.859(14)
Q(17.5)	23627.870(-11)	23627.927(-18)		23627.949(-17)
Q(18.5)		23626.926(-8)		
Q(19.5)	23625.819(2)	23625.849(24)		
Q(20.5)	23624.736(-15)	23624.762(12)		23624.804(-17)
Q(21.5)	23623.544(24)			
Q(22.5)	23622.375(-14)			

Table A.20 (continued)

R(2.5)	23639.552(11)	23639.601(5)	23639.632(9)	23639.643(18)
R(3.5)	23640.297(8)	23640.344(6)	23640.370(14)	23640.400(5)
R(4.5)	23640.987(7)	23641.037(1)	23641.064(9)	23641.099(-5)
R(5.5)	23641.630(0)	23641.677(-2)	23641.708(2)	23641.735(-5)
R(6.5)	23642.185(26)	23642.249(8)	23642.295(-3)	23642.301(11)
R(7.5)	23642.741(-3)	23642.793(-7)	23642.824(-4)	23642.849(-9)
R(8.5)	23643.208(5)	23643.260(1)	23643.286(10)	23643.307(8)
R(9.5)	23643.647(-13)	23643.692(-9)	23643.720(-3)	23643.737(-1)
R(10.5)	23643.986(14)	23644.036(14)	23644.061(24)	23644.076(27)
R(11.5)	23644.301(13)	23644.368(-3)	23644.391(7)	23644.413(3)
R(12.5)	23644.557(16)	23644.602(24)	23644.658(1)	23644.671(5)
R(13.5)	23644.768(12)	23644.824(9)	23644.862(3)	23644.889(-7)
R(14.5)	23644.924(8)	23644.992(-6)	23645.015(3)	23645.025(8)
R(15.5)	23645.043(-12)	23645.089(-2)	23645.116(1)	
R(16.5)		23645.150(-17)		
R(20.5)			23644.790(19)	
R(21.5)			23644.580(5)	23644.566(26)
R(22.5)	23644.199(21)	23644.305(-18)	23644.299(10)	23644.302(11)
R(23.5)	23643.880(10)	23643.962(-4)	23643.980(-1)	23643.986(-5)
R(24.5)	23643.513(-7)	23643.579(-3)		
R(25.5)	23643.076(-8)			
R(26.5)	23642.595(-17)	23642.622(28)		
R(27.5)	23642.039(-6)			
R(30.5)	23640.057(19)			
Fitted Spectroscopic Constants				
ν_0	23636.5418(27)	23636.5833(28)	23636.6162(32)	23636.6360(33)
B_0'	0.465101(31)	0.465328(50)	0.465629(29)	0.465777(25)
r_0' (Å)	1.666488(56)	1.666679(90)	1.666443(52)	1.666484(45)
B_0''	0.491921(34)	0.492121(36)	0.492469(42)	0.492660(36)
r_0'' (Å)	1.620422(56)	1.620673(59)	1.620395(69)	1.620379(59)

APPENDIX B

ROTATIONALLY RESOLVED SPECTRA, TABULATED LINE POSITIONS AND FITTED PARAMETERS OF IrSi

PART I. VIBRONICALLY RESOLVED SPECTRA OF IrSi

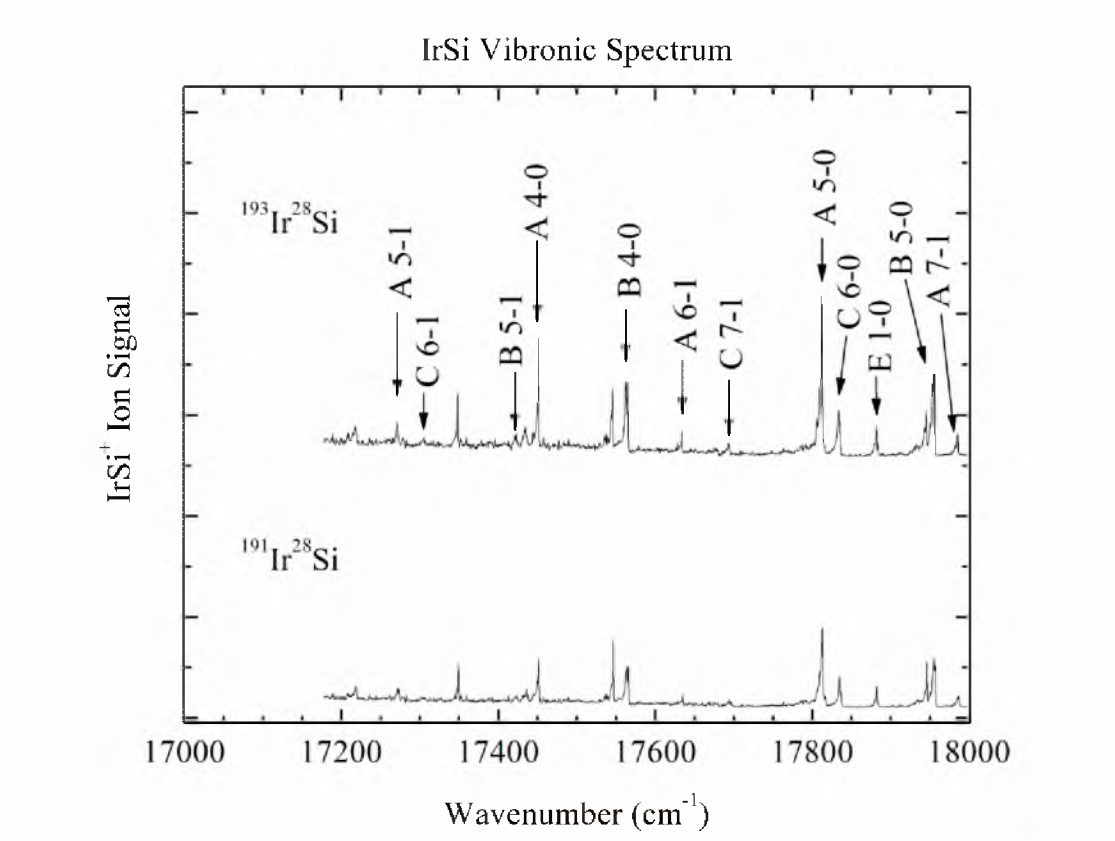

Figure B.1 Vibronically resolved spectra of $^{191}Ir^{28}Si$ and $^{193}Ir^{28}Si$ over the 17000-18000 cm^{-1} range. Bands from the A-X, B-X, C-X, and E-X systems are indicated.

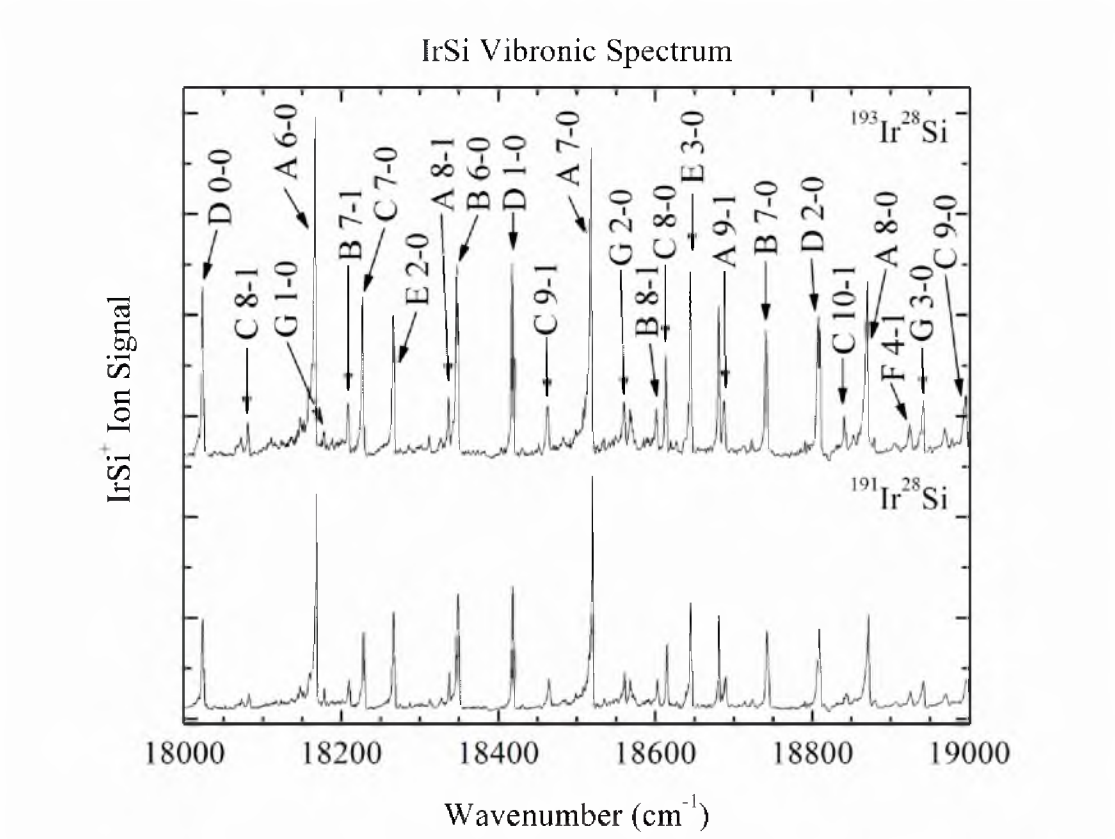

Figure B.2 Vibronically resolved spectra of $^{191}Ir^{28}Si$ and $^{193}Ir^{28}Si$ over the 18000-19000 cm^{-1} range. Bands from the A-X, B-X, C-X, D-X, E-X, F-X, and G-X systems are indicated.

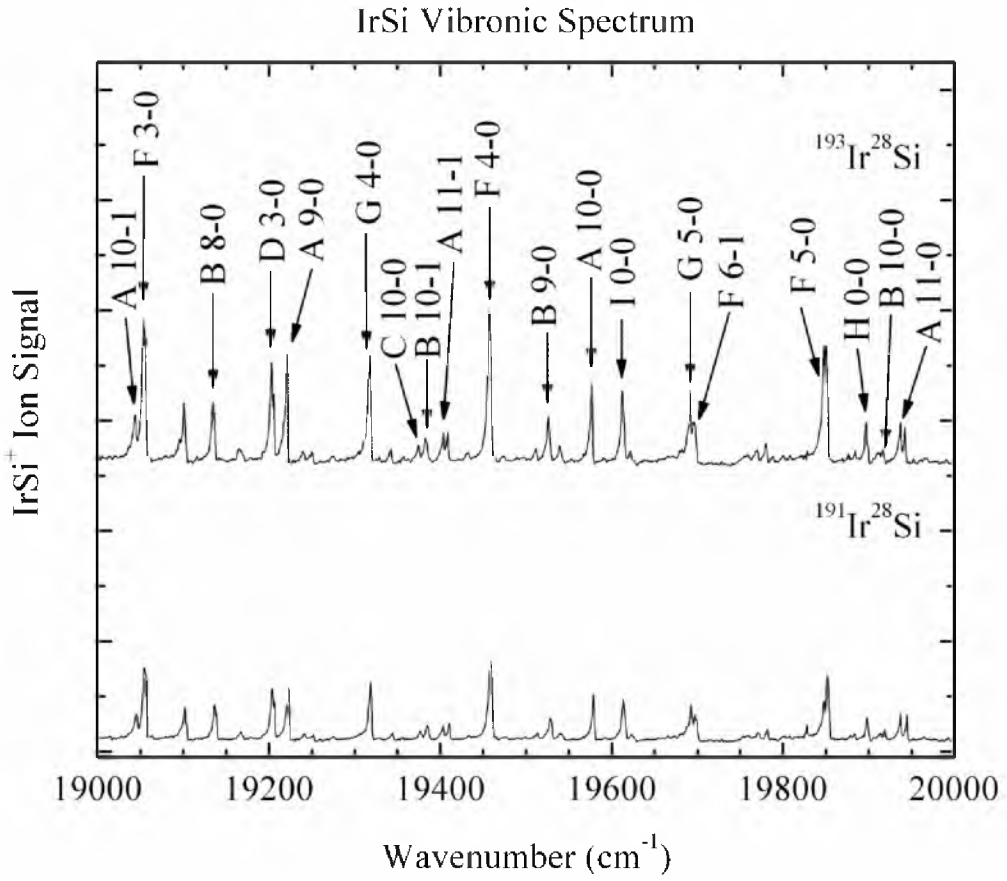

Figure B.3 Vibronically resolved spectra of $^{191}Ir^{28}Si$ and $^{193}Ir^{28}Si$ over the 19000-20000 cm^{-1} range. Bands from the A-X, B-X, C-X, D-X, F-X, G-X, H-X, and I-X systems are indicated.

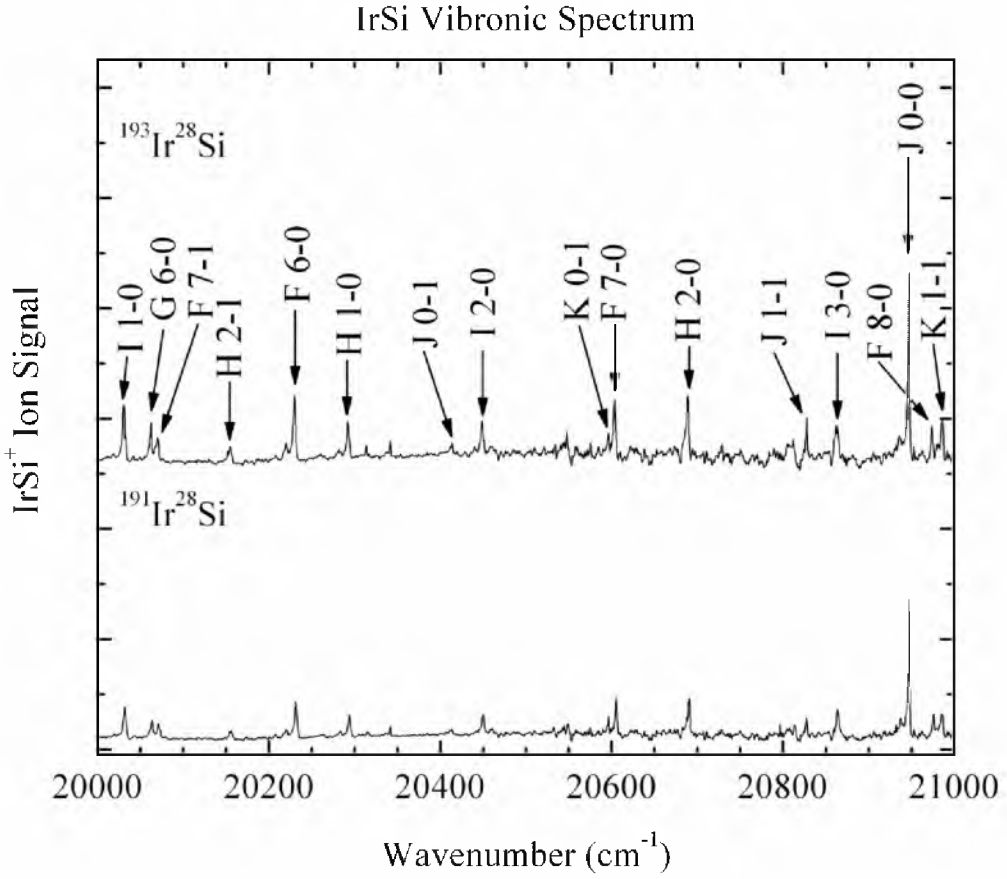

Figure B.4 Vibronically resolved spectra of $^{191}Ir^{28}Si$ and $^{193}Ir^{28}Si$ over the 20000-21000 cm^{-1} range. Bands from the F-X, G-X, H-X, I-X, J-X, and L-X systems are indicated.

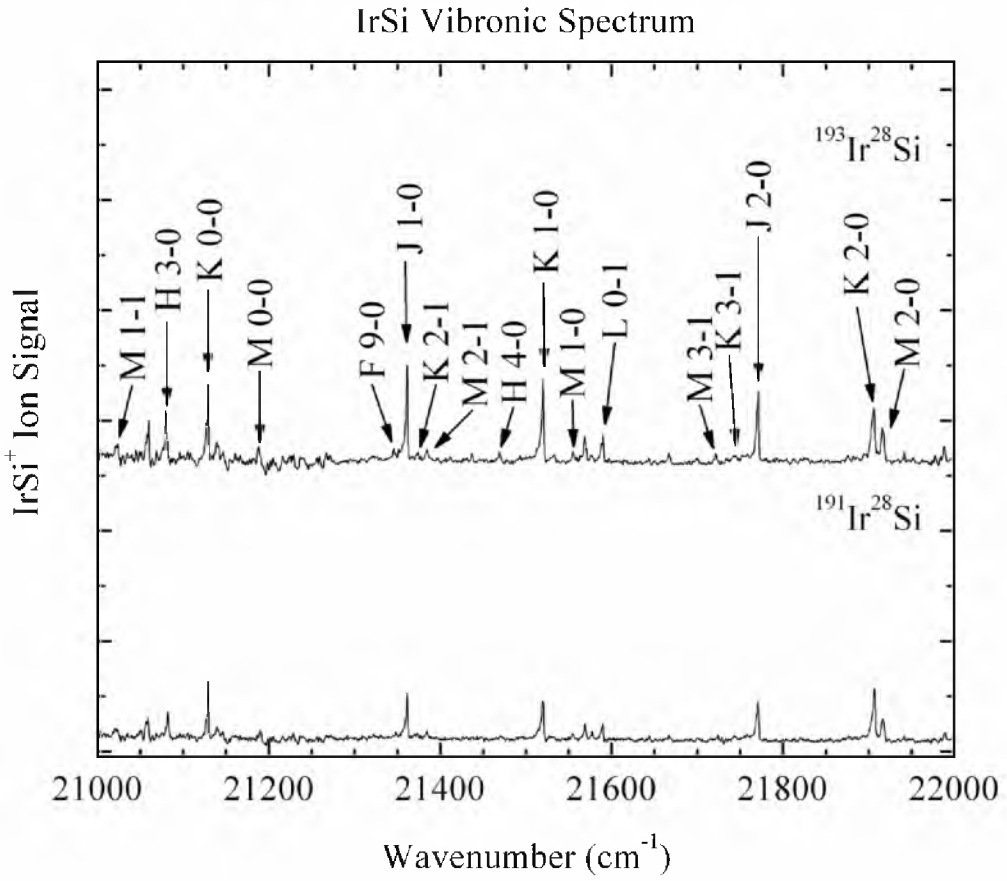

Figure B.5 Vibronically resolved spectra of $^{191}Ir^{28}Si$ and $^{193}Ir^{28}Si$ over the 21000-22000 cm^{-1} range. Bands from the F-X, H-X, J-X, K-X, L-X, and M-X systems are indicated.

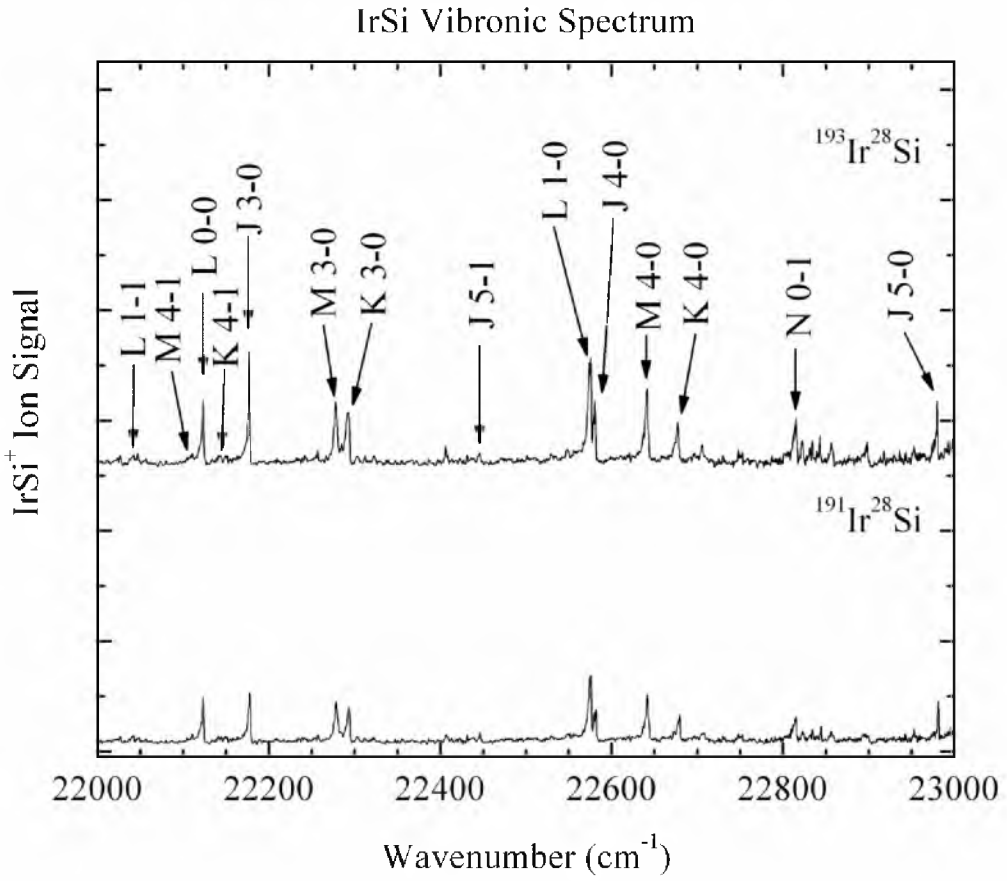

Figure B.6 Vibronically resolved spectra of $^{191}Ir^{28}Si$ and $^{193}Ir^{28}Si$ over the 22000-23000 cm^{-1} range. Bands from the J-X, K-X, L-X, M-X, and N-X systems are indicated.

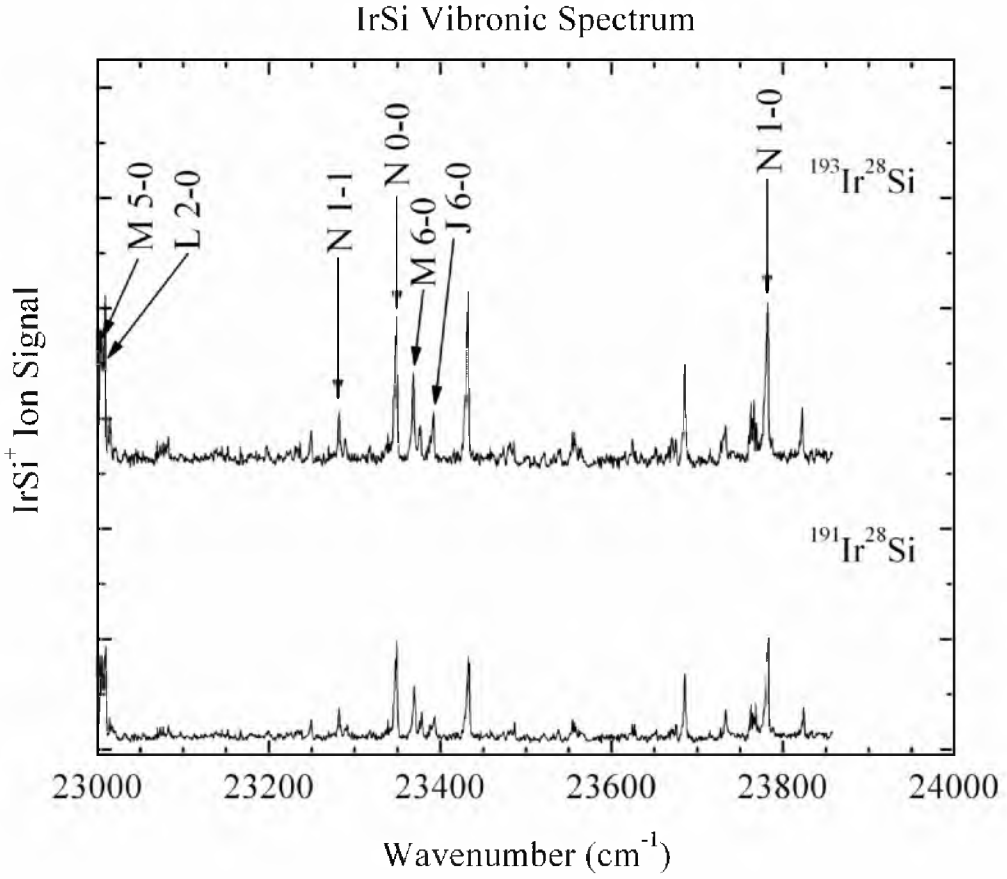

Figure B.7 Vibronically resolved spectra of $^{191}Ir^{28}Si$ and $^{193}Ir^{28}Si$ over the 23000-24000 cm^{-1} range. Bands from the J-X, L-X, M-X, and N-X systems are indicated.

Table B.1 Measured band head positions for $^{191}Ir^{28}Si$ and $^{193}Ir^{28}Si$.[a]

Band designation	Intensity	$^{191}Ir^{28}Si$		$^{193}Ir^{28}Si$		Isotope Shift from Band Head	Isotope Shift from ν_0	Lifetime (μs)
		Band Head	ν_0	Band Head	ν_0			
	m	23824.79		23822.80		1.98		
N-X 1-0	s	23783.46	23781.8000	23783.22	23781.4956	0.24	0.3044	0.71(16)
	w	23734.98		23734.07		0.91		
	vw	23715.24		23715.42		-0.18		
	s	23687.82	23686.4986	23686.87	23686.0427	0.95	0.4559	4.23(12)
	vw	23676.60		23676.09		0.51		
	vw	23672.20		23671.39		0.81		
	vw	23487.43		23486.27		1.17		
	vs	23434.61	23432.4970	23433.01	23431.1720	1.60	1.3250	2.99(26)
	w	23394.83		23392.84		1.99		
J-X 6-0	w	23379.36		23377.43		1.92		
M-X 5-0	s	23371.82		23369.50		2.32		
N-X 0-0	vs	23350.09	23347.8670	23350.13	23347.8577	-0.04	0.0093	0.93(2)
	vw	23292.15		23290.55		1.61		
	w	23282.64		23282.58		0.07		
N-X 1-1	w	23250.54		23250.42		0.12		
	vw	23238.75		23237.02		1.73		
	w	23018.05		23016.27		1.78		
L-X 2-0	vs	23010.38		23009.54		0.84		2.66(9)
M-X 4-0	s	23006.97		23005.22		1.75		
J-X 5-0	m	22981.83		22980.67		1.17		
	vw	22953.30		22953.53		-0.23		
	vw	22900.17		22898.87		1.30		
	vw	22858.99		22858.78		0.22		

[a] Quantities are given in cm^{-1} units unless otherwise specified. Intensities are relative and qualitative: vs, very strong; s, strong; m, medium; w, weak; vw, very weak.

Table B.1 (continued)

Band designation	Intensity	$^{191}Ir^{28}Si$		$^{193}Ir^{28}Si$		Isotope Shift from Band Head	Isotope Shift from ν_0	Lifetime (μs)
		Band Head	ν_0	Band Head	ν_0			
	vw	22844.79		22843.35		1.44		
	vw	22835.85		22835.10		0.74		
	vw	22824.76		22823.40		1.36		
N-X 0-1	w	22815.82		22816.31		-0.49		
	vw	22752.75		22752.95		-0.20		
	vw	22708.97		22706.66		2.31		
K-X 4-0	w	22679.90		22678.46		1.44		2.75(5)
M-X 3-0	m	22644.25		22643.48		0.77		2.10(18)
J-X 4-0	m	22582.44		22581.28		1.16		
L-X 1-0	s	22576.79	22575.0541	22576.53	22574.7361	0.27	0.3180	
J-X 5-1	vw	22447.21		22446.84		0.38		
	vw	22431.83		22432.01		-0.18		
	vw	22409.58		22408.63		0.95		
	vw	22387.07		22387.54		-0.47		
K-X 3-0	m	22294.72		22294.10		0.63		2.79(14)
M-X 2-0	m	22281.19		22279.93		1.27		2.23(9)
	vw	22258.54		22257.41		1.13		
J-X 3-0	s	22178.74	22177.5440	22177.77	22176.7500	0.97	0.7940	5.72(28)
L-X 0-0	s	22124.17	22122.6843	22123.95	22122.6612	0.21	0.0231	2.06(5)
M-X 4-1	vw	22112.52		22112.35		0.17		
L-X 1-1	vw	22042.75		22042.85		-0.10		
	vw	22027.27		22027.54		-0.27		
	vw	21990.51		21989.76		0.75		
	vw	21979.54		21978.71		0.83		

[a] Quantities are given in cm^{-1} units unless otherwise specified. Intensities are relative and qualitative: vs, very strong; s, strong; m, medium; w, weak; vw, very weak.

Table B.1 (continued)

Band designation	Intensity	$^{191}Ir^{28}Si$		$^{193}Ir^{28}Si$		Isotope Shift from Band Head	Isotope Shift from ν_0	Lifetime (μs)
		Band Head	ν_0	Band Head	ν_0			
L-X 1-1	vw	21942.19		21942.14		0.05		
M-X 1-0	m	21918.69	21918.9692	21918.35	21918.7268	0.34	0.2424	2.38(8)
K-X 2-0	m	21908.14	21906.8399	21907.57	21906.3267	0.57	0.5132	2.59(1)
J-X 2-0	s	21772.20	21770.6652	21772.04	21770.1522	0.17	0.5130	6.11(5)
K-X 3-1	vw	21760.17		21760.27		-0.10		
M-X 3-1	vw	21745.83		21746.99		-1.16		
	vw	21724.88		21723.33		1.55		
	vw	21702.09		21701.50		0.59		
	vw	21670.17		21668.60		1.57		
L-X 0-1	w	21590.65		21591.08		-0.43		
	vw	21578.54		21578.73		-0.19		
	w	21569.99		21570.94		-0.94		
M-X 0-0	vw	21556.18		21556.49		-0.31		
	vw	21534.39		21534.26		0.13		
K-X 1-0	vs	21521.13	21519.6138	21520.80	21519.3462	0.33	0.2676	2.61(6)
H-X 4-0	vw	21474.58		21470.75		3.83		
	vw	21443.58		21438.20		5.38		
M-X 1-1	vw	21385.99		21385.67		0.32		
K-X 2-1	vw	21375.26		21375.17		0.09		
J-X 1-0	s	21362.34	21360.3516	21362.13	21360.0964	0.20	0.2552	6.39(24)
F-X 9-0	vw	21349.91		21348.29		1.62		
	vw	21191.63		21190.01		1.62		
	vw	21141.98		21142.18		-0.20		
K-X 0-0	s	21129.82	21129.0989	21129.90	21129.0858	-0.08	0.0131	2.38(16)

[a] Quantities are given in cm^{-1} units unless otherwise specified. Intensities are relative and qualitative: vs, very strong; s, strong; m, medium; w, weak; vw, very weak.

Table B.1 (continued)

Band designation	Intensity	$^{191}Ir^{28}Si$		$^{193}Ir^{28}Si$		Isotope Shift from Band Head	Isotope Shift from ν_0	Lifetime (μs)
		Band Head	ν_0	Band Head	ν_0			
H-X 3-0	m	21083.80		21081.20		2.60		
	m	21060.01		21060.63		-0.62		
M-X 0-1	vw	21024.47		21024.45		0.02		
K-X 1-1	w	20987.34		20987.31		0.03		
F-X 8-0	w	20976.48		20975.37		1.11		
J-X 0-0	vs	20948.03	20946.5700	20947.91	20946.5791	0.12	-0.0091	7.25(30)
I-X 3-0	m	20865.75		20865.18		0.57		
J-X 1-1	m	20828.64		20828.46		0.17		
	vw	20815.33		20813.64		1.69		
	vw	20730.75		20729.91		0.84		
H-X 2-0	m	20691.65		20690.29		1.36		
F-X 7-0	m	20606.69		20604.98		1.72		
K-X 0-1	vw	20597.11		20597.05		0.06		
	vw	20576.42		20576.14		0.28		
	vw	20550.44		20549.05		1.39		
I-X 2-0	w	20451.80		20451.48		0.32		
J-X 0-1	vw	20414.58		20414.67		-0.10		
	vw	20342.27		20342.22		0.05		
	vw	20316.71		20314.21		2.50		
H-X 1-0	w	20296.56		20294.64		1.92		
F-X 6-0	m	20234.43		20231.62		2.81		
	vw	20222.19		20221.60		0.59		
H-X 2-1	vw	20157.51		20157.48		0.03		
F-X 7-1	vw	20073.63		20071.76		1.86		

[a] Quantities are given in cm^{-1} units unless otherwise specified. Intensities are relative and qualitative: vs, very strong; s, strong; m, medium; w, weak; vw, very weak.

Table B.1 (continued)

Band designation	Intensity	$^{191}Ir^{28}Si$		$^{193}Ir^{28}Si$		Isotope Shift from Band Head	Isotope Shift from ν_0	Lifetime (μs)
		Band Head	ν_0	Band Head	ν_0			
G-X 6-0	w	20064.78		20063.31		1.47		
	vw	20045.67		20042.34		3.32		
I-X 1-0	m	20034.38		20033.44		0.94		
	vw	20021.45		20019.75		1.70		
	vw	20009.39		20002.30		7.08		
	vw	19993.81		19991.93		1.88		
	vw	19967.57		19968.66		-1.10		
	vw	19953.34		19953.24		0.10		
	w	19945.29		19943.04		2.25		
A-X 11-0	w	19938.05		19937.99		0.06		
B-X 10-0	vw	19920.82		19918.61		2.21		
H-X 0-0	w	19900.57		19899.76		0.81		
	vw	19884.92		19885.06		-0.14		
	vw	19879.93		19877.07		2.86		
F-X 5-0	s	19854.27		19852.28		1.99		
	vw	19783.22		19781.48		1.74		
	vw	19773.09		19771.04		2.05		
F-X 6-1	w	19700.46		19698.62		1.84		
G-X 5-0	m	19694.25		19692.50				
	vw	19682.95		19682.85		0.09		
	vw	19627.50		19623.11		4.39		
I-X 0-0	m	19616.51		19615.15		1.35		
A-X 10-0	m	19579.97	19578.8610	19578.04	19576.8578	1.93	2.0032	
	vw	19570.92		19568.74		2.18		

[a] Quantities are given in cm^{-1} units unless otherwise specified. Intensities are relative and qualitative: vs, very strong; s, strong; m, medium; w, weak; vw, very weak.

Table B.1 (continued)

Band designation	Intensity	$^{191}Ir^{28}Si$		$^{193}Ir^{28}Si$		Isotope Shift from Band Head	Isotope Shift from ν_0	Lifetime (μs)
		Band Head	ν_0	Band Head	ν_0			
A-X 10-0	vw	19543.81		19541.44		2.37		
B-X 9-0	w	19530.68		19528.14		2.54		
	vw	19514.46		19512.76		1.70		
	vw	19478.31		19475.57		2.74		
F-X 4-0	s	19461.13	19459.7939	19459.89	19458.7183	1.24	1.0756	
	vw	19435.20		19433.84		1.36		
	w	19411.83		19409.46		2.36		
A-X 11-1	w	19404.24		19404.62		-0.38		
	w	19387.18		19385.26		1.92		
C-X 10-0	vw	19379.24		19375.78		3.46		
	vw	19357.27		19357.80		-0.53		
	vw	19345.30		19343.38		1.92		
G-X 4-0	s	19320.08	19318.8026	19319.17	19317.8435	0.91	0.9591	
	vw	19277.82		19277.05		0.77		
	vw	19252.74		19251.47		1.27		
	vw	19243.04		19241.97		1.07		
A-X 9-0	m	19224.43		19222.35		2.08		
D-X 3-0	m	19207.07	19205.1928	19206.29	19204.4066	0.79	0.7862	8.83(21)
	vw	19170.54		19170.78		-0.24		
B-X 8-0	m	19139.35		19137.20		2.14		
	m	19104.44		19103.68		0.76		
F-X 3-0	vs	19057.98	19056.1096	19056.89	19055.3686	1.09	0.7410	6.00(20)
A-X 10-1	m	19046.75		19045.00		1.75		
C-X 9-0	m	19000.53		18996.75		3.78		

[a] Quantities are given in cm^{-1} units unless otherwise specified. Intensities are relative and qualitative: vs, very strong; s, strong; m, medium; w, weak; vw, very weak.

Table B.1 (continued)

Band designation	Intensity	$^{191}Ir^{28}Si$		$^{193}Ir^{28}Si$		Isotope Shift from Band Head	Isotope Shift from ν_0	Lifetime (μs)
		Band Head	ν_0	Band Head	ν_0			
	vw	18980.31		18979.13		1.18		
	w	18972.37		18971.80		0.57		
G-X 3-0	m	18943.08		18942.38		0.70		
F-X 4-1	w	18927.67		18926.67		1.00		
A-X 8-0	s	18872.86		18870.78		2.08		
C-X 10-1	w	18845.82		18844.00		1.82		
D-X 2-0	s	18811.08	18809.2783	18810.60	18808.6668	0.48	0.6115	6.57(13)
B-X 7-0	s	18745.36	18744.1086	18743.01	18742.3968	2.35	1.7118	1.49(6)
	vw	18725.38		18724.12		1.26		
A-X 9-1	m	18690.76		18689.06		1.70		
	s	18682.88		18682.73		0.15		
E-X 3-0	vs	18647.38		18646.92		0.46		8.42(74)
	vw	18629.81		18628.43		1.38		
	vw	18622.55		18619.75		2.80		
C-X 8-0	m	18616.26		18615.55		0.72		
B-X 8-1	w	18605.09		18603.13		1.96		
	w	18569.88		18571.99		-2.11		
G-X 2-0	w	18562.03		18561.62		0.40		
	vw	18537.46		18535.56		1.90		
	vw	18529.39		18527.12		2.27		
A-X 7-0	vs	18520.77	18519.9267	18519.15	18518.3803	1.62	1.5464	2.30(19)
	vw	18486.32		18484.45		1.87		
C-X 9-1	w	18466.82		18464.38		2.43		
	vw	18453.60		18452.41		1.19		

[a] Quantities are given in cm^{-1} units unless otherwise specified. Intensities are relative and qualitative: vs, very strong; s, strong; m, medium; w, weak; vw, very weak.

Table B.1 (continued)

Band designation	Intensity	$^{191}Ir^{28}Si$		$^{193}Ir^{28}Si$		Isotope Shift from Band Head	Isotope Shift from ν_0	Lifetime (μs)
		Band Head	ν_0	Band Head	ν_0			
D-X 1-0	vs	18420.53	18419.2633	18420.26	18418.8985	0.27	0.3648	5.24(21)
B-X 6-0	vs	18350.92	18349.8878	18349.42	18348.4722	1.50	1.4156	1.26(2)
A-X 8-1	m	18338.55		18337.54		1.01		
	vw	18331.26		18328.41		2.84		
	vw	18315.28		18313.86		1.41		
	vw	18302.50		18302.40		0.11		
	vw	18287.83		18286.56		1.27		
E-X 2-0	s	18268.90	18267.2942	18268.49	18266.9015	0.41	0.3927	8.50(23)
C-X 7-0	s	18230.66	18229.4193	18229.18	18227.7317	1.48	1.6876	4.20(13)
B-X 7-1	w	18211.87		18210.62		1.25		
G-X 1-0	vw	18178.99		18179.07		-0.08		
A-X 6-0	vs	18169.22	18167.7443	18167.85	18166.4400	1.36	1.3043	2.45(16)
C-X 8-1	w	18084.56		18082.92		1.63		
	vw	18075.77		18074.39		1.39		
D-X 0-0	s	18025.81	18023.7785	18025.80	18023.6992	0.01	0.0793	5.23(20)
A-X 7-1	w	17987.15		17985.54		1.61		
B-X 5-0	m	17957.28	17956.4130	17956.10	17955.3049	1.19	1.1081	1.16(6)
	w	17946.41		17945.66		0.75		
E-X 1-0	w	17884.13		17884.02		0.11		
C-X 6-0	m	17837.16		17835.64		1.52		6.17(10)
	vw	17817.31		17815.95		1.37		
A-X 5-0	s	17813.54	17812.7943	17812.70	17811.7907	0.84	1.0036	2.63(4)
C-X 7-1	vw	17696.92		17694.32		2.60		
A-X 6-1	vw	17635.22		17633.85		1.37		

[a] Quantities are given in cm^{-1} units unless otherwise specified. Intensities are relative and qualitative: vs, very strong; s, strong; m, medium; w, weak; vw, very weak.

Table B.1 (continued)

Band designation	Intensity	$^{191}Ir^{28}Si$		$^{193}Ir^{28}Si$		Isotope Shift from Band Head	Isotope Shift from ν_0	Lifetime (μs)
		Band Head	ν_0	Band Head	ν_0			
	vw	17628.86		17628.76		0.10		
	vw	17579.33		17579.48		-0.15		
B-X 4-0	m	17566.13		17565.24		0.89		
	m	17546.81		17546.25		0.55		
	vw	17537.59		17537.36		0.22		
A-X 4-0	m	17452.24	17450.7376	17451.43	17450.1329	0.81	0.6047	2.84(12)
	vw	17445.54		17445.07		0.47		
	vw	17437.99		17436.68		1.31		
B-X 5-1	vw	17423.51		17423.25		0.26		
	vw	17360.00		17359.87		0.13		
	w	17349.97		17348.48		1.49		
C-X 6-1	vw			17305.18				
	vw	17283.37		17283.24		0.13		
A-X 5-1	vw	17274.00		17271.76		2.24		
	vw	17220.01		17219.39		0.63		

[a] Quantities are given in cm^{-1} units unless otherwise specified. Intensities are relative and qualitative: vs, very strong; s, strong; m, medium; w, weak; vw, very weak.

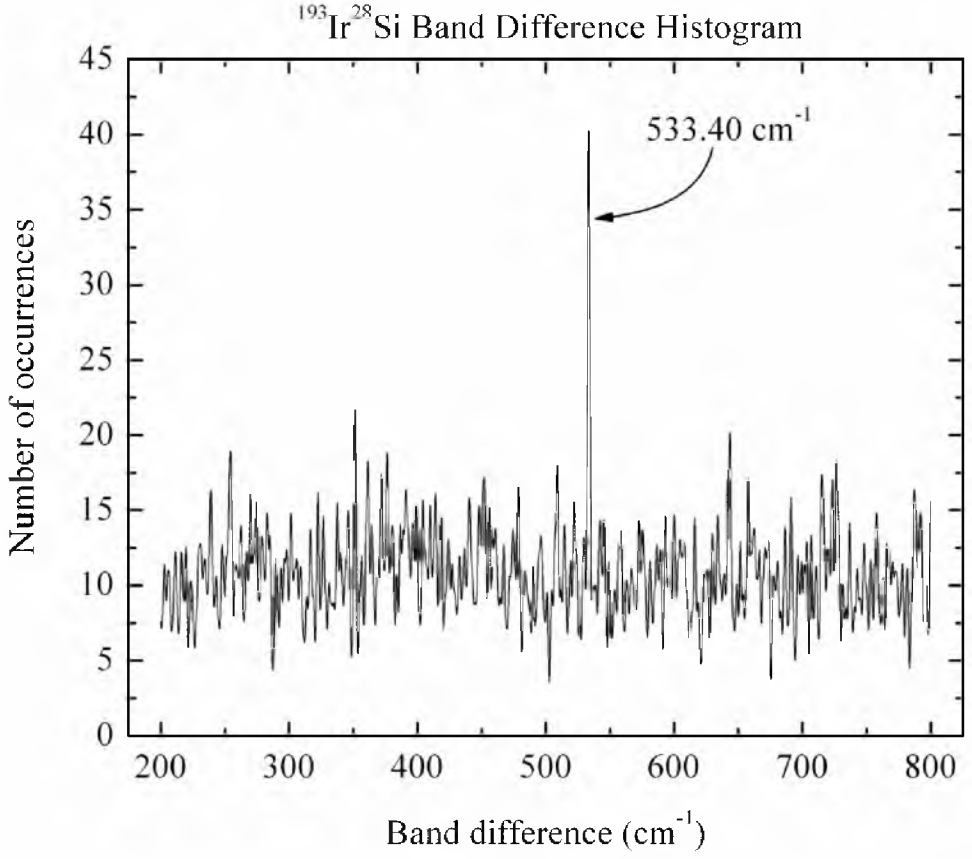

Figure B.8 Band difference histogram for $^{193}Ir^{28}Si$, demonstrating that $\Delta G_{1/2}'' = 533.4$ cm^{-1}.

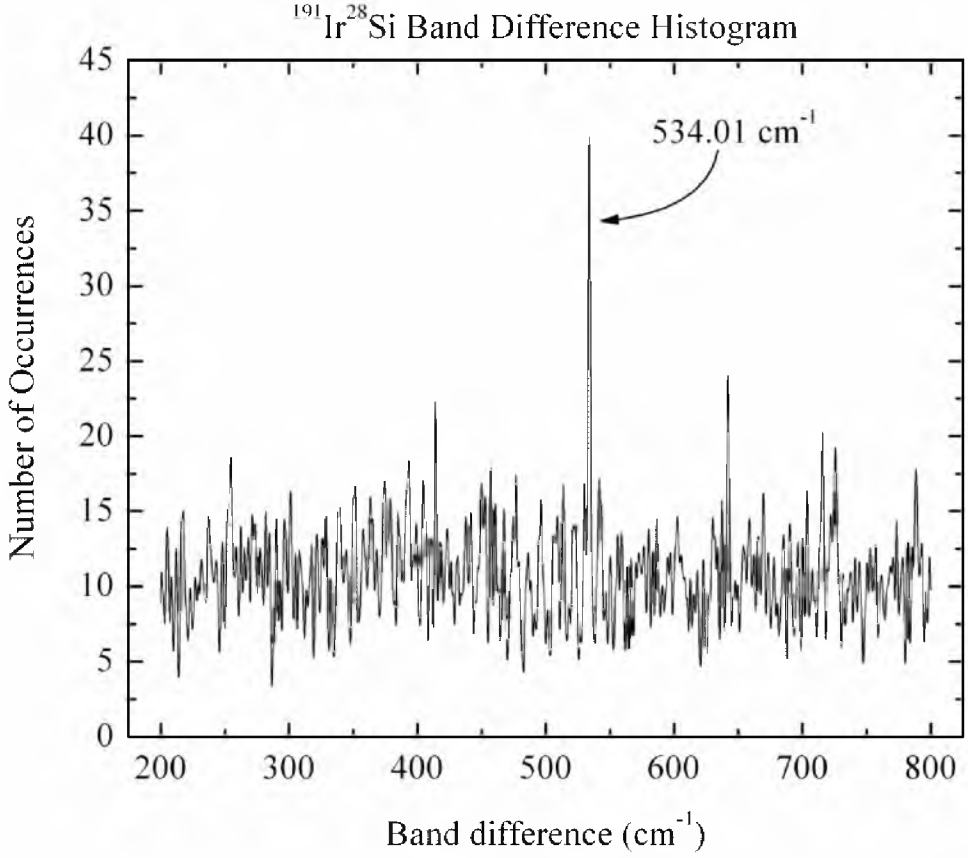

Figure B.9 Band difference histogram for $^{193}Ir^{28}Si$, demonstrating that $\Delta G_{1/2}'' = 534.0$ cm^{-1}.

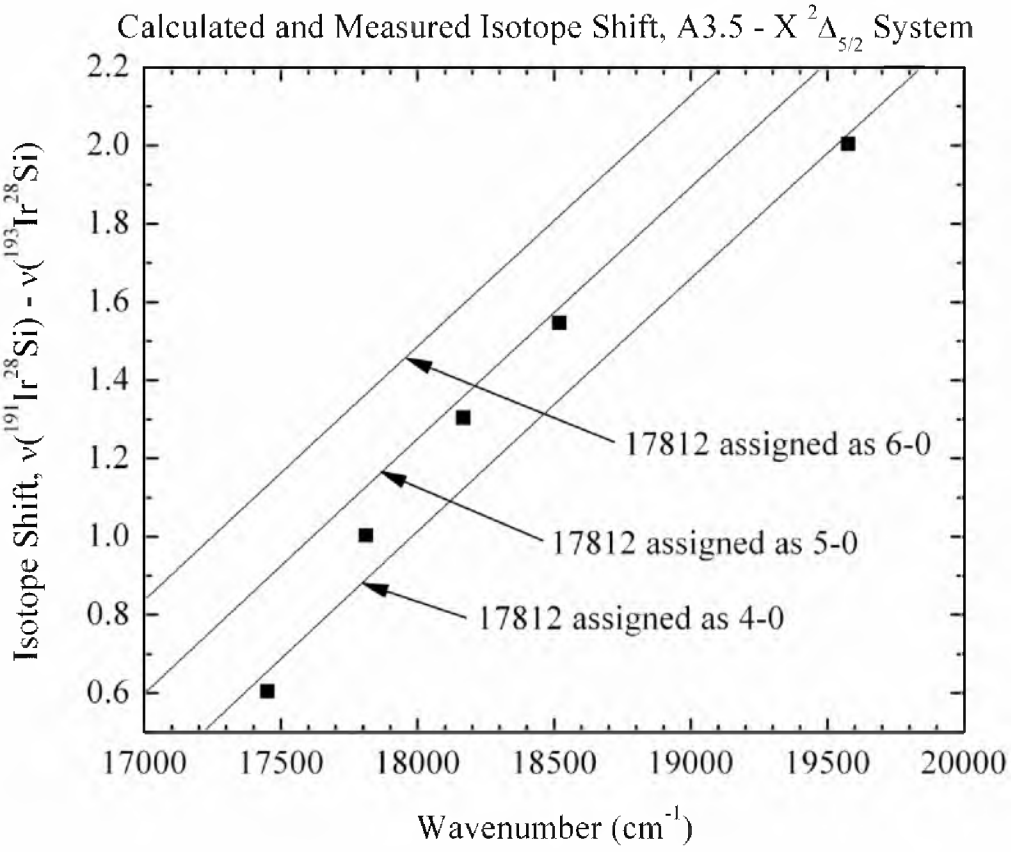

Figure B.10 Calculated (lines) and measured (black squares) isotope shifts of various bands of the A-X system. Based on this plot, we have assigned the 17812 cm^{-1} band as the 5-0 band, although the data are also consistent with its assignment as the 4-0 band.

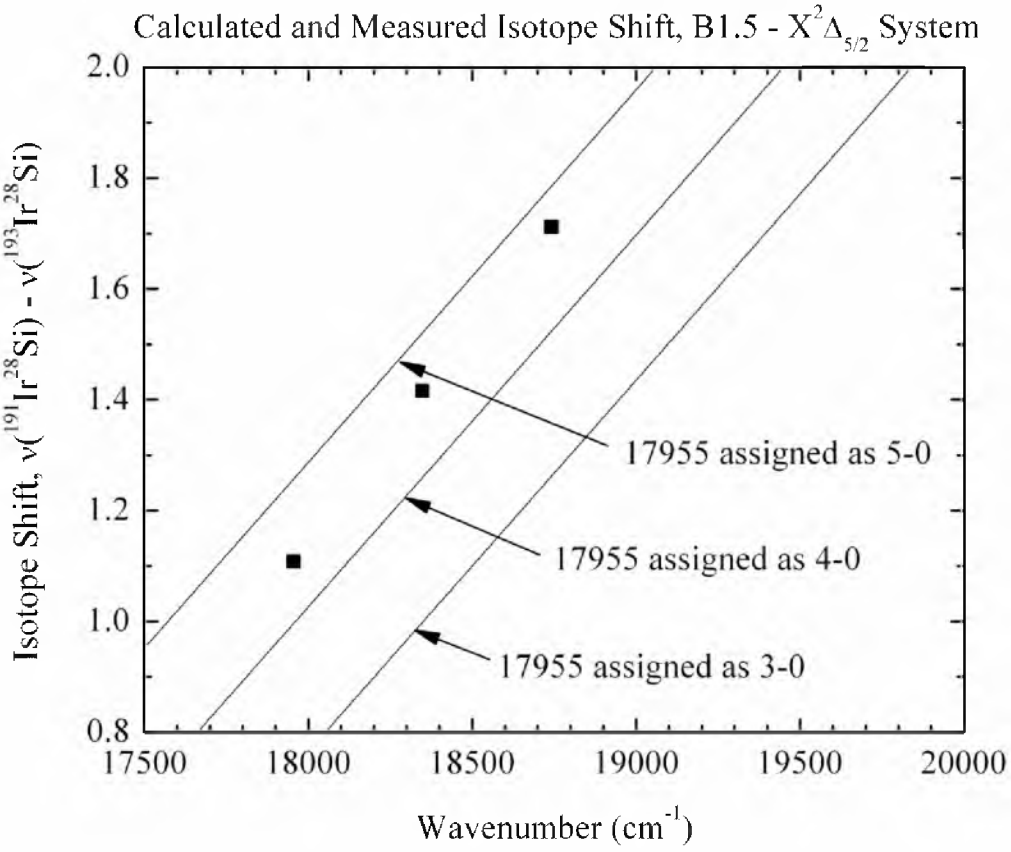

Figure B.11 Calculated (lines) and measured (black squares) isotope shifts of various bands of the B-X system. Based on this plot, we have assigned the 17955 cm^{-1} band as the 5-0 band, although it is also conceivable that this band is the 4-0 band.

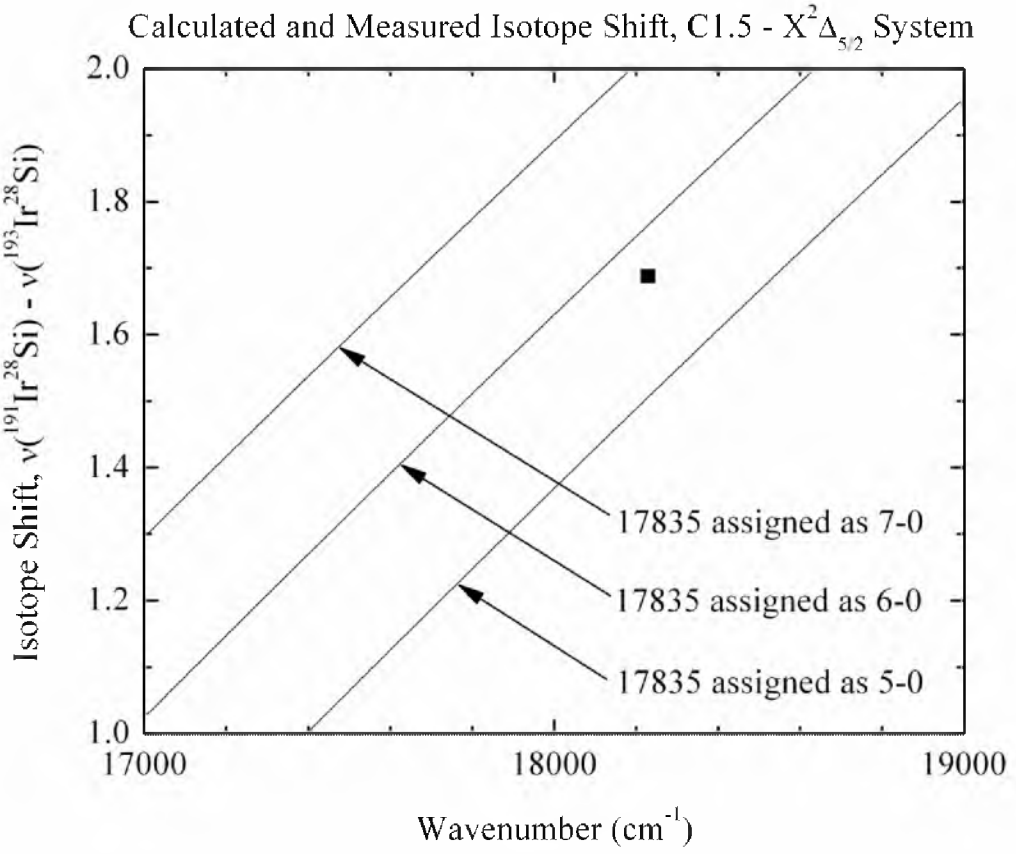

Figure B.12 Calculated (lines) and measured (black square) isotope shifts of various bands of the C-X system. Based on this plot, we have assigned the 17835 cm^{-1} band as the 6-0 band, although its assignment as the 5-0 band is conceivable.

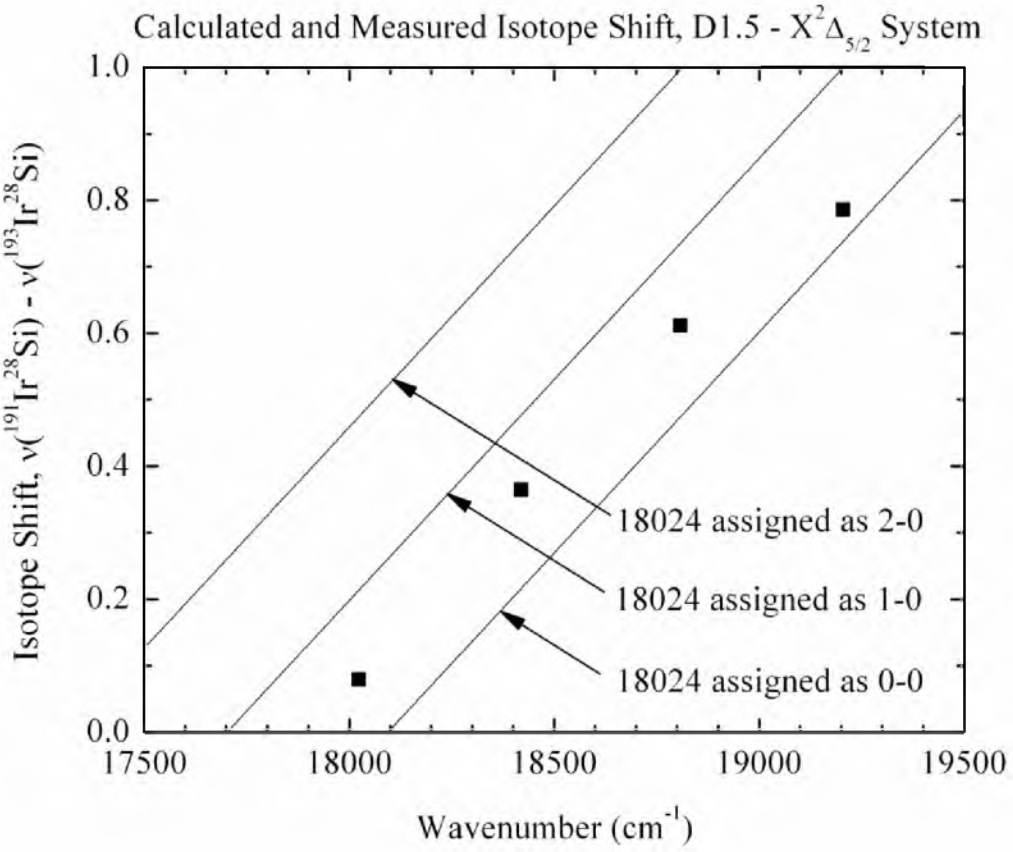

Figure B.13 Calculated (lines) and measured (black squares) isotope shifts of various bands of the D-X system. Although this plot suggests that the 18024 cm^{-1} band could be either the 1-0 or 0-0 band, we have assigned it as 0-0 based on the lack of an apparent 0-0 band to the red of the reasonably intense 18024 cm^{-1} band.

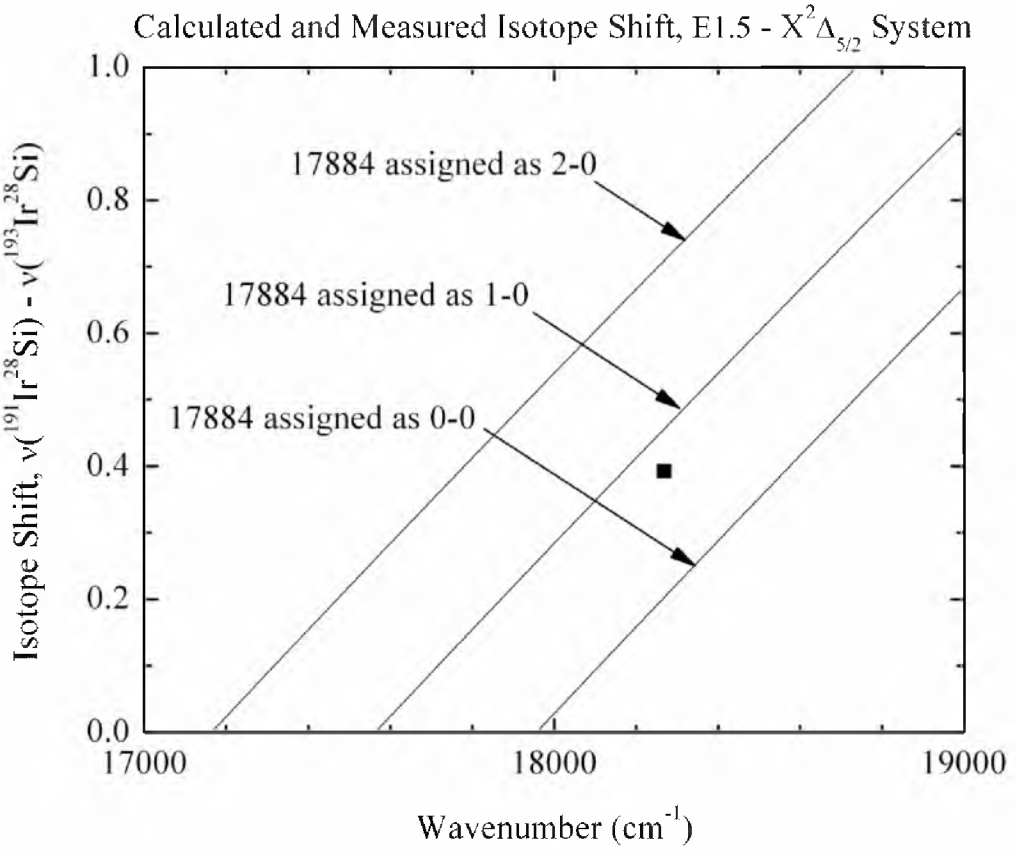

Figure B.14 Calculated (lines) and measured (black square) isotope shifts of various bands of the E-X system. Based on this plot, we have assigned the 17884 cm^{-1} band as the 1-0 band, although its assignment as the 0-0 band is conceivable.

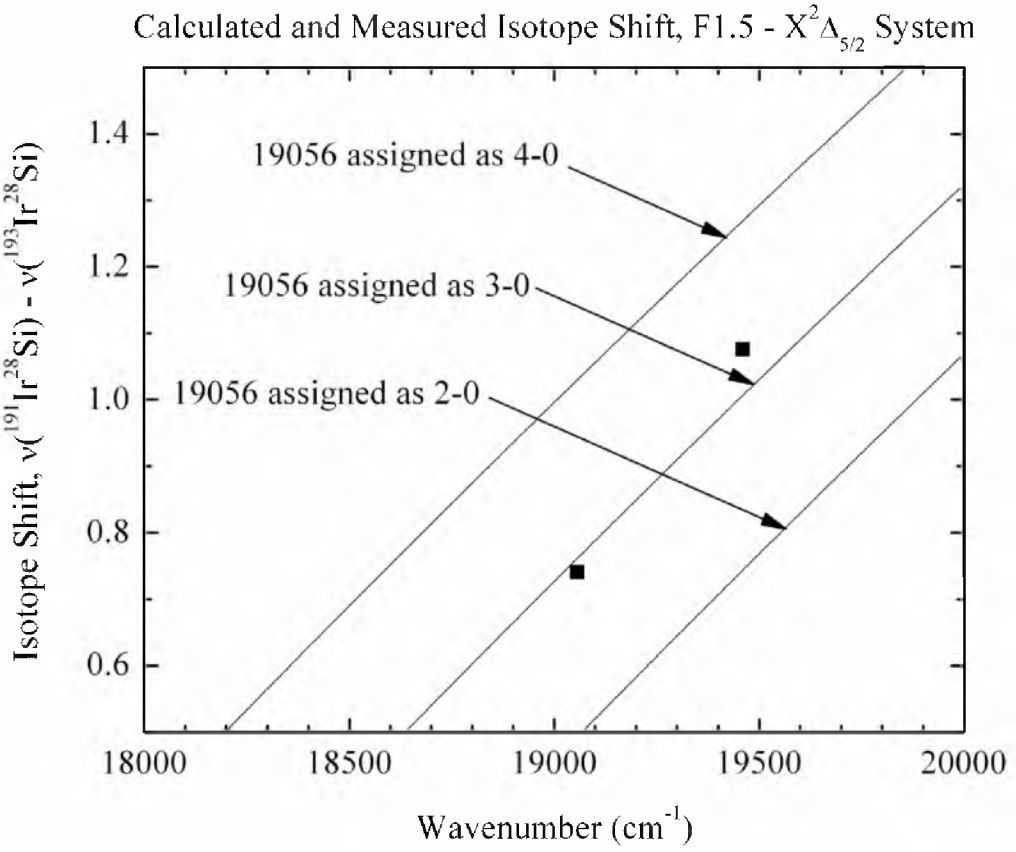

Figure B.15 Calculated (lines) and measured (black squares) isotope shifts of various bands of the F-X system. Based on this plot, we have assigned the 19056 cm^{-1} band as the 3-0 band.

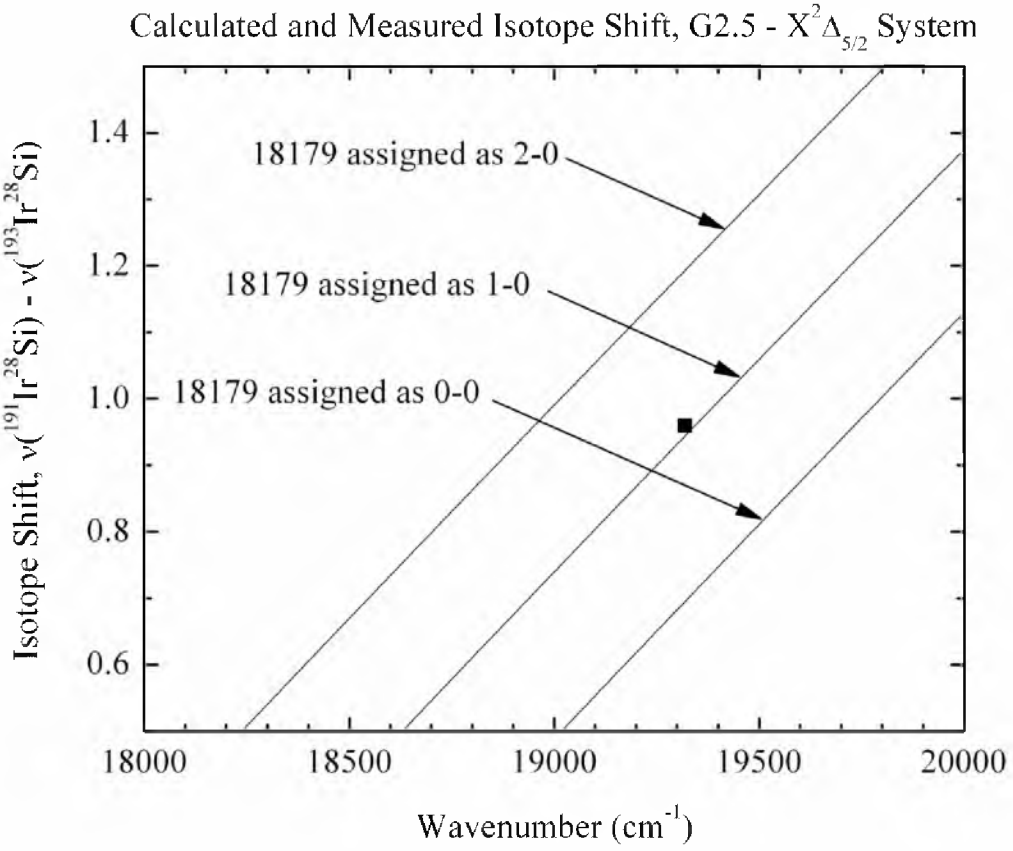

Figure B.16 Calculated (lines) and measured (black square) isotope shifts of various bands of the G-X system. Based on this plot, we have assigned the 18179 cm^{-1} band as the 1-0 band.

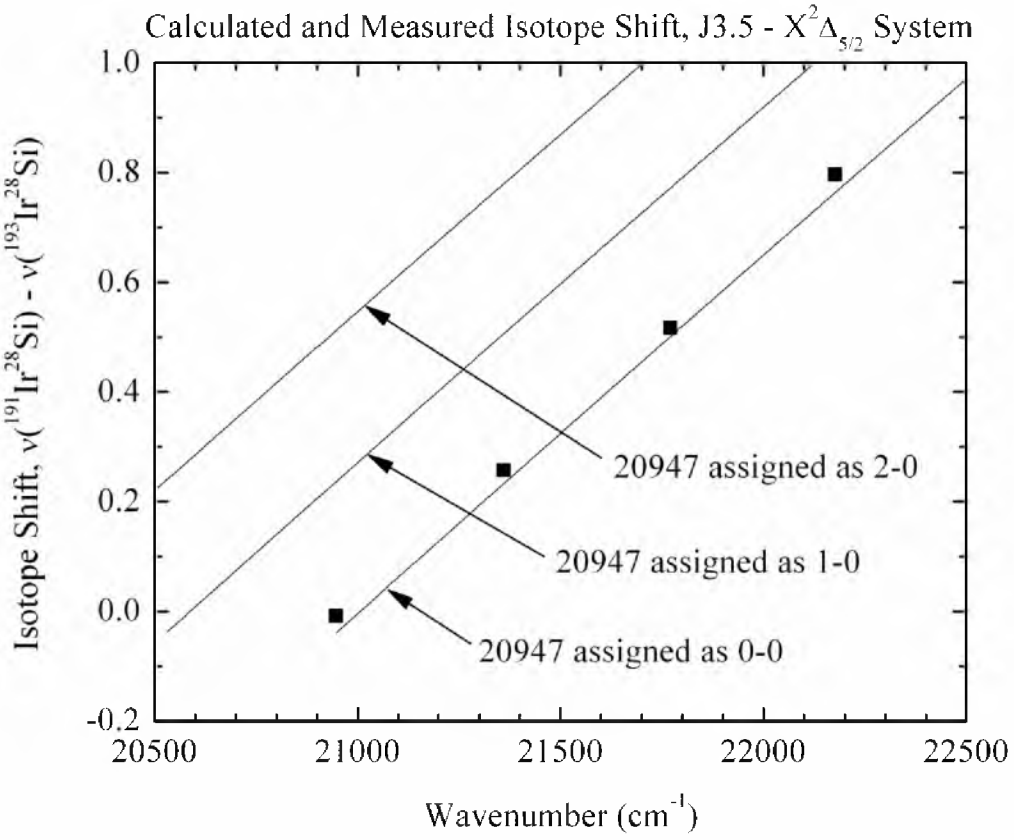

Figure B.17 Calculated (lines) and measured (black squares) isotope shifts of various bands of the J-X system. Based on this plot, we have assigned the 20947 cm^{-1} band as the 0-0 band. This is confirmed by the lack of another band at the appropriate energy to the red of this intense feature.

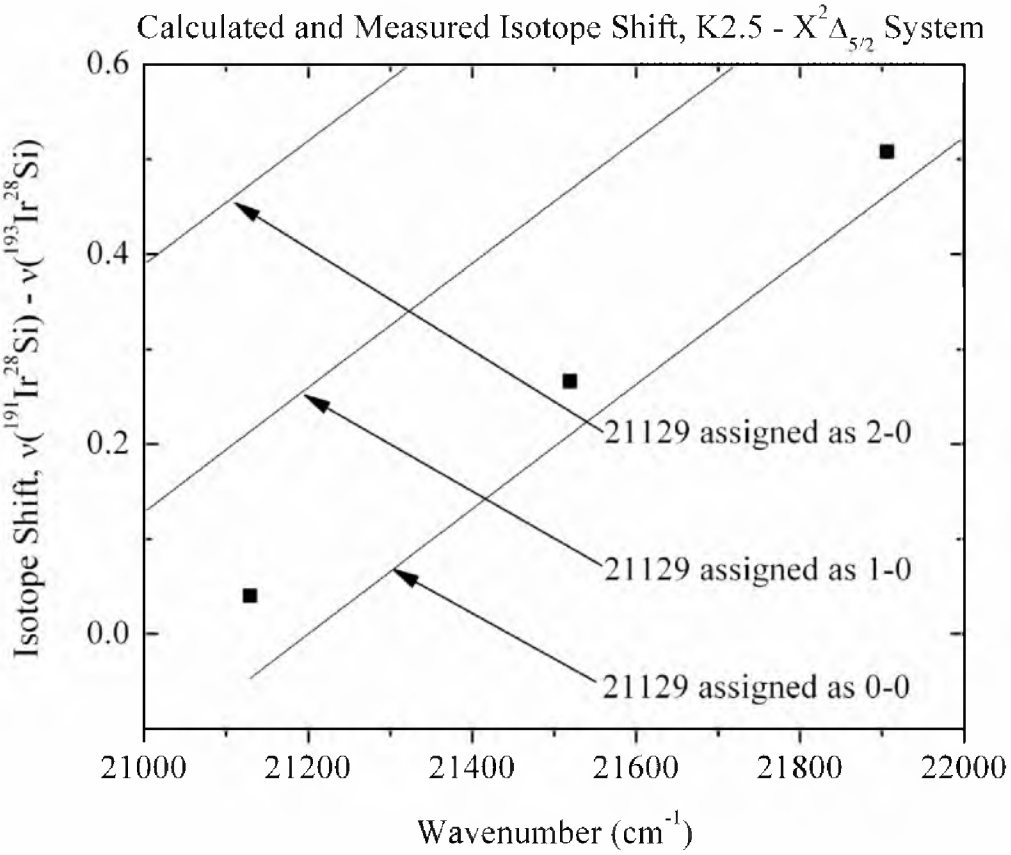

Figure B.18 Calculated (lines) and measured (black squares) isotope shifts of various bands of the K-X system. Based on this plot, we have assigned the 21129 cm^{-1} band as the 0-0 band. Although from this plot it looks as if the 21129 cm^{-1} band could be the 1-0 band, its assignment as the 0-0 band is confirmed by the lack of another band at the appropriate position to the red of this feature.

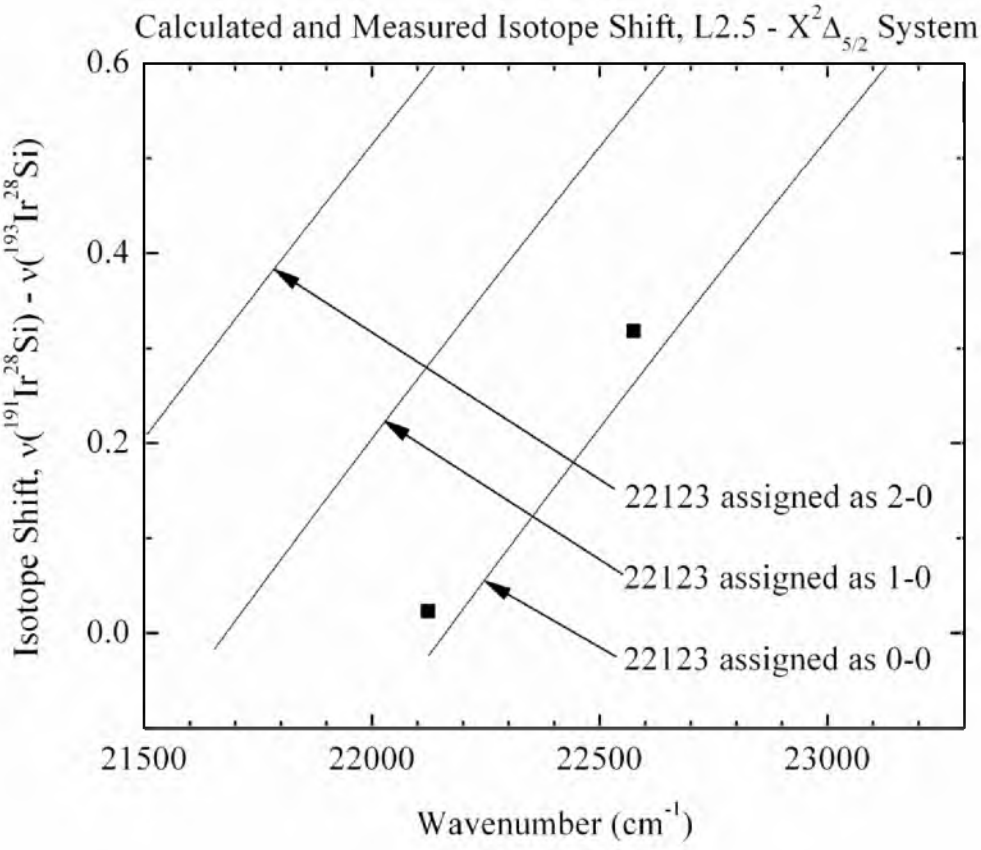

Figure B.19 Calculated (lines) and measured (black squares) isotope shifts of various bands of the L-X system. Based on this plot, we have assigned the 22123 cm^{-1} band as the 0-0 band. This assignment is confirmed by the lack of another band at the appropriate position to the red of this feature.

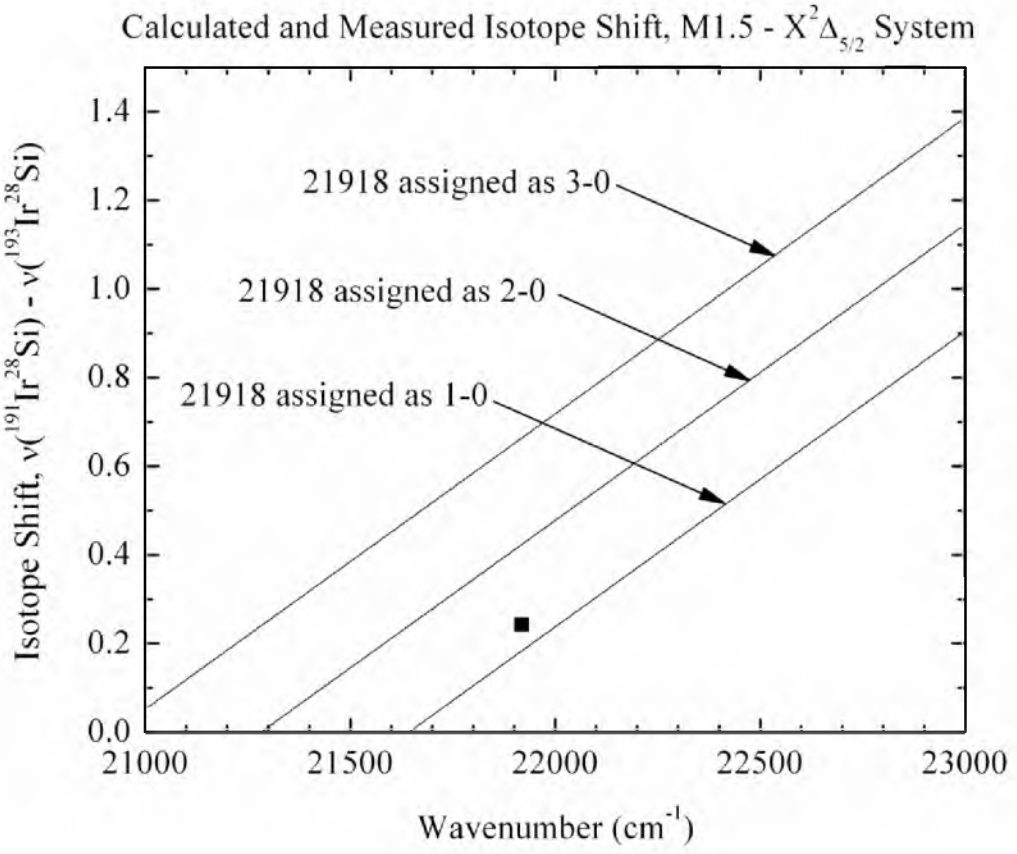

Figure B.20 Calculated (lines) and measured (black square) isotope shifts of various bands of the M-X system. Based on this plot, it looks as if the 21918 cm^{-1} band is the 1-0 band. However, features are present in the spectrum at the expected positions of the 1-0 and 0-0 bands when the 21918 cm^{-1} band is assigned as the 2-0 band. Because we have not rotationally resolved other bands of the M-X system, we are reluctant to base the vibrational assignment on just this single measurement. We tentatively assign the 21918 cm^{-1} band as the 2-0 band, based on the presence of additional features at the positions expected for the 1-0 and 0-0 bands.

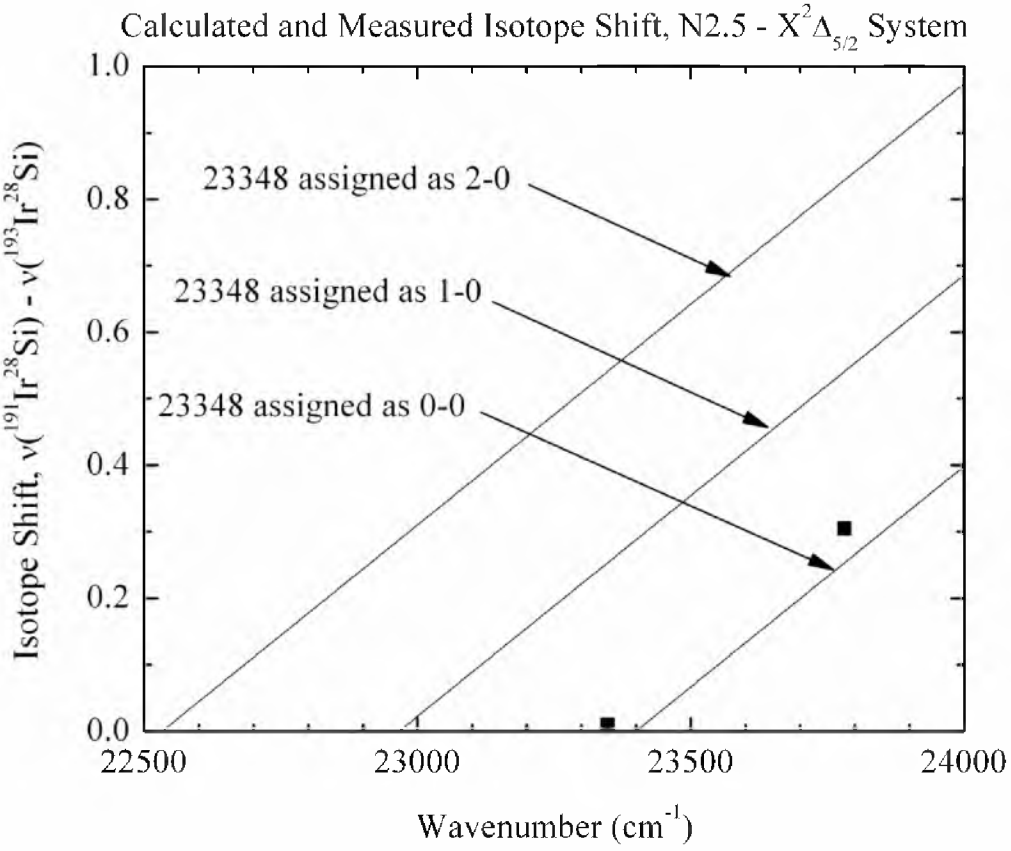

Figure B.21 Calculated (lines) and measured (black squares) isotope shifts of various bands of the N-X system. Based on this plot, we have assigned the 23348 cm^{-1} band as the 0-0 band. This assignment is confirmed by the lack of another band at the appropriate position to the red of this feature.

Table B. 2 Vibronic Fits of Band Head Positions

Band System	Band	$^{191}Ir^{28}Si$	$^{193}Ir^{28}Si$
A[16.0]3.5 ← X $^2\Delta_{5/2}$ Note: Vibrational numbering is slightly uncertain. It is conceivable that v′ should be decreased by 1 unit.	4-0	17452.24(-379)	17451.43(-380)
	5-1	17274.00(-302)	17271.76(-430)
	5-0	17813.54(291)	17812.70(354)
	6-1	17635.22(373)	17633.85(376)
	6-0	18169.22(412)	18167.85(467)
	7-1	17987.15(133)	17985.54(133)
	7-0	18520.77(134)	18519.15(184)
	8-1	18338.55(-147)	18337.54(-89)
	8-0	18872.86(-77)	18870.78(-75)
	9-1	18690.76(-332)	18689.06(-369)
	9-0	19224.43(-326)	19222.35(-349)
	10-1	19046.75(-126)	19045.00(-216)
	10-0	19579.97(-164)	19578.04(-222)
	11-1	19404.24(244)	19404.62(294)
	11-0	19938.05(264)	19937.99(322)
	Fitted Spectroscopic Constants		
	T_0 (cm^{-1})	16036.28(1072)	16040.49(1230)
	ω_e' (cm^{-1})	355.27(313)	353.44(359)
	$\omega_e'x_e'$ (cm^{-1})	0.067(190)	-0.049(218)
	$\Delta G_{1/2}''$ (cm^{-1})	533.61(48)	533.10(50)
B[16.0]1.5 ← X $^2\Delta_{5/2}$ Note: Vibrational numbering is slightly uncertain. It is conceivable that v′ should be decreased by 1 unit.	4-0	17566.13(189)	17565.24(160)
	5-1	17423.51(-129)	17423.25(-89)
	5-0	17957.28(-113)	17956.10(-113)
	6-0	18350.92(-117)	18349.42(-103)
	7-1	18211.87(20)	18210.62(43)
	7-0	18745.36(7)	18743.01(-28)
	8-1	18605.09(71)	18603.13(48)
	8-0	19139.35(136)	19137.20(145)
	9-0	19530.68(47)	19528.14(30)
	10-0	19920.82(-112)	19918.61(-94)
	Fitted Spectroscopic Constants		
	T_0 (cm^{-1})	15982.72(344)	15985.52(305)
	ω_e' (cm^{-1})	396.60(464)	395.47(533)
	$\omega_e'x_e'$ (cm^{-1})	0.243(138)	0.188(123)
	$\Delta G_{1/2}''$ (cm^{-1})	533.61(48)	533.10(50)

Table B.2 (continued)

Band System	Band	$^{191}Ir^{28}Si$	$^{193}Ir^{28}Si$
C[15.4]1.5 ← X $^2\Delta_{5/2}$ Note: Vibrational numbering is slightly uncertain. It is conceivable that v′ should be decreased by 1 unit.	6-1		17305.18(122)
	6-0	17837.16(-55)	17835.64(-141)
	7-1	17696.92(60)	17694.32(-88)
	7-0	18230.66(73)	18229.18(88)
	8-1	18084.56(59)	18082.92(79)
	8-0	18616.26(-132)	18615.55(32)
	9-1	18466.82(-23)	18464.38(-38)
	9-0	19000.53(-13)	18996.75(-110)
	10-1	18845.82(25)	18844.00(93)
	10-0	19379.24(6)	19375.78(-38)
	Fitted Spectroscopic Constants		
	T_0 (cm^{-1})	15388.49(469)	15399.02(608)
	ω_e' (cm^{-1})	424.19(515)	421.43(400)
	$\omega_e'x_e'$ (cm^{-1})	2.283(297)	2.156(235)
	$\Delta G_{1/2}''$ (cm^{-1})	533.61(48)	533.10(50)
D[18.0]1.5 ← X $^2\Delta_{5/2}$ Note: Vibrational numbering is slightly uncertain. It is conceivable that v′ should be increased by 1 unit.	0-0	18025.81(-48)	18025.80(-47)
	1-0	18420.53(144)	18420.26(142)
	2-0	18811.08(-144)	18810.60(-142)
	3-0	19207.07(48)	19206.29(47)
	Fitted Spectroscopic Constants		
	T_0 (cm^{-1})	18026.29(36)	18026.27(35)
	ω_e' (cm^{-1})	392.16(170)	391.95(239)
	$\omega_e'x_e'$ (cm^{-1})	-0.317(414)	-0.307(582)
	$\Delta G_{1/2}''$ (cm^{-1})	533.61(48)	533.10(50)
E[17.5]1.5 ← X $^2\Delta_{5/2}$ Note: Vibrational numbering is slightly uncertain. It is conceivable that v′ should be changed by ±1 unit.	1-0	17884.13	17884.02
	2-0	18268.9	18268.49
	3-0	18647.38	18646.92
	Fitted Spectroscopic Constants		
	T_0 (cm^{-1})	17493.07	17493.51
	ω_e' (cm^{-1})	397.35	396.55
	$\omega_e'x_e'$ (cm^{-1})	3.145	3.02
	$\Delta G_{1/2}''$ (cm^{-1})	533.61(48)	533.10(50)

Table B.2 (continued)

Band System	Band	$^{191}Ir^{28}Si$	$^{193}Ir^{28}Si$
F[17.8]1.5 ← X $^2\Delta_{5/2}$ Vibrational numbering seems definite.	3-0	19057.98(-447)	19056.89(-463)
	4-1	18927.67(202)	18926.67(211)
	4-0	19461.13(187)	19459.89(223)
	5-0	19854.27(476)	19852.28(479)
	6-1	19700.46(86)	19698.62(70)
	6-0	20234.43(123)	20231.62(60)
	7-1	20073.63(-311)	20071.76(-337)
	7-0	20606.69(-366)	20604.98(-325)
	8-0	20976.48(-446)	20975.37(-376)
	9-0	21349.91(494)	21348.29(457)
	Fitted Spectroscopic Constants		
	T_0 (cm^{-1})	17832.71(532)	17835.22(508)
	ω_e' (cm^{-1})	423.02	421.39
	$\omega_e'x_e'$ (cm^{-1})	3.277	3.155
	$\Delta G_{1/2}''$ (cm^{-1})	533.61(48)	533.10(50)
G[17.8]2.5 ← X $^2\Delta_{5/2}$ Note: Vibrational numbering is slightly uncertain, as it is based on the isotope shift of a single band. It is conceivable that v′ should be changed by ±1 unit.	1-0	18178.99(19)	18179.07(18)
	2-0	18562.03(-42)	18561.62(-46)
	3-0	18943.08(20)	18942.38(27)
	4-0	19320.08(-2)	19319.17(18)
	5-0	19694.25(15)	19692.50(-21)
	6-0	20064.78(-10)	20063.31(4)
	Fitted Spectroscopic Constants		
	T_0 (cm^{-1})	17791.93(13)	17792.54(15)
	ω_e' (cm^{-1})	390.08	389.51
	$\omega_e'x_e'$ (cm^{-1})	1.608	1.579
	$\Delta G_{1/2}''$ (cm^{-1})	533.61(48)	533.10(50)
H ← X $^2\Delta_{5/2}$ Vibrational numbering is completely unknown. Likewise, Ω′ is also unknown. No rotationally resolved studies were attempted.	0-0	19900.57(9)	19899.76(40)
	1-0	20296.56(-25)	20294.64(-118)
	2-1	20157.51(-15)	20157.48(71)
	2-0	20691.65(38)	20690.29(42)
	3-0	21083.80(-6)	21081.20(-32)
	4-0	21474.58(-1)	21470.75(-3)
	Fitted Spectroscopic Constants		
	T_0 (cm^{-1})	19900.48(6)	19899.36(18)
	ω_e' (cm^{-1})	398.19	398.86
	$\omega_e'x_e'$ (cm^{-1})	0.933(1078)	1.201(1040)
	$\Delta G_{1/2}''$ (cm^{-1})	533.61(48)	533.10(50)

Table B.2 (continued)

Band System	Band	$^{191}Ir^{28}Si$	$^{193}Ir^{28}Si$
$I \leftarrow X\ ^2\Delta_{5/2}$	0-0	19616.51(15)	19615.15(20)
	1-0	20034.38(-45)	20033.44(-61)
Vibrational numbering is completely unknown. Likewise, Ω' is also unknown. No rotationally resolved studies were attempted.	2-0	20451.80(45)	20451.48(61)
	3-0	20865.75(-15)	20865.18(-20)
	Fitted Spectroscopic Constants		
	T_0 (cm^{-1})	19616.36(8)	19614.95(11)
	ω_e' (cm^{-1})	420.43(916)	421.40(884)
	$\omega_e'x_e'$ (cm^{-1})	0.980(2234)	1.148(2156)
	$\Delta G_{1/2}''$ (cm^{-1})	533.61(48)	533.10(50)
$J[20.9]3.5 \leftarrow X\ ^2\Delta_{5/2}$	0-1	20414.58(-20)	20414.67(-32)
	0-0	20948.03(-36)	20947.91(-18)
Vibrational numbering is definite.	1-1	20828.64(32)	20828.46(-1)
	1-0	21362.34(41)	21362.13(56)
	2-0	21772.20(14)	21772.04(47)
	3-0	22178.74(-5)	22177.77(-34)
	4-0	22582.44(33)	22581.28(12)
	5-1	22447.21(-121)	22446.84(-81)
	5-0	22981.83(-20)	22980.67(-7)
	6-0	23379.36(81)	23377.43(58)
	Fitted Spectroscopic Constants		
	T_0 (cm^{-1})	20948.39(12)	20948.09(10)
	ω_e' (cm^{-1})	416.94(26)	416.96(30)
	$\omega_e'x_e'$ (cm^{-1})	1.701(37)	1.737(43)
	$\Delta G_{1/2}''$ (cm^{-1})	533.61(48)	533.10(50)
$K[21.1]2.5 \leftarrow X\ ^2\Delta_{5/2}$	0-1	20597.11(15)	20597.05(-10)
	0-0	21129.82(-75)	21129.90(-34)
Vibrational numbering is definite.	1-1	20987.34(51)	20987.31(29)
	1-0	21521.13(69)	21520.80(68)
	2-1	21375.26(34)	21375.17(22)
	2-0	21908.14(-39)	21907.57(-48)
	3-1	21760.17(-104)	21760.27(-68)
	3-0	22294.72(-10)	22294.10(5)
	4-0	22679.90(58)	22678.46(36)
	Fitted Spectroscopic Constants		
	T_0 (cm^{-1})	21130.57(13)	21130.24(9)
	ω_e' (cm^{-1})	391.67(39)	391.81(46)
	$\omega_e'x_e'$ (cm^{-1})	0.895(74)	0.969(229)
	$\Delta G_{1/2}''$ (cm^{-1})	533.61(48)	533.10(50)

Table B.2 (continued)

Band System	Band	$^{191}Ir^{28}Si$	$^{193}Ir^{28}Si$
L[22.1]2.5 ← X $^2\Delta_{5/2}$ Vibrational numbering is definite.	0-1	21590.65(4)	21591.08(11)
	0-0	22124.17(-4)	22123.95(-11)
	1-1	22042.75(-22)	22042.85(-29)
	1-0	22576.79(22)	22576.53(29)
	2-0	23010.38(0)	23009.54(0)
	Fitted Spectroscopic Constants		
	T_0 (cm^{-1})	22124.21(2)	22124.06(3)
	ω_e' (cm^{-1})	470.91(95)	471.05(295)
	$\omega_e'x_e'$ (cm^{-1})	9.277(325)	9.436(1010)
	$\Delta G_{1/2}''$ (cm^{-1})	533.61(48)	533.10(50)
M[21.2]1.5 ← X $^2\Delta_{5/2}$ Note: Vibrational numbering is slightly uncertain, as it is based on the isotope shift of a single band. It is conceivable that v′ should be changed by ±1 unit, although it is unlikely that it should be decreased by one unit, as this would require dropping a band that fits this progression.	0-0	21191.63(-157)	21190.01(-200)
	1-1	21024.47(220)	21024.45(225)
	1-0	21556.18(30)	21556.49(119)
	2-1	21385.99(91)	21385.67(38)
	2-0	21918.69(0)	21918.35(-3)
	3-1	21745.83(-218)	21746.99(-118)
	3-0	22281.19(-43)	22279.93(-133)
	4-1	22112.52(145)	22112.35(151)
	4-0	22644.25(-43)	22643.48(-45)
	5-0	23006.97(-89)	23005.22(-118)
	6-0	23371.82(65)	23369.50(84)
	Fitted Spectroscopic Constants		
	T_0 (cm^{-1})	21193.20(33)	21192.01(34)
	ω_e' (cm^{-1})	362.55	363.5
	$\omega_e'x_e'$ (cm^{-1})	-0.063	0.103
	$\Delta G_{1/2}''$ (cm^{-1})	533.61(48)	533.10(50)
N[23.3]2.5 ← X $^2\Delta_{5/2}$ Vibrational numbering is definite.	0-1	22815.82(-33)	22816.31(-36)
	0-0	23350.09(33)	23350.13(36)
	1-1	23250.54(34)	23250.42(15)
	1-0	23783.46(-34)	23783.22(-15)
	Fitted Spectroscopic Constants		
	T_0 (cm^{-1})	23349.76	23349.77(4)
	ω_e' (cm^{-1})	434.04	433.6
	$\Delta G_{1/2}''$ (cm^{-1})	533.61(48)	533.10(50)

PART II. ROTATIONALLY RESOLVED SPECTRA OF IrSi

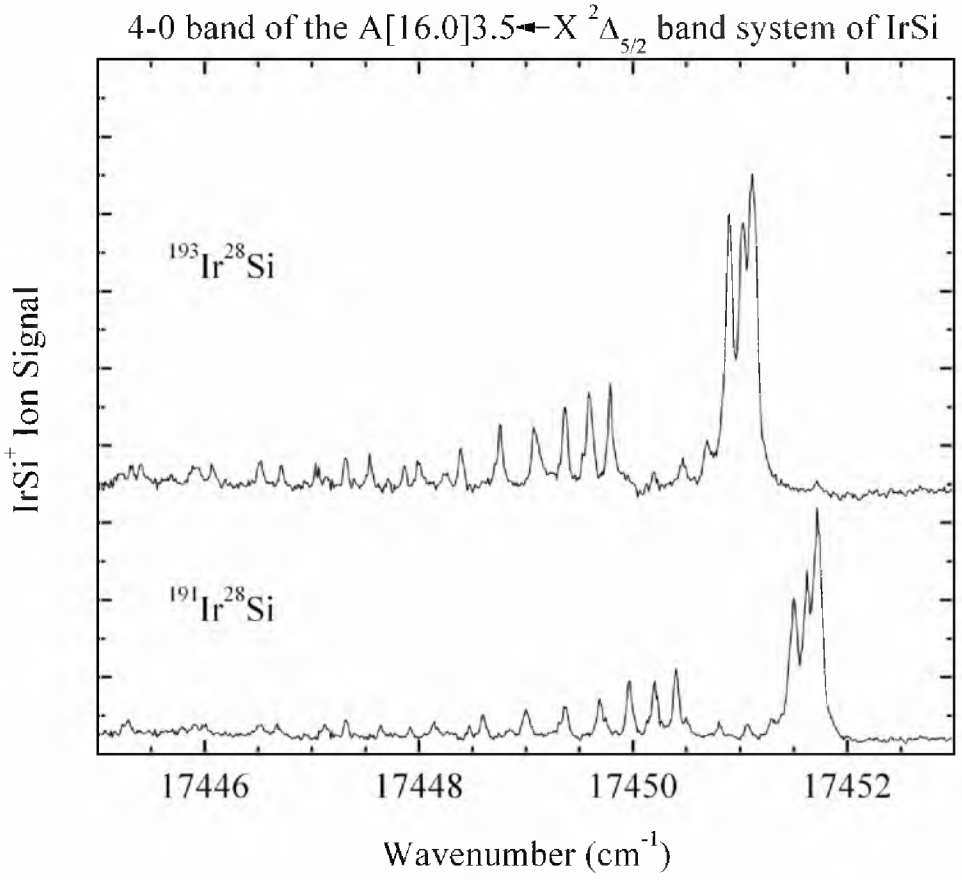

Figure B.22 Rotationally resolved spectra of the 4-0 band of the A[16.0]3.5 ← X $^2\Delta_{5/2}$ band system of IrSi.

Table B.3 Line positions for the 4-0 band of the A[16.0]3.5 ← X $^2\Delta_{5/2}$ band system of IrSi[a]

Line	$^{191}Ir^{28}Si$	$^{193}Ir^{28}Si$
P(5.5)	17448.471(-4)	17447.866(-2)
P(6.5)	17447.920(-5)	17447.318(-5)
P(7.5)	17447.322(-3)	17446.714(3)
P(8.5)	17446.677(4)	17446.076(4)
P(9.5)	17445.996(4)	17445.403(-4)
P(10.5)	17445.286(-10)	
Q(3.5)	17450.403(-3)	17449.786(9)
Q(4.5)	17450.202(4)	17449.594(7)
Q(5.5)	17449.964(7)	17449.369(-3)
Q(6.5)	17449.691(0)	17449.083(4)
Q(7.5)	17449.371(-2)	17448.756(9)
Q(8.5)	17449.001(4)	17448.391(9)
Q(9.5)	17448.598(-2)	17447.998(-5)
Q(10.5)	17448.140(6)	17447.544(-2)
Q(11.5)	17447.644(7)	17447.046(2)
Q(12.5)	17447.125(-10)	17446.515(-4)
Q(13.5)	17446.517(19)	17445.929(3)
Q(14.5)	17445.910(3)	
R(2.5)	17451.503(3)	17450.900(0)
R(3.5)	17451.624(5)	17451.026(-2)
R(4.5)	17451.721(-12)	17451.114(-11)
R(10.5)	17451.306(-17)	17450.694(-13)
R(11.5)	17451.068(1)	17450.464(-3)
R(12.5)	17450.809(-4)	17450.197(0)
R(13.5)	17450.498(1)	
R(14.5)		17449.533(8)
R(15.5)	17449.744(14)	
R(16.5)	17449.318(5)	
R(17.5)		17448.247(-11)
R(18.5)		17447.714(1)
R(19.5)	17447.774(-14)	
R(21.5)		17445.888(6)
Spectroscopic Constants		
ν_0 (cm^{-1})	17450.7376(24)	17450.1329(18)
B' (cm^{-1})	0.136668(26)	0.136497(20)
r′ (Å)	2.24829(21)	2.24821(17)
B_0'' (cm^{-1})	0.158134(17)	0.157956(19)
r_0'' (Å)	2.09013(11)	2.08992(13)

[a] Residuals in the fit of the data to the form $\nu = \nu_0 + B' J'(J' + 1) - B'' J'' (J'' + 1)$ are provided in parentheses following each line position, in units of 0.001 cm^{-1}. Error limits (1σ) are given in parentheses following each spectroscopic constant, in units of the last quoted digit. All rotationally resolved bands originated from the same lower state (the ground vibronic level). In order to improve the accuracy of the spectroscopic constants, all of the bands were simultaneously fitted under the constraint that they have the same value of B″.

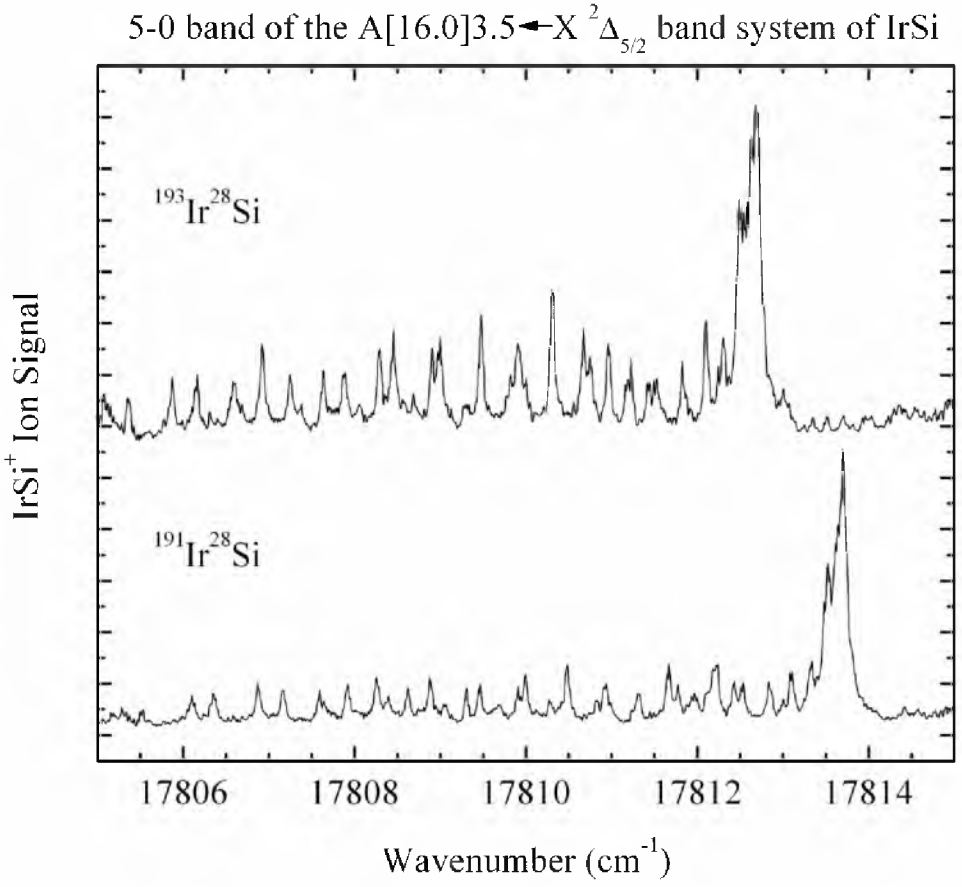

Figure B.23 Rotationally resolved spectra of the 5-0 band of the A[16.0]3.5 ← X $^2\Delta_{5/2}$ band system of IrSi.

Table B.4 Line positions for the 5-0 band of the A[16.0]3.5 ← X $^2\Delta_{5/2}$ band system of IrSi[a]

Line	$^{191}Ir^{28}Si$	$^{193}Ir^{28}Si$
P(4.5)	17810.986(20)	17809.992(12)
P(5.5)	17810.478(4)	17809.477(3)
P(6.5)	17809.908(2)	17808.904(5)
P(7.5)	17809.305(-13)	17808.291(2)
P(8.5)	17808.626(2)	17807.636(-7)
P(9.5)	17807.920(-2)	17806.927(-8)
P(10.5)	17807.163(-2)	17806.156(7)
P(11.5)	17806.351(7)	17805.363(-2)
P(12.5)	17805.515(-6)	
Q(3.5)	17812.426(4)	17811.432(-6)
Q(4.5)	17812.228(-7)	17811.232(-14)
Q(5.5)	17811.967(-1)	17810.965(-2)
Q(6.5)	17811.664(1)	17810.675(-14)
Q(7.5)	17811.316(1)	17810.311(3)
Q(8.5)	17810.926(-3)	17809.910(11)
Q(9.5)	17810.478(5)	17809.477(3)
Q(10.5)	17809.994(2)	17808.994(1)
Q(11.5)		17808.452(9)
Q(12.5)	17808.885(-2)	17807.881(1)
Q(13.5)	17808.256(1)	17807.250(7)
Q(14.5)	17807.590(-5)	17806.596(-10)
Q(15.5)	17806.872(-5)	17805.873(-5)
Q(16.5)	17806.102(-1)	
Q(17.5)	17805.293(-3)	
R(2.5)	17813.548(-12)	17812.540(-8)
R(3.5)	17813.642(2)	17812.633(6)
R(4.5)	17813.699(6)	
R(6.5)	17813.674(15)	
R(7.5)	17813.613(-3)	
R(8.5)	17813.482(5)	17812.498(-16)
R(9.5)	17813.327(-11)	17812.304(7)
R(10.5)	17813.095(4)	17812.097(-3)
R(11.5)	17812.843(-7)	17811.824(7)
R(12.5)	17812.525(1)	17811.527(-5)
R(13.5)	17812.181(-11)	17811.162(5)
R(14.5)	17811.773(-5)	17810.750(15)

[a] Residuals in the fit of the data to the form $\nu = \nu_0 + B' J'(J' + 1) - B'' J'' (J'' + 1)$ are provided in parentheses following each line position, in units of 0.001 cm^{-1}. Error limits (1σ) are given in parentheses following each spectroscopic constant, in units of the last quoted digit. All rotationally resolved bands originated from the same lower state (the ground vibronic level). In order to improve the accuracy of the spectroscopic constants, all of the bands were simultaneously fitted under the constraint that they have the same value of B''.

Table B.4 (continued)

R(15.5)	17811.316(4)	17810.311(5)
R(16.5)	17810.826(-1)	17809.817(4)
R(17.5)	17810.281(2)	17809.294(-14)
R(18.5)	17809.691(5)	17808.685(8)
R(19.5)	17809.052(9)	17808.060(0)
R(20.5)	17808.395(-14)	17807.380(-1)
R(21.5)	17807.640(14)	
R(22.5)		17805.873(7)
R(23.5)		17805.074(-13)
Spectroscopic Constants		
ν_0 (cm^{-1})	17812.7943(18)	17811.7907(20)
B' (cm^{-1})	0.134954(14)	0.134796(14)
r′ (Å)	2.26253(12)	2.26235(12)
B_0'' (cm^{-1})	0.158134(17)	0.157956(19)
r_0'' (Å)	2.09013(11)	2.08992(13)

[a] Residuals in the fit of the data to the form $\nu = \nu_0 + B' J'(J' + 1) - B'' J'' (J'' + 1)$ are provided in parentheses following each line position, in units of 0.001 cm^{-1}. Error limits (1σ) are given in parentheses following each spectroscopic constant, in units of the last quoted digit. All rotationally resolved bands originated from the same lower state (the ground vibronic level). In order to improve the accuracy of the spectroscopic constants, all of the bands were simultaneously fitted under the constraint that they have the same value of B″.

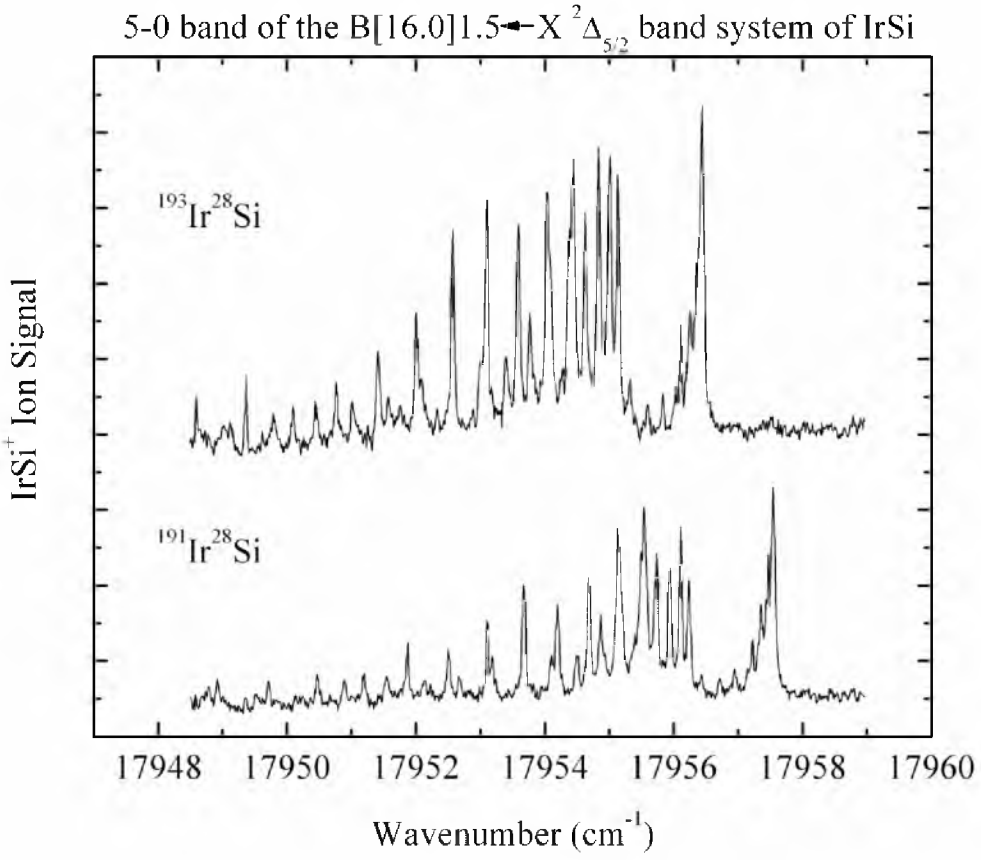

Figure B.24 Rotationally resolved spectra of the 5-0 band of the B[16.0]1.5 ← X $^2\Delta_{5/2}$ band system of IrSi.

Table B.5 Line positions for the 5-0 band of the B[16.0]1.5 ← X $^2\Delta_{5/2}$ band system of IrSi[a]

Line	$^{191}Ir^{28}Si$	$^{193}Ir^{28}Si$
P(2.5)	17955.547(4)	17954.438(6)
P(3.5)	17955.143(-4)	17954.035(-2)
P(4.5)	17954.690(-1)	17953.588(-5)
P(5.5)	17954.195(6)	17953.101(-5)
P(6.5)	17953.676(-1)	17952.572(-2)
P(7.5)	17953.107(3)	17952.007(-1)
P(8.5)	17952.508(0)	17951.411(-7)
P(9.5)	17951.865(1)	17950.764(0)
P(10.5)	17951.187(1)	17950.095(-10)
P(11.5)	17950.472(-2)	17949.366(3)
P(12.5)	17949.706(9)	
P(13.5)	17948.910(11)	
Q(2.5)	17956.237(8)	17955.136(2)
Q(3.5)	17956.114(-2)	17955.007(-2)
Q(4.5)	17955.934(6)	17954.834(-1)
Q(5.5)	17955.734(-4)	17954.625(-2)
Q(6.5)	17955.499(-17)	17954.384(-9)
Q(7.5)	17955.191(5)	17954.080(9)
Q(8.5)	17954.868(3)	17953.767(-2)
Q(9.5)	17954.503(5)	17953.390(13)
Q(10.5)	17954.104(3)	17953.000(2)
Q(11.5)	17953.676(-8)	17952.572(-9)
Q(12.5)	17953.182(8)	17952.083(4)
Q(13.5)	17952.678(-3)	17951.574(-2)
Q(14.5)	17952.131(-10)	17951.008(11)
Q(15.5)	17951.544(-15)	17950.446(-19)
Q(16.5)	17950.889(10)	17949.789(8)
Q(17.5)		17949.116(15)
Q(18.5)	17949.513(11)	
Q(19.5)	17948.775(4)	
R(2.5)	17957.225(-5)	17956.111(-1)
R(3.5)	17957.354(10)	17956.259(-4)
R(4.5)	17957.471(-1)	17956.352(9)
R(5.5)		17956.414(14)
R(9.5)	17957.437(-9)	17956.322(-3)

[a] Residuals in the fit of the data to the form $\nu = \nu_0 + B' J'(J' + 1) - B'' J'' (J'' + 1)$ are provided in parentheses following each line position, in units of 0.001 cm^{-1}. Error limits (1σ) are given in parentheses following each spectroscopic constant, in units of the last quoted digit. All rotationally resolved bands originated from the same lower state (the ground vibronic level). In order to improve the accuracy of the spectroscopic constants, all of the bands were simultaneously fitted under the constraint that they have the same value of B''.

Table B.5 (continued)

R(10.5)	17957.312(-7)	17956.199(-3)
R(11.5)	17957.148(-4)	17956.037(-2)
R(12.5)	17956.944(1)	17955.835(2)
R(13.5)	17956.713(-6)	17955.600(0)
R(14.5)	17956.438(-7)	17955.319(5)
R(17.5)		17954.266(3)
R(20.5)		17952.881(-10)
R(21.5)	17953.432(-1)	17952.326(2)
R(22.5)		17951.752(-4)
Spectroscopic Constants		
ν_0 (cm^{-1})	17956.4130(17)	17955.3049(16)
B' (cm^{-1})	0.139037(15)	0.138884(14)
r′ (Å)	2.22906(12)	2.22881(11)
B_0'' (cm^{-1})	0.158134(17)	0.157956(19)
r_0'' (Å)	2.09013(11)	2.08992(13)

[a] Residuals in the fit of the data to the form $\nu = \nu_0 + B' J'(J' + 1) - B'' J'' (J'' + 1)$ are provided in parentheses following each line position, in units of 0.001 cm^{-1}. Error limits (1σ) are given in parentheses following each spectroscopic constant, in units of the last quoted digit. All rotationally resolved bands originated from the same lower state (the ground vibronic level). In order to improve the accuracy of the spectroscopic constants, all of the bands were simultaneously fitted under the constraint that they have the same value of B″.

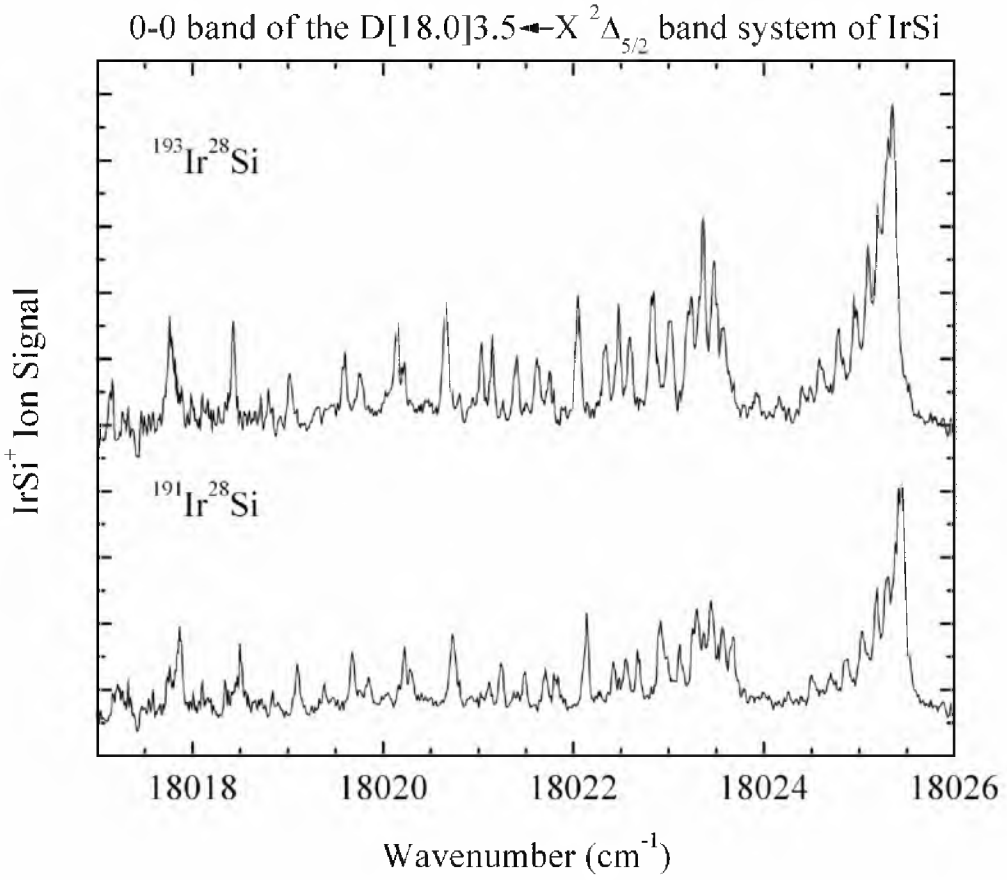

Figure B.25 Rotationally resolved spectra of the 0-0 band of the D[18.0]1.5 ← X $^2\Delta_{5/2}$ band system of IrSi.

Table B.6 Line positions for the 0-0 band of the D[18.0]1.5 ← X $^2\Delta_{5/2}$ band system of IrSi[a]

Line	$^{191}Ir^{28}Si$	$^{193}Ir^{28}Si$
P(2.5)	18022.926(11)	18022.841(17)
P(3.5)	18022.550(2)	18022.477(-3)
P(4.5)	18022.141(0)	18022.047(16)
P(5.5)	18021.701(0)	18021.620(3)
P(6.5)	18021.242(-7)	18021.147(11)
P(7.5)	18020.730(12)	18020.657(7)
P(8.5)	18020.223(-2)	18020.144(-1)
P(9.5)	18019.677(-3)	18019.587(8)
P(10.5)	18019.101(-3)	18019.023(-3)
P(11.5)	18018.503(-7)	18018.427(-9)
P(12.5)	18017.868(-2)	
P(13.5)		18017.145(-15)
Q(2.5)	18023.667(-8)	18023.571(9)
Q(3.5)	18023.566(-2)	18023.476(8)
Q(4.5)	18023.441(1)	18023.360(1)
Q(5.5)	18023.297(-6)	18023.204(7)
Q(6.5)	18023.114(0)	
Q(7.5)	18022.899(10)	18022.820(8)
Q(8.5)	18022.677(1)	18022.596(1)
Q(9.5)	18022.419(0)	18022.336(1)
Q(10.5)	18022.110(22)	18022.047(4)
Q(11.5)	18021.812(7)	18021.749(-13)
Q(12.5)		18021.398(-3)
Q(13.5)		18021.033(-6)
Q(14.5)		18020.657(-27)
Q(15.5)		18020.217(-10)
Q(16.5)		18019.755(1)
R(2.5)		18024.590(-1)
R(3.5)	18024.860(5)	18024.781(2)
R(4.5)	18025.030(1)	18024.960(-12)
R(5.5)	18025.184(-15)	18025.094(-7)
R(6.5)	18025.293(-11)	18025.211(-13)
R(7.5)	18025.381(-15)	18025.283(-1)
R(8.5)	18025.417(7)	18025.349(-10)
R(9.5)	18025.450(4)	18025.376(-8)

[a] Residuals in the fit of the data to the form $\nu = \nu_0 + B' J'(J' + 1) - B'' J'' (J'' + 1)$ are provided in parentheses following each line position, in units of 0.001 cm^{-1}. Error limits (1σ) are given in parentheses following each spectroscopic constant, in units of the last quoted digit. All rotationally resolved bands originated from the same lower state (the ground vibronic level). In order to improve the accuracy of the spectroscopic constants, all of the bands were simultaneously fitted under the constraint that they have the same value of B''.

Table B.6 (continued)

R(10.5)	18025.450(6)	18025.376(-6)
R(11.5)		18025.349(-5)
R(12.5)		18025.304(-13)
R(15.5)		18024.960(9)
R(16.5)		18024.781(26)
R(17.5)		18024.590(27)
R(18.5)	18024.496(1)	18024.400(2)
R(19.5)	18024.259(-5)	18024.161(-4)
Spectroscopic Constants		
ν_0 (cm^{-1})	18023.7785(20)	18023.6992(26)
B' (cm^{-1})	0.144503(26)	0.144302(21)
r′ (Å)	2.18649(20)	2.18656(16)
B_0'' (cm^{-1})	0.158134(17)	0.157956(19)
r_0'' (Å)	2.09013(11)	2.08992(13)

[a] Residuals in the fit of the data to the form $\nu = \nu_0 + B' J'(J' + 1) - B'' J'' (J'' + 1)$ are provided in parentheses following each line position, in units of 0.001 cm^{-1}. Error limits (1σ) are given in parentheses following each spectroscopic constant, in units of the last quoted digit. All rotationally resolved bands originated from the same lower state (the ground vibronic level). In order to improve the accuracy of the spectroscopic constants, all of the bands were simultaneously fitted under the constraint that they have the same value of B″.

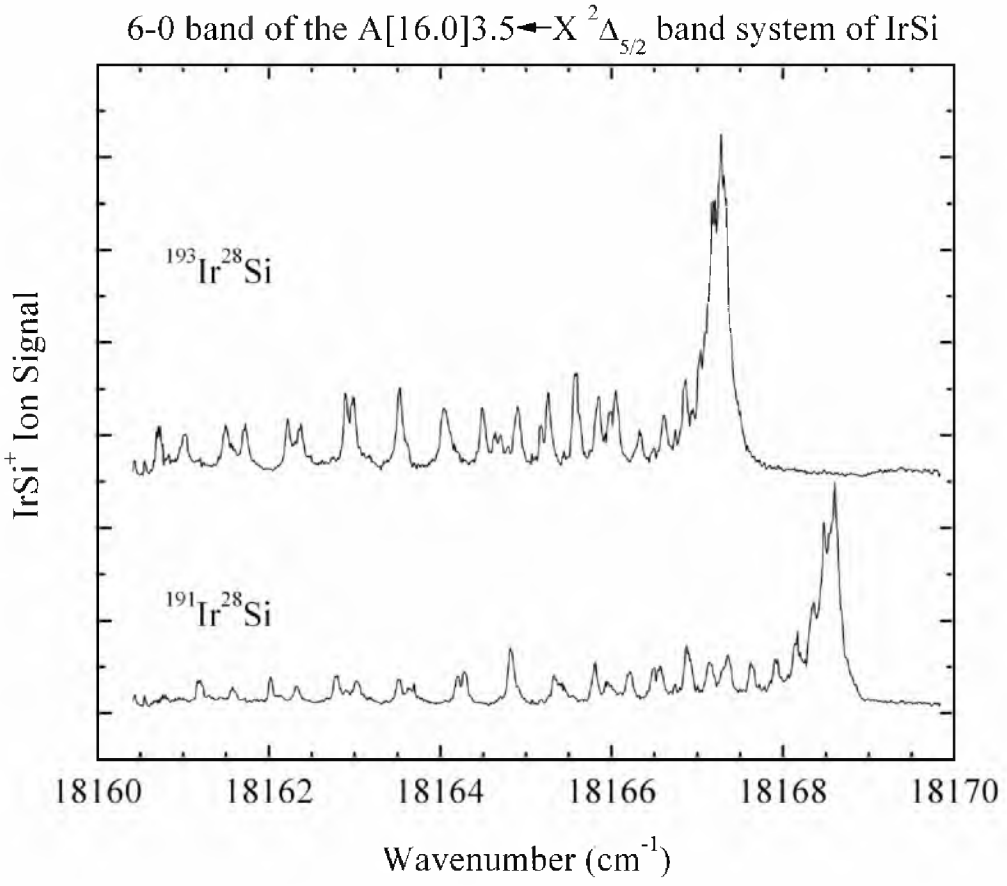

Figure B.26 Rotationally resolved spectra of the 6-0 band of the A[16.0]3.5 ← X $^2\Delta_{5/2}$ band system of IrSi.

Table B.7 Line positions for the 6-0 band of the A[16.0]3.5 ← X $^2\Delta_{5/2}$ band system of IrSi[a]

Line	$^{191}Ir^{28}Si$	$^{193}Ir^{28}Si$
P(4.5)	18165.955(-14)	18164.635(4)
P(5.5)	18165.421(-13)	18164.113(-7)
P(6.5)	18164.825(2)	18163.524(1)
P(7.5)	18164.207(-9)	18162.894(2)
P(8.5)	18163.517(3)	18162.219(0)
P(9.5)	18162.789(6)	18161.499(-5)
P(10.5)	18162.021(-1)	18160.714(6)
P(11.5)	18161.198(0)	
Q(3.5)	18167.356(9)	18166.050(10)
Q(4.5)	18167.145(3)	18165.846(-2)
Q(5.5)	18166.882(1)	18165.582(-3)
Q(6.5)	18166.563(7)	18165.258(8)
Q(7.5)	18166.207(2)	18164.903(1)
Q(8.5)	18165.806(-6)	18164.492(3)
Q(9.5)	18165.328(13)	18164.046(-8)
Q(10.5)	18164.825(10)	18163.524(8)
Q(11.5)	18164.283(-1)	18162.978(0)
Q(12.5)	18163.691(-12)	18162.362(14)
Q(13.5)	18163.024(5)	18161.721(4)
Q(14.5)	18162.327(4)	18161.014(13)
Q(15.5)	18161.584(0)	
R(2.5)	18168.480(-8)	18167.172(-6)
R(3.5)		18167.279(-13)
R(4.5)		18167.319(-3)
R(5.5)		18167.319(0)
R(6.5)		18167.279(-5)
R(7.5)	18168.480(8)	
R(8.5)	18168.350(-4)	18167.029(9)
R(9.5)	18168.158(-1)	18166.859(-10)
R(10.5)	18167.916(3)	18166.613(-2)
R(11.5)	18167.637(-4)	18166.332(-7)
R(12.5)	18167.305(-7)	18165.983(7)
R(13.5)	18166.912(4)	18165.619(-11)
R(14.5)	18166.485(1)	18165.178(-1)
R(15.5)		18164.701(-3)
R(17.5)	18164.899(6)	

[a] Residuals in the fit of the data to the form $\nu = \nu_0 + B' J'(J' + 1) - B'' J'' (J'' + 1)$ are provided in parentheses following each line position, in units of 0.001 cm^{-1}. Error limits (1σ) are given in parentheses following each spectroscopic constant, in units of the last quoted digit. All rotationally resolved bands originated from the same lower state (the ground vibronic level). In order to improve the accuracy of the spectroscopic constants, all of the bands were simultaneously fitted under the constraint that they have the same value of B''.

Table B.7 (continued)

R(19.5)		18162.306(-5)
R(20.5)	18162.898(-8)	
Spectroscopic Constants		
ν_0 (cm^{-1})	18167.7443(19)	18166.4400(19)
B' (cm^{-1})	0.134045(25)	0.133872(24)
r′ (Å)	2.27018(21)	2.27014(20)
B_0'' (cm^{-1})	0.158134(17)	0.157956(19)
r_0'' (Å)	2.09013(11)	2.08992(13)

[a] Residuals in the fit of the data to the form $\nu = \nu_0 + B' J'(J' + 1) - B'' J'' (J'' + 1)$ are provided in parentheses following each line position, in units of 0.001 cm^{-1}. Error limits (1σ) are given in parentheses following each spectroscopic constant, in units of the last quoted digit. All rotationally resolved bands originated from the same lower state (the ground vibronic level). In order to improve the accuracy of the spectroscopic constants, all of the bands were simultaneously fitted under the constraint that they have the same value of B″.

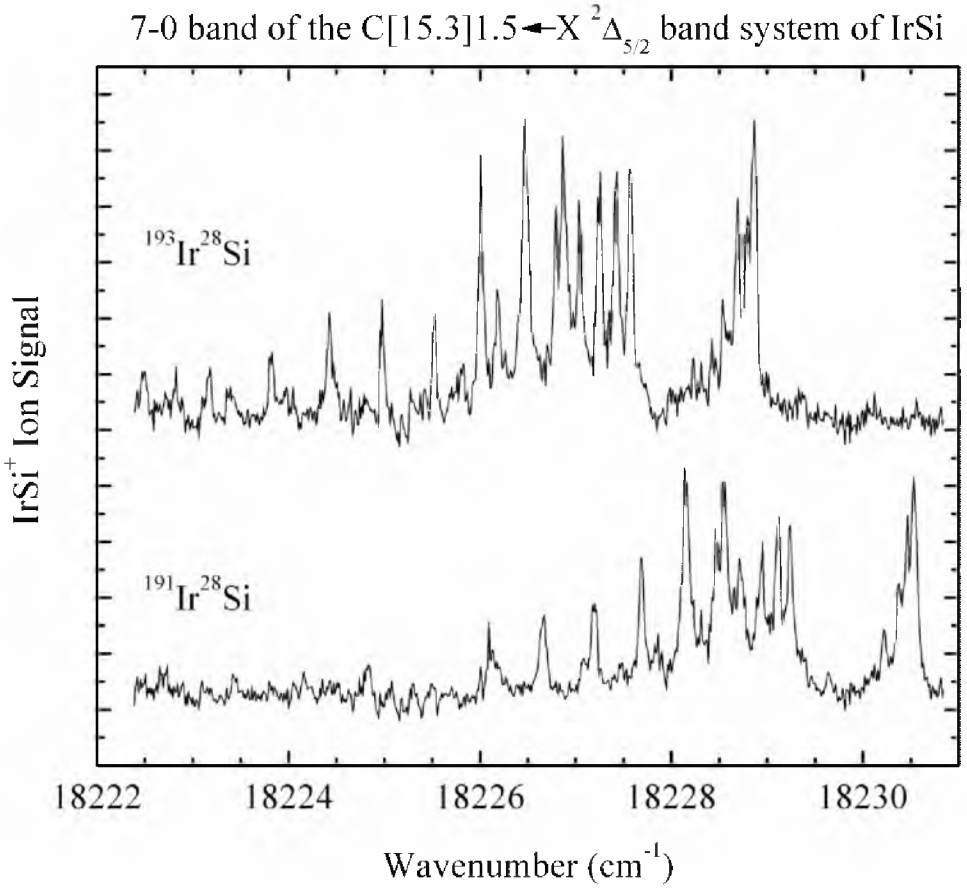

Figure B.27 Rotationally resolved spectra of the 7-0 band of the C[15.3]1.5 ← X $^2\Delta_{5/2}$ band system of IrSi.

Table B.8 Line positions for the 7-0 band of the C[15.3]1.5 ← X $^2\Delta_{5/2}$ band system of IrSi[a]

Line	$^{191}Ir^{28}Si$	$^{193}Ir^{28}Si$
P(2.5)	18228.547(9)	18226.871(-1)
P(3.5)	18228.152(-10)	18226.466(-9)
P(4.5)	18227.687(3)	18226.006(1)
P(5.5)	18227.196(3)	18225.522(-5)
P(6.5)	18226.670(-2)	18224.976(14)
P(7.5)	18226.093(7)	18224.427(-4)
P(8.5)	18225.505(-13)	18223.815(4)
P(9.5)	18224.831(14)	18223.166(9)
P(10.5)	18224.153(6)	18222.480(13)
P(11.5)	18223.424(11)	
Q(2.5)	18229.243(6)	18227.569(-6)
Q(3.5)	18229.116(-3)	18227.420(8)
Q(4.5)	18228.942(-3)	18227.250(5)
Q(5.5)	18228.721(4)	18227.041(2)
Q(6.5)	18228.470(1)	18226.795(-3)
Q(7.5)		18226.491(12)
Q(8.5)	18227.842(8)	18226.179(-3)
Q(9.5)	18227.477(4)	18225.814(-4)
Q(10.5)	18227.084(-12)	
Q(11.5)	18226.637(-12)	
Q(13.5)		18223.980(-19)
Q(14.5)		18223.392(10)
Q(15.5)		18222.816(-11)
Q(17.5)	18223.123(3)	
R(2.5)	18230.224(-4)	18228.538(-4)
R(3.5)	18230.376(-14)	18228.687(-11)
R(4.5)	18230.462(2)	18228.791(-10)
R(5.5)	18230.531(-4)	
R(11.5)		18228.422(8)
R(12.5)		18228.227(-1)
R(13.5)	18229.641(-4)	18227.977(6)
Spectroscopic Constants		
ν_0 (cm^{-1})	18229.4193(22)	18227.7317(25)
B' (cm^{-1})	0.138696(39)	0.138691(40)
r′ (Å)	2.23180(31)	2.23036(32)
B_0'' (cm^{-1})	0.158134(17)	0.157956(19)
r_0'' (Å)	2.09013(11)	2.08992(13)

[a] Residuals in the fit of the data to the form $\nu = \nu_0 + B' J'(J' + 1) - B'' J'' (J'' + 1)$ are provided in parentheses following each line position, in units of 0.001 cm^{-1}. Error limits (1σ) are given in parentheses following each spectroscopic constant, in units of the last quoted digit. All rotationally resolved bands originated from the same lower state (the ground vibronic level). In order to improve the accuracy of the spectroscopic constants, all of the bands were simultaneously fitted under the constraint that they have the same value of B″.

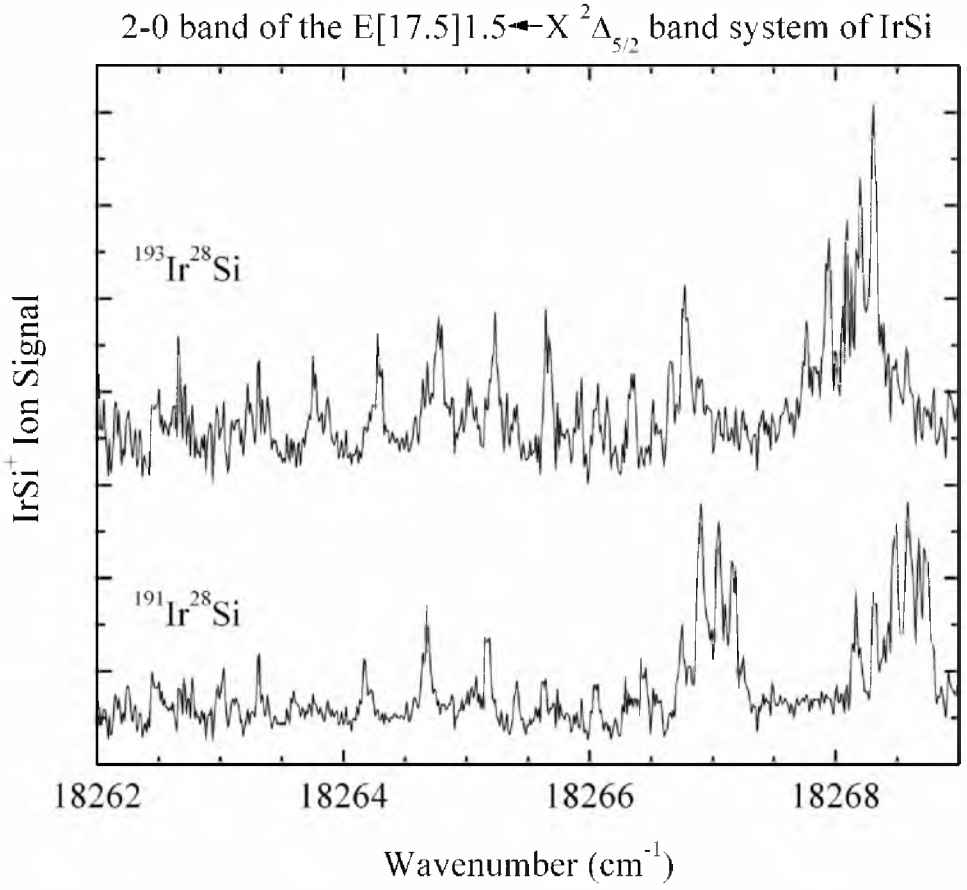

Figure B.28 Rotationally resolved spectra of the 2-0 band of the E[17.5]1.5 ← X $^2\Delta_{5/2}$ band system of IrSi.

Table B.9 Line positions for the 2-0 band of the E[17.5]1.5 ← X $^2\Delta_{5/2}$ band system of IrSi[a]

Line	$^{191}Ir^{28}Si$	$^{193}Ir^{28}Si$
P(2.5)	18266.437(8)	18266.055(-1)
P(3.5)	18266.053(-1)	18265.659(2)
P(4.5)	18265.631(-5)	18265.231(5)
P(5.5)	18265.171(-2)	18264.774(7)
P(6.5)	18264.684(-1)	18264.293(3)
P(7.5)	18264.174(-10)	18263.762(17)
P(8.5)		18263.232(0)
P(9.5)	18263.025(9)	18262.665(-12)
P(10.5)	18262.441(-19)	
Q(2.5)	18267.166(-8)	18266.776(-9)
Q(3.5)	18267.045(4)	18266.658(0)
Q(4.5)	18266.904(5)	18266.538(-19)
Q(5.5)	18266.749(-11)	18266.345(4)
Q(6.5)		18266.148(1)
Q(7.5)	18266.294(9)	18265.926(-10)
Q(8.5)		18265.659(-5)
Q(10.5)	18265.408(9)	18265.025(11)
Q(11.5)		18264.681(0)
Q(12.5)		18264.293(1)
Q(13.5)		18263.871(6)
R(2.5)	18268.165(-8)	18267.765(-1)
R(3.5)	18268.317(16)	18267.937(3)
R(4.5)	18268.479(-2)	18268.088(-1)
R(5.5)	18268.588(4)	18268.204(-2)
R(6.5)	18268.674(1)	
R(7.5)	18268.725(2)	
R(8.5)	18268.750(-2)	
R(14.5)		18267.837(10)
R(18.5)	18267.247(0)	18266.896(-10)
Spectroscopic Constants		
ν_0 (cm^{-1})	18267.2942(22)	18266.9015(21)
B' (cm^{-1})	0.142586(37)	0.142508(37)
r′ (Å)	2.20114(29)	2.20028(29)
B_0'' (cm^{-1})	0.158134(17)	0.157956(19)
r_0'' (Å)	2.09013(11)	2.08992(13)

[a] Residuals in the fit of the data to the form $\nu = \nu_0 + B' J'(J' + 1) - B'' J'' (J'' + 1)$ are provided in parentheses following each line position, in units of 0.001 cm^{-1}. Error limits (1σ) are given in parentheses following each spectroscopic constant, in units of the last quoted digit. All rotationally resolved bands originated from the same lower state (the ground vibronic level). In order to improve the accuracy of the spectroscopic constants, all of the bands were simultaneously fitted under the constraint that they have the same value of B″.

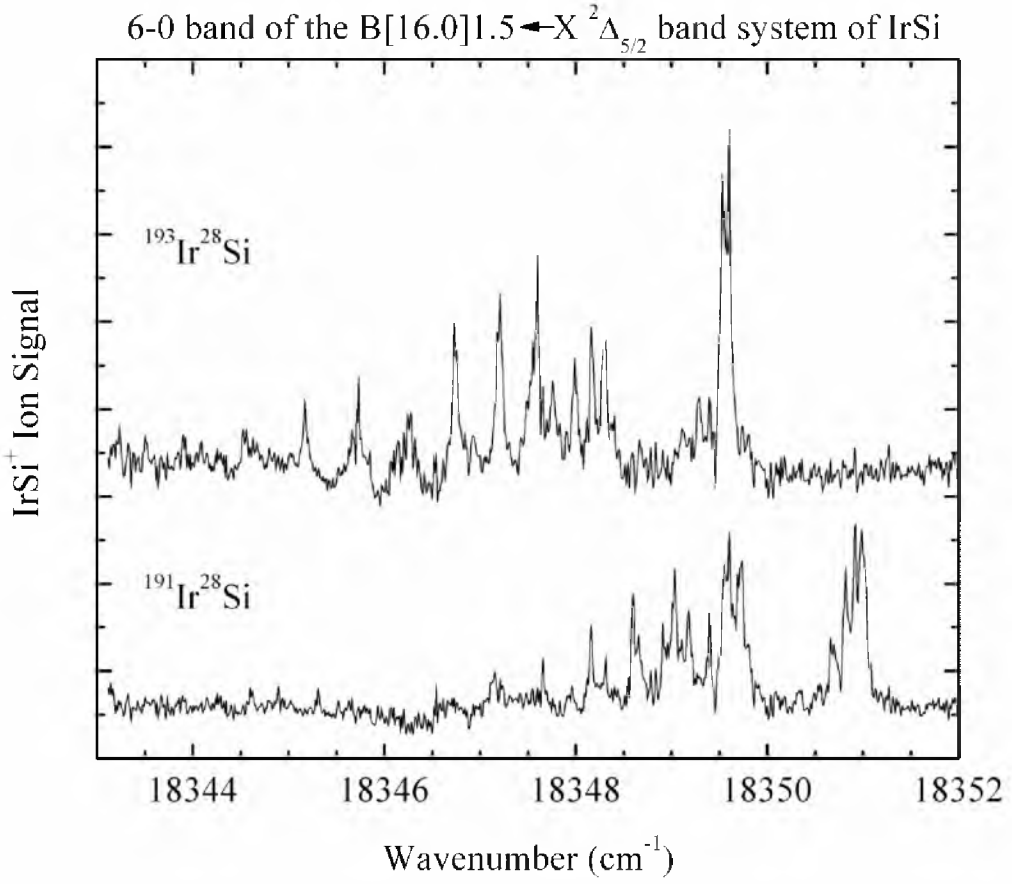

Figure B.29 Rotationally resolved spectra of the 6-0 band of the B[16.0]1.5 ← X $^2\Delta_{5/2}$ band system of IrSi.

Table B.10 Line positions for the 6-0 band of the B[16.0]1.5 ← X $^2\Delta_{5/2}$ band system of IrSi[a]

Line	$^{191}Ir^{28}Si$	$^{193}Ir^{28}Si$
P(2.5)	18349.044(-20)	18347.597(13)
P(3.5)	18348.618(-9)	18347.206(-10)
P(4.5)	18348.161(-5)	18346.743(2)
P(5.5)	18347.648(16)	18346.258(-5)
P(6.5)	18347.138(-6)	18345.734(-11)
P(7.5)	18346.556(5)	18345.166(-11)
P(8.5)	18345.948(2)	18344.545(2)
P(9.5)	18345.320(-18)	18343.892(9)
P(10.5)	18344.609(4)	
P(11.5)	18343.885(1)	
Q(2.5)	18349.708(8)	18348.290(12)
Q(3.5)	18349.566(14)	18348.178(-12)
Q(4.5)	18349.418(-15)	18347.998(-8)
Q(5.5)	18349.175(12)	18347.760(16)
Q(6.5)	18348.926(7)	18347.522(2)
Q(7.5)		18347.227(5)
Q(8.5)	18348.298(8)	18346.897(5)
Q(9.5)	18347.944(-10)	
Q(10.5)	18347.531(-8)	18346.131(-7)
Q(11.5)		18345.686(-10)
Q(13.5)		18344.656(8)
Q(14.5)		18344.088(13)
Q(15.5)		18343.512(-14)
R(2.5)	18350.680(6)	
R(3.5)	18350.819(7)	18349.429(-17)
R(4.5)	18350.934(-7)	18349.511(4)
R(5.5)		18349.564(13)
R(11.5)		18349.137(1)
R(12.5)	18350.315(8)	
R(13.5)	18350.073(-2)	
Spectroscopic Constants		
ν_0 (cm^{-1})	18349.8878(32)	18348.4722(30)
B' (cm^{-1})	0.138547(36)	0.138506(35)
r′ (Å)	2.23300(29)	2.23184(28)
B_0'' (cm^{-1})	0.158134(17)	0.157956(19)
r_0'' (Å)	2.09013(11)	2.08992(13)

[a] Residuals in the fit of the data to the form $\nu = \nu_0 + B' J'(J' + 1) - B'' J'' (J'' + 1)$ are provided in parentheses following each line position, in units of 0.001 cm^{-1}. Error limits (1σ) are given in parentheses following each spectroscopic constant, in units of the last quoted digit. All rotationally resolved bands originated from the same lower state (the ground vibronic level). In order to improve the accuracy of the spectroscopic constants, all of the bands were simultaneously fitted under the constraint that they have the same value of B″.

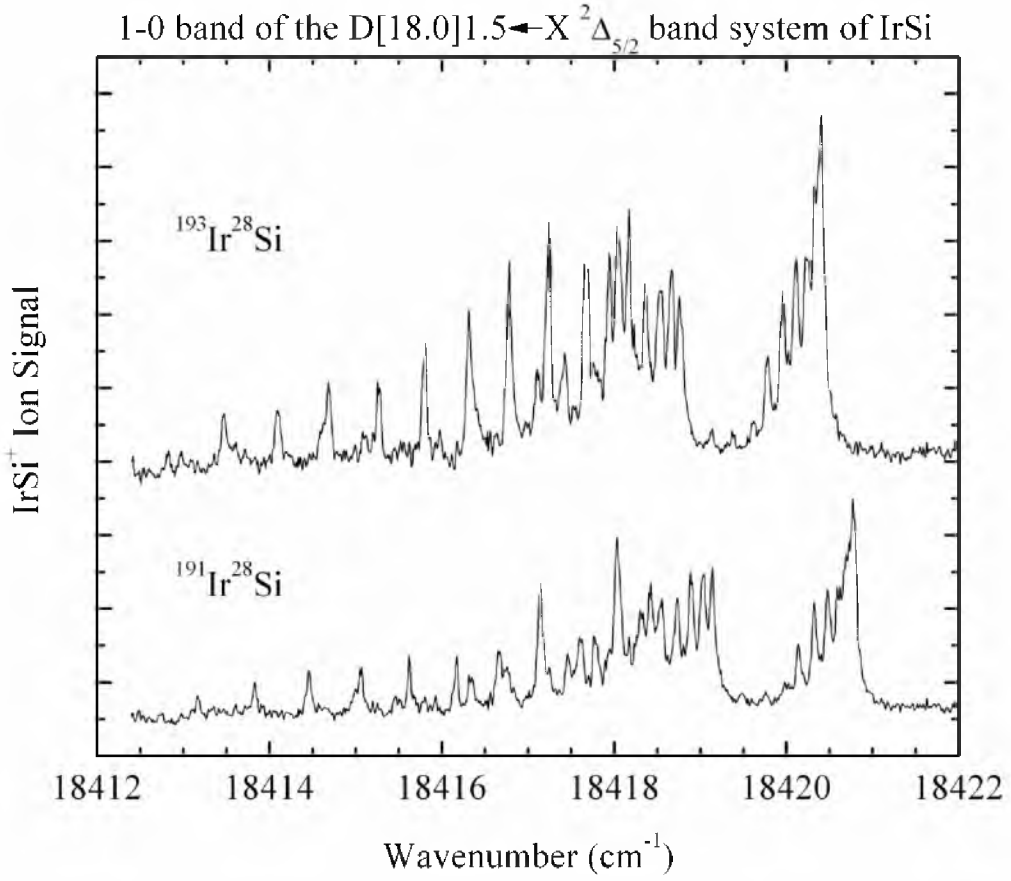

Figure B.30 Rotationally resolved spectra of the 1-0 band of the D[18.0]1.5 ← X $^2\Delta_{5/2}$ band system of IrSi.

Table B.11 Line positions for the 1-0 band of the D[18.0]1.5 ← X $^2\Delta_{5/2}$ band system of IrSi[a]

Line	$^{191}Ir^{28}Si$	$^{193}Ir^{28}Si$
P(2.5)	18418.420(-3)	18418.044(9)
P(3.5)	18418.038(-12)	18417.678(-15)
P(4.5)	18417.610(-4)	18417.242(1)
P(5.5)	18417.141(15)	18416.782(12)
P(6.5)	18416.666(10)	18416.315(-1)
P(7.5)	18416.173(-6)	18415.800(6)
P(8.5)	18415.624(4)	18415.270(-2)
P(9.5)	18415.063(-5)	18414.687(12)
P(10.5)	18414.459(1)	18414.093(8)
P(11.5)	18413.829(3)	18413.469(5)
P(12.5)	18413.171(3)	18412.823(-7)
P(13.5)	18412.480(6)	
Q(2.5)	18419.137(-4)	18418.762(7)
Q(3.5)	18419.032(-3)	18418.669(-4)
Q(4.5)	18418.895(1)	18418.535(-3)
Q(5.5)	18418.735(-3)	18418.362(6)
Q(6.5)	18418.541(-2)	18418.172(3)
Q(7.5)	18418.319(-3)	18417.945(8)
Q(8.5)	18418.063(1)	
Q(9.5)	18417.782(-1)	18417.428(-9)
Q(10.5)	18417.462(7)	18417.112(-5)
Q(12.5)	18416.748(7)	
Q(13.5)	18416.336(18)	18415.976(19)
Q(14.5)	18415.930(-7)	
Q(15.5)	18415.458(5)	18415.100(4)
Q(16.5)	18414.986(-14)	18414.620(-5)
Q(19.5)		18412.972(-5)
R(2.5)	18420.137(0)	18419.782(-12)
R(3.5)	18420.323(-4)	18419.960(-7)
R(4.5)	18420.476(-4)	18420.110(-4)
R(5.5)	18420.587(8)	18420.245(-17)
R(6.5)	18420.691(-3)	
R(12.5)	18420.621(2)	
R(13.5)	18420.515(-6)	
R(14.5)		18420.017(-16)
R(15.5)	18420.195(-5)	

[a] Residuals in the fit of the data to the form $\nu = \nu_0 + B' J'(J' + 1) - B'' J'' (J'' + 1)$ are provided in parentheses following each line position, in units of 0.001 cm^{-1}. Error limits (1σ) are given in parentheses following each spectroscopic constant, in units of the last quoted digit. All rotationally resolved bands originated from the same lower state (the ground vibronic level). In order to improve the accuracy of the spectroscopic constants, all of the bands were simultaneously fitted under the constraint that they have the same value of B''.

Table B.11 (continued)

R(16.5)	18419.984(2)	18419.616(7)
R(17.5)	18419.758(-6)	18419.383(7)
R(18.5)	18419.487(2)	18419.131(-4)
Spectroscopic Constants		
ν_0 (cm^{-1})	18419.2633(16)	18418.8985(23)
B' (cm^{-1})	0.143272(21)	0.143119(24)
r′ (Å)	2.19587(16)	2.19558(18)
B_0'' (cm^{-1})	0.158134(17)	0.157956(19)
r_0'' (Å)	2.09013(11)	2.08992(13)

[a] Residuals in the fit of the data to the form $\nu = \nu_0 + B' J'(J' + 1) - B'' J'' (J'' + 1)$ are provided in parentheses following each line position, in units of 0.001 cm^{-1}. Error limits (1σ) are given in parentheses following each spectroscopic constant, in units of the last quoted digit. All rotationally resolved bands originated from the same lower state (the ground vibronic level). In order to improve the accuracy of the spectroscopic constants, all of the bands were simultaneously fitted under the constraint that they have the same value of B″.

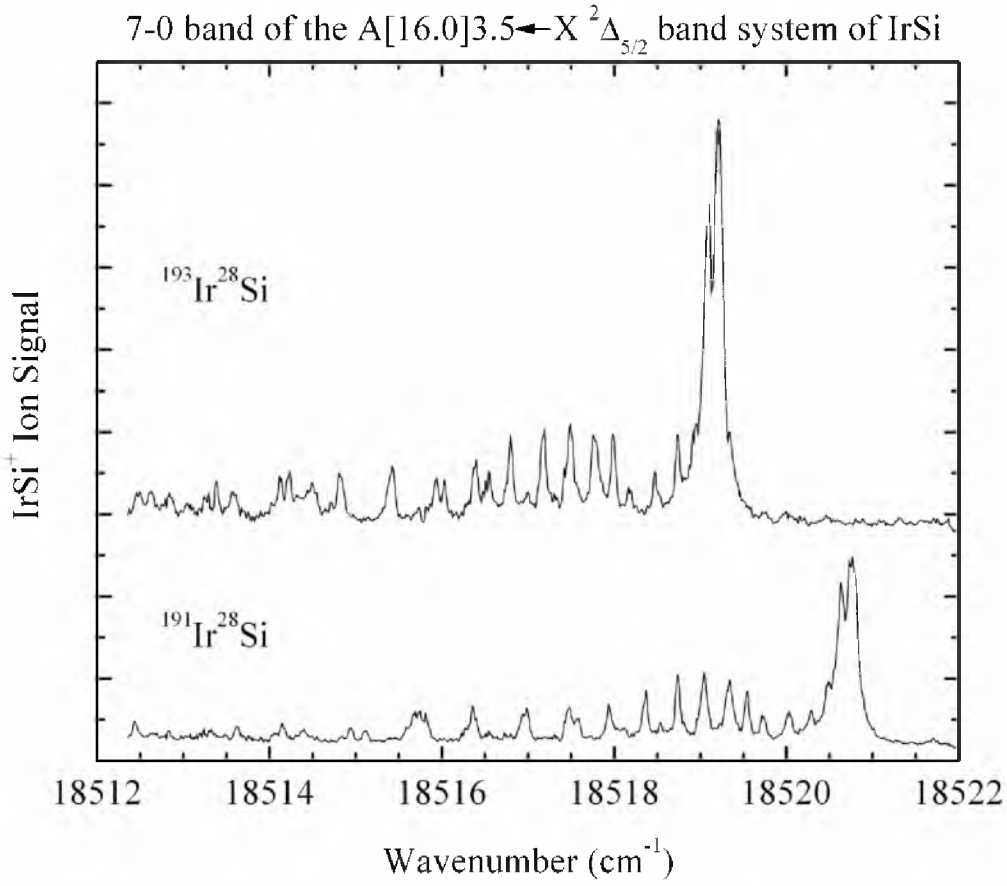

Figure B.31 Rotationally resolved spectra of the 7-0 band of the A[16.0]3.5 ← X $^2\Delta_{5/2}$ band system of IrSi.

Table B.12 Line positions for the 7-0 band of the A[16.0]3.5 ← X $^2\Delta_{5/2}$ band system of IrSi[a]

Line	$^{191}Ir^{28}Si$	$^{193}Ir^{28}Si$
P(4.5)	18518.114(3)	18516.551(21)
P(5.5)	18517.573(6)	18516.033(1)
P(6.5)	18516.981(12)	
P(7.5)	18516.359(-2)	18514.823(-11)
P(8.5)	18515.678(-6)	18514.126(0)
P(9.5)	18514.941(-3)	18513.381(12)
P(10.5)	18514.154(1)	18512.627(-17)
P(11.5)	18513.313(10)	
P(12.5)	18512.440(2)	
Q(3.5)	18519.540(-1)	18517.988(5)
Q(4.5)	18519.341(-23)	18517.777(-5)
Q(5.5)	18519.043(5)	18517.491(10)
Q(6.5)	18518.740(-11)	18517.178(4)
Q(7.5)	18518.362(-2)	18516.801(11)
Q(8.5)	18517.940(3)	18516.389(5)
Q(9.5)	18517.474(2)	18515.935(-8)
Q(10.5)	18516.959(1)	18515.421(-10)
Q(11.5)	18516.397(-2)	18514.823(22)
Q(12.5)		18514.226(4)
Q(13.5)	18515.113(5)	18513.571(-5)
Q(14.5)	18514.395(10)	18512.841(11)
Q(15.5)	18513.624(20)	
Q(16.5)	18512.834(-2)	
R(7.5)	18520.637(-5)	18519.088(-9)
R(8.5)	18520.494(-13)	18518.950(-22)
R(9.5)	18520.289(-8)	18518.739(-12)
R(10.5)	18520.032(0)	18518.473(4)
R(11.5)	18519.730(4)	18518.182(-3)
R(14.5)	18518.540(6)	18516.998(-11)
R(15.5)	18518.036(14)	
R(18.5)	18516.286(-13)	18514.716(-8)
R(20.5)	18514.837(5)	18513.264(9)
R(21.5)	18514.069(-17)	18512.478(4)
Spectroscopic Constants		
ν_0 (cm^{-1})	18519.9267(25)	18518.3803(31)
B' (cm^{-1})	0.133566(19)	0.133359(26)
r′ (Å)	2.27425(16)	2.27451(22)
B_0'' (cm^{-1})	0.158134(17)	0.157956(19)
r_0'' (Å)	2.09013(11)	2.08992(13)

[a] Residuals in the fit of the data to the form $\nu = \nu_0 + B' J'(J' + 1) - B'' J'' (J'' + 1)$ are provided in parentheses following each line position, in units of 0.001 cm^{-1}. Error limits (1σ) are given in parentheses following each spectroscopic constant, in units of the last quoted digit. All rotationally resolved bands originated from the same lower state (the ground vibronic level). In order to improve the accuracy of the spectroscopic constants, all of the bands were simultaneously fitted under the constraint that they have the same value of B″.

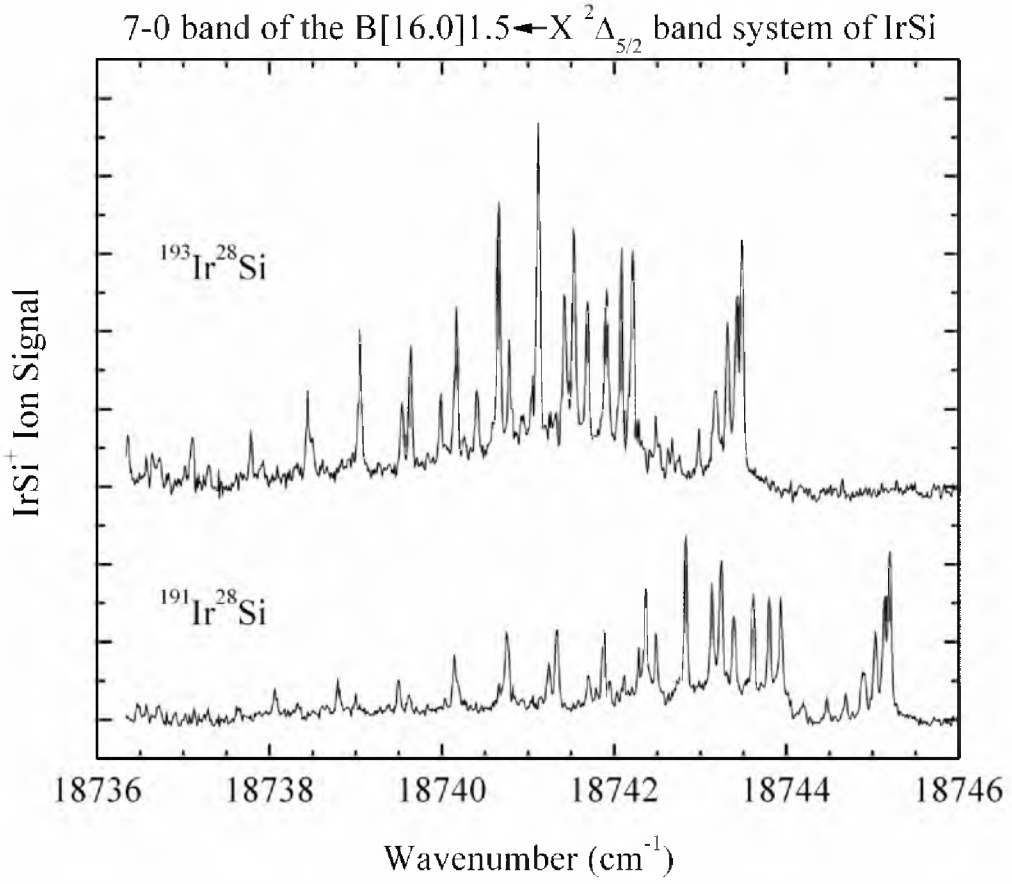

Figure B.32 Rotationally resolved spectra of the 7-0 band of the B[16.0]1.5 ← X $^2\Delta_{5/2}$ band system of IrSi.

Table B.13 Line positions for the 7-0 band of the B[16.0]1.5 ← X $^2\Delta_{5/2}$ band system of IrSi[a]

Line	$^{191}Ir^{28}Si$	$^{193}Ir^{28}Si$
P(2.5)	18743.243(0)	18741.533(-1)
P(3.5)	18742.832(-5)	18741.122(-5)
P(4.5)	18742.366(5)	18740.661(0)
P(5.5)	18741.879(-4)	18740.170(-4)
P(6.5)	18741.336(3)	18739.639(-8)
P(7.5)	18740.758(4)	18739.050(6)
P(8.5)	18740.147(0)	18738.442(-2)
P(9.5)	18739.497(-6)	18737.786(-1)
P(10.5)	18738.794(1)	18737.107(-16)
P(11.5)	18738.063(-4)	18736.349(7)
P(12.5)	18737.288(-5)	
P(13.5)	18736.474(-6)	
Q(2.5)	18743.936(-2)	18742.216(6)
Q(3.5)	18743.801(-7)	18742.084(-2)
Q(4.5)	18743.614(0)	18741.913(-9)
Q(5.5)	18743.390(5)	18741.689(-5)
Q(6.5)	18743.136(-1)	18741.426(-1)
Q(7.5)	18742.832(3)	18741.122(4)
Q(8.5)	18742.488(8)	18740.784(3)
Q(9.5)	18742.117(-1)	18740.408(0)
Q(10.5)	18741.701(-5)	18739.986(3)
Q(11.5)	18741.242(-5)	18739.536(-5)
Q(12.5)	18740.742(-5)	18739.030(2)
Q(13.5)	18740.189(9)	18738.497(-3)
Q(14.5)	18739.618(0)	18737.922(-7)
Q(15.5)	18739.002(-3)	18737.296(2)
Q(16.5)	18738.325(14)	18736.638(2)
Q(17.5)	18737.635(5)	
Q(18.5)	18736.905(-4)	
R(2.5)	18744.898(3)	18743.177(12)
R(3.5)	18745.033(4)	18743.316(9)
R(4.5)	18745.136(-2)	18743.423(-1)
R(11.5)	18744.688(2)	18742.984(-3)
R(12.5)	18744.468(-1)	18742.748(11)
R(13.5)	18744.198(6)	18742.484(12)

[a] Residuals in the fit of the data to the form $\nu = \nu_0 + B' J'(J' + 1) - B'' J'' (J'' + 1)$ are provided in parentheses following each line position, in units of 0.001 cm^{-1}. Error limits (1σ) are given in parentheses following each spectroscopic constant, in units of the last quoted digit. All rotationally resolved bands originated from the same lower state (the ground vibronic level). In order to improve the accuracy of the spectroscopic constants, all of the bands were simultaneously fitted under the constraint that they have the same value of B''.

Table B.13 (continued)

R(14.5)		18742.184(10)
R(17.5)		18741.054(-5)
R(18.5)	18742.285(4)	18740.593(-7)
R(19.5)	18741.794(-7)	
R(21.5)	18740.663(-2)	
R(22.5)	18740.039(-1)	
Spectroscopic Constants		
ν_0 (cm^{-1})	18744.108564(1141)	18742.396801(1695)
B' (cm^{-1})	0.138155(18)	0.138017(28)
r′ (Å)	2.23616(15)	2.23580(23)
B_0'' (cm^{-1})	0.158134(17)	0.157956(19)
r_0'' (Å)	2.09013(11)	2.08992(13)

[a] Residuals in the fit of the data to the form $\nu = \nu_0 + B' J'(J' + 1) - B'' J'' (J'' + 1)$ are provided in parentheses following each line position, in units of 0.001 cm^{-1}. Error limits (1σ) are given in parentheses following each spectroscopic constant, in units of the last quoted digit. All rotationally resolved bands originated from the same lower state (the ground vibronic level). In order to improve the accuracy of the spectroscopic constants, all of the bands were simultaneously fitted under the constraint that they have the same value of B″.

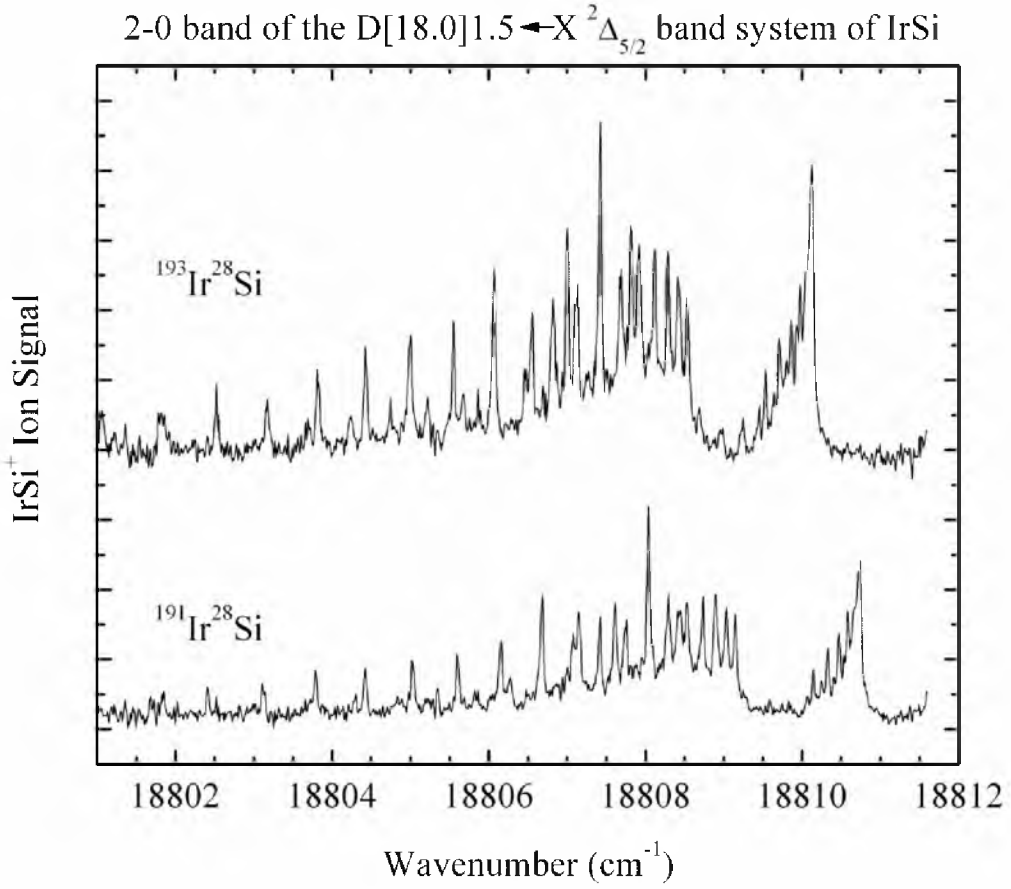

Figure B.33 Rotationally resolved spectra of the 2-0 band of the D[18.0]1.5 ← X $^2\Delta_{5/2}$ band system of IrSi.

Table B.14 Line positions for the 2-0 band of the D[18.0]1.5 ← X $^2\Delta_{5/2}$ band system of IrSi[a]

Line	$^{191}Ir^{28}Si$	$^{193}Ir^{28}Si$
P(2.5)	18808.432(-2)	18807.817(3)
P(3.5)	18808.038(-1)	18807.423(4)
P(4.5)	18807.611(2)	18807.003(0)
P(5.5)	18807.150(9)	18806.555(-5)
P(6.5)	18806.680(-7)	18806.067(-2)
P(7.5)	18806.153(4)	18805.549(0)
P(8.5)	18805.602(8)	18804.996(7)
P(9.5)	18805.028(4)	18804.428(-2)
P(10.5)	18804.424(0)	18803.819(0)
P(11.5)	18803.790(-6)	18803.165(16)
P(12.5)	18803.113(2)	18802.518(-7)
P(13.5)	18802.412(1)	18801.811(1)
P(14.5)	18801.685(-3)	18801.068(14)
Q(2.5)	18809.148(-4)	18808.534(-1)
Q(3.5)	18809.037(-1)	18808.423(2)
Q(4.5)	18808.895(3)	18808.290(-3)
Q(5.5)	18808.735(-6)	18808.117(1)
Q(6.5)	18808.529(-1)	18807.916(2)
Q(7.5)	18808.294(4)	18807.685(4)
Q(8.5)	18808.038(-1)	18807.423(5)
Q(9.5)	18807.748(-4)	18807.123(13)
Q(10.5)	18807.420(2)	18806.826(-12)
Q(11.5)	18807.076(-8)	18806.466(-5)
Q(12.5)	18806.680(3)	18806.067(10)
Q(13.5)	18806.275(-7)	18805.674(-12)
Q(14.5)	18805.821(1)	18805.218(0)
Q(15.5)	18805.348(-3)	18804.745(-3)
Q(16.5)	18804.836(2)	18804.234(1)
Q(17.5)	18804.290(10)	18803.694(4)
R(2.5)	18810.143(0)	18809.534(-3)
R(3.5)	18810.326(-5)	18809.707(2)
R(4.5)	18810.469(-1)	18809.863(-7)
R(5.5)	18810.583(2)	18809.976(-3)
R(6.5)	18810.663(7)	
R(7.5)	18810.729(-4)	18810.108(5)
R(8.5)	18810.749(0)	

[a] Residuals in the fit of the data to the form $\nu = \nu_0 + B' J'(J' + 1) - B'' J'' (J'' + 1)$ are provided in parentheses following each line position, in units of 0.001 cm^{-1}. Error limits (1σ) are given in parentheses following each spectroscopic constant, in units of the last quoted digit. All rotationally resolved bands originated from the same lower state (the ground vibronic level). In order to improve the accuracy of the spectroscopic constants, all of the bands were simultaneously fitted under the constraint that they have the same value of B''.

Table B.14 (continued)

R(10.5)		18810.108(-14)
R(11.5)	18810.623(14)	
R(12.5)	18810.536(1)	18809.932(-4)
R(13.5)	18810.406(2)	18809.802(-4)
R(14.5)	18810.251(-3)	18809.648(-9)
R(15.5)	18810.071(-14)	18809.454(-6)
R(16.5)	18809.830(5)	18809.245(-18)
R(17.5)	18809.586(-4)	18808.960(15)
Spectroscopic Constants		
ν_0 (cm^{-1})	18809.278282(1277)	18808.666816(1872)
B' (cm^{-1})	0.142757(22)	0.142610(26)
r′ (Å)	2.19982(17)	2.19950(20)
B_0'' (cm^{-1})	0.158134(17)	0.157956(19)
r_0'' (Å)	2.09013(11)	2.08992(13)

[a] Residuals in the fit of the data to the form $\nu = \nu_0 + B' J'(J' + 1) - B'' J'' (J'' + 1)$ are provided in parentheses following each line position, in units of 0.001 cm^{-1}. Error limits (1σ) are given in parentheses following each spectroscopic constant, in units of the last quoted digit. All rotationally resolved bands originated from the same lower state (the ground vibronic level). In order to improve the accuracy of the spectroscopic constants, all of the bands were simultaneously fitted under the constraint that they have the same value of B″.

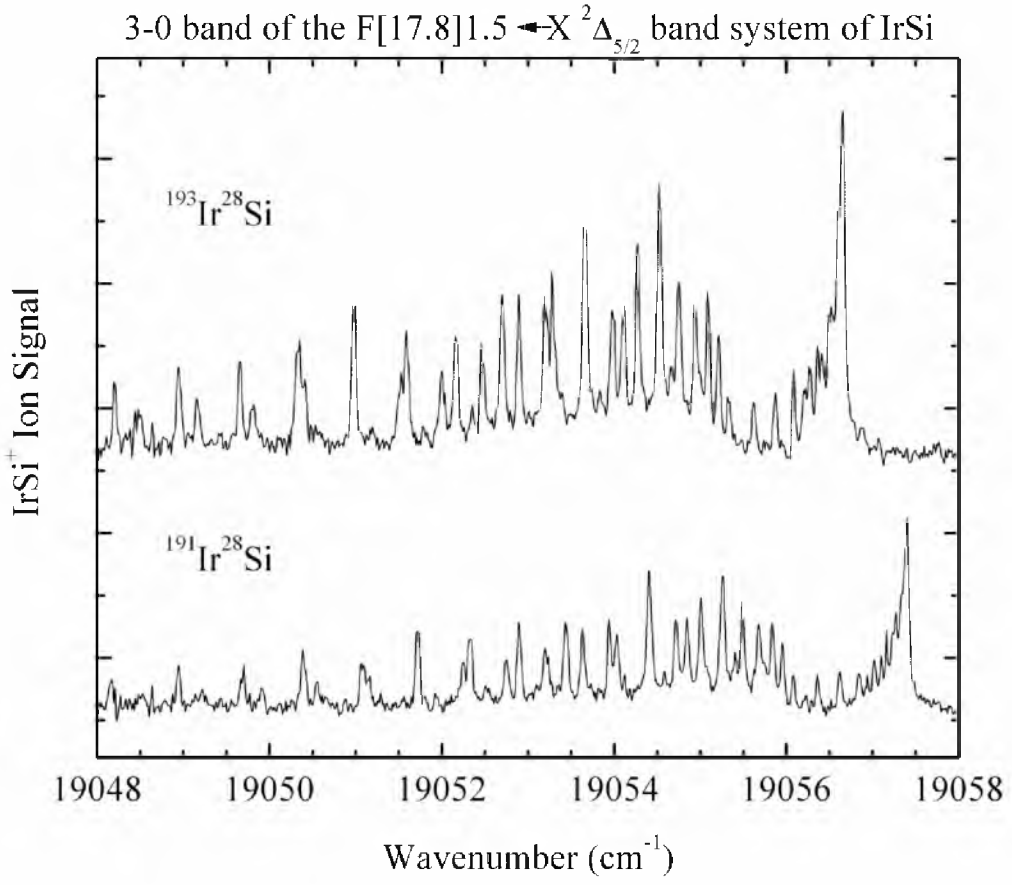

Figure B.34 Rotationally resolved spectra of the 3-0 band of the F[17.8]1.5 ← X $^2\Delta_{5/2}$ band system of IrSi.

Table B.15 Line positions for the 3-0 band of the F[17.8]1.5 ← X $^2\Delta_{5/2}$ band system of IrSi[a]

Line	$^{191}Ir^{28}Si$	$^{193}Ir^{28}Si$
P(2.5)	19055.261(-6)	19054.526(-12)
P(3.5)	19054.846(6)	19054.111(1)
P(4.5)	19054.408(8)	19053.664(12)
P(5.5)	19053.942(3)	19053.208(-2)
P(6.5)	19053.442(-3)	19052.703(-2)
P(7.5)	19052.896(3)	19052.165(-4)
P(8.5)	19052.329(-4)	19051.586(1)
P(9.5)	19051.719(-3)	19050.979(0)
P(10.5)	19051.078(-5)	19050.336(1)
P(11.5)	19050.392(4)	19049.657(3)
P(12.5)	19049.699(-15)	19048.945(3)
P(13.5)	19048.946(-9)	19048.204(-1)
P(14.5)	19048.161(-4)	
Q(2.5)	19055.953(6)	19055.214(4)
Q(3.5)	19055.836(3)	19055.090(8)
Q(4.5)	19055.678(6)	19054.939(4)
Q(5.5)	19055.490(5)	19054.751(3)
Q(6.5)	19055.261(10)	19054.526(4)
Q(7.5)	19055.009(4)	19054.271(1)
Q(8.5)	19054.717(4)	19053.983(-3)
Q(9.5)		19053.664(-10)
Q(10.5)	19054.029(4)	19053.282(11)
Q(11.5)	19053.633(4)	19052.897(0)
Q(12.5)	19053.199(8)	19052.471(-3)
Q(13.5)	19052.745(-2)	19051.998(5)
Q(14.5)	19052.248(-3)	19051.516(-11)
Q(15.5)		19050.979(-7)
Q(16.5)	19051.149(-5)	19050.413(-9)
Q(17.5)	19050.551(-9)	19049.807(-5)
Q(18.5)	19049.913(-8)	19049.157(10)
Q(19.5)	19049.217(18)	19048.482(13)
R(2.5)	19056.943(3)	19056.213(-9)
R(3.5)	19057.102(5)	19056.363(1)
R(4.5)	19057.236(-2)	19056.493(-1)
R(5.5)	19057.332(-5)	

[a] Residuals in the fit of the data to the form $\nu = \nu_0 + B' J'(J' + 1) - B'' J'' (J'' + 1)$ are provided in parentheses following each line position, in units of 0.001 cm^{-1}. Error limits (1σ) are given in parentheses following each spectroscopic constant, in units of the last quoted digit. All rotationally resolved bands originated from the same lower state (the ground vibronic level). In order to improve the accuracy of the spectroscopic constants, all of the bands were simultaneously fitted under the constraint that they have the same value of B''.

Table B.15 (continued)

R(6.5)	19057.390(-4)	
R(7.5)	19057.405(4)	
R(8.5)	19057.405(-7)	
R(9.5)	19057.366(-13)	
R(10.5)	19057.268(6)	19056.528(3)
R(11.5)	19057.163(-2)	19056.413(3)
R(12.5)	19057.017(-4)	19056.271(-3)
R(13.5)	19056.844(-14)	19056.084(2)
R(14.5)	19056.618(-5)	19055.873(-5)
R(15.5)	19056.360(2)	19055.621(-4)
R(16.5)	19056.079(-3)	19055.331(0)
R(17.5)	19055.748(8)	
R(18.5)	19055.405(-3)	
R(20.5)	19054.581(9)	
R(21.5)	19054.124(8)	
Spectroscopic Constants		
ν_0 (cm^{-1})	19056.1096(15)	19055.3686(15)
B' (cm^{-1})	0.140935(20)	0.140763(26)
r′ (Å)	2.21400(16)	2.21388(20)
B_0'' (cm^{-1})	0.158134(17)	0.157956(19)
r_0'' (Å)	2.09013(11)	2.08992(13)

[a] Residuals in the fit of the data to the form $\nu = \nu_0 + B' J'(J' + 1) - B'' J'' (J'' + 1)$ are provided in parentheses following each line position, in units of 0.001 cm^{-1}. Error limits (1σ) are given in parentheses following each spectroscopic constant, in units of the last quoted digit. All rotationally resolved bands originated from the same lower state (the ground vibronic level). In order to improve the accuracy of the spectroscopic constants, all of the bands were simultaneously fitted under the constraint that they have the same value of B″.

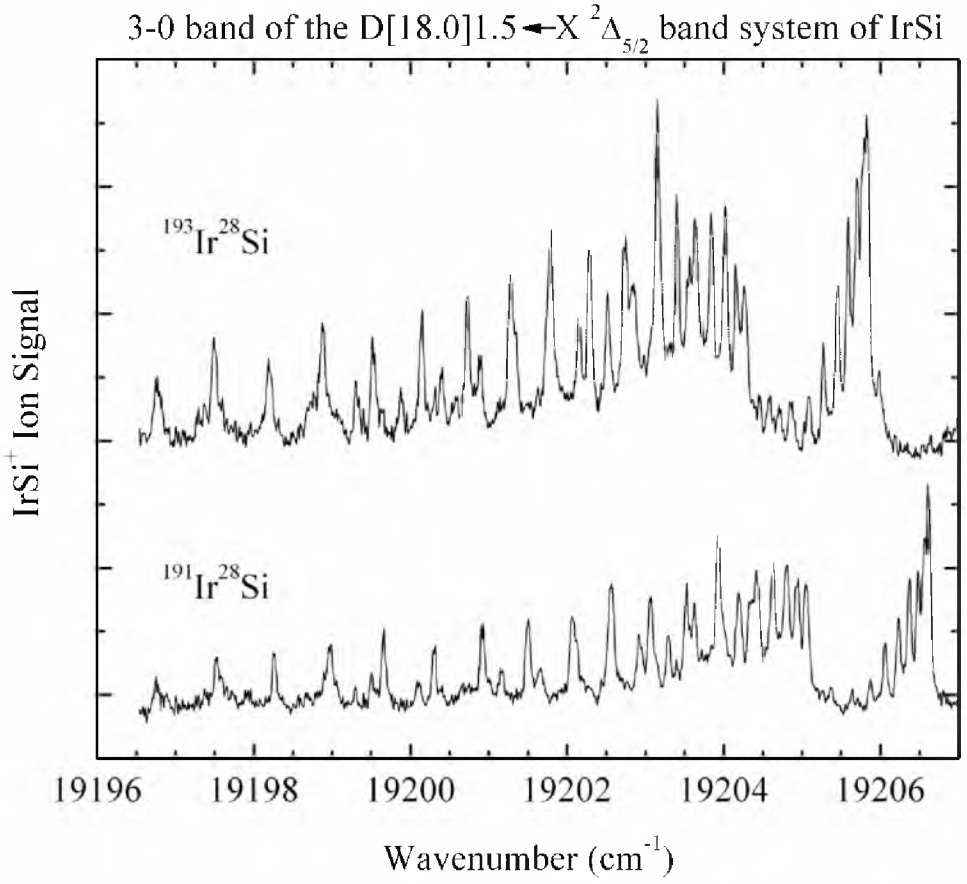

Figure B.35 Rotationally resolved spectra of the 3-0 band of the D[18.0]1.5 ← X $^2\Delta_{5/2}$ band system of IrSi.

Table B.16 Line positions for the 3-0 band of the D[18.0]1.5 ← X $^2\Delta_{5/2}$ band system of IrSi[a]

Line	$^{191}Ir^{28}Si$	$^{193}Ir^{28}Si$
P(2.5)	19204.349(-6)	19203.566(-8)
P(3.5)	19203.935(13)	19203.155(9)
P(4.5)	19203.523(-1)	19202.741(-3)
P(5.5)	19203.062(2)	19202.287(-6)
P(6.5)	19202.563(12)	19201.790(2)
P(7.5)	19202.070(-17)	19201.279(-6)
P(8.5)	19201.500(1)	19200.725(-4)
P(9.5)	19200.919(-1)	19200.148(-9)
P(10.5)	19200.305(-3)	19199.525(0)
P(11.5)	19199.658(-2)	19198.884(-6)
P(12.5)	19198.978(-1)	19198.199(3)
P(13.5)	19198.259(8)	19197.498(-4)
P(14.5)	19197.527(0)	19196.771(-16)
P(15.5)	19196.757(-3)	
Q(2.5)	19205.053(3)	19204.260(10)
Q(3.5)	19204.934(11)	19204.160(-1)
Q(4.5)	19204.803(1)	19204.017(2)
Q(5.5)	19204.630(0)	19203.842(4)
Q(6.5)	19204.416(10)	19203.637(5)
Q(7.5)	19204.194(-4)	19203.402(4)
Q(8.5)	19203.919(3)	
Q(9.5)	19203.627(-4)	19202.843(-1)
Q(10.5)	19203.296(-3)	19202.520(-8)
Q(11.5)	19202.922(9)	19202.155(-4)
Q(12.5)	19202.563(-25)	
Q(13.5)		19201.332(3)
Q(14.5)	19201.654(2)	19200.890(-10)
Q(15.5)	19201.167(1)	19200.400(-6)
Q(16.5)	19200.662(-13)	19199.879(-3)
Q(17.5)	19200.102(-4)	19199.317(9)
Q(18.5)	19199.505(11)	19198.769(-23)
Q(19.5)	19198.897(5)	
R(2.5)	19206.057(-5)	
R(3.5)	19206.235(-8)	
R(4.5)	19206.374(-4)	

[a] Residuals in the fit of the data to the form $\nu = \nu_0 + B' J'(J' + 1) - B'' J'' (J'' + 1)$ are provided in parentheses following each line position, in units of 0.001 cm^{-1}. Error limits (1σ) are given in parentheses following each spectroscopic constant, in units of the last quoted digit. All rotationally resolved bands originated from the same lower state (the ground vibronic level). In order to improve the accuracy of the spectroscopic constants, all of the bands were simultaneously fitted under the constraint that they have the same value of B''.

Table B.16 (continued)

R(5.5)	19206.483(-1)	
R(6.5)	19206.566(-5)	
R(7.5)	19206.610(0)	
R(9.5)	19206.610(3)	
R(10.5)	19206.566(2)	19205.770(14)
R(11.5)	19206.483(8)	19205.702(5)
R(12.5)	19206.374(8)	19205.590(10)
R(13.5)	19206.235(7)	19205.450(10)
R(14.5)	19206.057(13)	19205.272(18)
R(15.5)	19205.876(-9)	19205.086(2)
R(16.5)	19205.641(-8)	19204.856(-1)
R(17.5)	19205.369(-2)	19204.579(11)
Spectroscopic Constants		
ν_0 (cm^{-1})	19205.1928(18)	19204.4066(24)
B' (cm^{-1})	0.142397(20)	0.142265(27)
r′ (Å)	2.20260(16)	2.20216(21)
B_0'' (cm^{-1})	0.158134(17)	0.157956(19)
r_0'' (Å)	2.09013(11)	2.08992(13)

[a] Residuals in the fit of the data to the form $\nu = \nu_0 + B' J'(J' + 1) - B'' J'' (J'' + 1)$ are provided in parentheses following each line position, in units of 0.001 cm^{-1}. Error limits (1σ) are given in parentheses following each spectroscopic constant, in units of the last quoted digit. All rotationally resolved bands originated from the same lower state (the ground vibronic level). In order to improve the accuracy of the spectroscopic constants, all of the bands were simultaneously fitted under the constraint that they have the same value of B″.

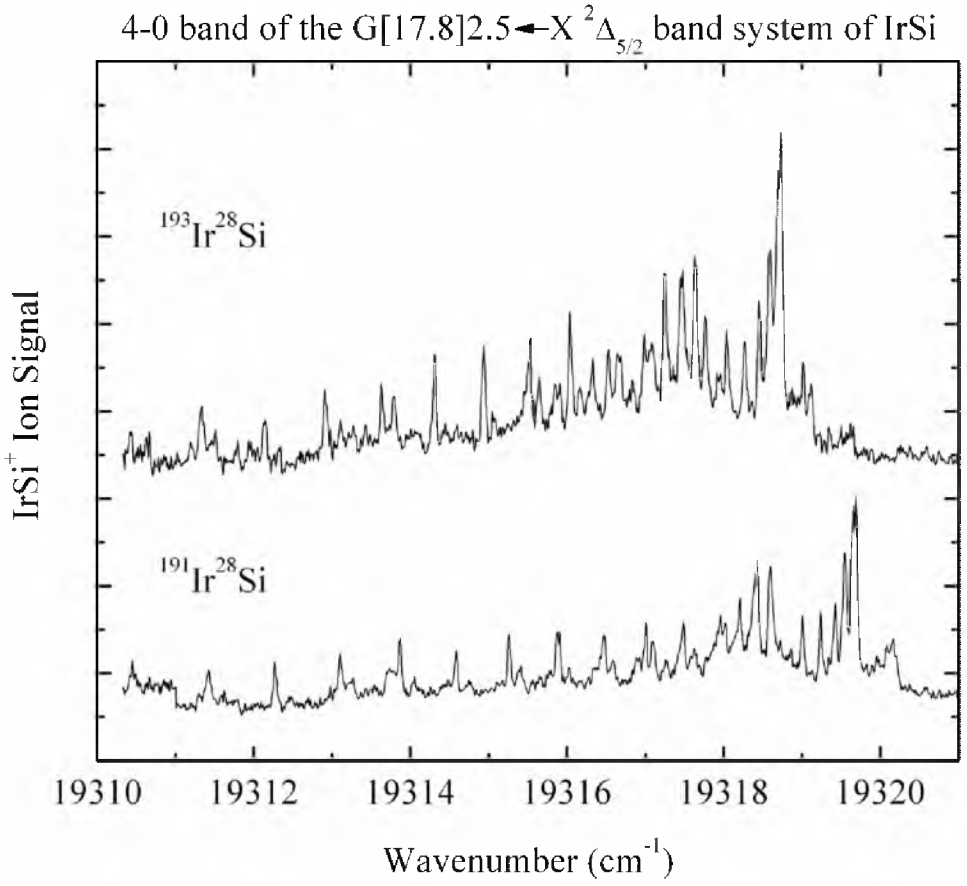

Figure B.36 Rotationally resolved spectra of the 4-0 band of the G[17.8]2.5 ← X $^2\Delta_{5/2}$ band system of IrSi.

Table B.17 Line positions for the 4-0 band of the G[17.8]2.5 ← X $^2\Delta_{5/2}$ band system of IrSi[a]

Line	$^{191}Ir^{28}Si$	$^{193}Ir^{28}Si$
P(3.5)	19317.484(2)	19316.530(-1)
P(4.5)	19317.011(-9)	19316.038(8)
P(5.5)	19316.474(-2)	19315.523(-9)
P(6.5)	19315.883(9)	19314.936(0)
P(7.5)	19315.257(8)	19314.310(0)
P(8.5)	19314.583(7)	19313.629(6)
P(9.5)	19313.867(1)	19312.918(-5)
P(10.5)	19313.103(-6)	19312.140(3)
P(11.5)	19312.269(9)	19311.334(-8)
P(12.5)	19311.426(-14)	19310.438(22)
Q(2.5)	19318.597(-3)	19317.639(-5)
Q(3.5)	19318.419(7)	19317.467(1)
Q(4.5)	19318.212(-1)	19317.248(4)
Q(5.5)	19317.961(-13)	19316.987(2)
Q(6.5)	19317.628(9)	19316.659(20)
Q(7.5)	19317.268(10)	19316.328(-8)
Q(8.5)	19316.891(-19)	19315.912(2)
R(2.5)	19319.545(-12)	19318.588(-15)
R(3.5)	19319.641(-7)	
R(7.5)	19319.545(15)	19318.588(11)
R(8.5)	19319.423(0)	19318.459(3)
R(9.5)	19319.235(1)	19318.269(6)
R(10.5)	19319.009(-6)	19318.043(-1)
R(11.5)	19318.722(-1)	19317.768(-7)
R(13.5)	19318.021(-7)	19317.075(-20)
R(15.5)	19317.095(21)	19316.165(-8)
R(16.5)	19316.584(12)	19315.644(-7)
R(17.5)	19316.026(2)	19315.065(4)
R(18.5)	19315.408(3)	19314.448(5)
R(19.5)	19314.748(-1)	19313.787(2)
R(20.5)	19314.042(-7)	19313.107(-30)
R(21.5)	19313.266(10)	19312.321(-3)
R(22.5)	19312.473(-5)	19311.511(1)
R(23.5)	19311.625(-12)	19310.629(27)
Spectroscopic Constants		
ν_0 (cm^{-1})	19318.8026(22)	19317.8435(27)
B' (cm^{-1})	0.134223(17)	0.134064(23)
r′ (Å)	2.26868(14)	2.26852(20)
B_0'' (cm^{-1})	0.158134(17)	0.157956(19)
r_0'' (Å)	2.09013(11)	2.08992(13)

[a] Residuals in the fit of the data to the form $\nu = \nu_0 + B' J'(J' + 1) - B'' J'' (J'' + 1)$ are provided in parentheses following each line position, in units of 0.001 cm^{-1}. Error limits (1σ) are given in parentheses following each spectroscopic constant, in units of the last quoted digit. All rotationally resolved bands originated from the same lower state (the ground vibronic level). In order to improve the accuracy of the spectroscopic constants, all of the bands were simultaneously fitted under the constraint that they have the same value of B″.

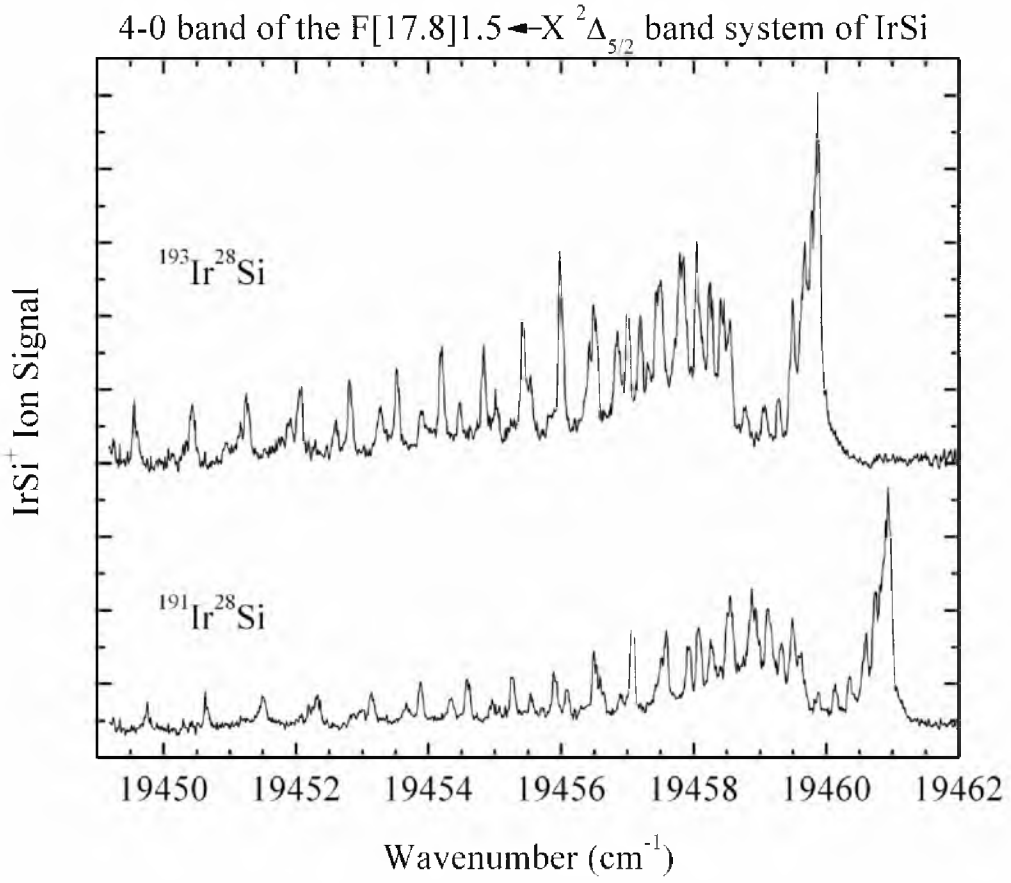

Figure B.37 Rotationally resolved spectra of the 4-0 band of the F[17.8]1.5 ← X $^2\Delta_{5/2}$ band system of IrSi.

Table B.18 Line positions for the 4-0 band of the F[17.8]1.5 ← X $^2\Delta_{5/2}$ band system of IrSi[a]

Line	$^{191}Ir^{28}Si$	$^{193}Ir^{28}Si$
P(2.5)	19458.938(-5)	19457.842(15)
P(3.5)	19458.509(13)	19457.449(-1)
P(4.5)	19458.075(-2)	19457.006(-7)
P(5.5)	19457.579(8)	19456.507(7)
P(6.5)	19457.073(-10)	19455.990(0)
P(7.5)	19456.504(-2)	19455.427(1)
P(8.5)	19455.904(-2)	19454.836(-7)
P(9.5)	19455.262(3)	19454.193(-1)
P(10.5)	19454.589(2)	19453.520(-2)
P(11.5)	19453.879(-1)	19452.815(-10)
P(12.5)	19453.136(-9)	19452.065(-10)
P(13.5)	19452.318(21)	19451.257(10)
P(14.5)	19451.502(12)	19450.433(8)
P(15.5)	19450.641(8)	19449.568(9)
P(16.5)	19449.756(-8)	
Q(2.5)	19459.624(5)	19458.551(3)
Q(3.5)	19459.494(3)	19458.429(-8)
Q(4.5)	19459.321(5)	19458.257(-7)
Q(5.5)	19459.122(-3)	19458.047(-4)
Q(6.5)	19458.882(-9)	19457.789(8)
Q(7.5)	19458.579(11)	19457.500(15)
Q(8.5)	19458.273(-3)	19457.196(-3)
Q(9.5)	19457.924(-13)	19456.852(-18)
Q(10.5)	19457.516(-1)	19456.432(6)
Q(11.5)	19457.073(8)	19455.990(13)
Q(12.5)	19456.596(13)	19455.532(0)
Q(13.5)	19456.089(10)	19455.023(-1)
Q(14.5)	19455.545(6)	19454.471(3)
Q(15.5)	19454.962(4)	19453.892(-3)
Q(16.5)	19454.339(5)	19453.275(-10)
Q(17.5)	19453.669(14)	19452.600(5)
Q(18.5)	19452.994(-9)	19451.901(4)
R(2.5)	19460.603(0)	
R(3.5)		19459.671(2)
R(4.5)		19459.781(0)

[a] Residuals in the fit of the data to the form $\nu = \nu_0 + B' J'(J' + 1) - B'' J'' (J'' + 1)$ are provided in parentheses following each line position, in units of 0.001 cm^{-1}. Error limits (1σ) are given in parentheses following each spectroscopic constant, in units of the last quoted digit. All rotationally resolved bands originated from the same lower state (the ground vibronic level). In order to improve the accuracy of the spectroscopic constants, all of the bands were simultaneously fitted under the constraint that they have the same value of B''.

Table B.18 (continued)

R(5.5)	19460.933(-3)	
R(6.5)		
R(7.5)		
R(8.5)	19460.933(-17)	
R(9.5)		
R(10.5)	19460.742(-24)	19459.632(5)
R(11.5)	19460.574(-12)	19459.497(-17)
R(12.5)	19460.355(14)	19459.280(6)
R(13.5)	19460.141(-3)	19459.067(-12)
R(14.5)	19459.874(-5)	19458.785(0)
R(15.5)	19459.586(-24)	
Spectroscopic Constants		
ν_0 (cm^{-1})	19459.7939(27)	19458.7183(22)
B' (cm^{-1})	0.139258(17)	0.139071(18)
r′ (Å)	2.22729(14)	2.22731(14)
B_0'' (cm^{-1})	0.158134(17)	0.157956(19)
r_0'' (Å)	2.09013(11)	2.08992(13)

[a] Residuals in the fit of the data to the form $\nu = \nu_0 + B' J'(J' + 1) - B'' J'' (J'' + 1)$ are provided in parentheses following each line position, in units of 0.001 cm^{-1}. Error limits (1σ) are given in parentheses following each spectroscopic constant, in units of the last quoted digit. All rotationally resolved bands originated from the same lower state (the ground vibronic level). In order to improve the accuracy of the spectroscopic constants, all of the bands were simultaneously fitted under the constraint that they have the same value of B″.

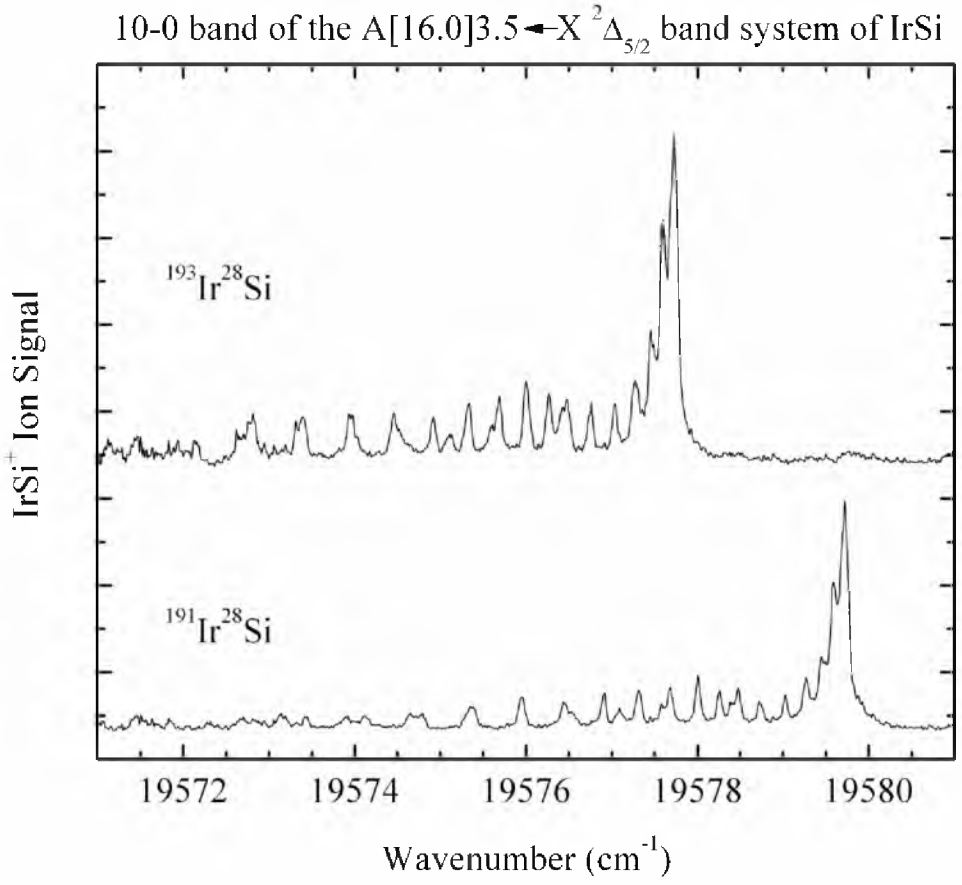

Figure B.38 Rotationally resolved spectra of the 10-0 band of the A[16.0]3.5 ← X $^2\Delta_{5/2}$ band system of IrSi.

Table B.19 Line positions for the 10-0 band of the A[16.0]3.5 ← X $^2\Delta_{5/2}$ band system of IrSi[a]

Line	$^{191}Ir^{28}Si$	$^{193}Ir^{28}Si$
P(5.5)	19576.529(-6)	19574.516(8)
P(6.5)		19573.953(-9)
P(7.5)		19573.319(-4)
P(8.5)	19574.643(-12)	19572.631(8)
P(9.5)	19573.895(8)	
P(10.5)	19573.136(-8)	19571.126(14)
P(11.5)	19572.289(15)	
P(12.5)	19571.429(2)	
Q(3.5)	19578.474(6)	19576.477(2)
Q(4.5)	19578.256(6)	19576.268(-6)
Q(5.5)	19578.003(-7)	19576.002(-4)
Q(6.5)	19577.679(3)	19575.688(-4)
Q(7.5)	19577.317(2)	19575.327(-4)
Q(8.5)	19576.912(-4)	19574.911(3)
Q(9.5)	19576.445(3)	19574.455(2)
Q(10.5)	19575.951(-10)	19573.953(-2)
Q(11.5)	19575.384(0)	19573.393(5)
Q(12.5)	19574.780(0)	19572.799(-3)
Q(13.5)	19574.126(1)	19572.144(2)
Q(14.5)	19573.432(-6)	19571.450(-1)
Q(15.5)	19572.681(-6)	
Q(17.5)	19571.018(13)	
R(4.5)		19577.730(5)
R(5.5)		19577.730(8)
R(6.5)	19579.696(-5)	19577.693(0)
R(7.5)	19579.589(7)	19577.600(0)
R(8.5)	19579.446(7)	19577.457(2)
R(9.5)	19579.268(-7)	19577.275(-6)
R(10.5)	19579.024(-3)	19577.035(-4)
R(11.5)	19578.729(4)	19576.751(-6)
R(12.5)	19578.398(-2)	19576.427(-16)
R(13.5)	19578.003(8)	
R(14.5)	19577.585(-8)	19575.597(3)
R(15.5)	19577.093(3)	19575.110(11)
R(17.5)		19574.027(-7)

[a] Residuals in the fit of the data to the form $\nu = \nu_0 + B' J'(J' + 1) - B'' J'' (J'' + 1)$ are provided in parentheses following each line position, in units of 0.001 cm^{-1}. Error limits (1σ) are given in parentheses following each spectroscopic constant, in units of the last quoted digit. All rotationally resolved bands originated from the same lower state (the ground vibronic level). In order to improve the accuracy of the spectroscopic constants, all of the bands were simultaneously fitted under the constraint that they have the same value of B''.

Table B.19 (continued)

R(18.5)	19575.366(-6)	19573.393(4)
R(21.5)	19573.189(0)	
Spectroscopic Constants		
ν_0 (cm^{-1})	19578.8610(20)	19576.8578(19)
B' (cm^{-1})	0.133948(16)	0.133889(18)
r′ (Å)	2.27101(14)	2.27000(15)
B_0'' (cm^{-1})	0.158134(17)	0.157956(19)
r_0'' (Å)	2.09013(11)	2.08992(13)

[a] Residuals in the fit of the data to the form $\nu = \nu_0 + B' J'(J' + 1) - B'' J'' (J'' + 1)$ are provided in parentheses following each line position, in units of 0.001 cm^{-1}. Error limits (1σ) are given in parentheses following each spectroscopic constant, in units of the last quoted digit. All rotationally resolved bands originated from the same lower state (the ground vibronic level). In order to improve the accuracy of the spectroscopic constants, all of the bands were simultaneously fitted under the constraint that they have the same value of B″.

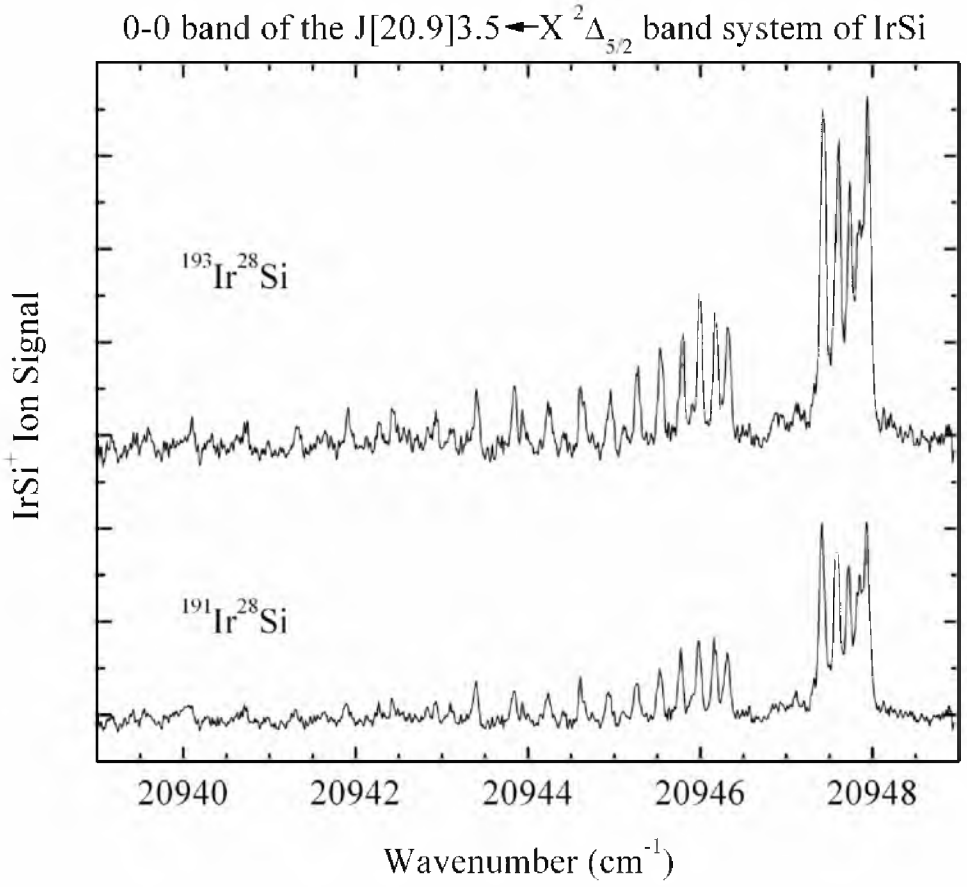

Figure B.39 Rotationally resolved spectra of the 0-0 band of the J[20.9]3.5 ← X $^2\Delta_{5/2}$ band system of IrSi.

Table B.20 Line positions for the 0-0 band of the J[20.9]3.5 ← X $^2\Delta_{5/2}$ band system of IrSi[a]

Line	$^{191}Ir^{28}Si$	$^{193}Ir^{28}Si$
P(4.5)		20944.912(-10)
P(5.5)		20944.437(4)
P(6.5)	20943.933(1)	20943.936(10)
P(7.5)	20943.400(6)	20943.407(12)
P(8.5)	20942.832(14)	
P(9.5)	20942.268(-15)	20942.276(-8)
P(10.5)	20941.637(-9)	20941.647(-2)
P(12.5)	20940.280(1)	
P(13.5)	20939.543(15)	20939.593(-15)
P(15.5)	20938.002(14)	
P(16.5)	20937.211(-15)	
Q(3.5)	20946.312(3)	20946.325(-2)
Q(4.5)	20946.164(3)	20946.167(11)
Q(5.5)	20945.977(13)	20945.997(2)
Q(6.5)	20945.773(5)	20945.799(-11)
Q(7.5)	20945.528(6)	20945.530(15)
Q(8.5)	20945.265(-7)	20945.281(-11)
Q(9.5)	20944.935(14)	20944.960(2)
Q(10.5)	20944.607(1)	20944.605(16)
Q(11.5)	20944.238(-4)	20944.261(-13)
Q(12.5)	20943.836(-8)	20943.841(1)
Q(13.5)	20943.400(-11)	20943.397(8)
Q(14.5)	20942.929(-11)	20942.932(2)
Q(15.5)	20942.417(-2)	20942.429(2)
Q(16.5)	20941.886(-8)	20941.913(-17)
Q(17.5)	20941.304(5)	20941.321(8)
Q(18.5)	20940.706(2)	20940.741(-12)
Q(19.5)	20940.064(10)	20940.096(0)
Q(21.5)	20938.695(15)	20938.752(-17)
Q(22.5)		20938.000(5)
Q(23.5)	20937.211(4)	20937.242(0)
Q(25.5)	20935.594(-4)	20935.613(7)
R(2.5)	20947.415(6)	20947.419(10)
R(3.5)	20947.584(7)	20947.607(-7)
R(4.5)	20947.723(6)	20947.732(4)
R(5.5)	20947.848(-14)	20947.849(-6)

[a] Residuals in the fit of the data to the form $\nu = \nu_0 + B' J'(J' + 1) - B'' J'' (J'' + 1)$ are provided in parentheses following each line position, in units of 0.001 cm^{-1}. Error limits (1σ) are given in parentheses following each spectroscopic constant, in units of the last quoted digit. All rotationally resolved bands originated from the same lower state (the ground vibronic level). In order to improve the accuracy of the spectroscopic constants, all of the bands were simultaneously fitted under the constraint that they have the same value of B''.

Table B.20 (continued)

R(6.5)	20947.927(-21)	
R(14.5)	20947.321(-4)	20947.320(8)
R(15.5)	20947.114(-17)	20947.108(1)
R(16.5)		20946.870(-12)
R(17.5)		20946.569(4)
R(19.5)		20945.912(-4)
R(20.5)		20945.530(-4)
R(21.5)		20945.113(0)
R(22.5)		20944.653(14)
R(25.5)	20943.100(10)	20943.128(5)
R(26.5)		20942.558(-1)
R(31.5)	20939.162(-5)	
R(33.5)	20937.596(-16)	
R(35.5)	20935.858(14)	
Spectroscopic Constants		
ν_0 (cm^{-1})	20946.5700(21)	20946.5791(21)
B' (cm^{-1})	0.141884(21)	0.141740(20)
r′ (Å)	2.20658(16)	2.20624(16)
B_0'' (cm^{-1})	0.158134(17)	0.157956(19)
r_0'' (Å)	2.09013(11)	2.08992(13)

[a] Residuals in the fit of the data to the form $\nu = \nu_0 + B' J'(J' + 1) - B'' J'' (J'' + 1)$ are provided in parentheses following each line position, in units of 0.001 cm^{-1}. Error limits (1σ) are given in parentheses following each spectroscopic constant, in units of the last quoted digit. All rotationally resolved bands originated from the same lower state (the ground vibronic level). In order to improve the accuracy of the spectroscopic constants, all of the bands were simultaneously fitted under the constraint that they have the same value of B″.

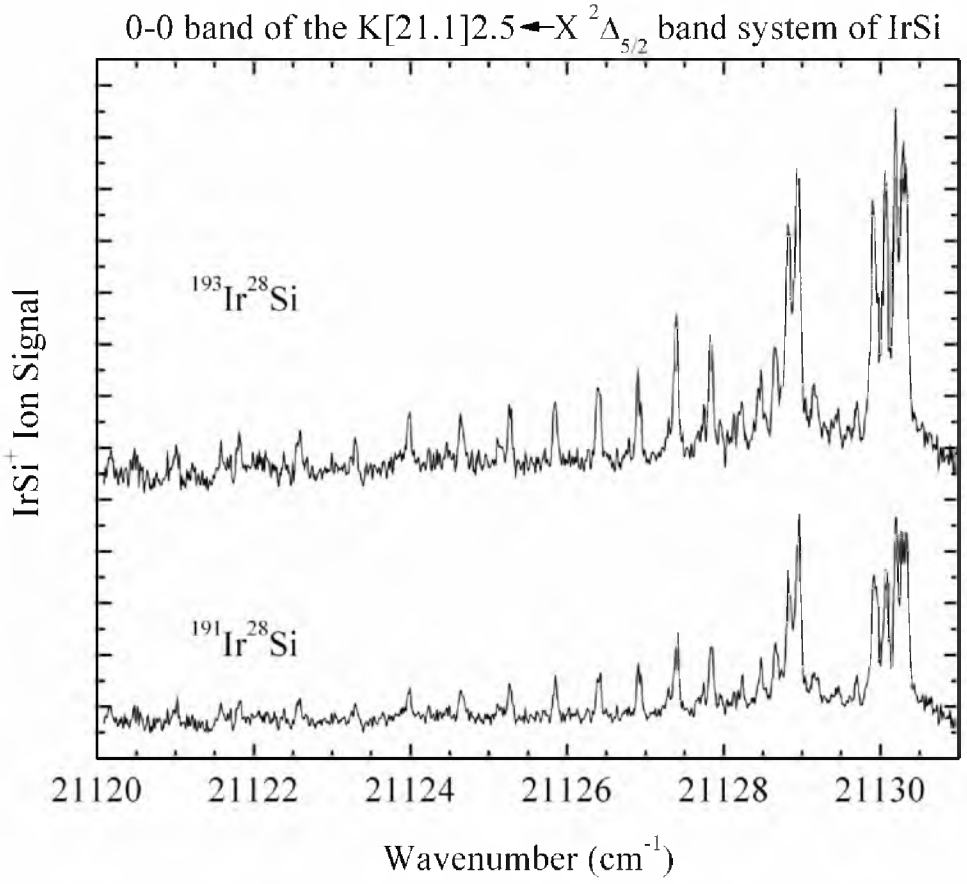

Figure B.40 Rotationally resolved spectra of the 0-0 band of the K[21.1]2.5 ← X $^2\Delta_{5/2}$ band system of IrSi.

Table B.21 Line positions for the 0-0 band of the K[21.1]2.5 ← $X\,^2\Delta_{5/2}$ band system of IrSi[a]

Line	$^{191}Ir^{28}Si$	$^{193}Ir^{28}Si$
P(3.5)	21127.842(-6)	21127.826(-1)
P(4.5)	21127.400(-4)	21127.395(-9)
P(5.5)	21126.908(11)	21126.906(4)
P(6.5)	21126.404(3)	21126.393(6)
P(7.5)	21125.853(6)	21125.846(7)
P(8.5)	21125.260(17)	21125.258(14)
P(9.5)	21124.641(17)	21124.638(16)
P(10.5)	21123.995(8)	21123.996(6)
P(11.5)	21123.295(19)	21123.293(21)
P(12.5)	21122.583(5)	21122.584(7)
P(13.5)	21121.809(18)	21121.816(17)
P(14.5)	21121.006(25)	21121.010(28)
Q(2.5)	21128.951(-8)	21128.936(-5)
Q(3.5)	21128.824(-5)	21128.827(-20)
Q(4.5)	21128.668(-10)	21128.648(-1)
Q(5.5)	21128.476(-13)	21128.471(-18)
Q(6.5)	21128.237(-5)	21128.229(-6)
Q(7.5)	21127.961(4)	21127.947(9)
Q(10.5)	21126.940(11)	21126.941(7)
Q(14.5)		21125.108(-3)
R(2.5)	21129.945(-19)	21129.915(-3)
R(3.5)	21130.087(-5)	21130.066(3)
R(4.5)	21130.203(-1)	21130.193(-3)
R(5.5)	21130.298(-10)	21130.299(-23)
R(6.5)		21130.324(2)
R(9.5)	21130.271(0)	
R(10.5)	21130.189(-10)	
R(11.5)	21130.063(-13)	
R(12.5)		21129.898(-14)
R(13.5)	21129.700(-14)	21129.702(-16)
R(14.5)	21129.462(-11)	21129.462(-9)
R(15.5)		21129.183(1)
R(16.5)		21128.896(-15)
R(19.5)	21127.745(-4)	
R(20.5)	21127.299(-7)	

[a] Residuals in the fit of the data to the form $\nu = \nu_0 + B' J'(J' + 1) - B'' J'' (J'' + 1)$ are provided in parentheses following each line position, in units of 0.001 cm^{-1}. Error limits (1σ) are given in parentheses following each spectroscopic constant, in units of the last quoted digit. All rotationally resolved bands originated from the same lower state (the ground vibronic level). In order to improve the accuracy of the spectroscopic constants, all of the bands were simultaneously fitted under the constraint that they have the same value of B''.

Table B.21 (continued)

Spectroscopic Constants		
ν_0 (cm^{-1})	21129.0989(29)	21129.0858(35)
B' (cm^{-1})	0.140343(27)	0.140246(26)
r′ (Å)	2.21866(21)	2.21796(21)
B_0'' (cm^{-1})	0.158134(17)	0.157956(19)
r_0'' (Å)	2.09013(11)	2.08992(13)

[a] Residuals in the fit of the data to the form $\nu = \nu_0 + B' J'(J' + 1) - B'' J'' (J'' + 1)$ are provided in parentheses following each line position, in units of 0.001 cm^{-1}. Error limits (1σ) are given in parentheses following each spectroscopic constant, in units of the last quoted digit. All rotationally resolved bands originated from the same lower state (the ground vibronic level). In order to improve the accuracy of the spectroscopic constants, all of the bands were simultaneously fitted under the constraint that they have the same value of B″.

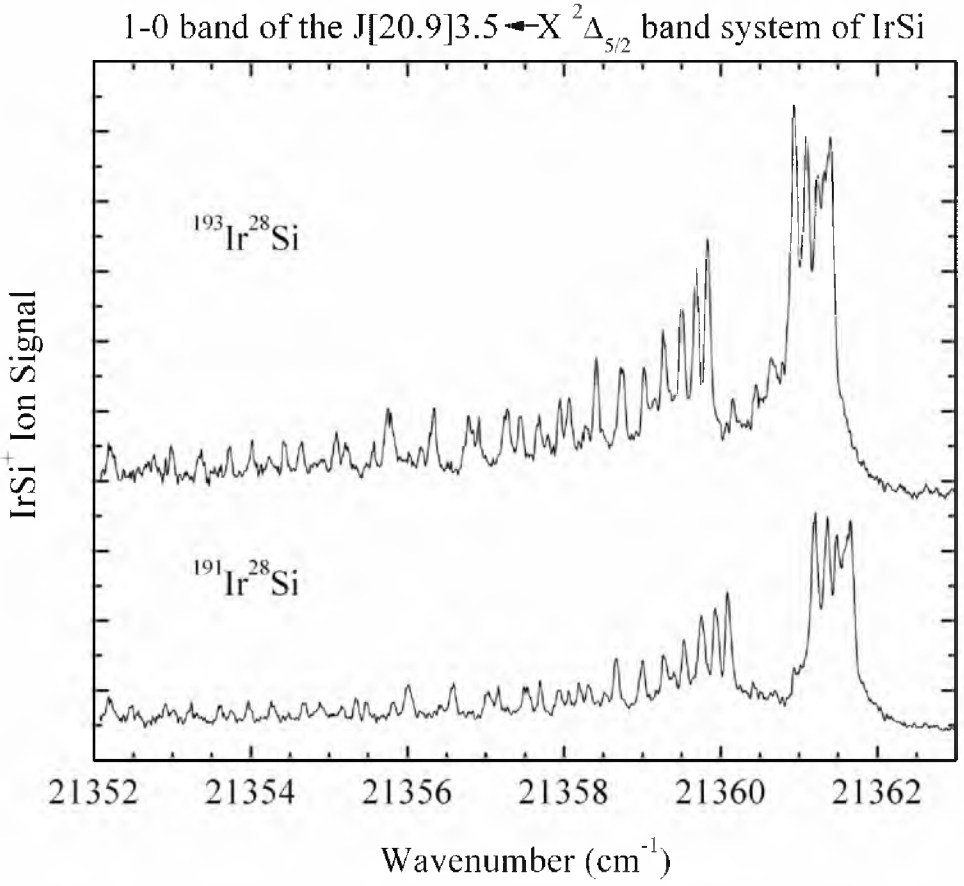

Figure B.41 Rotationally resolved spectra of the 1-0 band of the J[20.9]3.5 ← X $^2\Delta_{5/2}$ band system of IrSi.

Table B.22 Line positions for the 1-0 band of the J[20.9]3.5 ← $X\,^2\Delta_{5/2}$ band system of IrSi[a]

Line	$^{191}Ir^{28}Si$	$^{193}Ir^{28}Si$
P(4.5)	21358.659(3)	21358.407(2)
P(5.5)	21358.185(9)	21357.950(-9)
P(6.5)	21357.683(9)	21357.437(2)
P(7.5)	21357.159(-3)	21356.909(-5)
P(8.5)	21356.589(-2)	21356.333(2)
P(9.5)	21355.990(-7)	21355.745(-13)
P(10.5)	21355.335(10)	21355.093(2)
P(11.5)	21354.683(-8)	21354.419(5)
P(12.5)	21353.973(-3)	21353.728(-7)
P(13.5)	21353.238(-7)	21352.980(3)
P(14.5)	21352.481(-23)	21352.202(8)
Q(3.5)	21360.088(-3)	21359.832(-1)
Q(4.5)	21359.929(5)	21359.688(-9)
Q(5.5)	21359.747(0)	21359.499(-7)
Q(6.5)	21359.535(-7)	21359.262(11)
Q(7.5)	21359.264(11)	21359.025(-5)
Q(8.5)	21359.001(-14)	21358.732(1)
Q(9.5)	21358.659(7)	21358.407(6)
Q(10.5)	21358.307(5)	21358.068(-10)
Q(11.5)	21357.941(-18)	21357.681(-12)
Q(12.5)	21357.488(12)	21357.240(8)
Q(13.5)	21357.030(14)	21356.782(9)
Q(14.5)	21356.563(-8)	21356.290(12)
Q(15.5)	21356.027(4)	21355.788(-10)
Q(16.5)	21355.478(-5)	21355.203(18)
Q(17.5)	21354.883(-1)	21354.644(-14)
Q(18.5)	21354.250(6)	21354.015(-10)
Q(19.5)	21353.616(-18)	21353.351(-5)
Q(20.5)	21352.914(-9)	
Q(21.5)	21352.176(3)	
R(2.5)	21361.196(-3)	21360.933(3)
R(3.5)	21361.352(5)	21361.087(13)
R(4.5)	21361.478(10)	21361.237(-6)
R(5.5)		21361.325(2)
R(6.5)		21361.398(-9)
R(14.5)	21360.933(0)	21360.650(25)

[a] Residuals in the fit of the data to the form $\nu = \nu_0 + B' J'(J' + 1) - B'' J'' (J'' + 1)$ are provided in parentheses following each line position, in units of 0.001 cm^{-1}. Error limits (1σ) are given in parentheses following each spectroscopic constant, in units of the last quoted digit. All rotationally resolved bands originated from the same lower state (the ground vibronic level). In order to improve the accuracy of the spectroscopic constants, all of the bands were simultaneously fitted under the constraint that they have the same value of B''.

Table B.22 (continued)

R(15.5)	21360.682(10)	21360.445(-11)
R(16.5)	21360.409(7)	21360.152(6)
R(19.5)	21359.395(-7)	
R(21.5)	21358.522(13)	
R(22.5)	21358.061(-4)	
R(23.5)	21357.530(15)	21357.275(12)
R(24.5)	21357.003(-3)	21356.726(16)
R(25.5)	21356.425(-4)	
R(26.5)	21355.813(-5)	21355.561(-10)
R(27.5)	21355.159(2)	
R(28.5)	21354.485(-4)	21354.236(-13)
R(30.5)	21353.009(9)	
Spectroscopic Constants		
ν_0 (cm^{-1})	21360.3516(19)	21360.0964(22)
B' (cm^{-1})	0.141239(20)	0.141071(19)
r′ (Å)	2.21161(16)	2.21146(15)
B_0'' (cm^{-1})	0.158134(17)	0.157956(19)
r_0'' (Å)	2.09013(11)	2.08992(13)

[a] Residuals in the fit of the data to the form $\nu = \nu_0 + B' J'(J' + 1) - B'' J'' (J'' + 1)$ are provided in parentheses following each line position, in units of 0.001 cm^{-1}. Error limits (1σ) are given in parentheses following each spectroscopic constant, in units of the last quoted digit. All rotationally resolved bands originated from the same lower state (the ground vibronic level). In order to improve the accuracy of the spectroscopic constants, all of the bands were simultaneously fitted under the constraint that they have the same value of B″.

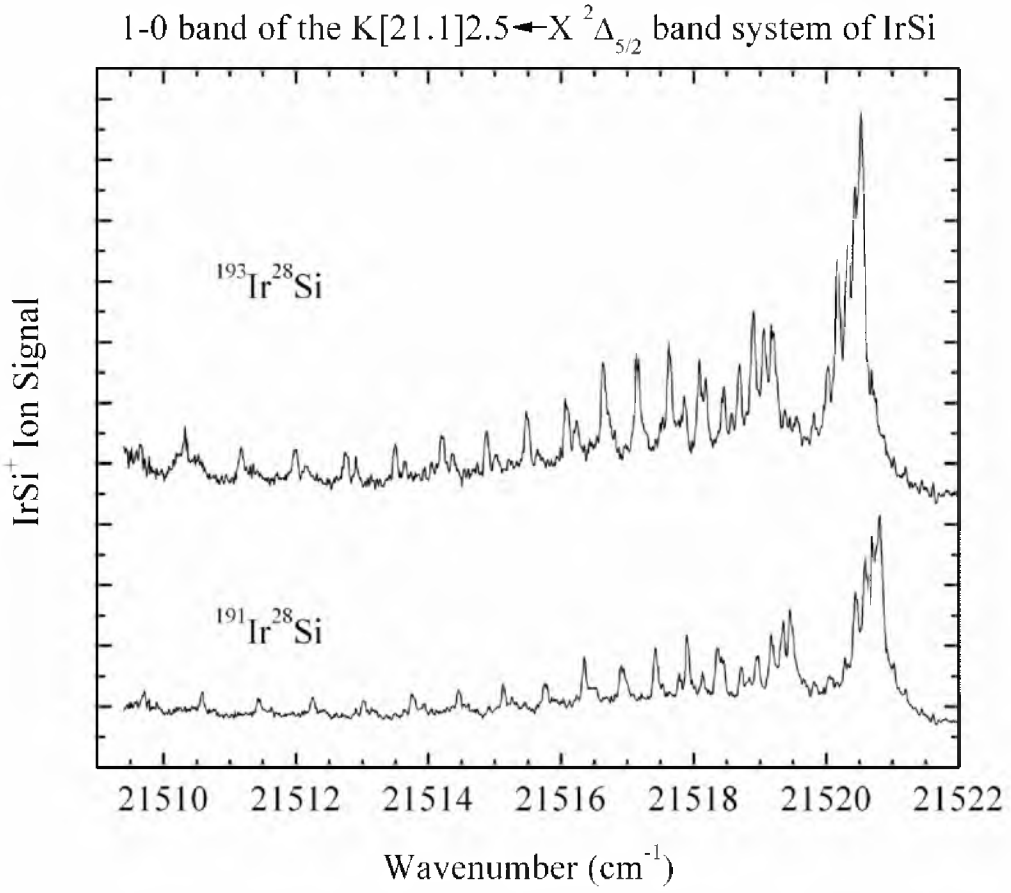

Figure B.42 Rotationally resolved spectra of the 1-0 band of the K[21.1]2.5 ← X $^2\Delta_{5/2}$ band system of IrSi.

Table B.23 Line positions for the 1-0 band of the K[21.1]2.5 ← X $^2\Delta_{5/2}$ band system of IrSi[a]

Line	$^{191}Ir^{28}Si$	$^{193}Ir^{28}Si$
P(3.5)	21518.360(-14)	21518.085(-5)
P(4.5)	21517.894(8)	21517.625(11)
P(5.5)	21517.424(-4)	21517.144(10)
P(6.5)	21516.902(-1)	21516.636(1)
P(7.5)	21516.354(-8)	21516.065(17)
P(8.5)	21515.746(9)	21515.471(21)
P(9.5)	21515.122(5)	21514.870(-6)
P(10.5)	21514.452(9)	21514.199(1)
P(11.5)	21513.757(2)	21513.497(2)
P(12.5)	21513.027(-6)	21512.743(17)
P(13.5)	21512.252(-7)	21511.992(-6)
P(14.5)	21511.429(4)	21511.169(6)
P(15.5)	21510.585(-1)	21510.322(5)
P(16.5)	21509.709(-11)	
Q(2.5)	21519.467(-13)	21519.177(9)
Q(3.5)	21519.340(-16)	21519.053(4)
Q(4.5)	21519.171(-12)	21518.905(-13)
Q(5.5)	21518.966(-9)	21518.692(-2)
Q(6.5)	21518.713(5)	21518.456(-4)
Q(7.5)	21518.442(1)	21518.184(-7)
Q(8.5)	21518.133(-2)	21517.858(7)
Q(9.5)	21517.779(3)	
Q(11.5)	21516.967(7)	
Q(12.5)	21516.504(11)	
Q(15.5)	21514.915(1)	
R(2.5)	21520.438(-6)	21520.164(-2)
R(3.5)	21520.584(-1)	21520.328(-14)
R(4.5)	21520.687(10)	21520.432(-4)
R(5.5)		21520.522(-17)
R(6.5)	21520.812(3)	
R(12.5)	21520.277(12)	21520.026(-6)
R(13.5)	21520.053(19)	21519.812(-8)
R(14.5)	21519.810(9)	21519.554(-3)
R(16.5)	21519.199(4)	
R(17.5)	21518.841(-2)	21518.571(2)
R(20.5)	21517.532(-3)	

[a] Residuals in the fit of the data to the form $\nu = \nu_0 + B' J'(J' + 1) - B'' J'' (J'' + 1)$ are provided in parentheses following each line position, in units of 0.001 cm^{-1}. Error limits (1σ) are given in parentheses following each spectroscopic constant, in units of the last quoted digit. All rotationally resolved bands originated from the same lower state (the ground vibronic level). In order to improve the accuracy of the spectroscopic constants, all of the bands were simultaneously fitted under the constraint that they have the same value of B″.

Table B.23 (continued)

R(22.5)		21516.231(-22)
R(23.5)		21515.640(-14)
R(24.5)	21515.261(7)	21515.018(-12)
R(25.5)	21514.598(13)	21514.367(-17)
R(26.5)	21513.930(-14)	21513.640(17)
R(27.5)	21513.179(7)	21512.908(20)
R(28.5)	21512.414(5)	21512.145(16)
R(29.5)	21511.626(-11)	21511.356(3)
R(30.5)	21510.787(-13)	21510.525(-6)
R(31.5)	21509.894(2)	
Spectroscopic Constants		
ν_0 (cm^{-1})	21519.6138(18)	21519.3462(24)
B' (cm^{-1})	0.139768(20)	0.139613(19)
r′ (Å)	2.22322(16)	2.22298(15)
B_0'' (cm^{-1})	0.158134(17)	0.157956(19)
r_0'' (Å)	2.09013(11)	2.08992(13)

[a] Residuals in the fit of the data to the form $\nu = \nu_0 + B' J'(J' + 1) - B'' J'' (J'' + 1)$ are provided in parentheses following each line position, in units of 0.001 cm^{-1}. Error limits (1σ) are given in parentheses following each spectroscopic constant, in units of the last quoted digit. All rotationally resolved bands originated from the same lower state (the ground vibronic level). In order to improve the accuracy of the spectroscopic constants, all of the bands were simultaneously fitted under the constraint that they have the same value of B″.

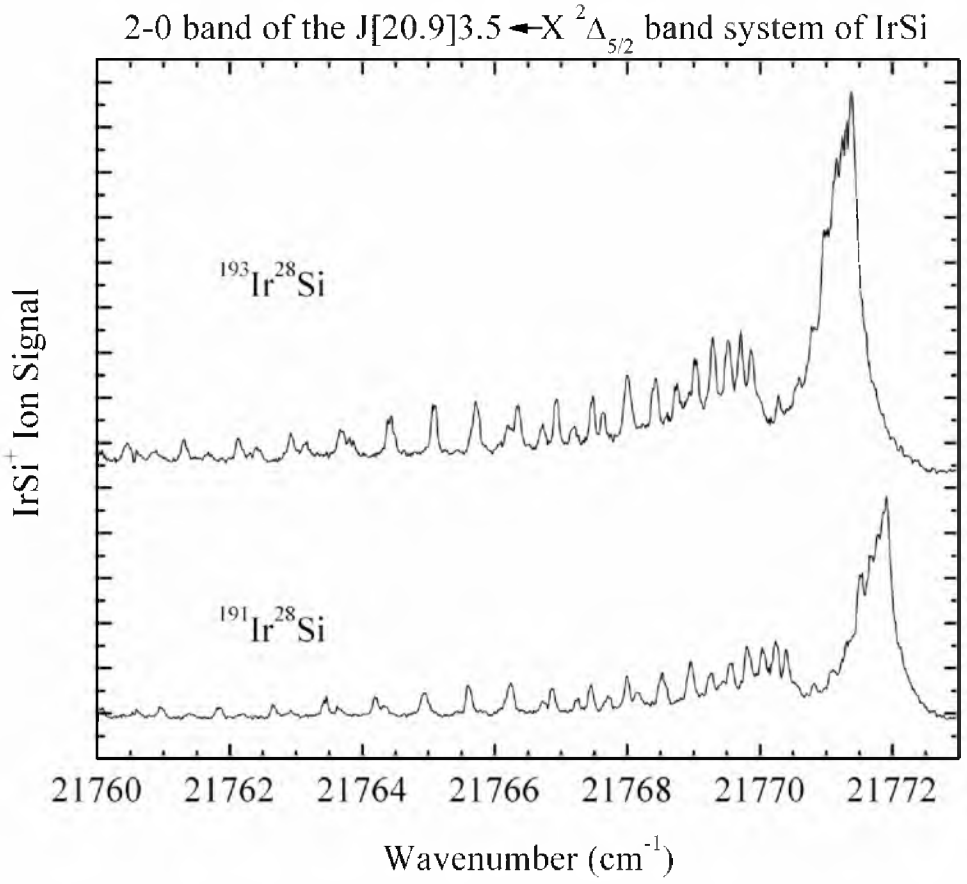

Figure B.43 Rotationally resolved spectra of the 2-0 band of the J[20.9]3.5 ← X $^2\Delta_{5/2}$ band system of IrSi.

Table B.24 Line positions for the 2-0 band of the J[20.9]3.5 ← X $^2\Delta_{5/2}$ band system of IrSi[a]

Line	$^{191}Ir^{28}Si$	$^{193}Ir^{28}Si$
P(4.5)	21768.952(14)	21768.435(19)
P(5.5)	21768.499(-7)	21767.998(-18)
P(6.5)	21767.991(-8)	21767.489(-18)
P(7.5)	21767.440(-1)	21766.933(-6)
P(8.5)	21766.861(-2)	21766.351(-4)
P(9.5)	21766.237(8)	21765.727(6)
P(10.5)	21765.594(2)	21765.096(-12)
P(11.5)	21764.922(-10)	21764.391(8)
P(12.5)	21764.191(1)	21763.687(-8)
P(13.5)	21763.455(-18)	21762.919(5)
P(14.5)	21762.653(-6)	21762.125(9)
P(15.5)	21761.831(-8)	21761.304(4)
P(16.5)	21760.962(2)	21760.434(14)
P(17.5)	21760.061(7)	
Q(3.5)	21770.393(-4)	21769.858(18)
Q(4.5)	21770.226(5)	21769.708(9)
Q(5.5)	21770.030(9)	21769.527(-3)
Q(6.5)	21769.797(13)	21769.280(16)
Q(7.5)	21769.530(18)	21769.030(2)
Q(8.5)	21769.256(-7)	21768.745(-11)
Q(9.5)		21768.388(12)
Q(10.5)	21768.552(-4)	
Q(11.5)	21768.154(-9)	21767.634(-6)
Q(12.5)	21767.714(-7)	21767.197(-8)
Q(13.5)	21767.244(-11)	21766.725(-11)
Q(14.5)	21766.713(12)	21766.200(5)
Q(15.5)		21765.659(1)
Q(16.5)	21765.594(9)	21765.096(-15)
Q(17.5)		21764.477(-11)
Q(18.5)	21764.329(12)	21763.814(3)
Q(19.5)	21763.661(-4)	21763.137(-6)
Q(20.5)	21762.921(18)	21762.403(8)
Q(21.5)	21762.189(-4)	21761.656(-1)
Q(22.5)	21761.402(-6)	21760.867(-1)
Q(23.5)	21760.576(-4)	
R(2.5)	21771.507(-11)	21770.994(-12)

[a] Residuals in the fit of the data to the form $\nu = \nu_0 + B' J'(J' + 1) - B'' J'' (J'' + 1)$ are provided in parentheses following each line position, in units of 0.001 cm^{-1}. Error limits (1σ) are given in parentheses following each spectroscopic constant, in units of the last quoted digit. All rotationally resolved bands originated from the same lower state (the ground vibronic level). In order to improve the accuracy of the spectroscopic constants, all of the bands were simultaneously fitted under the constraint that they have the same value of B″.

Table B.24 (continued)

R(3.5)	21771.667(-12)	21771.153(-14)
R(4.5)	21771.780(-2)	21771.244(18)
R(5.5)	21771.860(6)	21771.352(-2)
R(6.5)	21771.905(14)	
R(12.5)		21770.966(13)
R(13.5)	21771.306(5)	21770.799(-13)
R(14.5)	21771.097(-14)	21770.559(-2)
R(15.5)	21770.816(6)	21770.277(16)
Spectroscopic Constants		
ν_0 (cm^{-1})	21770.6652(23)	21770.1522(28)
B' (cm^{-1})	0.140603(23)	0.140393(18)
r′ (Å)	2.21661(18)	2.21680(14)
B_0'' (cm^{-1})	0.158134(17)	0.157956(19)
r_0'' (Å)	2.09013(11)	2.08992(13)

[a] Residuals in the fit of the data to the form $\nu = \nu_0 + B' J'(J' + 1) - B'' J'' (J'' + 1)$ are provided in parentheses following each line position, in units of 0.001 cm^{-1}. Error limits (1σ) are given in parentheses following each spectroscopic constant, in units of the last quoted digit. All rotationally resolved bands originated from the same lower state (the ground vibronic level). In order to improve the accuracy of the spectroscopic constants, all of the bands were simultaneously fitted under the constraint that they have the same value of B″.

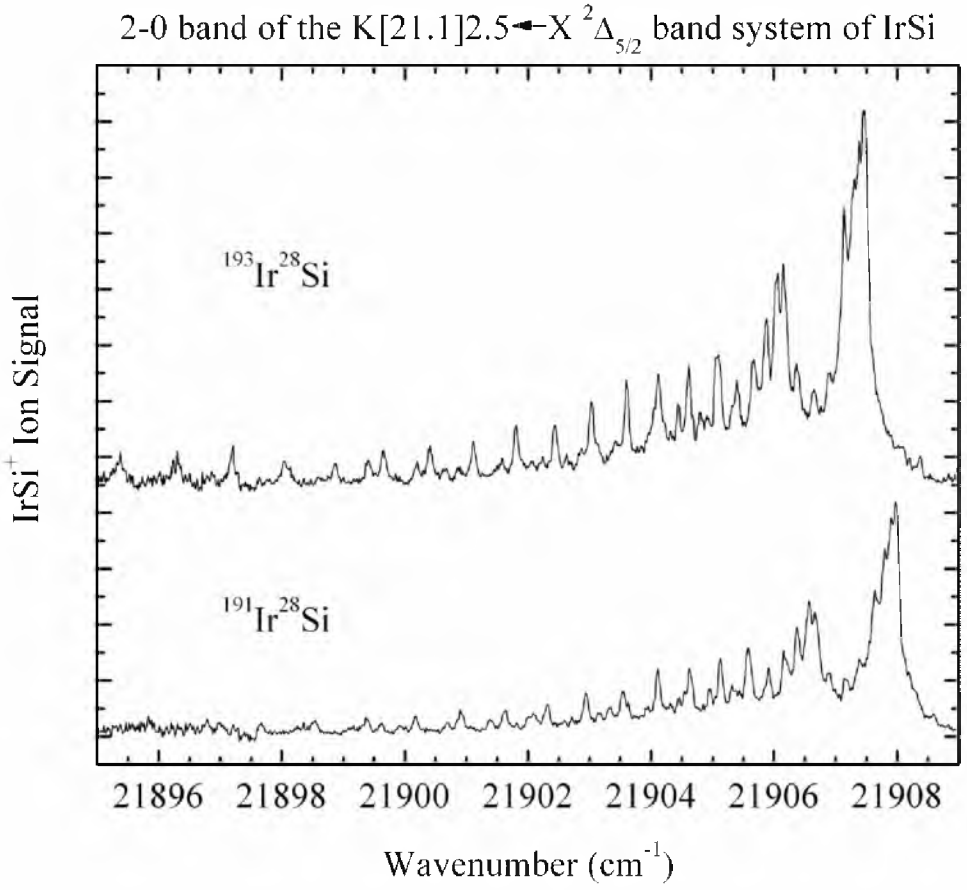

Figure B.44 Rotationally resolved spectra of the 2-0 band of the K[21.1]2.5 ← X $^2\Delta_{5/2}$ band system of IrSi.

Table B.25 Line positions for the 2-0 band of the K[21.1]2.5 ← X $^2\Delta_{5/2}$ band system of IrSi[a]

Line	$^{191}Ir^{28}Si$	$^{193}Ir^{28}Si$
P(3.5)	21905.574(-7)	21905.058(-3)
P(4.5)	21905.126(-8)	21904.615(-8)
P(5.5)	21904.624(7)	21904.120(1)
P(6.5)	21904.107(0)	21903.598(-2)
P(7.5)	21903.540(3)	21903.035(-1)
P(8.5)	21902.939(4)	21902.437(-2)
P(9.5)	21902.323(-19)	21901.807(-11)
P(10.5)	21901.641(-13)	21901.108(12)
P(11.5)	21900.902(11)	21900.410(-3)
P(12.5)	21900.175(-14)	21899.650(6)
P(13.5)	21899.372(-1)	21898.872(-6)
P(14.5)	21898.546(-3)	21898.052(-13)
P(15.5)	21897.666(11)	21897.204(-30)
P(16.5)		21896.291(-20)
Q(2.5)	21906.664(10)	21906.147(14)
Q(3.5)	21906.537(4)	21906.023(5)
Q(4.5)	21906.368(3)	21905.873(-15)
Q(5.5)	21906.160(2)	21905.656(-6)
Q(6.5)	21905.914(1)	21905.389(14)
Q(7.5)		21905.104(15)
Q(8.5)	21905.311(-2)	21904.790(7)
Q(9.5)	21904.959(-10)	21904.442(-5)
Q(10.5)	21904.548(2)	
Q(11.5)	21904.107(8)	
R(2.5)	21907.635(13)	21907.134(1)
R(3.5)	21907.802(-8)	21907.289(-10)
R(4.5)	21907.902(0)	21907.377(11)
R(5.5)	21907.978(-6)	21907.458(-1)
R(12.5)	21907.383(15)	21906.895(-11)
R(13.5)	21907.169(-5)	21906.644(7)
R(14.5)	21906.899(-6)	21906.360(20)
R(15.5)	21906.582(2)	21906.059(12)
R(17.5)		21905.319(20)
R(18.5)		21904.905(12)
R(20.5)	21904.459(9)	
R(21.5)	21903.930(1)	21903.423(-1)
R(22.5)		21902.856(-8)
R(23.5)		21902.234(1)

[a] Residuals in the fit of the data to the form $\nu = \nu_0 + B' J'(J' + 1) - B'' J'' (J'' + 1)$ are provided in parentheses following each line position, in units of 0.001 cm^{-1}. Error limits (1σ) are given in parentheses following each spectroscopic constant, in units of the last quoted digit. All rotationally resolved bands originated from the same lower state (the ground vibronic level). In order to improve the accuracy of the spectroscopic constants, all of the bands were simultaneously fitted under the constraint that they have the same value of B″.

Table B.25 (continued)

R(24.5)	21902.086(6)	21901.584(1)
R(25.5)	21901.389(15)	21900.894(4)
R(26.5)	21900.688(-11)	21900.187(-15)
R(27.5)	21899.926(-13)	21899.401(8)
Spectroscopic Constants		
ν_0 (cm^{-1})	21906.8399(19)	21906.3267(25)
B' (cm^{-1})	0.139174(20)	0.139019(15)
r′ (Å)	2.22796(16)	2.22772(12)
B_0'' (cm^{-1})	0.158134(17)	0.157956(19)
r_0'' (Å)	2.09013(11)	2.08992(13)

[a] Residuals in the fit of the data to the form $\nu = \nu_0 + B' J'(J' + 1) - B'' J'' (J'' + 1)$ are provided in parentheses following each line position, in units of 0.001 cm^{-1}. Error limits (1σ) are given in parentheses following each spectroscopic constant, in units of the last quoted digit. All rotationally resolved bands originated from the same lower state (the ground vibronic level). In order to improve the accuracy of the spectroscopic constants, all of the bands were simultaneously fitted under the constraint that they have the same value of B″.

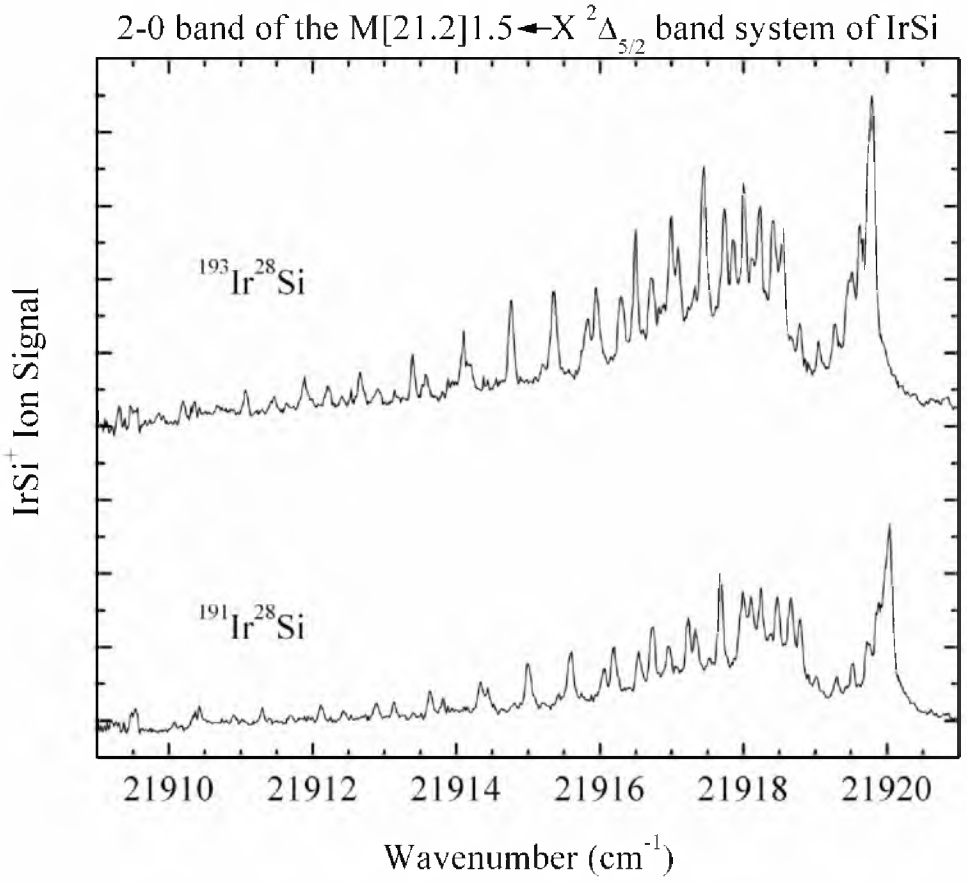

Figure B.45 Rotationally resolved spectra of the 2-0 band of the M[21.2]1.5 ← X $^2\Delta_{5/2}$ band system of IrSi.

Table B.26 Line positions for the 2-0 band of the M[21.2]1.5 ← X $^2\Delta_{5/2}$ band system of IrSi[a]

Line	$^{191}Ir^{28}Si$	$^{193}Ir^{28}Si$
P(2.5)	21918.098(5)	21917.859(2)
P(3.5)	21917.681(5)	21917.452(-8)
P(4.5)	21917.234(-6)	21916.995(-7)
P(5.5)	21916.731(-1)	21916.499(-9)
P(6.5)	21916.194(-2)	21915.952(1)
P(7.5)	21915.604(9)	21915.359(16)
P(8.5)	21914.992(2)	21914.761(-4)
P(9.5)	21914.337(-3)	21914.106(-8)
P(10.5)	21913.635(0)	21913.389(10)
P(11.5)	21912.883(12)	21912.661(-1)
P(12.5)	21912.119(-4)	21911.890(-9)
P(13.5)	21911.300(-6)	21911.061(0)
P(14.5)	21910.422(11)	21910.195(6)
P(15.5)	21909.527(4)	21909.307(-7)
Q(2.5)	21918.788(4)	21918.550(1)
Q(3.5)	21918.666(-14)	21918.411(-2)
Q(4.5)	21918.473(-3)	21918.235(-7)
Q(5.5)	21918.251(-3)	21918.002(4)
Q(6.5)	21917.991(-6)	21917.733(11)
Q(7.5)		21917.452(-10)
Q(8.5)	21917.331(8)	21917.090(9)
Q(9.5)	21916.964(-8)	21916.718(-2)
Q(10.5)	21916.543(-11)	21916.295(-2)
Q(11.5)	21916.064(4)	21915.831(-1)
Q(14.5)	21914.440(-7)	21914.185(12)
Q(15.5)	21913.815(-8)	21913.573(-1)
Q(16.5)	21913.143(-1)	21912.900(7)
Q(17.5)	21912.428(7)	21912.206(-4)
Q(18.5)	21911.691(-3)	21911.465(-9)
Q(19.5)	21910.902(-1)	
Q(20.5)	21910.070(4)	
R(2.5)		21919.512(3)
R(3.5)	21919.878(15)	
R(5.5)	21920.040(1)	21919.790(7)
R(10.5)		21919.464(-2)
R(11.5)	21919.518(-1)	21919.276(-1)

[a] Residuals in the fit of the data to the form $\nu = \nu_0 + B' J'(J' + 1) - B'' J'' (J'' + 1)$ are provided in parentheses following each line position, in units of 0.001 cm^{-1}. Error limits (1σ) are given in parentheses following each spectroscopic constant, in units of the last quoted digit. All rotationally resolved bands originated from the same lower state (the ground vibronic level). In order to improve the accuracy of the spectroscopic constants, all of the bands were simultaneously fitted under the constraint that they have the same value of B''.

Table B.26 (continued)

R(12.5)	21919.298(-10)	21919.043(3)
R(13.5)	21919.011(8)	21918.786(-8)
R(15.5)		21918.111(9)
Spectroscopic Constants		
ν_0 (cm^{-1})	21918.9692(18)	21918.7268(19)
B' (cm^{-1})	0.137950(34)	0.137802(31)
r′ (Å)	2.23782(28)	2.23754(25)
B_0'' (cm^{-1})	0.158134(17)	0.157956(19)
r_0'' (Å)	2.09013(11)	2.08992(13)

[a] Residuals in the fit of the data to the form $\nu = \nu_0 + B' J'(J' + 1) - B'' J'' (J'' + 1)$ are provided in parentheses following each line position, in units of 0.001 cm^{-1}. Error limits (1σ) are given in parentheses following each spectroscopic constant, in units of the last quoted digit. All rotationally resolved bands originated from the same lower state (the ground vibronic level). In order to improve the accuracy of the spectroscopic constants, all of the bands were simultaneously fitted under the constraint that they have the same value of B″.

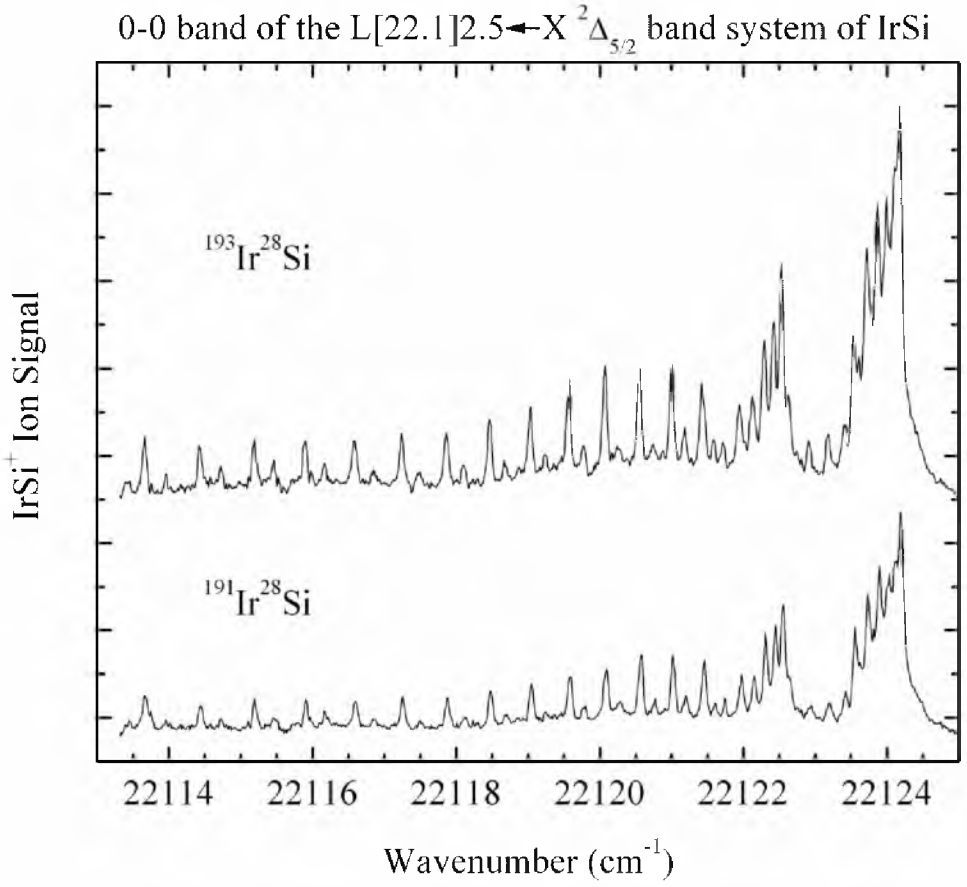

Figure B.46 Rotationally resolved spectra of the 0-0 band of the L[22.1]2.5 ← X $^2\Delta_{5/2}$ band system of IrSi.

Table B.27 Line positions for the 0-0 band of the L[22.1]2.5 ← X $^2\Delta_{5/2}$ band system of IrSi[a]

Line	$^{191}Ir^{28}Si$	$^{193}Ir^{28}Si$
P(3.5)	22121.458(-10)	22121.424(2)
P(4.5)	22121.018(9)	22121.002(5)
P(5.5)	22120.584(-5)	22120.558(0)
P(6.5)	22120.096(3)	22120.075(4)
P(7.5)	22119.593(-2)	22119.574(-3)
P(8.5)	22119.051(2)	22119.039(-5)
P(9.5)	22118.480(5)	22118.458(9)
P(10.5)	22117.880(7)	22117.860(10)
P(11.5)	22117.254(6)	22117.241(3)
P(12.5)	22116.596(7)	22116.579(9)
P(13.5)	22115.912(5)	22115.901(2)
P(14.5)	22115.189(12)	22115.183(5)
P(15.5)	22114.441(14)	22114.417(26)
P(16.5)	22113.645(35)	22113.668(2)
Q(2.5)	22122.562(-7)	22122.528(4)
Q(3.5)	22122.442(9)	22122.427(2)
Q(4.5)	22122.306(12)	22122.297(-2)
Q(5.5)	22122.152(3)	22122.129(4)
Q(6.5)	22121.977(-15)	22121.942(-1)
Q(7.5)	22121.751(-11)	22121.716(3)
Q(9.5)	22121.195(12)	
Q(10.5)		22120.873(4)
R(2.5)	22123.555(3)	22123.537(-3)
R(3.5)	22123.735(6)	22123.715(2)
R(4.5)	22123.897(-2)	22123.871(-1)
R(5.5)	22124.032(-14)	22123.995(-1)
R(6.5)	22124.120(-7)	22124.118(-29)
R(7.5)	22124.194(-17)	22124.176(-23)
R(15.5)		22123.608(-1)
R(16.5)	22123.432(-6)	22123.417(-11)
R(17.5)	22123.207(-12)	22123.183(-8)
R(18.5)	22122.942(-9)	22122.907(8)
R(19.5)		22122.625(0)
R(22.5)	22121.609(-16)	22121.590(-12)
R(23.5)	22121.195(-12)	22121.187(-18)
R(24.5)	22120.771(-26)	22120.730(2)

[a] Residuals in the fit of the data to the form $\nu = \nu_0 + B' J'(J' + 1) - B'' J'' (J'' + 1)$ are provided in parentheses following each line position, in units of 0.001 cm^{-1}. Error limits (1σ) are given in parentheses following each spectroscopic constant, in units of the last quoted digit. All rotationally resolved bands originated from the same lower state (the ground vibronic level). In order to improve the accuracy of the spectroscopic constants, all of the bands were simultaneously fitted under the constraint that they have the same value of B''.

Table B.27 (continued)

R(25.5)	22120.279(-2)	22120.262(3)
R(26.5)	22119.780(-2)	22119.769(-1)
R(27.5)	22119.235(16)	22119.244(-2)
R(28.5)	22118.689(5)	22118.666(21)
R(29.5)	22118.123(-17)	22118.107(-6)
R(30.5)	22117.495(-5)	22117.491(-5)
R(31.5)	22116.851(-6)	22116.855(-13)
R(32.5)	22116.159(9)	22116.167(0)
R(33.5)	22115.457(7)	22115.466(-2)
R(34.5)	22114.721(8)	22114.719(11)
R(35.5)	22113.956(8)	22113.963(5)
Spectroscopic Constants		
ν_0 (cm^{-1})	22122.6843(23)	22122.6612(19)
B' (cm^{-1})	0.143329(26)	0.143181(23)
r′ (Å)	2.19543(20)	2.19511(18)
B_0'' (cm^{-1})	0.158134(17)	0.157956(19)
r_0'' (Å)	2.09013(11)	2.08992(13)

[a] Residuals in the fit of the data to the form $\nu = \nu_0 + B' J'(J' + 1) - B'' J'' (J'' + 1)$ are provided in parentheses following each line position, in units of 0.001 cm^{-1}. Error limits (1σ) are given in parentheses following each spectroscopic constant, in units of the last quoted digit. All rotationally resolved bands originated from the same lower state (the ground vibronic level). In order to improve the accuracy of the spectroscopic constants, all of the bands were simultaneously fitted under the constraint that they have the same value of B″.

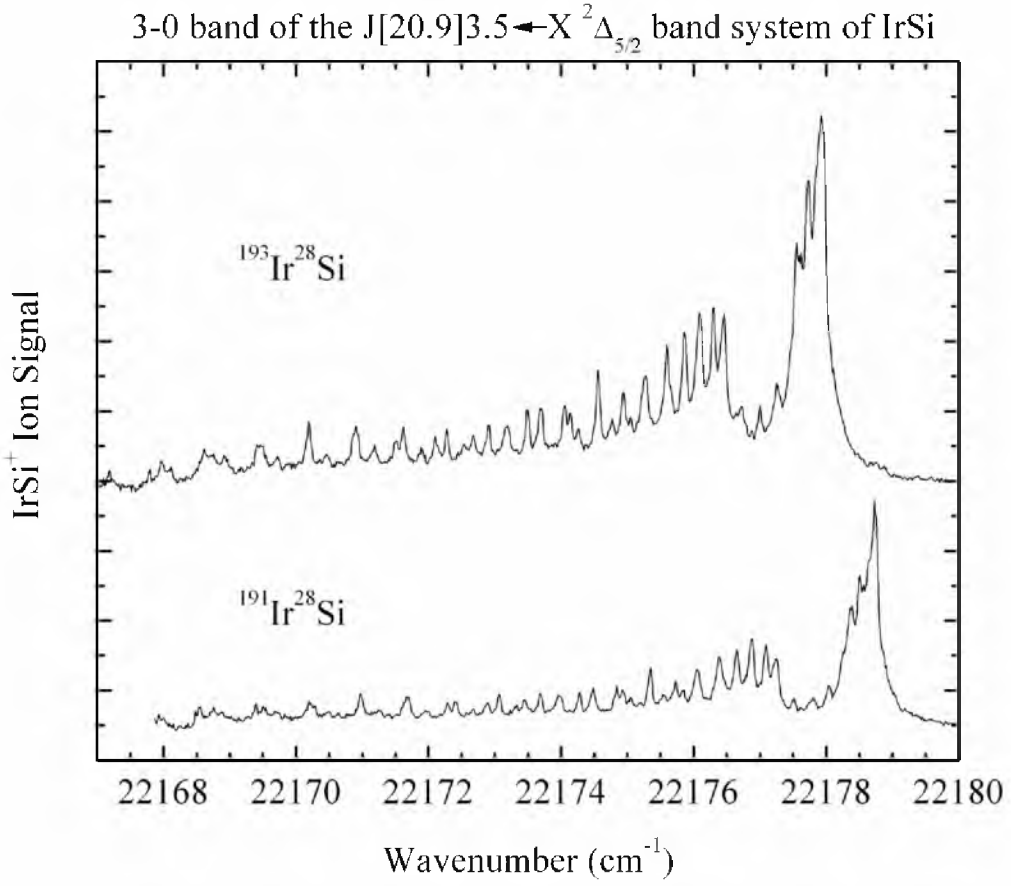

Figure B.47 Rotationally resolved spectra of the 3-0 band of the J[20.9]3.5 ← X $^2\Delta_{5/2}$ band system of IrSi.

Table B.28 Line positions for the 3-0 band of the J[20.9]3.5 ← X $^2\Delta_{5/2}$ band system of IrSi[a]

Line	$^{191}Ir^{28}Si$	$^{193}Ir^{28}Si$
P(4.5)	22175.835(-1)	22175.044(-2)
P(5.5)	22175.354(0)	22174.557(6)
P(6.5)	22174.836(1)	22174.059(-12)
P(7.5)	22174.280(4)	22173.487(8)
P(8.5)	22173.688(8)	22172.905(1)
P(9.5)	22173.066(3)	22172.278(4)
P(10.5)	22172.404(4)	22171.618(3)
P(11.5)		22170.912(12)
P(12.5)	22170.976(-2)	22170.189(1)
P(13.5)	22170.194(9)	22169.417(3)
P(14.5)	22169.399(-4)	22168.613(0)
P(15.5)	22168.541(10)	
Q(3.5)	22177.252(6)	22176.464(0)
Q(4.5)	22177.091(3)	22176.296(4)
Q(5.5)	22176.883(11)	22176.088(13)
Q(6.5)	22176.655(2)	22175.861(3)
Q(7.5)	22176.388(-4)	22175.595(-3)
Q(8.5)	22176.054(20)	22175.270(13)
Q(9.5)	22175.732(-4)	22174.939(-1)
Q(10.5)	22175.354(-8)	22174.557(-1)
Q(11.5)	22174.926(1)	22174.140(-2)
Q(12.5)	22174.487(-14)	22173.700(-16)
Q(13.5)	22173.960(21)	22173.187(7)
Q(14.5)	22173.448(6)	22172.677(-10)
Q(15.5)	22172.892(-2)	22172.100(5)
Q(16.5)	22172.286(3)	22171.496(9)
Q(17.5)	22171.670(-18)	
Q(18.5)	22170.976(2)	22170.189(8)
Q(19.5)	22170.287(-18)	22169.476(12)
Q(20.5)	22169.504(19)	22168.754(-11)
Q(21.5)	22168.748(-8)	22167.961(1)
Q(22.5)	22167.916(6)	
R(3.5)	22178.507(10)	22177.733(-11)
R(4.5)	22178.652(-19)	22177.858(-20)
R(5.5)	22178.730(-17)	22177.928(-10)
R(10.5)	22178.566(-1)	

[a] Residuals in the fit of the data to the form $\nu = \nu_0 + B' J'(J' + 1) - B'' J'' (J'' + 1)$ are provided in parentheses following each line position, in units of 0.001 cm^{-1}. Error limits (1σ) are given in parentheses following each spectroscopic constant, in units of the last quoted digit. All rotationally resolved bands originated from the same lower state (the ground vibronic level). In order to improve the accuracy of the spectroscopic constants, all of the bands were simultaneously fitted under the constraint that they have the same value of B″.

Table B.28 (continued)

R(11.5)		22177.625(8)
R(12.5)	22178.255(-4)	
R(13.5)	22178.042(-3)	22177.256(-8)
R(14.5)	22177.801(-10)	22176.999(2)
R(15.5)	22177.506(1)	22176.714(4)
R(20.5)	22175.548(-8)	22174.774(-20)
R(21.5)	22175.053(-16)	22174.259(-6)
R(24.5)	22173.334(-23)	22172.540(-10)
R(25.5)	22172.674(-11)	22171.897(-14)
R(26.5)		22171.182(18)
R(27.5)	22171.248(9)	
R(28.5)	22170.482(17)	22169.722(4)
R(29.5)	22169.687(18)	22168.917(16)
R(30.5)	22168.878(-3)	22168.116(-12)
Spectroscopic Constants		
ν_0 (cm^{-1})	22177.5440(23)	22176.7500(20)
B' (cm^{-1})	0.139935(19)	0.139791(17)
r′ (Å)	2.22189(15)	2.22156(14)
B_0'' (cm^{-1})	0.158134(17)	0.157956(19)
r_0'' (Å)	2.09013(11)	2.08992(13)

[a] Residuals in the fit of the data to the form $\nu = \nu_0 + B' J'(J' + 1) - B'' J'' (J'' + 1)$ are provided in parentheses following each line position, in units of 0.001 cm^{-1}. Error limits (1σ) are given in parentheses following each spectroscopic constant, in units of the last quoted digit. All rotationally resolved bands originated from the same lower state (the ground vibronic level). In order to improve the accuracy of the spectroscopic constants, all of the bands were simultaneously fitted under the constraint that they have the same value of B″.

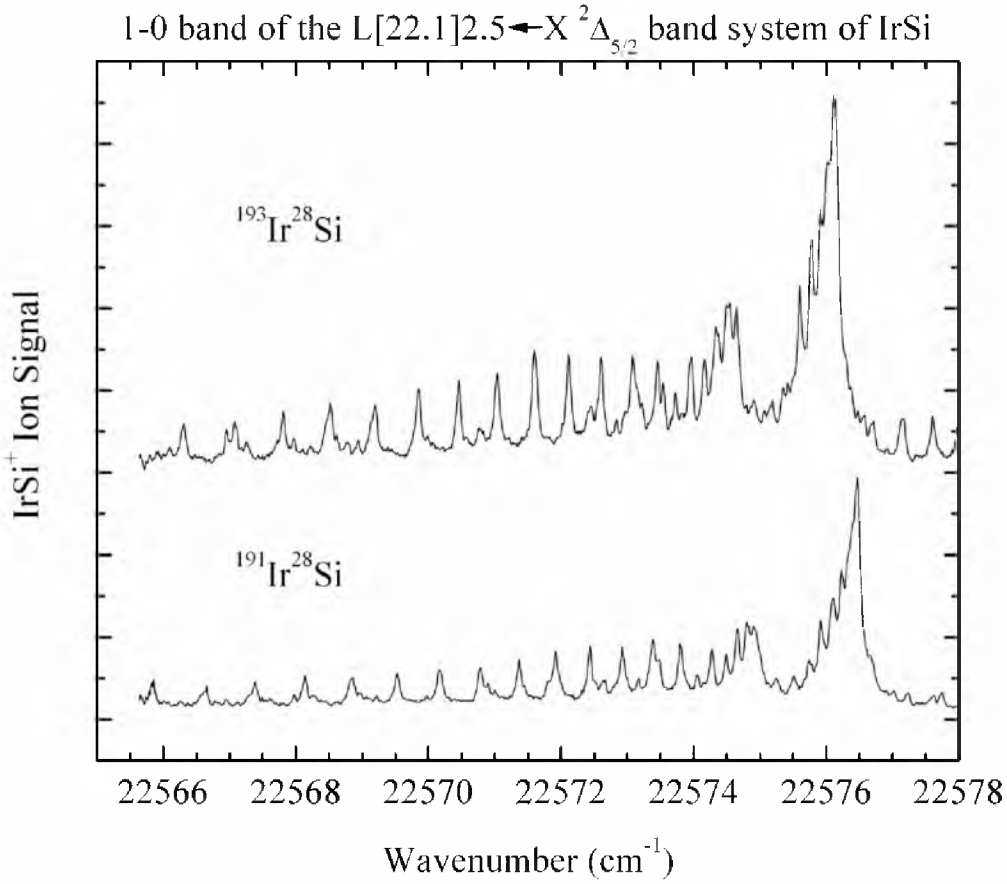

Figure B.48 Rotationally resolved spectra of the 1-0 band of the L[22.1]2.5 ← X $^2\Delta_{5/2}$ band system of IrSi. The features to the high wavenumber side of the R band head are P lines of the J[20.9]3.5 ← X $^2\Delta_{5/2}$ 4-0 band.

Table B.29 Line positions for the 1-0 band of the L[22.1]2.5 ← X $^2\Delta_{5/2}$ band system of IrSi[a]

Line	$^{191}Ir^{28}Si$	$^{193}Ir^{28}Si$
P(3.5)	22573.798(12)	
P(4.5)	22573.392(-8)	22573.084(-17)
P(5.5)	22572.922(5)	22572.607(2)
P(6.5)	22572.436(2)	22572.114(6)
P(7.5)	22571.923(-6)	22571.597(1)
P(8.5)	22571.369(-2)	22571.038(8)
P(9.5)	22570.781(2)	22570.457(5)
P(10.5)	22570.173(-4)	22569.851(-5)
P(11.5)	22569.531(-7)	22569.195(5)
P(12.5)	22568.860(-13)	22568.520(1)
P(13.5)	22568.134(5)	22567.808(3)
P(14.5)	22567.380(19)	22567.076(-6)
P(15.5)	22566.651(-23)	22566.300(-3)
P(16.5)	22565.842(-17)	
Q(2.5)	22574.905(12)	
Q(3.5)	22574.804(3)	22574.499(-11)
Q(4.5)	22574.662(4)	22574.347(-1)
Q(5.5)	22574.496(-2)	22574.171(2)
Q(6.5)	22574.276(14)	22573.961(7)
Q(7.5)	22574.057(-3)	22573.723(9)
Q(8.5)		22573.454(10)
Q(9.5)	22573.483(7)	
Q(10.5)	22573.171(-10)	22572.838(-5)
Q(11.5)		22572.456(15)
Q(17.5)	22569.975(3)	
R(2.5)	22575.913(1)	22575.603(-9)
R(3.5)	22576.104(-15)	22575.773(-5)
R(4.5)	22576.228(5)	22575.919(-9)
R(5.5)		22576.014(7)
R(7.5)	22576.470(6)	
R(13.5)		22575.773(1)
R(15.5)	22575.739(6)	
R(16.5)	22575.515(-3)	
R(17.5)	22575.244(5)	22574.903(-8)
R(27.5)	22570.899(-14)	

[a] Residuals in the fit of the data to the form $\nu = \nu_0 + B' J'(J' + 1) - B'' J'' (J'' + 1)$ are provided in parentheses following each line position, in units of 0.001 cm^{-1}. Error limits (1σ) are given in parentheses following each spectroscopic constant, in units of the last quoted digit. All rotationally resolved bands originated from the same lower state (the ground vibronic level). In order to improve the accuracy of the spectroscopic constants, all of the bands were simultaneously fitted under the constraint that they have the same value of B''.

Table B.29 (continued)

R(30.5)	22568.951(14)	
R(31.5)	22568.245(17)	
R(33.5)	22566.776(-14)	
Spectroscopic Constants		
ν_0 (cm^{-1})	22575.0541(22)	22574.7361(23)
B' (cm^{-1})	0.142455(19)	0.142194(27)
r′ (Å)	2.20215(15)	2.20271(21)
B_0'' (cm^{-1})	0.158134(17)	0.157956(19)
r_0'' (Å)	2.09013(11)	2.08992(13)

[a] Residuals in the fit of the data to the form $\nu = \nu_0 + B' J'(J' + 1) - B'' J'' (J'' + 1)$ are provided in parentheses following each line position, in units of 0.001 cm^{-1}. Error limits (1σ) are given in parentheses following each spectroscopic constant, in units of the last quoted digit. All rotationally resolved bands originated from the same lower state (the ground vibronic level). In order to improve the accuracy of the spectroscopic constants, all of the bands were simultaneously fitted under the constraint that they have the same value of B″.

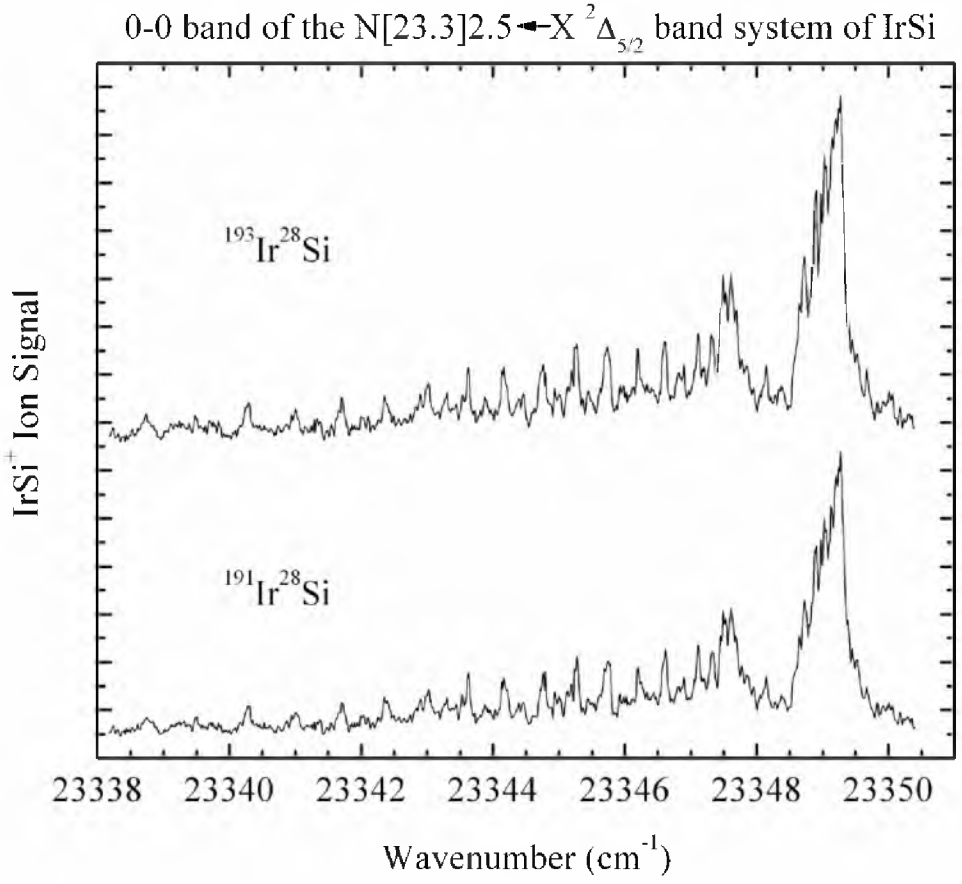

Figure B.49 Rotationally resolved spectra of the 0-0 band of the N[23.3]2.5 ← X $^2\Delta_{5/2}$ band system of IrSi.

Table B.30 Line positions for the 0-0 band of the N[23.3]2.5 ← X $^2\Delta_{5/2}$ band system of IrSi[a]

Line	$^{191}Ir^{28}Si$	$^{193}Ir^{28}Si$
P(3.5)	23346.606(19)	23346.602(15)
P(4.5)	23346.198(2)	23346.198(-4)
P(5.5)	23345.736(9)	23345.727(12)
P(6.5)	23345.267(-8)	23345.259(-6)
P(7.5)	23344.758(-15)	23344.750(-13)
P(8.5)	23344.184(11)	23344.174(16)
P(9.5)	23343.623(-7)	23343.623(-11)
P(10.5)	23343.005(1)	23343.003(0)
P(11.5)	23342.383(-17)	23342.367(-4)
P(12.5)	23341.712(-17)	23341.709(-16)
P(13.5)	23341.016(-24)	23341.006(-15)
P(14.5)	23340.283(-23)	23340.274(-15)
P(15.5)		23339.489(8)
P(16.5)	23338.742(-41)	23338.733(-30)
Q(3.5)	23347.616(8)	23347.614(1)
Q(4.5)	23347.473(12)	23347.482(-6)
Q(5.5)	23347.324(-9)	23347.317(-10)
Q(6.5)	23347.110(5)	23347.110(-4)
Q(7.5)	23346.894(-11)	23346.891(-16)
Q(8.5)	23346.606(15)	23346.602(11)
Q(10.5)		23345.978(19)
Q(11.5)		23345.622(19)
R(2.5)	23348.732(-1)	23348.720(1)
R(3.5)	23348.890(18)	23348.891(7)
R(4.5)	23349.041(13)	23349.040(4)
R(5.5)		23349.144(16)
R(6.5)		23349.247(-2)
R(13.5)	23348.973(11)	
R(16.5)	23348.388(17)	23348.383(13)
R(17.5)	23348.146(4)	23348.143(-2)
R(18.5)	23347.861(3)	23347.851(5)
R(19.5)	23347.530(17)	23347.533(7)
R(20.5)	23347.195(6)	23347.193(0)
R(21.5)	23346.813(9)	23346.814(2)
R(22.5)	23346.425(-12)	
R(25.5)	23345.002(-2)	

[a] Residuals in the fit of the data to the form $\nu = \nu_0 + B' J'(J' + 1) - B'' J'' (J'' + 1)$ are provided in parentheses following each line position, in units of 0.001 cm^{-1}. Error limits (1σ) are given in parentheses following each spectroscopic constant, in units of the last quoted digit. All rotationally resolved bands originated from the same lower state (the ground vibronic level). In order to improve the accuracy of the spectroscopic constants, all of the bands were simultaneously fitted under the constraint that they have the same value of B″.

Table B.30 (continued)

R(26.5)	23344.461(6)	
Spectroscopic Constants		
ν_0 (cm^{-1})	23347.8670(35)	23347.8577(29)
B' (cm^{-1})	0.142699(19)	0.142541(25)
r′ (Å)	2.20027(15)	2.20003(19)
B_0'' (cm^{-1})	0.158134(17)	0.157956(19)
r_0'' (Å)	2.09013(11)	2.08992(13)

[a] Residuals in the fit of the data to the form $\nu = \nu_0 + B' J'(J' + 1) - B'' J'' (J'' + 1)$ are provided in parentheses following each line position, in units of 0.001 cm^{-1}. Error limits (1σ) are given in parentheses following each spectroscopic constant, in units of the last quoted digit. All rotationally resolved bands originated from the same lower state (the ground vibronic level). In order to improve the accuracy of the spectroscopic constants, all of the bands were simultaneously fitted under the constraint that they have the same value of B″.

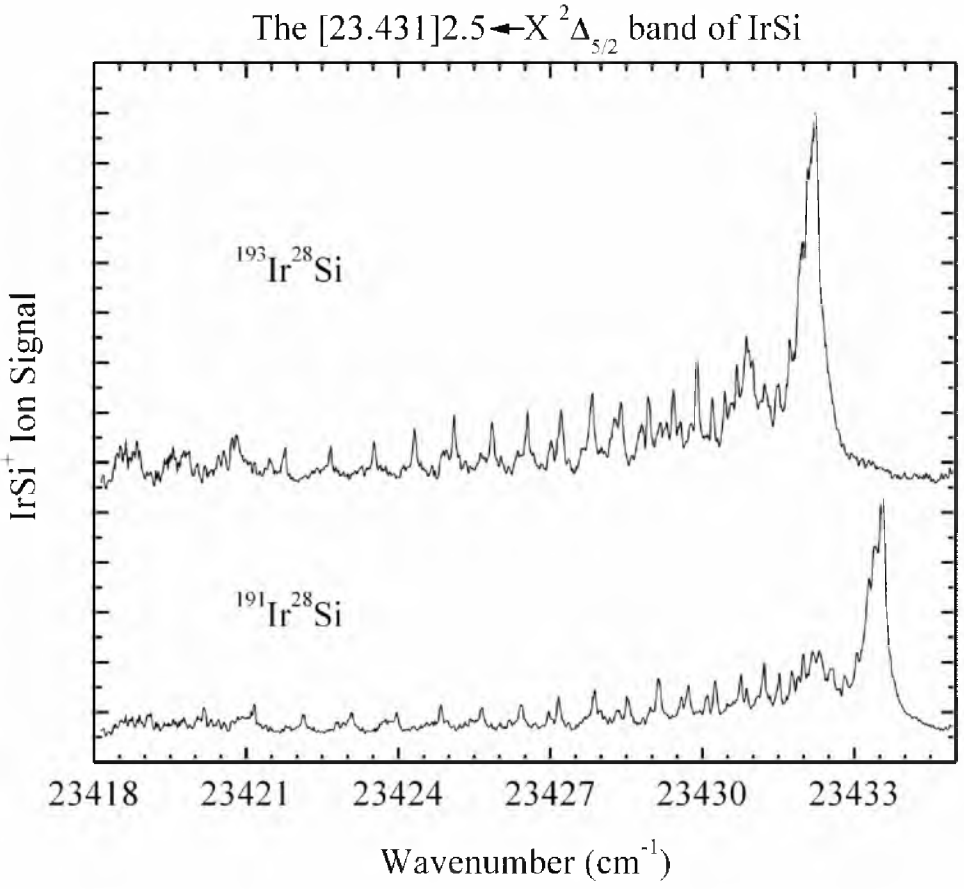

Figure B.50 Rotationally resolved spectra of the [23.431]2.5 ← X $^2\Delta_{5/2}$ band of IrSi.

Table B.31 Line positions for the [23.431]2.5 ← X $^2\Delta_{5/2}$ band of IrSi[a]

Line	$^{191}Ir^{28}Si$	$^{193}Ir^{28}Si$
P(3.5)	23431.223(-9)	23429.893(-3)
P(4.5)	23430.759(-2)	23429.428(6)
P(5.5)	23430.255(5)	23428.940(-3)
P(6.5)	23429.719(2)	23428.393(6)
P(7.5)	23429.136(8)	23427.821(2)
P(8.5)	23428.528(-3)	23427.212(-7)
P(9.5)	23427.867(0)	23426.549(-2)
P(10.5)	23427.160(8)	23425.853(-4)
P(11.5)	23426.426(3)	23425.101(10)
P(12.5)	23425.644(6)	23424.318(15)
P(13.5)	23424.838(-7)	23423.520(-6)
P(14.5)	23423.966(5)	23422.660(-4)
P(15.5)	23423.078(-7)	23421.763(-6)
P(16.5)	23422.128(3)	
P(17.5)	23421.162(-12)	
P(19.5)	23419.084(-16)	
Q(2.5)	23432.313(8)	23430.981(15)
Q(3.5)	23432.187(-7)	23430.875(-20)
Q(4.5)	23431.992(6)	23430.680(-5)
Q(5.5)	23431.768(9)	23430.444(10)
Q(6.5)	23431.517(-1)	23430.198(-6)
Q(7.5)	23431.223(-9)	23429.893(-3)
Q(8.5)	23430.873(-1)	23429.567(-18)
Q(9.5)	23430.490(-1)	23429.165(1)
Q(10.5)	23430.092(-26)	
Q(11.5)	23429.584(19)	23428.274(8)
Q(14.5)	23427.981(-8)	
Q(15.5)	23427.356(-6)	23426.020(10)
Q(16.5)	23426.691(-6)	
R(11.5)	23433.055(-2)	23431.727(1)
R(12.5)	23432.812(14)	23431.492(9)
R(13.5)	23432.544(15)	23431.230(4)
R(14.5)		23430.916(10)
R(15.5)	23431.890(14)	23430.583(-4)
R(17.5)	23431.091(-4)	
R(18.5)		23429.292(3)
R(19.5)		23428.804(-19)

[a] Residuals in the fit of the data to the form $\nu = \nu_0 + B' J'(J' + 1) - B'' J'' (J'' + 1)$ are provided in parentheses following each line position, in units of 0.001 cm^{-1}. Error limits (1σ) are given in parentheses following each spectroscopic constant, in units of the last quoted digit. All rotationally resolved bands originated from the same lower state (the ground vibronic level). In order to improve the accuracy of the spectroscopic constants, all of the bands were simultaneously fitted under the constraint that they have the same value of B″.

Table B.31 (continued)

R(21.5)	23428.986(-16)	23427.643(5)
R(22.5)	23428.333(7)	23427.015(4)
R(23.5)		23426.355(-5)
R(24.5)	23426.964(-5)	23425.634(6)
R(25.5)	23426.194(15)	23424.888(2)
R(26.5)	23425.427(-9)	23424.111(-11)
R(27.5)		23423.279(-9)
R(28.5)	23423.723(-7)	23422.398(2)
R(29.5)	23422.790(15)	23421.479(10)
Spectroscopic Constants		
ν_0 (cm^{-1})	23432.4970(22)	23431.1720(20)
B' (cm^{-1})	0.138005(18)	0.137848(22)
r′ (Å)	2.23738(15)	2.23716(18)
B_0'' (cm^{-1})	0.158134(17)	0.157956(19)
r_0'' (Å)	2.09013(11)	2.08992(13)

[a] Residuals in the fit of the data to the form $\nu = \nu_0 + B' J'(J' + 1) - B'' J'' (J'' + 1)$ are provided in parentheses following each line position, in units of 0.001 cm^{-1}. Error limits (1σ) are given in parentheses following each spectroscopic constant, in units of the last quoted digit. All rotationally resolved bands originated from the same lower state (the ground vibronic level). In order to improve the accuracy of the spectroscopic constants, all of the bands were simultaneously fitted under the constraint that they have the same value of B″.

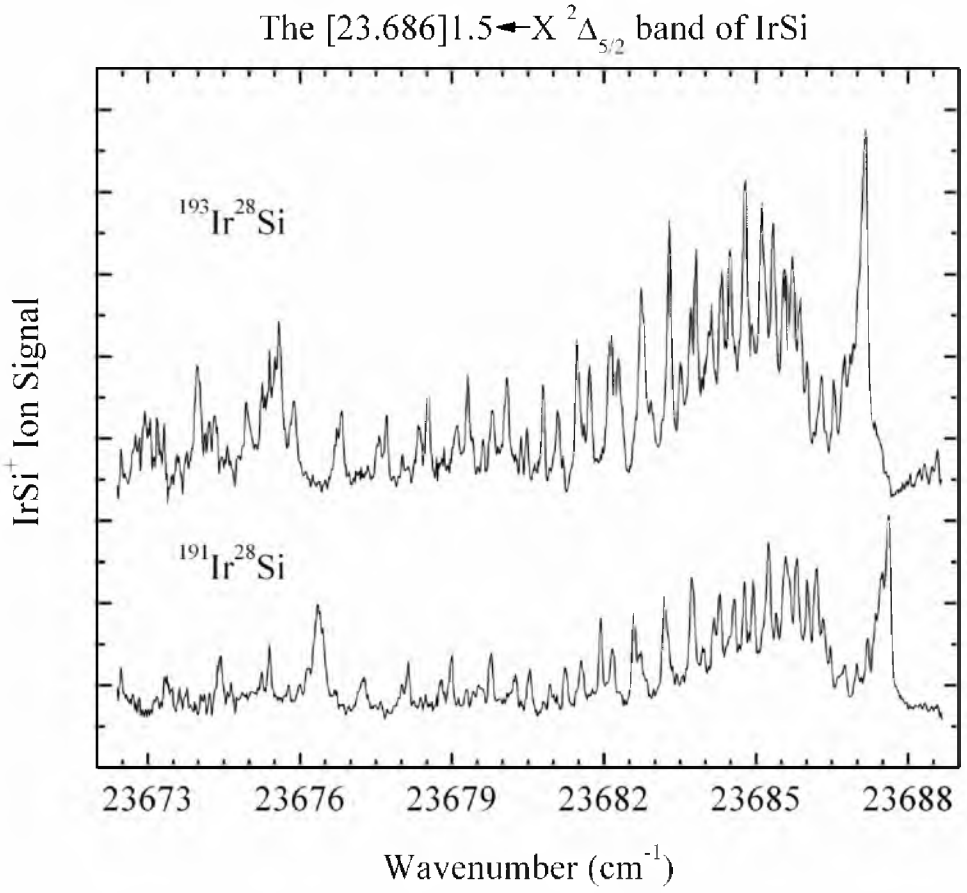

Figure B.51 Rotationally resolved spectra of the [23.686]1.5 ← X $^2\Delta_{5/2}$ band of IrSi.

Table B.32 Line positions for the [23.686]1.5 ← X $^2\Delta_{5/2}$ band of IrSi[a]

Line	$^{191}Ir^{28}Si$	$^{193}Ir^{28}Si$
P(2.5)	23685.646(-10)	
P(3.5)		23684.785(-17)
P(4.5)	23684.770(1)	23684.316(2)
P(5.5)	23684.284(-2)	23683.810(18)
P(6.5)	23683.746(8)	23683.291(10)
P(7.5)	23683.196(-9)	23682.743(-9)
P(8.5)	23682.593(-12)	23682.127(2)
P(9.5)	23681.937(0)	23681.473(13)
P(10.5)	23681.237(18)	23680.800(4)
P(11.5)	23680.534(-1)	23680.086(-3)
P(12.5)	23679.770(4)	23679.316(8)
P(13.5)	23678.990(-14)	23678.536(-10)
P(14.5)	23678.137(2)	23677.706(-16)
P(15.5)	23677.251(12)	23676.822(-7)
P(17.5)	23675.404(-7)	23674.948(2)
P(18.5)	23674.427(-21)	23673.982(-22)
P(19.5)		23672.948(-17)
Q(2.5)	23686.324(6)	23685.866(8)
Q(3.5)	23686.193(2)	23685.720(19)
Q(4.5)	23686.014(7)	23685.561(5)
Q(5.5)	23685.800(10)	23685.338(16)
Q(6.5)	23685.568(-10)	23685.113(-9)
Q(8.5)	23684.946(-4)	23684.486(1)
Q(9.5)	23684.570(6)	23684.107(14)
Q(10.5)	23684.172(-1)	23683.712(4)
Q(11.5)	23683.746(-19)	23683.291(-18)
Q(13.5)	23682.725(-1)	23682.284(-13)
Q(14.5)	23682.175(-10)	23681.716(-4)
Q(15.5)	23681.549(19)	
Q(16.5)	23680.933(-2)	23680.478(1)
Q(17.5)	23680.251(6)	23679.798(7)
Q(18.5)		23679.097(-6)
Q(19.5)	23678.782(10)	23678.354(-14)
Q(20.5)	23678.018(-17)	23677.561(-12)
Q(21.5)		23676.736(-15)
Q(23.5)		23674.948(0)
R(10.5)	23687.359(5)	

[a] Residuals in the fit of the data to the form $\nu = \nu_0 + B' J'(J' + 1) - B'' J'' (J'' + 1)$ are provided in parentheses following each line position, in units of 0.001 cm^{-1}. Error limits (1σ) are given in parentheses following each spectroscopic constant, in units of the last quoted digit. All rotationally resolved bands originated from the same lower state (the ground vibronic level). In order to improve the accuracy of the spectroscopic constants, all of the bands were simultaneously fitted under the constraint that they have the same value of B″.

Table B.32 (continued)

R(11.5)	23687.200(-2)	23686.743(-3)
R(12.5)	23686.986(8)	23686.539(-4)
R(13.5)	23686.744(7)	23686.294(-1)
R(14.5)	23686.467(3)	23686.009(2)
R(17.5)	23685.402(-7)	23684.927(9)
R(20.5)	23683.958(14)	23683.513(0)
R(21.5)		23682.937(25)
R(25.5)		23680.362(10)
R(26.5)		23679.611(17)
R(28.5)		23678.024(1)
Spectroscopic Constants		
ν_0 (cm^{-1})	23686.4986(27)	23686.0427(26)
B' (cm^{-1})	0.138855(25)	0.138687(25)
r′ (Å)	2.23052(20)	2.23039(20)
B_0'' (cm^{-1})	0.158134(17)	0.157956(19)
r_0'' (Å)	2.09013(11)	2.08992(13)

[a] Residuals in the fit of the data to the form $\nu = \nu_0 + B' J'(J' + 1) - B'' J'' (J'' + 1)$ are provided in parentheses following each line position, in units of 0.001 cm^{-1}. Error limits (1σ) are given in parentheses following each spectroscopic constant, in units of the last quoted digit. All rotationally resolved bands originated from the same lower state (the ground vibronic level). In order to improve the accuracy of the spectroscopic constants, all of the bands were simultaneously fitted under the constraint that they have the same value of B″.

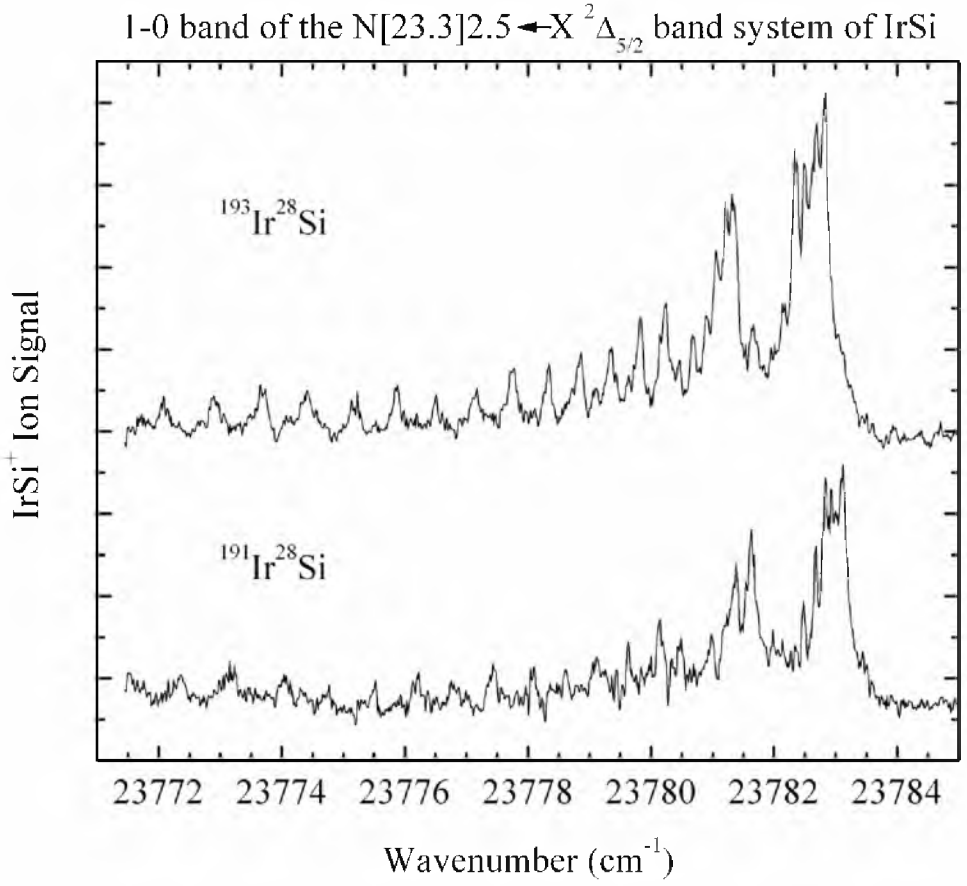

Figure B.52 Rotationally resolved spectra of the 1-0 band of the N[23.3]2.5 ← X $^2\Delta_{5/2}$ band system of IrSi.

Table B.33 Line positions for the 1-0 band of the N [23.3]2.5 ← X $2\Delta_{5/2}$ band system of IrSi[a]

Line	$^{191}Ir^{28}Si$	$^{193}Ir^{28}Si$
P(3.5)	23780.540(8)	23780.229(16)
P(4.5)	23780.119(-1)	23779.832(-19)
P(5.5)	23779.664(-11)	23779.353(-5)
P(6.5)	23779.158(-2)	23778.855(-5)
P(7.5)	23778.624(1)	23778.338(-19)
P(8.5)	23778.071(-9)	23777.751(4)
P(9.5)	23777.454(12)	23777.163(-6)
P(10.5)	23776.835(1)	23776.510(16)
P(11.5)	23776.186(-11)	23775.871(-7)
P(12.5)	23775.485(-5)	23775.156(11)
P(13.5)	23774.739(13)	23774.421(16)
P(14.5)	23774.019(-28)	23773.689(-16)
P(15.5)	23773.195(2)	23772.887(-9)
P(16.5)	23772.352(19)	23772.074(-26)
P(17.5)	23771.535(-24)	
Q(2.5)	23781.659(-3)	23781.357(-7)
Q(3.5)	23781.542(-1)	23781.217(17)
Q(4.5)	23781.389(3)	23781.075(11)
Q(5.5)	23781.217(-6)	23780.908(-4)
Q(6.5)	23781.009(-12)	23780.683(6)
Q(7.5)		23780.454(-14)
Q(8.5)	23780.475(-5)	23780.151(7)
Q(9.5)	23780.158(0)	23779.832(12)
Q(10.5)		
Q(11.5)	23779.434(-1)	23779.111(4)
Q(12.5)		23778.716(-14)
Q(13.5)		23778.266(-12)
Q(18.5)		23775.507(15)
R(2.5)	23782.644(3)	23782.351(-11)
R(3.5)	23782.801(15)	23782.496(12)
R(4.5)	23782.942(8)	23782.629(12)
R(12.5)	23782.836(10)	
R(13.5)	23782.674(12)	
R(14.5)	23782.485(6)	23782.158(0)
R(15.5)	23782.276(-11)	
R(16.5)	23781.992(12)	23781.658(5)

[a] Residuals in the fit of the data to the form $\nu = \nu_0 + B' J'(J' + 1) - B'' J'' (J'' + 1)$ are provided in parentheses following each line position, in units of 0.001 cm^{-1}. Error limits (1σ) are given in parentheses following each spectroscopic constant, in units of the last quoted digit. All rotationally resolved bands originated from the same lower state (the ground vibronic level). In order to improve the accuracy of the spectroscopic constants, all of the bands were simultaneously fitted under the constraint that they have the same value of B''.

Table B.33 (continued)

R(18.5)		23781.028(9)
Spectroscopic Constants		
ν_0 (cm^{-1})	23781.8000(31)	23781.4956(33)
B' (cm^{-1})	0.141670(29)	0.141398(32)
r′ (Å)	2.20825(23)	2.20890(25)
B_0'' (cm^{-1})	0.158134(17)	0.157956(19)
r_0'' (Å)	2.09013(11)	2.08992(13)

[a] Residuals in the fit of the data to the form $\nu = \nu_0 + B' J'(J' + 1) - B'' J'' (J'' + 1)$ are provided in parentheses following each line position, in units of 0.001 cm^{-1}. Error limits (1σ) are given in parentheses following each spectroscopic constant, in units of the last quoted digit. All rotationally resolved bands originated from the same lower state (the ground vibronic level). In order to improve the accuracy of the spectroscopic constants, all of the bands were simultaneously fitted under the constraint that they have the same value of B″.

Table B.34 Constants of the A[16.0]3.5 state based on rotationally resolved data.[a]

	$^{191}Ir^{28}Si$	$^{193}Ir^{28}Si$
Band	ν_0 (cm^{-1})	ν_0(cm^{-1})
4-0	17450.7376(-1.5475)	17450.1329(-1.5368)
5-0	17812.7943(2.4553)	17811.7907(2.4376)
6-0	18167.7443(0.8255)	18166.4400(0.8218)
7-0	18519.9267(-2.0978)	18518.3803(-2.0847)
10-0	19578.8610(0.3645)	19576.8578(0.3622)
Fitted Vibrational Constants:		
T_0 (cm^{-1})	16005.33(1461)	16006.75(1451)
ω_e' (cm^{-1})	365.42(472)	364.77(468)
$\omega_e'x_e'$ (cm^{-1})	0.737(308)	0.709(305)
k_e' (mdyn/Å)	1.920(50)	1.916(49)
Vibrational Level	B_v' (cm^{-1})	B_v' (cm^{-1})
4	0.136668(0.001103)	0.136497(0.001127)
5	0.134954(-0.000224)	0.134796(-0.000204)
6	0.134045(-0.000746)	0.133872(-0.000759)
7	0.133566(-0.000838)	0.133359(-0.000902)
10	0.133948(0.000705)	0.133889(0.000738)
Fitted Rotational Constants:		
B_e' (cm^{-1})	0.137306(1671)	0.137034(1731)
r_e' (Å)	2.243(14)	2.244(14)
α_e' (cm^{-1})	0.000387(613)	0.000370(635)
α_e' (cm^{-1}, Pekeris)	0.000408	0.000394

[a] Measured band origins have been fitted to the formula $\nu_{v'-0} = T_0 + v'\omega_e' - (v'^2 + v')\omega_e'x_e'$ to extract the spectroscopic constants T_0, ω_e', and $\omega_e'x_e'$. Provided in parentheses following the values of ν_0 are the residuals in the least-squares fit. The 1σ error limits in the fitted constants are provided in parentheses following the value, in units of the last digit quoted. Similarly, the measured B_v' values have been fitted to the formula $B_v' = B_e' - (v' + ½)\,\alpha_e'$ and residuals in the fit are given in parentheses. The equilibrium bond length, r_e' is then calculated from the B_e' value. The 1σ error limits are provided in parentheses following the fitted values of B_e', r_e', and α_e', in units of the last digit quoted.

The Pekeris relationship, which is valid for molecules that follow the Morse potential, provides an expression for the value of α_e in terms of B_e, ω_e, and $\omega_e x_e$ as:
$\alpha_e = [6(\omega_e x_e B_e^3)^{1/2} - 6B_e^2]/\omega_e$.

This expression is used to calculate α_e' (Pekeris), which is listed in the table above. In this case, the fitted value of α_e is close to that predicted by the Pekeris relationship, suggesting that the bands are relatively unperturbed and the potential function is reasonably well-approximated by a Morse potential, at least over the range probed in these experiments.

Table B.35 Constants of the B[16.0]1.5 state based on rotationally resolved data.[a]

	$^{191}Ir^{28}Si$	$^{193}Ir^{28}Si$
Band	ν_0 (cm^{-1})	ν_0(cm^{-1})
5-0	17956.4130	17955.3050
6-0	18349.8878	18348.4722
7-0	18744.1086	18742.3968
Fitted Vibrational Constants:		
T_0 (cm^{-1})	16000.2302	16000.8290
ω_e' (cm^{-1})	388.99843	388.62315
$\omega_e'x_e'$ (cm^{-1})	-0.37303	-0.37867
k_e' (mdyn/Å)	2.176	2.174
Vibrational Level	B_v' (cm^{-1})	B_v' (cm^{-1})
5	0.139037(0.000016)	0.138884(-0.000019)
6	0.138547(-0.000033)	0.138506(0.000037)
7	0.138155(0.000016)	0.138017(-0.000019)
Fitted Rotational Constants:		
B_e' (cm^{-1})	0.141446(199)	0.141287(225)
r_e' (Å)	2.2100(16)	2.2098(18)
α_e' (cm^{-1})	0.000441(77)	0.000433(88)
α_e' (cm^{-1}, Pekeris)	---	---

[a] Measured band origins have been fitted to the formula $\nu_{v'-0} = T_0 + v'\omega_e' - (v'^2 + v')\omega_e'x_e'$ to extract the spectroscopic constants T_0, ω_e', and $\omega_e'x_e'$. In this case, the three measured bands provide a unique solution for T_0, ω_e', and $\omega_e'x_e'$ so the residuals are zero and no error estimate can be provided for these constants. Similarly, the measured B_v' values have been fitted to the formula $B_v' = B_e' - (v' + ½)\,\alpha_e'$ and residuals in the fit are given in parentheses. The equilibrium bond length, r_e' is then calculated from the B_e' value. The 1σ error limits are provided in parentheses following the fitted values of B_e', r_e', and α_e', in units of the last digit quoted.

The Pekeris relationship, which is valid for molecules that follow the Morse potential, provides an expression for the value of α_e in terms of B_e, ω_e, and $\omega_e x_e$ as:
$\alpha_e = [6(\omega_e x_e B_e^3)^{1/2} - 6B_e^2]/\omega_e$.

This expression could not be used to estimate the value of α_e' in this case, due to the negative value of the anharmonicity. The negative value of $\omega_e'x_e'$ suggests that the B[16.0]1.5 state is perturbed. This is not surprising given the large number of Ω=1.5 states in the vicinity.

Table B.36 Constants of the D[18.0]1.5 state based on rotationally resolved data.[a]

	$^{191}Ir^{28}Si$	$^{193}Ir^{28}Si$
Band	ν_0 (cm^{-1})	ν_0(cm^{-1})
0-0	18023.7785(-0.5685)	18023.6992(-0.5701)
1-0	18419.2633(1.7054)	18418.8985(1.7104)
2-0	18809.2783(-1.7054)	18808.6668(-1.7104)
3-0	19205.1928(0.5685)	19204.4066(0.5701)
Fitted Vibrational Constants:		
T_0 (cm^{-1})	18024.35(248)	18024.27(249)
ω_e' (cm^{-1})	393.00(521)	392.65(523)
$\omega_e'x_e'$ (cm^{-1})	-0.107(1271)	-0.135(1275)
k_e' (mdyn/Å)	2.221(59)	2.220(59)
Vibrational Level	B_v' (cm^{-1})	B_v' (cm^{-1})
0	0.144503(0.000246)	0.144302(0.000235)
1	0.143272(-0.000302)	0.143119(-0.000286)
2	0.142757(-0.000134)	0.142610(-0.000133)
3	0.142397(0.000190)	0.142265(0.000184)
Fitted Rotational Constants:		
B_e' (cm^{-1})	0.144599(386)	0.144398(370)
r_e' (Å)	2.1858(29)	2.1873(28)
α_e' (cm^{-1})	0.000683(248)	0.000662(238)
α_e' (cm^{-1}, Pekeris)	---	---

[a] Measured band origins have been fitted to the formula $\nu_{v'-0} = T_0 + v'\omega_e' - (v'^2 + v')\omega_e'x_e'$ to extract the spectroscopic constants T_0, ω_e', and $\omega_e'x_e'$. Provided in parentheses following the values of ν_0 are the residuals in the least-squares fit. The 1σ error limits in the fitted constants are provided in parentheses following the value, in units of the last digit quoted. Similarly, the measured B_v' values have been fitted to the formula $B_v' = B_e' - (v' + ½)\,\alpha_e'$ and residuals in the fit are given in parentheses. The equilibrium bond length, r_e' is then calculated from the B_e' value. The 1σ error limits are provided in parentheses following the fitted values of B_e', r_e', and α_e', in units of the last digit quoted.

The Pekeris relationship, which is valid for molecules that follow the Morse potential, provides an expression for the value of α_e in terms of B_e, ω_e, and $\omega_e x_e$ as:
$\alpha_e = [6(\omega_e x_e\, B_e^3)^{1/2} - 6B_e^2]/\omega_e$.

This expression could not be used to estimate the value of α_e' in this case, due to the negative value of the anharmonicity. The negative value of $\omega_e'x_e'$ suggests that the D[18.0]1.5 state is perturbed. This is not surprising given the large number of Ω=1.5 states in the vicinity.

Table B.37 Constants of the F[17.8]1.5 state based on rotationally resolved data.[a]

	$^{191}Ir^{28}Si$	$^{193}Ir^{28}Si$
Band	ν_0 (cm^{-1})	ν_0(cm^{-1})
3-0	19056.1096	19055.3686
4-0	19459.7939	19458.7183
Fitted Vibrational Constants:		
T_0 (cm^{-1})	17845.06	17845.32
$\Delta G_{7/2}'$ (cm^{-1})	403.68	403.35
k_e' (mdyn/Å)	(2.343)[b]	(2.342)[b]
Vibrational Level	B_v' (cm^{-1})	B_v' (cm^{-1})
3	0.140935	0.140763
4	0.139258	0.139071
Fitted Rotational Constants:		
B_e' (cm^{-1})	0.146805(108)	0.146685(133)
r_e' (Å)	2.1693(8)	2.1687(10)
α_e' (cm^{-1})	0.001677(26)	0.001692(32)
α_e' (cm^{-1}, Pekeris)	---	---

[a] Measured band origins could not be fitted to the formula $\nu_{v'-0} = T_0 + v'\omega_e' - (v'^2 + v')\omega_e'x_e'$ to extract the spectroscopic constants T_0, ω_e', and $\omega_e'x_e'$ because only two bands were measured. The difference between these bands provided the value of $\Delta G_{7/2}'$. The value of T_0 was then calculated assuming zero anharmonicity. This is undoubtedly in error, but nevertheless provides an estimate of the correct value. Similarly, the measured B_v' values have been fitted to the formula $B_v' = B_e' - (v' + ½)\,\alpha_e'$. The fit is unique and exact, since two measurements are used to determine two spectroscopic constants. In this case, the 1σ errors in these constants (B_e' and α_e') are obtained by propagating the errors in the values of B_3' and B_4' that were obtained in the rotational fits. The equilibrium bond length, r_e' is then calculated from the B_e' value.

The Pekeris relationship, which is valid for molecules that follow the Morse potential, provides an expression for the value of α_e in terms of B_e, ω_e, and $\omega_e x_e$ as:
$\alpha_e = [6(\omega_e x_e B_e^3)^{1/2} - 6B_e^2]/\omega_e$.

This expression could not be used because we have no estimate of the anharmonicity for this state.

[b] The force constant provided for this state employs the value of $\Delta G_{7/2}'$ instead of ω_e'. Thus, it is most likely a lower limit to the true force constant of the state.

Table B.38 Constants of the J[20.9]3.5 state based on rotationally resolved data.[a]

	$^{191}Ir^{28}Si$	$^{193}Ir^{28}Si$
Band	ν_0 (cm^{-1})	ν_0(cm^{-1})
0-0	20946.5700(-0.0017)	20946.5791(-0.0002)
1-0	21360.3516(0.0050)	21360.0964(0.0006)
2-0	21770.6652(-0.0050)	21770.1522(-0.0006)
3-0	22177.5440(0.0017)	22176.7500(0.0002)
Fitted Vibrational Constants:		
T_0 (cm^{-1})	20946.5717(73)	20946.5793(8)
ω_e' (cm^{-1})	417.226(15)	416.976(2)
$\omega_e'x_e'$ (cm^{-1})	1.72568(372)	1.72986(41)
k_e' (mdyn/Å)	2.503(0)	2.503(0)
Vibrational Level	B_v' (cm^{-1})	B_v' (cm^{-1})
0	0.141884(-0.000004)	0.141740(0.000012)
1	0.141239(0.000000)	0.141071(-0.000004)
2	0.140603(0.000012)	0.140393(-0.000029)
3	0.139935(-0.000008)	0.139791(0.000021)
Fitted Rotational Constants:		
B_e' (cm^{-1})	0.142212(13)	0.142054(33)
r_e' (Å)	2.20403(10)	2.20380(16)
α_e' (cm^{-1})	0.000648(8)	0.000652(21)
α_e' (cm^{-1}, Pekeris)	0.000722	0.000723

[a] Measured band origins have been fitted to the formula $\nu_{v'-0} = T_0 + v'\omega_e' - (v'^2 + v')\omega_e'x_e'$ to extract the spectroscopic constants T_0, ω_e', and $\omega_e'x_e'$. Provided in parentheses following the values of ν_0 are the residuals in the least-squares fit. The 1σ error limits in the fitted constants are provided in parentheses following the value, in units of the last digit quoted. Similarly, the measured B_v' values have been fitted to the formula $B_v' = B_e' - (v' + ½)\,\alpha_e'$ and residuals in the fit are given in parentheses. The equilibrium bond length, r_e' is then calculated from the B_e' value. The 1σ error limits are provided in parentheses following the fitted values of B_e', r_e', and α_e', in units of the last digit quoted.

The Pekeris relationship, which is valid for molecules that follow the Morse potential, provides an expression for the value of α_e in terms of B_e, ω_e, and $\omega_e x_e$ as:
$\alpha_e = [6(\omega_e x_e\, B_e^3)^{1/2} - 6B_e^2]/\omega_e$.

This expression is used to calculate α_e' (Pekeris), which is listed in the table above. In this case, the fitted value of α_e is close to that predicted by the Pekeris relationship, suggesting that the bands are relatively unperturbed and the potential function is reasonably well-approximated by a Morse potential, at least over the range probed in these experiments.

Table B.39 Constants of the K[21.1]2.5 state based on rotationally resolved data.[a]

	$^{191}Ir^{28}Si$	$^{193}Ir^{28}Si$
Band	ν_0 (cm^{-1})	ν_0(cm^{-1})
0-0	21129.0989	21129.0858
1-0	21519.6139	21519.3462
2-0	21906.8399	21906.3267
Fitted Vibrational Constants:		
T_0 (cm^{-1})	21129.0989	21129.0858
ω_e' (cm^{-1})	393.80390	393.54013
$\omega_e'x_e'$ (cm^{-1})	1.64446	1.63989
k_e' (mdyn/Å)	2.230	2.230
Vibrational Level	B_v' (cm^{-1})	B_v' (cm^{-1})
0	0.140343(-0.000003)	0.140246(0.000007)
1	0.139768(0.000006)	0.139613(-0.000013)
2	0.139174(-0.000003)	0.139019(0.000007)
Fitted Rotational Constants:		
B_e' (cm^{-1})	0.140638(12)	0.140546(24)
r_e' (Å)	2.21633(10)	2.21559(19)
α_e' (cm^{-1})	0.000584(9)	0.000613(18)
α_e' (cm^{-1}, Pekeris)	0.000729	0.000728

[a] Measured band origins have been fitted to the formula $\nu_{v'-0} = T_0 + v'\omega_e' - (v'^2 + v')\omega_e'x_e'$ to extract the spectroscopic constants T_0, ω_e', and $\omega_e'x_e'$. In this case, only three bands were examined in high resolution, allowing an exact solution for these spectroscopic constants. As a result, the residuals are zero and no error estimates are available for the fitted constants.

Similarly, the measured B_v' values have been fitted to the formula $B_v' = B_e' - (v' + ½)\,\alpha_e'$ and residuals in the fit are given in parentheses. The equilibrium bond length, r_e' is then calculated from the B_e' value. The 1σ error limits are provided in parentheses following the fitted values of B_e', r_e', and α_e', in units of the last digit quoted.
The Pekeris relationship, which is valid for molecules that follow the Morse potential, provides an expression for the value of α_e in terms of B_e, ω_e, and $\omega_e x_e$ as:
$\alpha_e = [6(\omega_e x_e\, B_e^3)^{1/2} - 6B_e^2]/\omega_e$.

This expression is used to calculate α_e' (Pekeris), which is listed in the table above. In this case, the fitted value of α_e is close to that predicted by the Pekeris relationship, suggesting that the bands are relatively unperturbed and the potential function is reasonably well-approximated by a Morse potential, at least over the range probed in these experiments.

Table B.40 Constants of the L[22.1]2.5 state based on rotationally resolved data.

	$^{191}Ir^{28}Si$	$^{193}Ir^{28}Si$
Band	ν_0 (cm^{-1})	ν_0(cm^{-1})
0-0	22122.6843	22122.6612
1-0	22575.0541	22574.7361
Fitted Vibrational Constants:		
T_0 (cm^{-1})	22122.6843	22122.6612
$\Delta G_{1/2}'$ (cm^{-1})	452.3697	452.07492
k_e' (mdyn/Å)	(2.942)[b]	(2.942)[b]
Vibrational Level	B_v' (cm^{-1})	B_v' (cm^{-1})
0	0.143329	0.143181
1	0.142455	0.142194
Fitted Rotational Constants:		
B_e' (cm^{-1})	0.143766(40)	0.143675(37)
r_e' (Å)	2.19209(31)	2.19133(28)
α_e' (cm^{-1})	0.000874(32)	0.000987(35)
α_e' (cm^{-1}, Pekeris)	---	---

[a] Measured band origins could not be fitted to the formula $\nu_{v'-0} = T_0 + v'\omega_e' - (v'^2 + v')\omega_e'x_e'$ to extract the spectroscopic constants T_0, ω_e', and $\omega_e'x_e'$ because calibrated values of the band origins were only obtained for two bands. As a result, only T_0 and $\Delta G_{1/2}'$ could be determined, and the resulting values were exact, and no error limits could be provided.

Similarly, the measured B_v' values have been fitted to the formula $B_v' = B_e' - (v' + ½)\,\alpha_e'$. The fit is unique and exact, since two measurements are used to determine two spectroscopic constants. In this case, the 1σ errors in these constants (B_e' and α_e') are obtained by propagating the errors in the values of B_0' and B_1' that were obtained in the rotational fits. The equilibrium bond length, r_e' is then calculated from the B_e' value.

The Pekeris relationship, which is valid for molecules that follow the Morse potential, provides an expression for the value of α_e in terms of B_e, ω_e, and $\omega_e x_e$ as:
$\alpha_e = [6(\omega_e x_e B_e^3)^{1/2} - 6B_e^2]/\omega_e$.

This expression could not be used because we have no estimate of the anharmonicity for this state.

[b] The force constant provided for this state employs the value of $\Delta G_{1/2}'$ instead of ω_e'. Thus, it is most likely a lower limit to the true force constant of the state.

Table B.41 Constants of the N[23.3]2.5 state based on rotationally resolved data.[a]

	$^{191}Ir^{28}Si$	$^{193}Ir^{28}Si$
Band	ν_0 (cm^{-1})	ν_0(cm^{-1})
0-0	23347.8670	23347.8577
1-0	23781.8000	23781.4956
Fitted Vibrational Constants:		
T_0 (cm^{-1})	23347.8670	23347.8577
$\Delta G_{1/2}'$ (cm^{-1})	433.93297	433.63795
k_e' (mdyn/Å)	(2.707)[b]	(2.707)[b]
Vibrational Level	B_v' (cm^{-1})	B_v' (cm^{-1})
0	0.142699	0.142541
1	0.141670	0.141398
Fitted Rotational Constants:		
B_e' (cm^{-1})	0.143214(32)	0.143113(41)
r_e' (Å)	2.19631(25)	2.19563(32)
α_e' (cm^{-1})	0.001029(35)	0.001143(41)
α_e' (cm^{-1}, Pekeris)	---	---

[a] Measured band origins could not be fitted to the formula $\nu_{v'-0} = T_0 + v'\omega_e' - (v'^2 + v')\omega_e'x_e'$ to extract the spectroscopic constants T_0, ω_e', and $\omega_e'x_e'$ because calibrated values of the band origins were only obtained for two bands. As a result, only T_0 and $\Delta G_{1/2}'$ could be determined, and the resulting values were exact, and no error limits could be provided.

Similarly, the measured B_v' values have been fitted to the formula $B_v' = B_e' - (v' + ½)\,\alpha_e'$. The fit is unique and exact, since two measurements are used to determine two spectroscopic constants. In this case, the 1σ errors in these constants (B_e' and α_e') are obtained by propagating the errors in the values of B_0' and B_1' that were obtained in the rotational fits. The equilibrium bond length, r_e' is then calculated from the B_e' value.

The Pekeris relationship, which is valid for molecules that follow the Morse potential, provides an expression for the value of α_e in terms of B_e, ω_e, and $\omega_e x_e$ as:
$\alpha_e = [6(\omega_e x_e B_e^3)^{1/2} - 6B_e^2]/\omega_e$.

This expression could not be used because we have no estimate of the anharmonicity for this state.

[b] The force constant provided for this state employs the value of $\Delta G_{1/2}'$ instead of ω_e'. Thus, it is most likely a lower limit to the true force constant of the state.